PACIFIC EARTHQUAKE ENGINEERING
RESEARCH CENTER

PEER NGA-West2 Database

Timothy D. Ancheta
Pacific Earthquake Engineering Research Center

Robert B. Darragh
Pacific Engineering and Analysis

Jonathan P. Stewart
Emel Seyhan
University of California, Los Angeles

Walter J. Silva
Pacific Engineering and Analysis

Brian S. J. Chiou
California Department of Transportation

Katie E. Wooddell
Pacific Gas & Electric Company

Robert W. Graves
United States Geologic Survey

Albert R. Kottke
Pacific Earthquake Engineering Research Center

David M. Boore
United States Geologic Survey

Tadahiro Kishida
Pacific Earthquake Engineering Research Center

Jennifer L. Donahue
Geosyntec Consultants

PEER 2013/03
MAY 2013

PEER NGA-West2 Database

Timothy D. Ancheta
Pacific Earthquake Engineering Research Center

Robert B. Darragh
Pacific Engineering and Analysis

Jonathan P. Stewart
Emel Seyhan
University of California, Los Angeles

Walter J. Silva
Pacific Engineering and Analysis

Brian S. J. Chiou
California Department of Transporation

Katie E. Wooddell
Pacific Gas & Electric Company

Robert W. Graves
United States Geological Survey

Albert R. Kottke
Pacific Earthquake Engineering Research Center

David M. Boore
United States Geological Survey

Tadahiro Kishida
Pacific Earthquake Engineering Research Center

Jennifer L. Donahue
Geosyntec Consultants

PEER Report 2013/03
Pacific Earthquake Engineering Research Center
Headquarters at the University of California, Berkeley

May 2013

ABSTRACT

The NGA-West2 project database expands on the current PEER NGA ground-motion database to include worldwide ground-motion data recorded from shallow crustal earthquakes in active tectonic regimes post 2003. Since 2003, numerous well-recorded events have occurred worldwide, including the 2003 **M**6.6 Bam (Iran), 2004 **M**6 Parkfield (California), 2008 **M**7.9 Wenchuan (China), 2009 **M**6.3 L'Aquila (Italy), 2010 **M**7.2 El Mayor-Cucupah (California and Mexico), 2010 **M**7 Darfield (New Zealand), 2011 **M**6.2 Christchurch (New Zealand), and several well-recorded shallow crustal earthquakes in Japan, among other events. The expanded database also includes 21,336 three-component records from 600 shallow crustal events with small-to-moderate magnitude located in CA. The NGA database has been extensively expanded to include the recorded ground-motion data and metadata, in these and other recent events. The updated database has a magnitude range of 3 to 7.9, and a rupture distance range of 0.05 to 1533 km. The estimated or measured time-averaged shear-wave velocity in the top 30 m at the recording sites (V_{s30}) ranges from 94 to 2100 m/sec. The NGA-West2 database more than doubles the size of the previous NGA database for moderate-to-large magnitude events (**M** > 6). The database includes uniformly processed time series as well as response spectral ordinates for 111 periods ranging from 0.01 to 20 sec and 11 different damping ratios. Extensive metadata have also been collected and added to the database. The expanded database is currently being utilized by NGA researchers to update the 2008 ground-motion prediction equations.

ACKNOWLEDGMENTS

This project was sponsored by the Pacific Earthquake Engineering Research Center (PEER) and funded by the California Earthquake Authority (CEA), California Department of Transportation, and the Pacific Gas & Electric Company. Any opinions, findings, and conclusions or recommendations expressed in this material are those of the authors and do not necessarily reflect those of the above mentioned agencies.

The authors acknowledge Yousef Bozorgnia for his leadership, guidance, and enthusiasm of this multi-year project, and the PEER staff for their editing and project support.

We are grateful for Badie Rowshandel's of the CEA comprehensive review that clarified several important points in the report.

The authors gratefully acknowledge the sharing of strong-motion catalog/database and other documentation by the NGA ground motion prediction equation developers especially Norm Abrahamson, Gail Atkinson, Ken Campbell, Ed Idriss, and Bob Youngs. This project and PEER-NGA-West2 would not have succeeded without their unselfish contributions of time, data, informal and formal reviews, guidance, and thoughtful questions and concerns.

The authors would also like to thank Dave Wald for providing slopes for stations, Carlos Gutierrez for providing geology and slope based V_{s30} estimations, and Alan Yong for his kind help in terrain assignments. We thank Annemarie Baltay for her review of the small-to-moderate magnitude event catalog. Ronnie Kamai and Linda Al Atik kindly carried out QA of the small-to-moderate magnitude data.

The staff and agencies that record, process and disseminate earthquake data from California earthquakes are acknowledged both for their long-term efforts in this field, as well as,, response to requests for additional recordings, magnitudes, and other metadata. These are Peggy Helweg of BDSN, Ellen Yu of CIT-SCSN, Tony Shakal, Moh Huang and Hamid Haddadi of CGS-CSMIP, and Chris Stephens of the USGS.

In addition, many individuals and organizations also contributed data and expertise to the database development and they have our thanks. These individuals and organizations are Agbabian and Associates, ALYESKA, John Anderson, Jack Boatwright, Roger Borcherdt, Jon Bray, Central Weather Bureau of Taiwan, California Department of Transportation, California Earthquake Authority, CEORKA, Kandilli Observatory and Earthquake Engineering Research Institute of Boğaçizi University, Kevin Clahan, COSMOS, CUREE, Doug Dreger, Bill Ellsworth, ESD, Vladimir Graizer, Tom Hanks, Istanbul Technical University, Japan Meteorological Association, Japan Railroad, Rob Kayen, Kik-Net, K-Net, LADWP, Kandilli Observatory and Earthquake Engineering Research Institute of Boğaçizi University, William H. K. Lee, Martin Mai, NCREE, Bob Nigbor, Pacific Gas & Electric Company, Mark Petersen, Maury Power, Ellen Rathje, Cliff Roblee, Kyle Rollins, ROSRINE, SCEC, Linda Seekins, Seismic Networks (CIT-SCSN-SCEC, ISC, UCB-BDSN, USGS), Shannon and Wilson, Jaime Steidl, Paul Somerville, Paul Spudich, Jon Stewart, Ken Stokoe, USC, URS Corporation, Dave Wald, Jennie Watson-Lamprey, Donald Wells, Kuo-Liang Wen, Chris Wills, and Yuehua Zeng.

ERRATA
PEER Report No. 2013-03

PEER NGA-West Database

July 16, 2013

Page 125, in Appendix D:

Column	Column Name (units)	Description
BR	Rfn.Clst	Obsolete, no longer used
BS	Rfp.Clst	Obsolete, no longer used
BT	Rfn.Imd	Obsolete, no longer used
BU	T	Generalized T Coordinate at the site, produced using the algorithm in Appendix A of Spudich and Chiou (2008)

Page 130, in Appendix D:

Column	Column Name (units)	Description
JO	Dip_seg (deg)	Dip of the closest segment for multi-segment/multi-fault events. 0^{o} <= Dip <= 90^{o}.
JP	Rake_seg (deg)	Rake of the closest segment for multi-segment/multi-fault events. -180^{o} <= Rake <= 180^{o}

Page 70:

$$R_Y = -1 * (D + L/2) \tag{4.6}$$

Page 57, top of second paragraph:

An outlier in Figure 3.27 is KiK-net site TKCH08 …

CONTENTS

LIST OF FIGURES

LIST OF TABLES

1 Overview of NGA-West2 Ground Motion Database

1.1 MOTIVATION OF NGA-WEST2 GROUND MOTION DATA SET

In 2003, the Pacific Earthquake Engineering Research Center (PEER) initiated a large research program to develop next generation ground motion prediction equations (GMPEs or "attenuation relationships") for shallow crustal earthquakes in active tectonic regions (now called NGA-West1). The project concluded in 2008 and provided several important products, including a strong-motion database of recorded ground motions and a set of peer-reviewed GMPEs (Power et al. 2008). Many researchers, practitioners, and organizations throughout the world are now using the NGA-West1 models and the NGA-West1 database for research and engineering applications.

The importance of a common high-quality ground-motion database was recognized early in the NGA-West1 research program. Having project investigators use a common database fostered collaboration between GMPE development groups and made model-to-model comparisons more meaningful and could potentially reduce unwarranted model-to-model variation. It had also been recognized that some of the noted differences between previous GMPEs could be attributed to the unintentional differences in empirical databases. Such differences also made it difficult to conduct a fair and systematic comparison of GMPEs.

As successful as the original NGA-West1 program was, there were some additional and complementary ground motion issues and supporting research projects that could not be addressed in NGA-West1 program due to time constraints. NGA-West2 expands the original moderate-to-large magnitude NGA-West1 database with data from recent significant world-wide crustal earthquakes that occurred after 2003. Additionally, small-to-moderate magnitude California earthquakes were added to aid the "small magnitude" scaling of the NGA GMPEs, as well as several factors that are discussed in more detail in Chiou et al. (2010). The goals included evaluation of small-to-moderate magnitude scaling and GMPE extrapolation, possible regionalization within California, and "Single-Station" standard deviation.

First, several researchers observed that the NGA-West1 GMPEs over-predicted the small magnitude ground motions; therefore, by adding these extensive small-to-moderate data set, the "small magnitude" scaling of the NGA-West1 GMPEs is being updated. An earlier analysis by Chiou and Youngs (2006) found that their interim model on average under-predicted peak ground acceleration (PGA) from the $M \leq 4$ earthquakes and slightly over-predicted PGA from the $4.2 \leq M \leq 4.8$ earthquakes. Similar findings were obtained by Chiou and Youngs (2008b) against their final NGA-West1 model. Campbell (2008, 2011) found a similar bias in the NGA-West1 GMPE of Campbell and Bozorgnia (2008). Misfits to the California M < 5 data by the other NGA-West1 models have also been reported by Cua and Heaton (2008) and Atkinson and Morrison (2009). All these studies point to the need to modify the NGA-West1 models' scaling of ground motions for small and moderate earthquakes, which were poorly sampled in the previous NGA-West1 database; see Figure 1.2.

Second, due to the less frequent occurrence of moderate-to-large magnitude earthquakes and/or a sparse strong-motion seismic network, a large portion of the data collected from many active tectonic regions has been in the relatively small magnitude (M < 5) range [e.g., Bommer et al. (2007); and Atkinson and Morrison (2009)]. As a result, quantitative comparisons of the locally recorded ground motions with the NGA-West1 models often require extrapolating to a lower magnitude range than what was used in their development.

Third, California's advantage of having abundant ground motion data from well-recorded earthquakes in both the moderate-to-large (M ≥ 5.5) and the small-to-moderate (3 ≤ M ≤ 5.5) magnitude ranges also allows us to examine the regional variation of ground motion within California over a wide range of magnitude. The issue of regional variability has been an important topic for earthquake hazard analysis worldwide. Similar explorations, using different datasets from other regions have been conducted (Douglas 2004, 2007; Bommer et al. 2010; Atkinson and Morrison 2009).

Finally, the small magnitude database can also be used for constraining "Single-Station" (i.e., intra-site) standard deviation (sigma) of the NGA-West2 GMPEs. A formal definition of single-station standard deviation is defined in Al Atik et al. (2012).

The set of recordings from events included in the NGA-West1 database, the additional world-wide events post 2003, and the small-to-moderate magnitude California events comprise the NGA-West2 ground motion database. The project also continues to improve the metadata as well as add new supporting information to the NGA-West2 database to aid in the update of the NGA-West2 GMPEs.

1.2 WORLD-WIDE MODERATE-TO-LARGE MAGNITUDE CRUSTAL EARTHQUAKE DATA

The NGA-West2 database started with the NGA-West1 database (http://peer.berkeley.edu/peer_ground_motion_database) of ground motion recordings from shallow crustal events in active tectonic regions that was completed in 2003 (Chiou et al. 2008). The NGA-West2 database continues the similar methodology of data collection and record processing as in the previous database and includes additional selected earthquake records up to February 2011.

Since 2003, numerous well-recorded significant shallow crustal events have occurred worldwide, including the 2003 **M**6.6 Bam (Iran), 2004 **M**6 Parkfield (California), 2008 **M**7.9 Wenchuan (China), 2009 **M**6.3 L'Aquila (Italy), 2010 **M**7 El Mayor-Cucupah (California and Mexico), 2010 **M**7 Darfield (New Zealand), 2011 **M**6.3 Christchurch, and several well-recorded shallow crustal earthquakes in Japan. The NGA-West1 database has been extensively expanded to include the recorded ground-motion data and metadata from these and other recent events. Figure 1.1 shows the distribution of the epicenter locations of the selected worldwide shallow crustal events, and Figure 1.2 highlights the magnitude-closest distance distribution of the 174 NGA-West1 events and the 161 added events. These new data more than doubled the number of recordings with M > 5.5 from the earlier database (NGA-West 1).

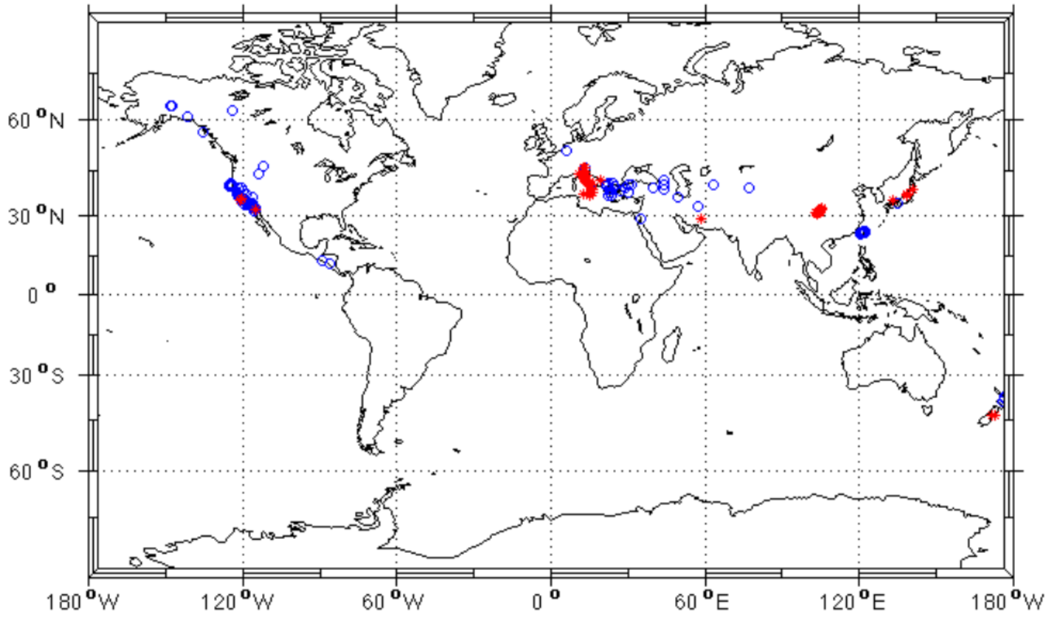

Figure 1.1 **Map of the epicentral distribution of the 335 selected world-wide events included in the NGA-West2 database. Open circles (blue) are events in the previous NGA-West1 database and solid stars (red) are events added in the NGA-West2 database.**

New events were selected based on a similar criteria used in the NGA-West1 project to ensure consistency within the dataset. Events are considered shallow crustal if they occur within the continental lithosphere. The region used to collect shallow events is considered "tectonically active" if the earthquake is not located in a stable continental region (SCR), within a subducting slab or on the interface between the slab and the continental lithosphere; typically these events are near a plate boundary. Additionally, events were not excluded if they occurred in close proximity (time and space) with a previous event. For example, 64 events after the **M**7.9 Wenchuan and two events following the 2009 **M**6.3 L'Aquila, Italy events were collected. The 1999 **M**6.1 Joshua Tree, California, event, which was left out of the NGA-West1 dataset due to time constraints, was populated in the new dataset.

There was considerable discussion on several of these earthquakes. For example, the working group recommended that the Wenchuan, China, earthquake rupture be classified as occurring in an active tectonic region. This recommendation was based on the observation that the region is undergoing active crustal shortening similar to other active mountain belts (Hubbard et al. 2010). However, it was noted that distance attenuation along some azimuths (particularly to the east) may have higher Q values more appropriate for stable continental regions (Wang and Lu 2011).

The Japanese data set was extensively expanded with the inclusion of the Tottori, Niigata, Chuetsu-oki, and Iwate earthquakes (see Table 2.1). The total number of recordings from Japan is now close to 2000 with the number of sites increasing from 22 to 1233 (Figure

3.1). The inclusion of these earthquakes allows for an examination of regional differences in attenuation, shallow site, and basin effects, among other source, path, and site attributes.

Records were collected from a number of agencies managing strong-motion networks located world-wide. Record selection followed a similar methodology used in the NGA-West1 project to ensure consistency within the dataset. Records were included for processing based on the following criteria:

1. Free-field record
2. Adequate signal-to-noise ratio
3. Location is known
4. Not co-located with another instrument on the same small pad

A recording may still be included in the dataset if the idealized conditions are not all met due to the importance of the recording. Cases where the criteria were relaxed include, but not limited to, single recording for an event and records in close proximity to the rupture plane. More details on record selection and quality are included in Sections 3.2 and 6 for the instrument siting information and record processing used.

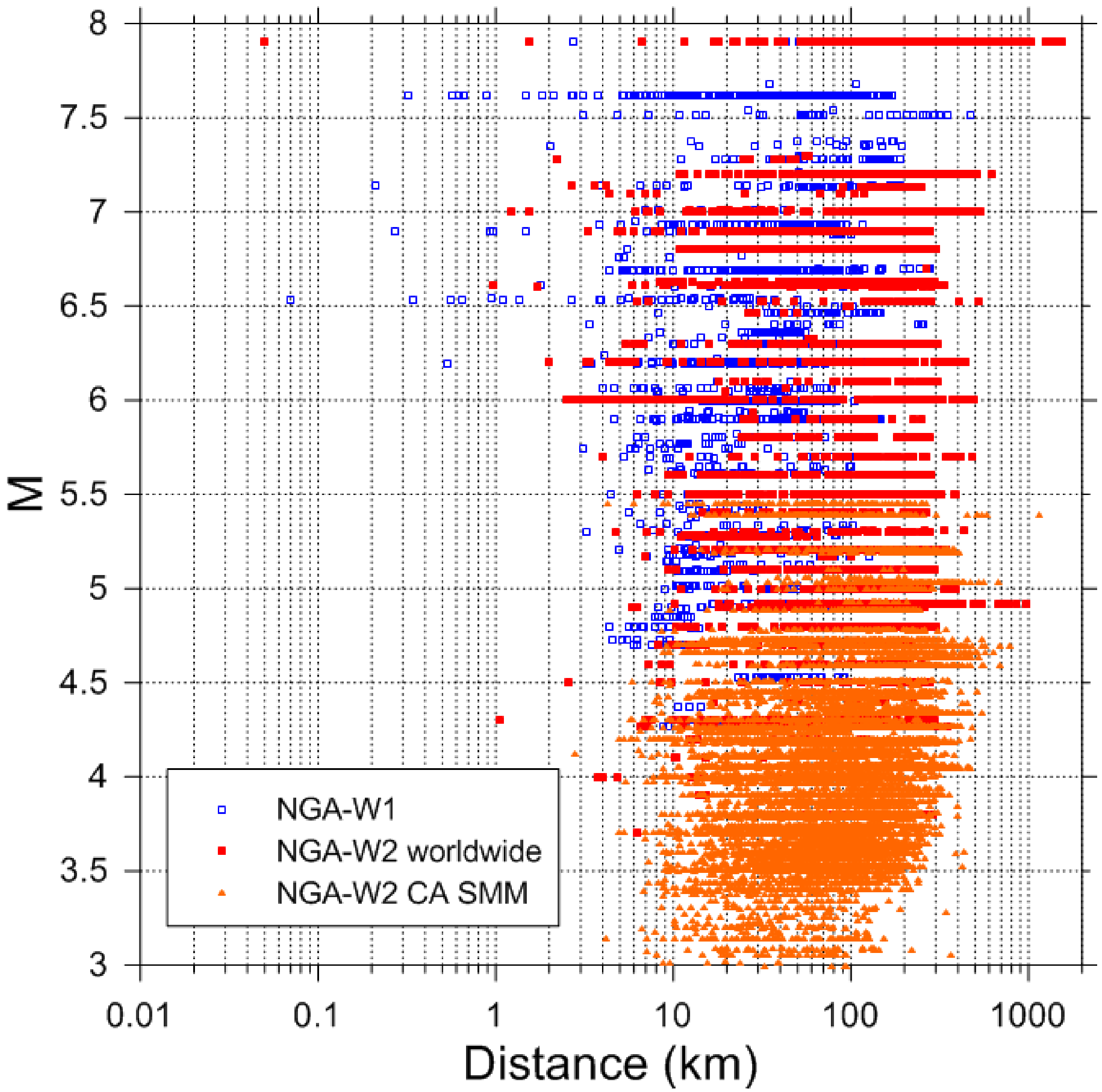

Figure 1.2 **Magnitude-distance distribution of strong-motion records in the NGA-West2 database (magnitudes 3 to 7.9). Open blue squares are stations included in the NGA-West1. Solid red squares are stations added from worldwide events. Orange triangles are stations added from California only from small-to-moderate magnitude events (magnitudes 3 to 5.5).**

1.3 CALIFORNIA SMALL-TO-MODERATE MAGNITUDE DATA

In addition to the world-wide moderate-to-large magnitude data, thousands of ground motions recorded from small-to-moderate magnitude events in California were also added, with M between 3 and 5.5. The collection of the small-to-moderate magnitude data set was motivated by several factors that are discussed in more detail in Chiou et al. (2010).

Records from small-to-moderate crustal California earthquakes were collected from the four major networks operating in California: Berkeley Digital Seismic Network (BDSN)/Northern California Earthquake Data Center (NCEDC), California Institute of Technology (CIT)/Southern California Seismic Network (SCSN)/Southern California Earthquake Center (SCEC), California Geological Survey (CGS)/California Strong Motion Program (CSMIP), and the United States Geological Survey (USGS). In collaboration with Ellen Yu of CIT\SCSN\SCEC and Peggy Helweg of BDSN\NCEDC, three-component data from continuously recording broadband or strong-motion channels were collected. Supplemental strong-motion data were obtained from California Geological Survey (CGS)\California Strong Motion Instrumentation Program (CSMIP), California Earthquake Strong Motion Data (CESMD), and the U. S, Geological Survey \National Strong Motion Program) (USGS\NSMP), which also both provided data for the moderate and large magnitude events. In total we received in excess of 230,000 recordings.

Similar to the world-wide data, recordings were selected for inclusion in the database based on several factors including favorable signal to noise ratio and recorder location (e.g., downhole, structural, and tunnel recording sites, among others, were excluded). Additional considerations specific to this dataset included availability of instrument parameters (e.g., natural frequency, damping, sample rate, and anti-alias filter corner) and complexity in the baseline error (e.g., baseline errors with multiple jumps or time dependent trends were excluded). Therefore, record selection was generally stricter than the world-wide data. In total 12,818 three-component records were collected from 266 events. The data set has a moment magnitude (M) range of 3 to 5.5, and a rupture distance range of 2 to 1100 km. Figure 1.3 shows the distribution of the epicenter locations, and Figure 1.2 highlights the magnitude-closest distance distribution of records collected from California small-to-moderate magnitude events.

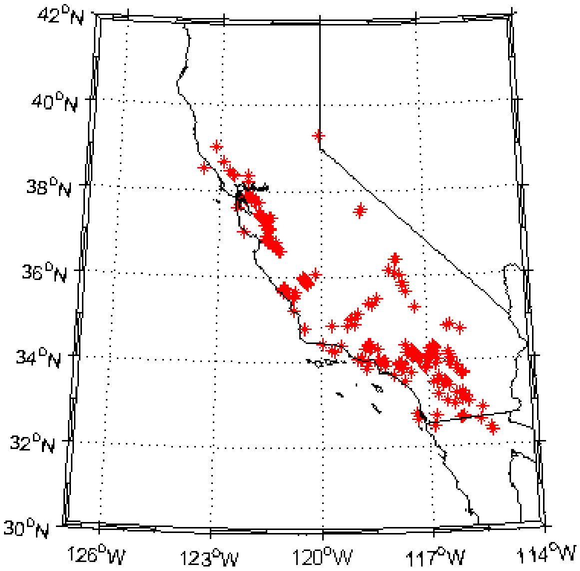

Figure 1.3 Map of the epicentral distribution of the 266 events added to the NGA-West2 database collected from the small-to-moderate magnitude data in California.

1.4 METADATA

The metadata tables were developed under direction of different NGA-West2 working groups, and final information in the data tables went through a significant review process. Each working group contained a panel of experts within that field of interest. Four metadata tables created by different working groups: the earthquake source table, site database, propagation path table, and record catalog. The data tables used in the NGA-West1 project (Chiou et al. 2008) were used as the start of the current tables. In addition to adding information to the NGA-West2 database from additional station/events, there was a significant review of existing metadata. New types of metadata were added to each data table (for example, R_x, the horizontal distance from the top of the fault to the site along a local strike-perpendicular direction) and significant improvements have been made toward uniformity and transparency in metadata collection and estimation. A summary flatfile was created from the metadata tables that contain the key information used by the individual NGA-West2 GMPE model developers.

The earthquake source table contains earthquake source information, such as moment magnitude, hypocenter location, fault rupture dimensions, and focal mechanism. Earthquakes are given a unique earthquake ID number (EQID) as they are added. The information contained within the source table was collected and reviewed by the NGA-West2 Source Working Group, as detailed in Section 2. Section 2 details the source data collection efforts and event parameter selection methodology, and lists the finite fault inversions reviewed for the added events. Information contained in the source table were collected from finite fault inversions, high-quality location and moment tensor catalogs, or from a simulated fault geometry. Review of available and selection of the preferred finite fault closely followed the methodology used in the NGA-West1 study. Additionally, all events were given a newly proposed fault classification aimed at consistently separating what was referred to in the NGA-West1 project as mainshock and aftershock events.

The site database is a collection of information for each recording station, such as station coordinate, various proxies used for V_{s30} estimation, and V_{s30} code indicating how V_{s30} was estimated. A station is given a unique station sequence number (SSN) as it is added. The information contained in the site database was collected and reviewed by the NGA-West2 Task 8 working group, as detailed in Section 3. Section 3 details the metadata collection and review efforts for all station locations included in the NGA-West2 database. The information in the site database has been extensively reviewed for correctness, and a significant effort was made to collect measured site properties when available and inferred site properties through site characteristics that are widely available (i.e., surficial geology or topographic slope).

The propagation path table is a set of computed site-source path parameters used by the various directivity modelers and GMPE developers. The majority of the work required in developing the path parameters included developing routines to generate stable and reliable path parameters. The developed routines required the selected finite fault geometry, hypocenter location, and the station location as input. The individual directivity modelers and Brian Chiou calculated the majority of the path parameters. Description of path parameters and methodology used in their estimation is included in Section 4. Each recording included has all the widely used and newly proposed site-source distance measures estimated, and all recordings from events with selected finite fault models have the recently developed directivity parameters estimated.

The record catalog is a list of the strong-motion recordings included in the database. The record catalog also contains the spectral values, peak ground motion measures (PGA, PGV, and PGD), and the filter corner frequencies. Each record is given a unique record sequence number (RSN) as it is added. Paired with each record included are a series of uniformly formatted text files containing the three-component as-recorded response spectra, a new intensity measure of orientation independent horizontal spectra, called RotDnn (Boore 2010), and the Arias Intensity for various durations. The available pseudo-spectral accelerations are now provided at 111 periods ranging from 0.01 to 20 sec and for 11 different damping ratios ranging from 0.5% to 30%. Section 5 details the time series metrics calculated for each record and the record catalog.

Subsets of the pertinent information in all the tables are summarized in the database flatfile, which is used by the various working groups in the NGA-West2 project. The three ID numbers (RSN, SSN, and EQID) facilitate a linkage between the tables and aided in the creation of the final flatfile. Details of the information contained in the flatfile are included in Section 7 and Appendix C.

2 Earthquake Source Table

2.1 ORGANIZATION AND OBJECTIVES OF EARTHQUAKE SOURCE TABLE

We began with the earthquake source table developed in the original NGA-West1 project described by Chiou et al. (2008). The earthquake source table contains basic information about the seismic source, including earthquake origin date and time, moment magnitude, hypocenter location, focal mechanism, occurrence of primary surface rupture, and tectonic environment, among other metadata. The NGA-West2 project added data from 161 additional moderate-to-large world-wide earthquakes and 266 small-to-moderate magnitude California earthquakes for a total of 266 earthquakes with **M** greater than about 3. In addition, finite fault models for 63 (NGA-West1) and 14 (NGA-West2, included in Table 2.1) earthquakes were collected and systematically evaluated. The finite fault model provided additional information such as the dimension of fault rupture and depth to the top of rupture.

Major participants in the development of the source tables included members of the NGA-West2 Source Working Group of Jack Boatwright (USGS), Brian Chiou (CDOT), Robert Darragh (PE&A), and Rob Graves (USGS) and the following additional project researchers: Timothy Ancheta (PEER), Katie Wooddell (PG&E), Tadahiro Kishida (PEER), and Annemarie Baltay (USGS). Additionally, the information contained in the tables was improved through numerous discussions with the GMPE developers not mentioned above.

The objectives of this work were to provide the GMPE developers with consistent source parameters and classifications for all the earthquakes in the NGA-West2 dataset. Section 2.2 details the finite fault review methodology and the selected finite fault models included in the earthquake source table. Considerations for multi-segment ruptures are detailed in Section 2.3. Section 2.4 details the catalogs used to extract source parameters for the California small-to-moderate magnitude events. When a finite fault geometry was not available, an updated version of the methodology used by Chiou and Youngs (2008) for simulating unavailable source parameters was adopted in the NGA-West2 database. A brief description of method is included in Section 2.5. A consistent event classification (aftershock/mainshock) was developed to reduce inconsistent event selection between the GMPE developer groups. Section 2.6 details the classification methodology and defines the newly proposed distinction between a Class 1 (mainshock) and Class 2 (aftershock) event. Details of the event classification of the earthquake swarms and the Wenchuan aftershock parameters are included in Section 2.7 and 2.8.

The key contents of the source table to be fed into the flatfile include the event time, magnitude, location, mechanism, and finite fault geometry (strike, dip, length, width, top of rupture, etc.). A link to the electronic version and explanation of the source table can be found in Appendix A.

2.2 FINITE FAULT MODELS

An earthquake's finite fault model is a critical piece of information from which numerous other source and path data were derived. In the NGA-West1 database the finite fault geometry was defined by the end points of the top edge of rupture, the depth to the bottom edge of rupture, the fault dip angle, and the strike direction (Figure 2.1). The finite fault geometry was typically obtained, in the order of preference, from field observation of primary surface rupture, coseismic slip distribution obtained by inversions of waveform and geodetic data, and observation of aftershock distribution. When a slip inversion model was available, that model was also used to extract information about the rise time, rupture velocity, and other data related to the spatial characteristics of (coseismic) fault slip (such as existence of shallow asperity, percent of moment release in the top 5 km of crust).

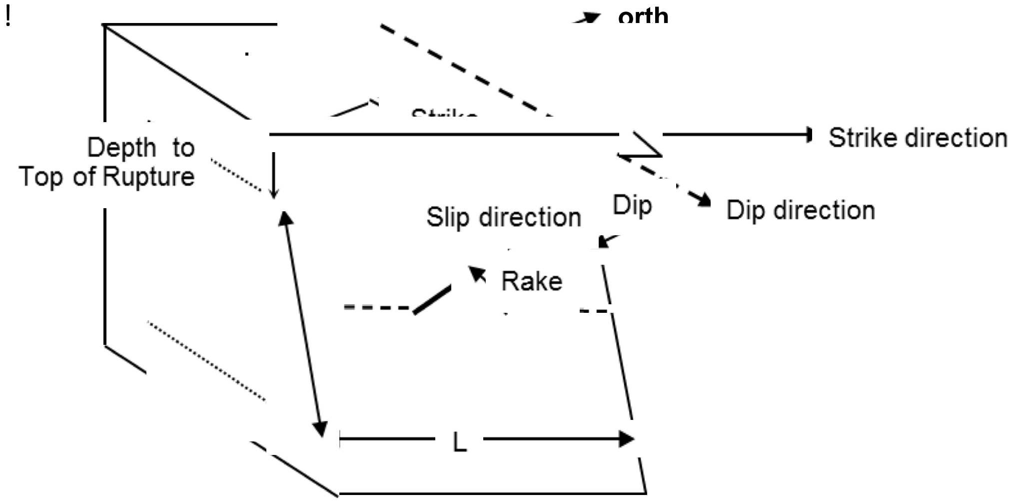

Figure 2.1 Schematic representation of strike, dip, rake, depth to top of rupture (Z_{TOR}), down dip width (W), and length (L).

The NGA-West1 finite fault models were built on three model collections previously used in ground-motion studies: PEER-NEAR (Silva et al. 1999a), USGS-Yucca Mountain (YM) (Spudich et al. 1996; Chiou et al. 2000). The PEER-NEAR is a set of finite fault models for shallow crustal earthquakes collected by Pacific Engineering and Analysis. Developed by USGS for the Yucca Mountain Project USGS-YM is for earthquakes in extensional regimes. These two model collections supplement each other, with only eight earthquakes overlapping between them. The third collection (Chiou et al. 2000] overlaps considerably with PEER-NEAR but contains several additional models that are not in PEER-NEAR.

We also expanded the collection by adding models for other earthquakes, especially more recent events. In total, finite fault models for 63 earthquakes were collected in NGA-West1. An additional 14 models were added in NGA-West2 (Table 2.1). Information about each finite fault model was obtained directly from the researchers or was extracted from their publications, some of which were in press. Some of the older models were presented in figures, therefore coordinates defining the fault rupture limits were manually digitized from those figures. We converted every model to a uniform format and to a latitude/longitude coordinate system.

The areal extent of the rupture was a main issue in evaluating the finite fault model. When a model included regions of zero or low level of slip near the edges, the model area was reduced or trimmed back. The consensus reached among the NGA GMPE developers and other attending seismologists at the June 2004 NGA developers meeting that regions with more than 50 cm of coseismic slip should not be trimmed off. Also, it was agreed that the final model should maintain the primary surface rupture observed in the field. Trimming the areal extent of the finite fault plane of newly added earthquakes is performed using the methodology used in the NGA-West1 project. An example application of the finite fault model selection and fault trimming is provided in Stewart et al. (2012) for one of the events in the database (L'Aquila, Italy).

If there were more than one rupture model for an earthquake, a careful evaluation of the available models was conducted to develop a preferred model. In general, the dimension of the preferred model is close to the average of the available models. The preferred finite fault models went through several iterations of reviews by NGA-West1 Working Group #4 (during a meeting in September 2003) and the NGA GMPE developers (during two ground motion prediction equation developer meetings in May and June of 2004). Furthermore, Paul Somerville, Nancy Collins, and their colleagues at URS Corporation (personal communication, 2004) systematically reviewed the finite fault models and provided useful feedback and recommendations that were incorporated into the final models for NGA-West1 (Chiou et al. 2008). For NGA-West2, the finite fault models were reviewed by the Source Working Group of Jack Boatwright, Brian Chiou, Robert Darragh, and Robert Graves at several working group meetings, and reported back to a larger group of GMPE developers. The preferred finite fault model for each added event is listed in Table 2.1 along with alternate models considered.

A number of events within the NGA-West2 database have multiple segments that were identified to have ruptured in the event. A discussion on the methodology for assigning event parameters is included in Section 2.3 below.

Table 2.1 NGA-West2: Finite fault models for earthquakes added in NGA-West2.

EQID	Earthquake Name	Year	Month-Day	Hour-Min	**M**	Primary Choice	Others
0262	Montenegro, Yugoslavia	1979	0415	0619	7.1	Benetaos and Kiratzi (2006)	
0146	Joshua Tree, California	1992	0423	0450	6.1	Hough and Dreger (1995)	
0176	Tottori, Japan	2000	1006	1330	6.6	Piatanesi et al. (2007)	Sekiguchi et al. (2000)
0177	San Simeon, California	2003	1222	1915	6.5	Ji et al. (2004)	Hardebeck et al. (2004), Dreger et al. (2004)
0178	Bam, Iran	2003	1226	0156	6.5	Jackson et al. (2006)	
0180	Niigata, Japan	2004	1023	0856	6.6	Asano and Iwata (2009)	Hikima and Koketsu (2005)
0179	Parkfield, California	2004	0929	1715	6.0	Custudio et al. (2005)	
0278	Chuetsu-oki, Japan	2007	0716	1013	6.8	Miyake et al. (2010)	Cirella et al. (2009)
0279	Iwate, Japan	2008	0613	2343	6.9	Suzuki et al. (2010)	
0274	L'Aquila, Italy	2009	0406	0133	6.3	Scognamiglio et al. (2010)	
0277	Wenchuan, China	2008	0512		7.9	Koketsu et al. (2009)	Shao et al. (2010), Wang et al. (2008)
0280	El Mayor-Cucupah, Mexico	2010	0404	2240	7.2	Wei et al. (2011)	Ji et al. (in prep.)
0281	Darfield, New Zealand	2010	0903	1635	7.0	Beavan et al. (2010)	
0346	Christchurch, New Zealand	2011	0221	2351	6.2	Holden (2011)	Beavan et al. (2011)

2.3 PARAMETERS FROM MULTI-SEGMENT EVENTS

Several earthquakes that have finite source models have multiple segments, e.g., Kern County, San Fernando, Kobe, Landers, and Hector Mine, among others. A rupture (generally defined as significant slip, greater than about 50 cm in a slip inversion) could occur on a multi-segment fault or on multiple faults. A multi-segment rupture consists of two or more contiguous planar quadrilaterals joined along their down-dip edges, sharing a single hypocenter. A multi-fault rupture occurs on two or more non-contiguous surfaces (which might each be multi-segment) and each surface having its own hypocenter. A list of the events with multi-segment ruptures along with the event parameters for each rectangular fault segments are included in Table A.2 in Appendix A.

The multi-segment/multi-fault nature of these events may have a significant impact on the resulting ground motions or parameters. Parameters that are affected include some directivity parameters, the source-to-site distance measures, and the reported event parameters. A description of how the directivity models developed under the NGA-West2 include multi-segment ruptures is included in the Task 1 Directivity summary report by PEER. For example, in the directivity model developed by Badie Rowshandel (personal communication, 2013), multi-segment rupture is directly included; that is, directivity contributions from a segment or a group of segments each rupturing from its "hypocenter", (that is the point of rupture initiation on each segment, for one of the segments it is the earthquake hypocenter, for other segments it is assumed to be the closest point to the segment that ruptured from the earthquake hypocenter or other appropriate point) are computed and summed. The method for determining event parameters reported in the source table and subsequently in the flatfile for multi-segment/multi-fault ruptures is described below. The method for determining the source-to-site distance measures in included in Section 4.2 and 4.3.

Following the methodology used in the NGA-West1 database, Brian Chiou (personal communication, 2012), assignment of the multi-segment/fault event parameters to be reported on the flatfile was based on a weighting scheme or summation. Typically, the fault length and area were based on a summation over the rectangular fault segments. Exceptions to this include events with significantly overlapping segments either along strike or down dip as listed in Table 2.2. Due to work estimating R_Y using the coordinate system (GC2 or second version of a generalized coordinate system) developed by Chiou and Spudich (personal communication, 2013) a number of fault lengths are modified to appropriately account for segment overlap. The impact of GC2 provides a smooth transformation of coordinates, especially for multi-segment/multi-fault earthquakes. After review of the new coordinate system and discussions with Chiou and Spudich, the length of the fault used in the calculations of R_Y was modified for a few events. An example is the 1971 San Fernando event.

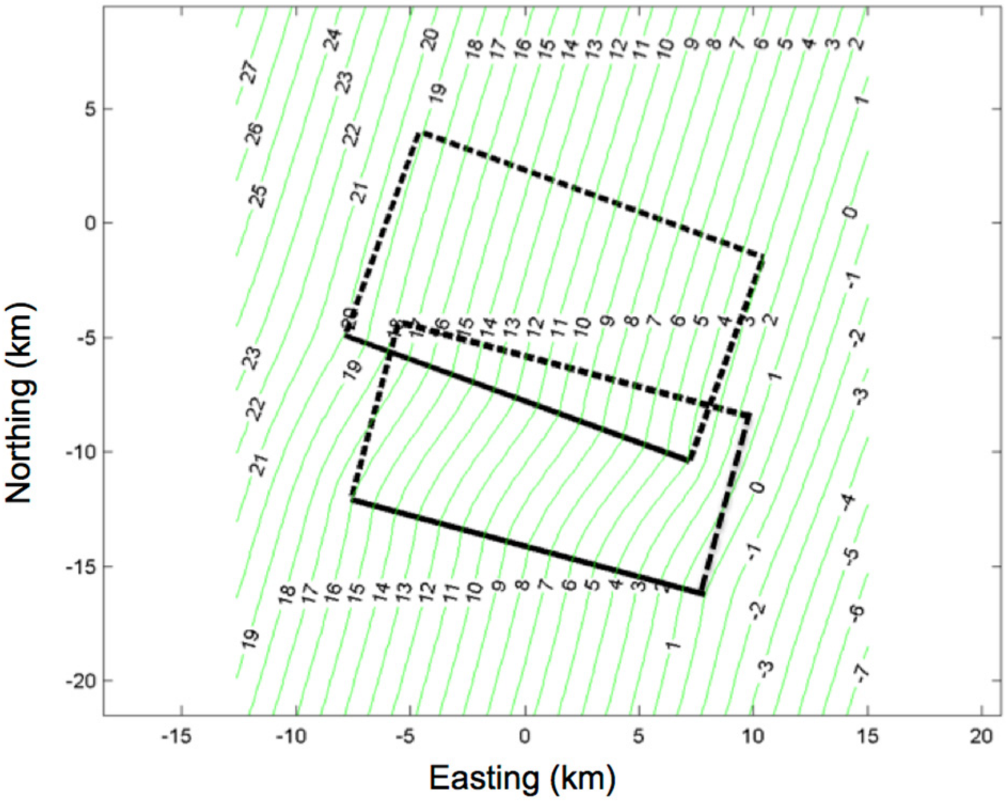

Figure 2.2 **Contour lines (thin green) of U for the 1971 San Fernando earthquake calculated from the Spudich and Chiou GC2. The solid and dashed lines represent the top of rupture and the surface projection of the finite fault planes respectively.**

The 1971 San Fernando earthquake is composed of two rupture planes, each with a length of about 16 km. But as seen in Figure 2.2, using a length of 16 km in the R_Y calculations would not be appropriate. Rather, a length of 20 km was used for the 1971 San Fernando earthquake in the R_Y calculations. Assigning new lengths to multi-segment, multi-fault earthquakes is only appropriate for four events listed below in Table 2.2:

Table 2.2 **Recommended event length incorporating segment overlap for applicable events.**

Earthquake	Recommended Length (km)
San Fernando (1971)	20
Hector Mine (1999)	44
Denali (2002)	305
El Mayor-Cucapah (2010)	125

The fault strike and dip reported was based on a weighted sum of the segment length and width, respectively. Additionally, most events in the dataset have consistent faulting mechanism (rake) across the various ruptured segments. Three earthquakes (Denali, El-Mayor Cucapah, and

Darfield) have significantly variable faulting mechanisms (rake) along strike. The El-Mayor Cucapah earthquake (similar to the Denali earthquake in the PEER-NGA West1 dataset) is a multi-segment rupture with variable faulting mechanisms (rake) along the strike of the rupture. The hypocenter (area of rupture initiation) occurred at depth on a blind normal fault. The finite fault model for the El-Mayor Cucapah earthquake consists of four segments (Table A.2). However, the long predominantly right-lateral strike slip segments with significant surface offset dominated the seismic moment over the other shorter segments of the faulting with various other mechanisms. Therefore, a rake was assigned consistent with a strike slip mechanism. In contrast, the Darfield, New Zealand, earthquake ruptured multi-segments with variable faulting mechanisms along the strike of the rupture. The hypocenter (rupture initiation) occurred at depth on a blind thrust fault. However, strike slip rupture with significant surface offset dominated all other segments of the faulting. The finite fault model for the Darfield earthquake has been appropriately simplified to include only a single strike-slip segment for PEER NGA-West2 based on the reference in Table 2.1.

2.4 EARTHQUAKE SOURCE PARAMETERS FOR CALIFORNIA SMALL-TO-MODERATE EARTHQUAKE DATA

Finite fault inversions are typically not available for events with moment magnitude less than about five. Therefore, for the events added from the California small-to-moderate events the source parameters were chosen from high-quality relocation and moment tensor catalogs, as available. Parameters that are typically available in the catalogs included the event time, magnitude, strike, dip, rake, hypocenter location, and hypocenter depth. The seismic network in California is split between the Northern California Seismic Network (NCSN) and the Southern California Seismic Network (SCSN) network. The boundary between the NCSN and SCSN instrumentation and data processing is shown in Allen et al. (1965), as a zigzag line starting off the central California coast at 35° N, 121° W and entering Nevada east of Mono Lake along 38° N. The boundary is significant for the available catalogs as events occurring in the separate zones are analyzed by the local network and collected into the local catalog (location and moment tensor). The 266 events included in the California data set have been re-plotted in Figure 2.3 relative to the boundary line. When an event occurred near the boundary, both California networks may give a location/moment tensor. In this case the preferred network solution used the boundary mentioned above. It was inferred that when an event occurred within that network’s boundaries, a larger number of stations may be utilized in the location/moment tensor solution. Figure 2.3 also shows the small and moderate magnitude earthquakes for which either NCSN (blue) or SCSN (red) metadata were preferred.

For northern California earthquakes, hypocenter location is taken in order of preference from Waldhauser and Schaff (2008) and then from the NCEDC catalog. Seismic moment, conjugate fault planes (strike and dip), and rake angle are taken from the NCEDC moment tensor catalog. For southern California earthquakes, hypocenter location is taken in order of preference from Hauksson, Yang, and Shearer (2012) and then from the SCSN\SCEC catalog. Seismic moment, conjugate fault planes (strike and dip), and rake angle are taken from Yang, Hauksson, and Shearer (2012) and from the SCSN\SCEC moment tensor catalog.

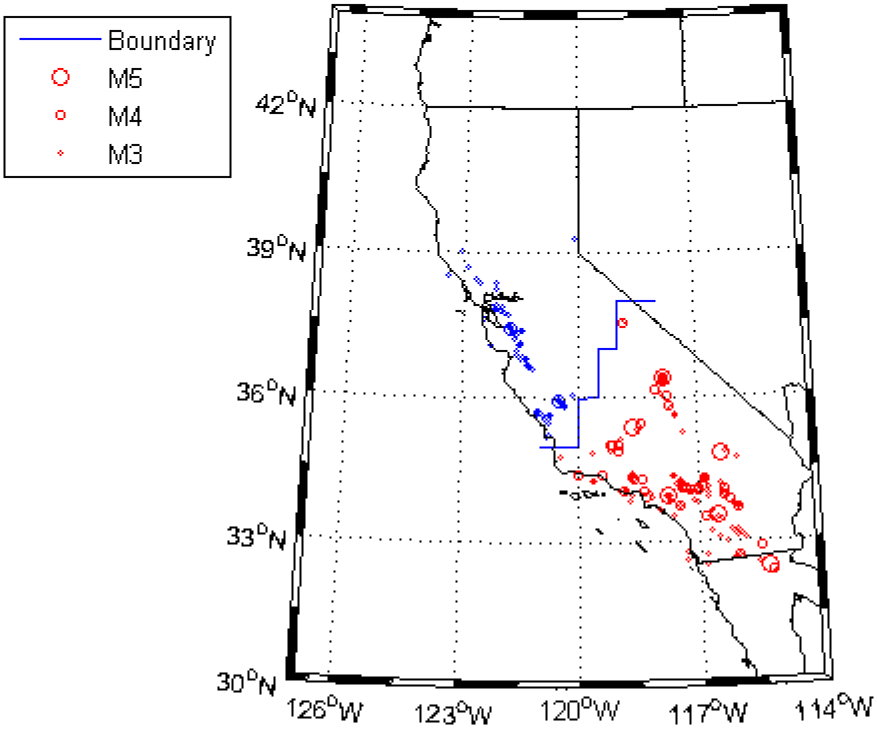

Figure 2.3 **Hypocenter Locations of the events selected in the SMM data set. Boundary separates the NCSN from SCSN. Events to the north (blue) of boundary preferred metadata from NCSN\BDSN. Events to the south of boundary (red) preferred metadata from SCSN\CIT.**

Conjugate fault planes of the high-quality moment tensor solution were used to define the probable rupture plane of an earthquake. To resolve the fault plane ambiguity, well-defined aftershock distributions were used, when available, to distinguish the fault plane from the conjugate plane. If an aftershock distribution is not available or does not favor a rupture plane, the probable rupture plane was selected according to regional trends. Unresolved fault planes are treated as a source of uncertainty in the calculation of distance measures (Section 2.4).

If a high-quality moment tensor solution (or fault plane solution) is not available for an earthquake, then its strike and dip are estimated from other associated events in the same region. For those earthquakes unassociated with other events, fault dips are assigned based on known or inferred mechanisms following Chiou and Youngs (2008) as follows: 90° for strike-slip, 40° for reverse, and 55° for normal. Unknown fault strike is treated in the calculation of distance measures as a uniformly distributed random variable between -180° and 180°. The selected unknown fault strike is based on the methodology described in Section 2.4.

2.5 METHOD OF SIMULATING A FINITE FAULT GEOMETRY

In the NGA-West1 flatfile, distance metrics such as the closest distance to the surface projection of the fault rupture plane, Joyner-Boore distance (R_{JB}), and the closest distance to the fault rupture plane (R_{RUP}) were missing when the finite fault model was not available. In NGA-West2, a decision was made by the NGA GMPE developers to adopt a method to simulate finite fault planes for events without a finite fault model but with minimal information of hypocenter, magnitude, and fault plane solution (or style of faulting). The goal of the simulation routine is to obtain an approximate fault rupture geometry that may be used to compute distance metrics and a few other path data (such as the source-site angle θ_{SITE}, the fault rupture width W, and the depth to the top of the rupture, Z_{TOR}) that require knowledge of finite fault geometry.

The simulation methodology is briefly described here, but a more detailed discussion is provided in Appendix B of the Chiou and Youngs (2008) report. In this methodology, the missing fault plane information is filled in by random sampling of pertinent probabilistic distributions of fault ruptured area, aspect ratio of ruptured area, and hypocenter position on the fault plane. The simulation routine generates a set of 101 random fault ruptures that are rotated and translated in space but fixed on the given hypocenter location. The strike and dip is fixed if reported.

During the NGA-West2 project the methodology was modified to provide a more stable simulated finite fault. In the previous methodology, the simulation was performed independently for each recording within an event. In the current implementation the routine computes the median R_{RUP} value of the 101 simulated ruptures using a grid of pseudo stations (~500 spaced around the epicenter at epicentral distances from 0 to 300 km). Use of a grid of pseudo stations instead of the observed recordings in the Chiou and Youngs (2008) approach ensures that adding or subtracting observed stations from the list would not affect the simulated rupture model. The selected fault plane is the simulated rupture that best fits the set of median R_{RUP} .

2.6 EVENT CLASSIFICATION: CLASS 1 VERSUS CLASS 2

Over the past twenty years, it has been observed that median ground motions from aftershocks are systematically lower than median ground motions from mainshocks by about 20–40% at short spectral periods (Boore and Atkinson 1989; Boore and Atkinson 1992; Abrahamson and Silva 2008). One explanation for this is that the mainshock rupture has reduced the stress on the fault surface. Aftershocks then may have lower stress drops and reduced stress short-period spectra that are controlled by stress drop. In contrast, seismic moment controls the long-period spectral levels, and hence no difference is observed. Given these observations, the NGA-West1 GMPE developers accounted for this difference either by removing aftershocks from the dataset (Boore and Atkinson 2008; Campbell and Bozorgnia 2008), or by including a term to account for a constant scale factor between mainshocks and aftershocks (Abrahamson and Silva 2008; Chiou and Youngs 2008). In the NGA-West1 project, each GMPE developer team made an independent classification of the earthquakes in their dataset.

However, classifying an earthquake as a mainshock or aftershock is not a straightforward problem. The term aftershock may mean different things to different people and organizations, and each defines it to suit their own concept of what an aftershock is. At best, aftershock is a loosely defined term, not the least because there is no clear distinction between aftershocks, triggered events, clusters, etc., with each presumably responding to different physical processes following the mainshock. In terms of ground motion, not all of these aftershock types systematically produce similar median ground motions. Based on observations reported in

Wooddell and Abrahamson (2012), triggered events that occur off the mainshock rupture plane, which are often called aftershocks, may have median ground motions that are similar to mainshocks (presumably because the mainshock rupture did not significantly reduce the stress on these other faults). However, events closer to the rupture plane were found to exhibit smaller median short-period ground motions than mainshocks as had been found previously.

Figure 2.4 compares the peak accelerations from the 22 February 2011 Christchurch earthquake, adjusted to a V_{s30} = 500 m/sec site condition, to the Abrahamson and Silva (2008) median PGA for mainshocks and for aftershocks. The PGA values from the Christchurch earthquake are more typical of a mainshock type earthquake of than an aftershock type earthquake. Similarly, the 28 June 1992, Big Bear earthquake is related to the 28 June 1992 Landers earthquake, but it ruptured a separate fault. Figure 2.5 compares the PGA values from the Big Bear earthquake with the Abrahamson and Silva (2008) median PGAs. As with Christchurch, the Big Bear PGAs are more consistent with the mainshock median than with the aftershock median. There is large variability in ground motions, so the comparisons for these two earthquakes are, by themselves, not conclusive, but they serve to demonstrate the issue.

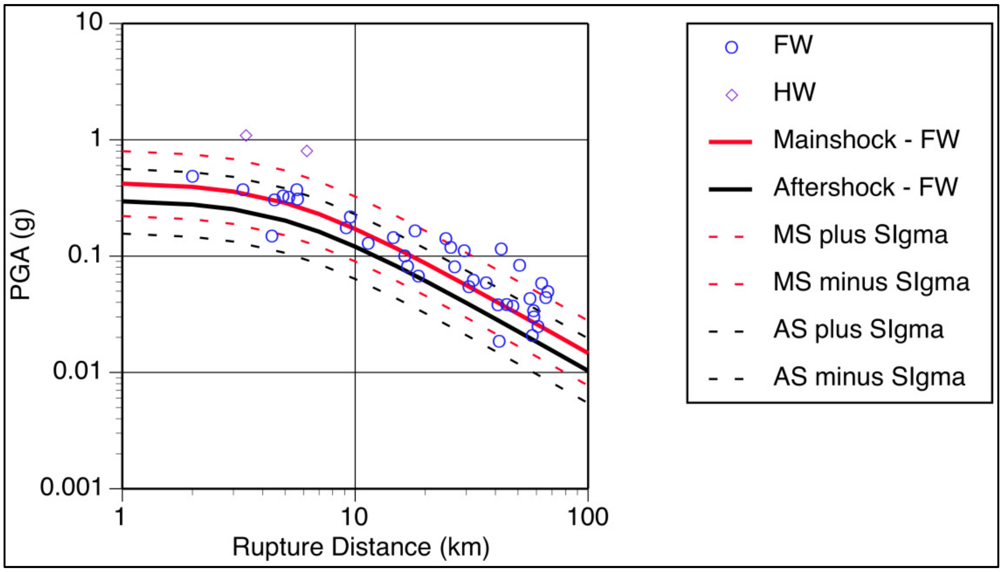

Figure 2.4 Peak ground accelerations normalized to a reference V_{s30} of 500 m/sec for the 2011 Christchurch earthquake compared with the Abramson and Silva 2008 GMPE for mainshocks and aftershocks.

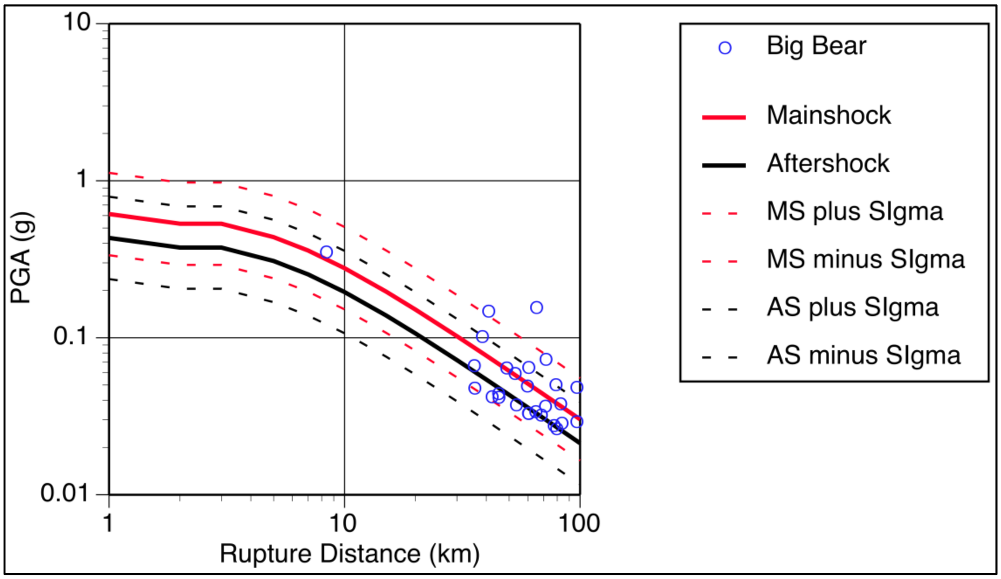

Figure 2.5 **Peak ground accelerations normalized to a reference Vs30 of 500 m/sec for the 1992 Big Bear earthquake compared with the Abrahamson and Silva 2008 GMPE for both mainshocks and aftershocks.**

Given observations such as these, earthquakes in the NGA-West2 database are grouped into two classes based on their distance to the rupture plane of the main event and their time with respect to the main event. Following Wooddell and Abrahamson (2012), Class 1 earthquakes are mainshocks, triggered events, or foreshocks that occur off the surface projection of the mainshock rupture plane, and Class 2 earthquakes are the earthquakes that occur within or near the surface projection of the mainshock rupture plane and within a time window for aftershocks. The hypothesis is that the earthquakes occurring within the fault plane or damaged region of the main event have a systematic bias toward lower median ground motion due to the lower stress drops from these earthquakes that re-rupture the fault plane. This is consistent with the results of Baltay et al. (2012), which showed that, on average, the stress drops for the mainshocks (Class 1 earthquakes) in the NGA-West2 dataset are about 1.6 times higher than the stress drops for the aftershocks (Class 2 earthquakes).

2.6.1 Methodology

The mainshock flag in the NGA-West2 database is used to select earthquakes for use in the attenuation model development. A MatLab script is used to distinguish Class 1 events (mainshocks, foreshocks, triggered events, and off-plane aftershocks) from Class 2 events (aftershocks that re-rupture the mainshock fault plane or occur within the damaged zone within a time window for aftershocks). This procedure is based on a windowing method that designates an event as a Class 2 event if it occurred inside the spatial and temporal windows of a larger Class 1 earthquake. The windowing approach used for the classifications in the NGA-West2 database uses the Gardner and Knopoff (1974) time window and a distance window based on the shortest distance between the centroid of Joyner-Boore rupture surface of the potential Class 2 earthquakes, and the closest point on the edge of the Joyner-Boore rupture surface of the Class 1 mainshock. We call this the centroid Joyner-Boore distance "CRJB."

The CRJB distance metric was adopted as an improvement on the Gardner and Knopoff (1974) distance metric, which is based on a radial distance from the mainshock epicenter. When analyzing the Wenchuan, China, earthquake and aftershock sequence, Wooddell and Abrahamson (2012) observed that the Gardner and Knopoff (1974) algorithm only identified 39 aftershocks. However in the NGA-West2 database, the Wenchuan, China, earthquake has 65 aftershock records associated with it, with dates ranging from 12 May to 5 August 2008. The Gardner and Knopoff (1974) algorithm misclassified many of the Wenchuan, China, aftershocks because it searches over a radial distance from the epicenter of about 90 km for a **M**7.9 earthquake. The rupture plane for the Wenchuan, China, earthquake spanned a length of approximately 300 km. By using the mainshock epicenter for measuring the separation distances between earthquakes, many of the earthquakes that are clearly related to the mainshock are not associated with the mainshock by the Gardner and Knopoff algorithm, as shown in Figure 2.6.

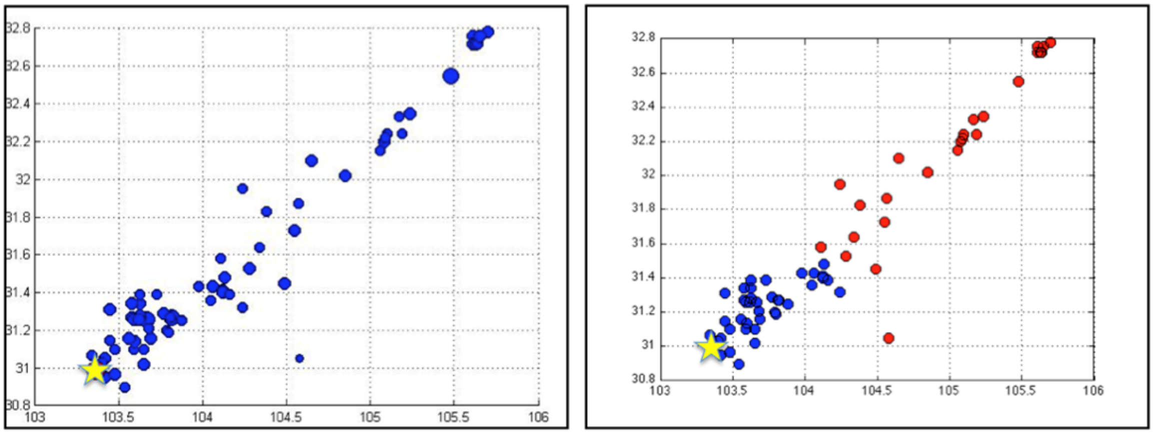

(a)

(b)

Figure 2.6 **(a) 2008 Wenchuan, China, Earthquake (yellow star) and aftershock sequence (blue dots); and (b) 2008 Wenchuan, China earthquake (yellow star), aftershocks as defined by the Gardner-Knopoff algorithm (blue dots) and events not associated with the event sequence (red dots).**

The Wenchuan, China, example demonstrates an obvious shortcoming of adopting the Gardner and Knopoff (1974) distance window for classifying earthquake sequences on long rupture planes. When the rupture plane is long, many of the dependent events located along the rupture plane but far from the hypocenter are either misclassified as Class 1 earthquakes or associated with the wrong sequence. Another disadvantage of defining the distance window radially from the mainshock epicenter is that Class 1 earthquakes (off-rupture plane earthquakes) can be misclassified as Class 2 earthquakes (along-rupture plane earthquakes). To address these shortcomings, two new distance metrics were proposed: ΔRJB and CRJB. Ultimately, the CRJB distance metric was used to classify the earthquakes in the NGA-West2 database.

Figure 2.7(b) shows how the CRJB distance metric is defined. For comparison, Figure 2.7(a) shows how the ΔRJB metric is defined. In each panel, the red lines are the surface projections of the top of the rupture planes, the dashed lines are the surface projections of the rupture planes, the yellow star is the epicenter of the Class 1 mainshock, and the orange stars are the epicenters of the aftershocks (potential Class 2 earthquakes).

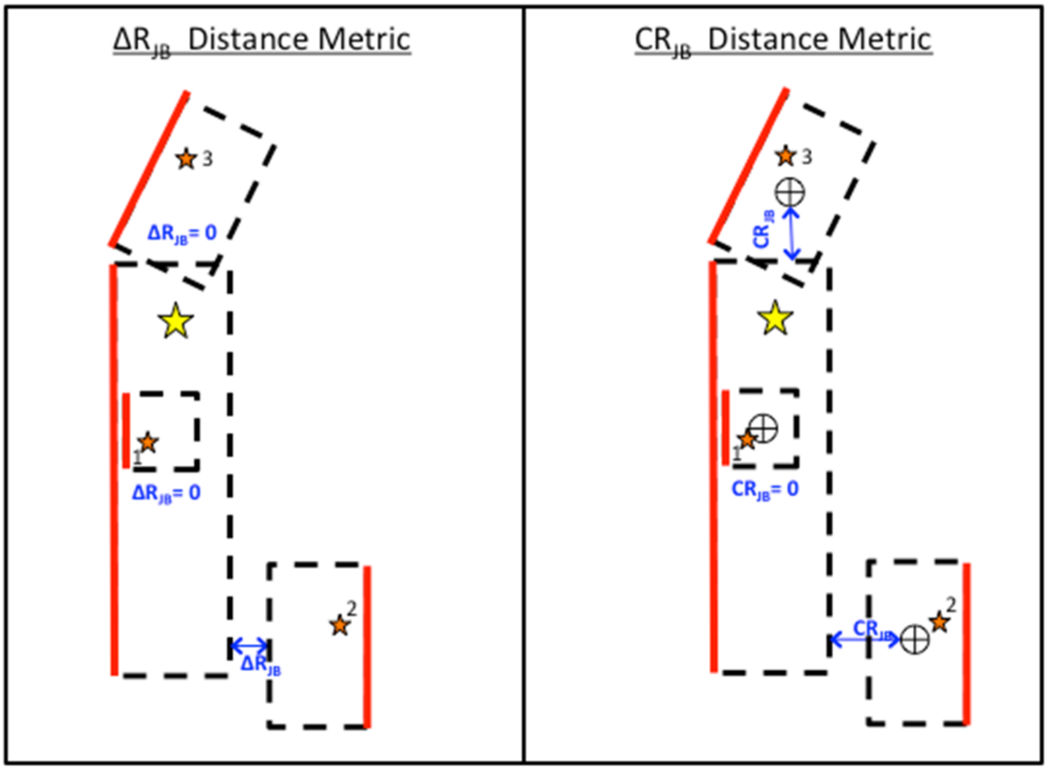

(a) (b)

Figure 2.7 Definitions of the ΔRJB and CRJB distance metrics.

The ΔRJB is related to the well-known Joyner-Boore distance metric, R_{jb}, used in ground motion models. The Joyner-Boore distance metric is defined as the shortest horizontal distance from a site to the vertical projection of the rupture plane. In the NGA-West2 work, we extended this concept to use the shortest separation distance between the Joyner-Boore rupture surface of the mainshock and Joyner-Boore rupture of the potential Class 2 earthquakes, hence the term ΔRJB. Figure 2.7(a), by definition, aftershocks inside the surface projection of the Class 1 mainshock rupture plane have a ΔRJB distance equal to zero and are Class 2 earthquakes.

One short-coming of this approach is that an earthquake may rupture a segment of the fault adjacent to the segment that ruptured in the mainshock, leading to a small (or zero) ΔRJB, while the majority of the rupture plane is located on a separate segment and may be much further from the mainshock rupture. In Figure 2.7, this is demonstrated by the relationship between the mainshock rupture plane and the rupture plane of aftershock #3. Therefore, we modified the definition to use the shortest distance between the centroid of Joyner-Boore rupture surface of the potential Class 2 earthquakes [shown with the open circles in Figure 2.7(b)] and the closest point on the edge of the Joyner-Boore rupture surface of the mainshock as shown in Figure 2.7(a). We call this the centroid Joyner-Boore distance "CRJB."

By reanalyzing the Wenchuan, China, sequence with the new CRJB distance metric and a cutoff (or maximum allowable) CRJB separation distance of 5 km, Wooddell and Abrahamson (2012) show that the simple modification of adding the rupture plane geometry and basing the separation distance calculation on the surface projection of the rupture plane results in a more appropriate classification of earthquakes for the purposes of ground motion estimation. In this example, 53 earthquakes in the Wenchuan sequence are identified as Class 2 aftershocks, and the rest have rupture plane centroids that are greater than 5 km from the surface projection of the rupture plane (see Figure 2.8).

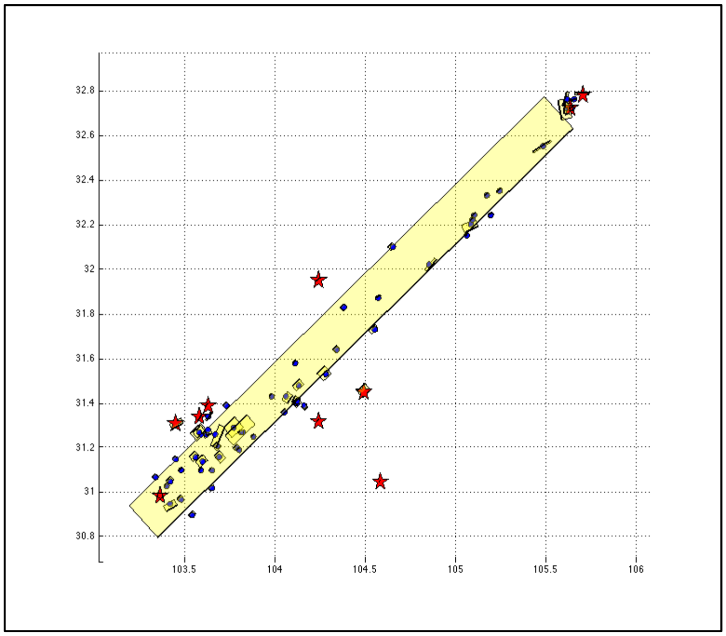

Figure 2.8 Example of identification of Class 1 and Class 2 earthquakes for the 2008 Wenchuan, China, Class 1 mainshock using a maximum CRJB of 5 km for defining Class 2 earthquakes. The red stars are the Class 1 earthquakes, and the blue circles show the centers of the Joyner-Boore rupture surfaces for the potential Class 2 earthquakes. The yellow rectangles are the surface projections of the rupture planes.

Rupture plane geometries are associated with all earthquakes in the NGA-West2 database, and the CRJB distance metric and the Gardner and Knopoff time window were used to classify the NGA-West2 earthquakes. Currently, the database includes six sets of columns for the results of the classification algorithm because the results can change as different values of the cutoff CRJB are used. For example, if the algorithm is run using a cutoff CRJB of zero, then only earthquakes that have a fault plane centroid within the surface projection of the Class 1 rupture plane are Class 2 earthquake candidates. If, however, a cutoff CRJB of 20 km is used, the algorithm will allow earthquakes with rupture plane centroids up to 20 km from the surface projection of the Class 1 rupture plane to be considered Class 2, as long as they are within the time window for aftershocks. The cutoff CRJB values used are 0, 2, 5, 10, 20, and 40 km.

As the centroid of a Class 2 earthquake moves further away from the surface projection of the Class 1 rupture plane (CRJB increases), we expect the median ground motion to increase back to the median ground motion level characteristic of Class 1 earthquakes because the earthquakes are no longer re-rupturing the Class 1 rupture plane or occur within a zone of less damaged crust and the stress drops should increase accordingly. Wooddell and Abrahamson (2012) evaluated the cutoff CRJB distance on a preliminary version of the NGA-West2 database using the inter-event residuals from the ground motion regression conducted following the random effects methodology described in Abrahamson and Youngs (1992). The event terms represent the average factor between median ground motion as given by the GMPE and the ground motion observed in individual earthquakes.

As an example, the PGA event terms for the potential Class 2 earthquakes (those that occur within the Gardner-Knopoff time window) are plotted as a function of the CRJB for PGA in Figure 2.9. The zero line (dashed black line) shows the median event term for Class 1 earthquakes. As with all ground motion data, there is significant variability of the event terms, but Figure 2.9 shows that for short CRJB distances (less than about 5 km), the medians of the event terms for Class 2 earthquakes are lower than for Class 1 mainshocks; however, at larger CRJB distances, the medians of the event terms for the potential Class 2 earthquakes become similar to the medians for Class 1 earthquakes.

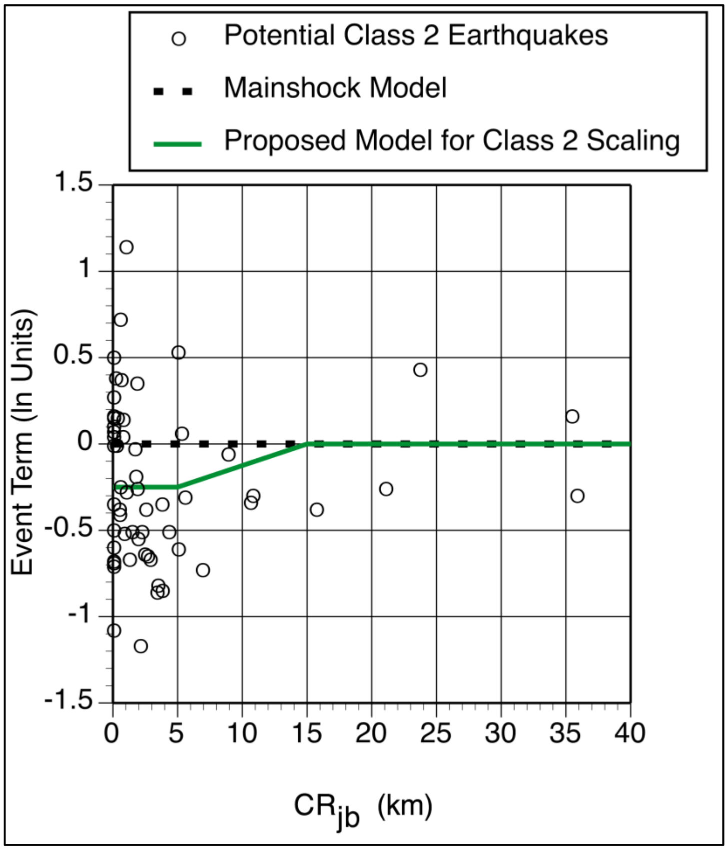

Figure 2.9 **Event terms plotted against CRJB for earthquakes in the NGA-West2 database (PGA).**

Based on this initial evaluation, Wooddell and Abrahamson (2012) propose to identify Class 2 earthquakes using the Gardner and Knopoff (1974) time window and a distance window with CRJB < 15 km. The effect on the median ground motion is tapered for CRJB at distances from 5 to 15 km, as shown in Equation (2.1) below.

$$T(CR_{JB}) = \begin{cases} c_1 & for\, CR_{JB} \le 5\, km \\ c_1 \left[\dfrac{CR_{JB} - 5}{10} \right] & for\, 5 < CR_{JB} < 15\, km \\ 0 & for\, CR_{JB} > 15\, km \end{cases} \tag{2.1}$$

This proposed functional form of the Class 2 earthquake scaling serves as an example of a CRJB taper model that can be used by the NGA-West2 developers. Each GMPE developer team can, however, develop an alternative functional form.

2.7 EARTHQUAKE SWARMS

The SCSN and NCSN recorded several earthquake swarms over the last decades that have been included in the California small-to-moderate magnitude event set. An earthquake swarm typically includes many small-to-moderate quakes occurring in a relatively short period of time. Earthquake swarms reported by NCSN and SCSN include the 2002–2003 San Ramon sequence, the September 2005 Obsidian Butte sequence, the December 2006 Berkeley sequence, and the February 2008 Calexico sequence. Although by definition no single event in an earthquake swarm is considered to be a mainshock, the largest event is usually classified as a mainshock by the windowing method. Occasionally, one or two larger events far apart in time and distance from the largest event are also classified as mainshocks.

2.8 WENCHUAN, CHINA, AFTERSHOCKS

The sixty-four aftershocks of the 2008 **M**7.9 Wenchuan, China, earthquake are a major addition to the PEER NGA-West2 data set. A PEER working group consisting of Tadahiro Kishida, Brian Chiou and Robert Darragh extensively reviewed the hypocenter location and fault mechanism of these aftershocks.

2.8.1 Hypocenter Locations

Hypocenter locations for sixty-four aftershocks were compared between the International Seismological Centre (ISC) and four other studies: Zhao et al. (2011), Hu et al. (2008), Zhen et al. (2009), and Kishida and Darragh (2012). The ISC was used as a base case as it was the most complete catalog. The comparisons detailed below show the locations from the four studies to be systematically shifted by about 20 km from the ISC locations. A recommended shift in the ISC location is given along with the location used in the earthquake source table.

In the Zhao et al. (2011) study, fifty-six out of the sixty-four aftershocks included in the NGA-West2 data set were relocated using double difference methods. In comparison to the ISC location, the average shift was 16.6 km at an azimuth of 283°. Hu et al. (2008) relocated eight events. The average shift between the ISC and the eight events was 20.4 km along an azimuth of 278°. Zhen et al. (2009) relocated ten events. The average shift between the ISC and the ten events was 18.4 km along an azimuth of 288°. Finally, Kishida and Darragh (2012) used S-P travel times at several stations from five of the largest aftershocks and found an average shift of 18.9 km at an azimuth of 294°.

Based on the above comparisons, the source table reports the locations from Zhao et al. (2011) when available. The Zhao et al. (2011) location was preferred as the double difference method was judged to produce the most reliable hypocenter locations. If hypocenter locations are not available by Zhao et al. (2011), then the hypocenter locations from the ISC are corrected by adding an average latitude, longitude, and depth shift, as shown in Table 2.3. The average latitude and longitude shift was based on a weighted average in the difference between the ISC the three studies: Zhao et al. (2011), Zhen et al. (2009), and Kishida and Darragh (2012). The average depth shift was based on the average difference in depth between Zhao et al. (2011) and the ISC. Table B.1 in Appendix B compares the ISC location with the locations adopted. Fifty-six hypocenters are from the Zhao et al. (2011) report, and the eight use the corrections in Table 2.3.

Table 2.3 Corrections in hypocenter locations from the ISC when results by Zhao et al. (2011) are not available.

	Latitude[1]	Longitude[1]	Depth (km)[2]
Average	0.037	-0.173	-1.2

1) Values are obtained by taking the weighted average from Zhao et al. (2011), Zhen et al. (2009) and Kishida and Darragh (2012). The weights depend on the number of aftershock data used in each study.

2) Values are obtained from the average depth change from the Zhao et al. (2011) double difference relocations.

2.8.2 Focal Mechanisms

Focal mechanisms of Wenchuan aftershocks were compiled from the ISC, Zhen et al. (2009), and Hu et al. (2008) studies. When multiple studies reported an earthquake mechanism, the working group recommended a preferred focal mechanism based on the following order: Zhen et al. 2009 (ten aftershocks); Hu et al. 2008 (twenty-one aftershocks); and ISC (one aftershock). When none is available from the listed studies (thirty-two aftershocks), the focal mechanism for the aftershock is taken to be the same as mechanism as the closer of the two Wenchuan mainshock finite fault segments. The recommended strike, dip, and rake angles are 228°, 35°, and 110° if aftershock hypocenter latitude is less than 31.81N, and 232°, 65°, and 165° if hypocenter is greater than 31.81N based of the two segments of the finite fault model. A comparison of mechanisms from Zhen et al. (2009) study of ten aftershocks with $M_S > 5.6$ and the NGA flatfile finds that they are similar. These fault mechanisms are based on P-wave polarity analysis. A second comparison between the fault mechanisms in the NGA-West2 flatfile and Hu et al. (2008) was also made. Hu et al. (2008) include mechanisms for thirty-one aftershocks and show that fault mechanisms are again similar. Table B.2 in Appendix B lists conjugate planes (preferred and auxiliary) from the selected study for each of the included events.

3 Development of Site Database

3.1 ORGANIZATION AND OBJECTIVES OF WORK FOR SITE DATABASE DEVELOPMENT

We began the site database development using Version 23 of the site database (last edited in 2006), which was developed in the original NGA project and is described by Chiou et al. (2008). The original PEER NGA site database attempted to collect all readily available public information on site conditions at strong-motion stations in the database. Appendix B of Chiou et al. (2008) provides definitions for the site classifications collected. These include the Geomatrix 3-letter site classification (D. Wells, personal communication, 2005), NEHRP site classification (BSSC 1994), and several others. The project also supported various investigations to systematically fill in missing site information with emphasis on V_{s30}. The current database project continues these efforts.

Major participants in the site database development for NGA-West 2 included certain members of the Task 8 working group (Emel Seyhan, Robert W. Graves, and Jonathan P. Stewart) and the following additional project researchers: Timothy D. Ancheta (PEER), Walter J. Silva and Robert Darragh (Pacific Engineering and Analysis, PEA), and Brian Chiou (Caltrans).

The objectives of the work described in this chapter were as follows: (1) provide site classifications for new sites added to the main flatfile in the NGA-West 2 project; (2) update the site database to include V_{s30} values based on newly available measurements; (3) improve the documentation and consistency of site descriptors used as proxies for the estimation of V_{s30}, both for sites in the previous site database and newly added sites; (4) develop evidence-based protocols for V_{s30} estimation from available proxies; and (5) update and augment estimates of basin depth parameters $Z_{1.0}$ and $Z_{2.5}$ for both existing and new sites (primarily California and Japan).

With respect to objectives (1), (2), (3), and (5) new information was compiled for addition to the site database. This information was provided/developed by a number of sources. Relative to the Version 23 database, substantial amounts of new V_{s30} data are available for Japan, Taiwan, California, Turkey, New Zealand, and Italy, most of which is from web sites or archival literature. Pacific Engineering and Analysis provided proxies for a number of sites that recorded new earthquakes. University of California, Los Angeles (UCLA) researchers gathered most of the new information on proxies, with assistance from Chris Wills and Carlos Gutierrez (California Geological Survey), and Dave Wald, Vince Quitoriano, and Alan Yong (USGS). Robert Graves, Albert Kottke, and Paul Spudich worked with the database team to compile updated basin depth parameters for southern California and the San Francisco Bay Area, and to obtain basin depth parameters for sites in Japan. The newly added information includes: V_{s30} values from measurements (see Section 3.3); velocity profile numbers and depths (principally in California, from PEA); various proxies including ground slopes, surface geology, Geomatrix 3rd letter classifications, and geomorphologic site classifications (see Section 3.4); and basin depths (see Section 3.6). Site parameters have been subject to peer reviews with extensive discussion to resolve technical issues and establish consensus-based protocols.

Key contents of the site database merged into the flatfile include V_{s30}, V_{s30} uncertainty, and shear-wave isosurface depths $Z_{1.0}$ and $Z_{2.5}$. A link to the electronic version of the site database and explanation of column names can be found in Appendix C.

3.2 STATUS OF PREVIOUS/CURRENT SITE DATABASE

In general, the site database contains metadata on conditions at the sites of strong-motion stations that have contributed data to the flatfile. The Version 23 site database from 2006 has 1611 world-wide stations that have recorded ground motions from shallow crustal earthquakes. The updated version of the site database for NGA-West2 has been expanded in two principal respects: (1) addition of new stations that had not produced usable recordings prior to the NGA-West2 project; and (2) incorporation of new site data for existing and new stations to provide more robust estimates of the site parameters used in GMPEs. Beyond the addition of these new data, the updated site database incorporates the results of a large amount of logistical book-keeping in regards to reconciling variations in stations names, station numbers, station locations, and other issues related to the 2006 site database, the current flatfile, and the current site database.

The total number of stations in the 2013 site database is 4149. We have estimated or measured V_{s30} for all sites but Robic (Italy) and Rimforest, Lake Arrowhead (California), but only 1144 of those values (28%) are based on geophysical measurements. The most common site information for stations is GMX 3rd letter classifications, which are available for 3180 stations (77%) via assignments by Geomatrix, PEA, and UCLA. Only 484 (12%) have surface geology information (principally from California), mostly because geology look-ups are labor intensive in most regions world-wide because it is performed using paper-based maps. The number of stations in the 2006 and current versions of the site database for the five most populated regions are shown in Figure 3.1. The 2013 site database has a large increase in the number of stations from Japan. Other geographic regions contributing significant numbers of stations include western North America (mostly California), Taiwan, China, and Mediterranean regions.

As shown in Figure 3.1, there are a substantial number of new sites added in WNA, which are mostly from southern California and the San Francisco Bay Area. Among those new California sites, most of the V_{s30} values from measurements (164 sites) are based on data provided by Yong et al. (2013). The surface geologic information was provided by Carlos Gutierrez (personal communication, 2012) and includes geologic unit and ground slope at 10-arc-sec resolution. Ground slope was also provided by David Wald and Vince Quitoriano of USGS (personal communication, 2012) at 30-arc-sec resolution for use with the slope proxy of Wald and Allen (2007). Geomatrix 3rd letter site classifications were also developed for nearly all of the new California stations by PEA.

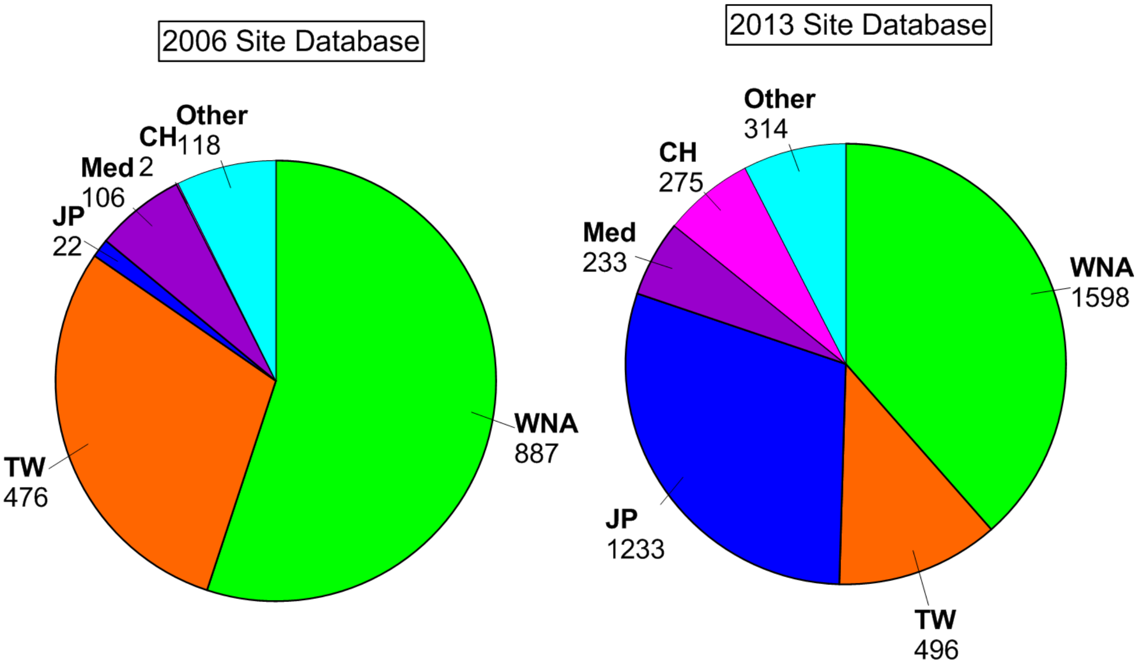

Figure 3.1 Pie charts of station numbers in 2006 and 2013 site database for five main regions. CH: China, JP: Japan, Med: Mediterranean, TW: Taiwan, WNA: Western North America (i.e., mostly California).

A substantial effort was made to assign Geomatrix 1st letter classifications, which are related to the structure type housing the instrument. Several additional 1st letter codes were added in this project to deal with unique structural types located in Italy. For example, 1st letter "P" is used for a massive 1−3 story castle.

For the newly added California sites, we looked up COSMOS site classification codes used by the four data providers SCSN\CIT, NCEDC\BDSN, CGS\CSMIP, and USGS\NSMP. These codes were correlated to GMX 1st letter by PE&A as shown in the table below. In addition, GMX 3rd letter was developed from BDSN descriptions of surface geology. For example, for Black Diamond Mines Park near Antioch, California, the BDSN description is "Sand, the instruments are sited about 150 m into an old mine tunnel, there is about 100 m of over-burden composed on sandstone, shale and coal." Station descriptions give useful site and embedment information that allows GMPE developers to choose appropriate site conditions.

Table 3.1 COSMOS codes for site classification and corresponding GMX 1st-letter code.

COSMOS Code	GMX 1st-letter	Description	Data Provider[1]
1	I	T-Hut	CGS, USGS
2	I	Armco	CGS, USGS
3	I,F	Sensors buried/set in ground (shallow, near surface). Also used by BDSN for US Array vault design described as: shallow burial at 2-5 ft, locations on rock are preferred.	All 4
4	A,B	Reference station (1-2 story, small, light building)	All 4
5	B,C,D,E	Base of building, larger than code 4.	All 4
10	G	Building Instrumentation	USGS
14	F	Tunnel	All 4
*		Unknown	CGS, USGS

[1] Data providers include: CGS, USGS, BDSN, CIT

3.3 MEASURED VELOCITY PROFILES

3.3.1 Previous and New Data Sources

The V_s profiles used for the calculation of V_{s30} are derived from a variety of sources including: (1) for WNA, profiles are obtained from the PE&A profile database (664 profiles) and Yong et al. (2013) (191 profiles), which are a combination of surface wave, downhole, suspension logging, and other methods; (2) for Japan, profiles are obtained from http://www.kyoshin.bosai.go.jp/kyoshin/db/index_en.html?all, mostly from downhole methods; (3) for Taiwan, profiles are obtained from http://www.cwb.gov.tw/ which are mostly suspension logging profiles; (4) for China, values of V_{s30} are tabulated in an unpublished document referred to as the "Yu and Silva report" and provided by Robert Darragh (personal communication, 2011), which are based mostly on downhole methods; (5) for Turkey, values of V_{s30} are tabulated by Sandikkaya et al. (2010) which are mostly derived from surface wave methods; and (6) for Italy, values of V_{s30} are tabulated by Scasserra et al. (2009) and http://itaca.mi.ingv.it/ItacaNet/, which are mostly derived from downhole, crosshole, and surface wave methods. All of the V_s profiles are available for independent review except for those in the PEA profile database, which is proprietary. As described in Chiou et al. (2008), the original sources for the PEA profiles are USGS, ROSRINE, CUREE, NCREE, Agbabian and Associates, Shannon and Wilson, Caltrans, and other organizations that have measured V_s profiles. While the V_s profiles from the PE&A profile database were not available for the present work, V_{s30} values were provided by PE&A staff along with PE&A profile ID number and total profile depth. Many of these values were also used in Version 23 of the site database (Chiou et al. 2008).

Of the 1611 stations in the 2006 site database, 1604 had V_{s30} information (either measured or inferred) and 380 had V_{s30} values based on measurements from profiles at least 30 m in depth (23.5%). In the 2013 site database, the number of V_{s30} values based on measurements with profile depths greater than 30 m has increased to 552 stations out of 4149 (13%). The distributions of measured and inferred V_{s30} values for the 2006 and 2013 site databases are shown in Figure 3.2. Note that most of the sites, and most of the measurements, are at soil sites. However, there are substantially more firm ground sites with V_{s30} values based on measurements in the 2013 version of the database (e.g., sites with V_{s30} > 750 m/sec number 46 in the 2006 database and 186 in 2013).

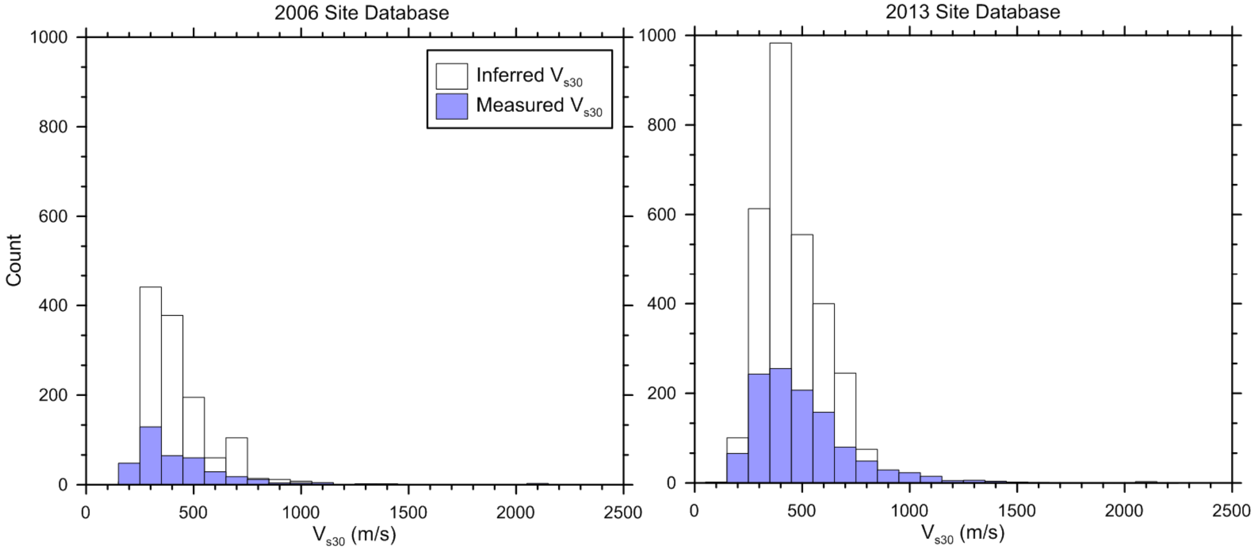

Figure 3.2 **Histograms of measured and inferred V_{s30} at the recording station sites in both the 2006 and 2013 site databases.**

Figure 3.3 shows the distribution of all sites and sites with V_{s30} values based on measurements by region in the 2006 and 2013 versions of the site database. Comparing the 2006 and 2013 numbers, the number of sites has increased modestly in WNA (mostly California), Taiwan, and the Mediterranean regions, but has increased substantially in Japan and China. In the 2013 site database, the regions with the highest percentages of V_{s30} values based on measurements are Taiwan (53%) and Japan (34%). Note that this figure only includes sites as "measured" when the profile depth is 30 m or greater.

The data in Figure 3.3 are misleading in the sense that many strong-motion stations have available profiles with depths (z_p) less than 30 m, which are not included in those histograms. The distribution of z_p by region is shown in Figure 3.4. Most of the profiles shallower than 30 m are from Japan in the K-net array (Kinoshita 1998). It should be noted that not all profiles have known profile depths. For Japan, 96% of the 1085 sites with measurements have known profile depths, and most of those depths are 10-21 m. For Taiwan, 89% of the 300 sites with measurements have assigned profile depths, and most of those depths (231) are > 30 m (77%). In

California there are 442 sites with V_{s30} from measurements, 97% of which (430) have known profile depths, and 350 of those depths have z_p > 30 m. The following section describes the estimation of V_{s30} from profiles with z_p < 30 m.

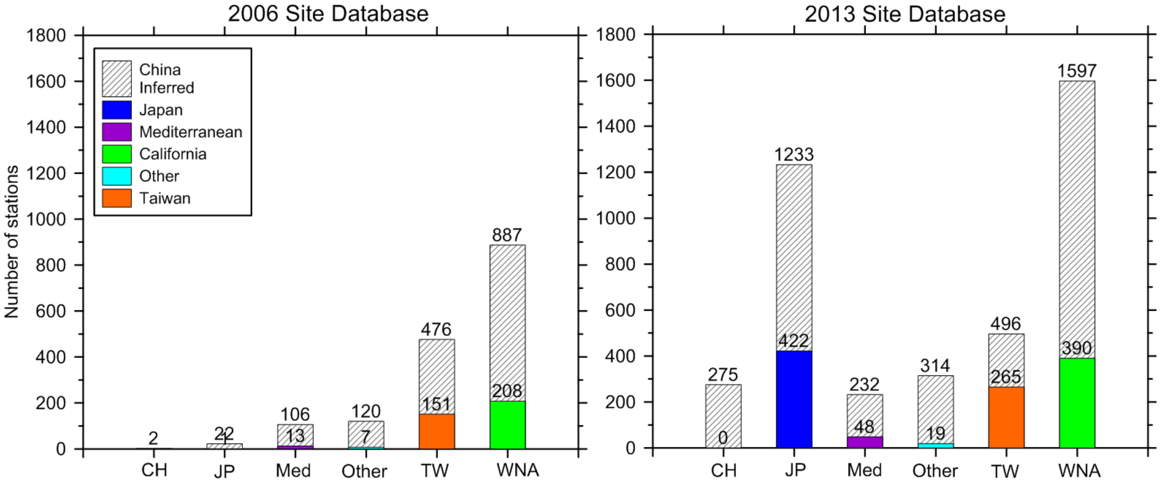

Figure 3.3 Histograms for sites with measured V_s and profile depths > 30 m in the 2006 and 2013 site databases for five main regions and other regions.

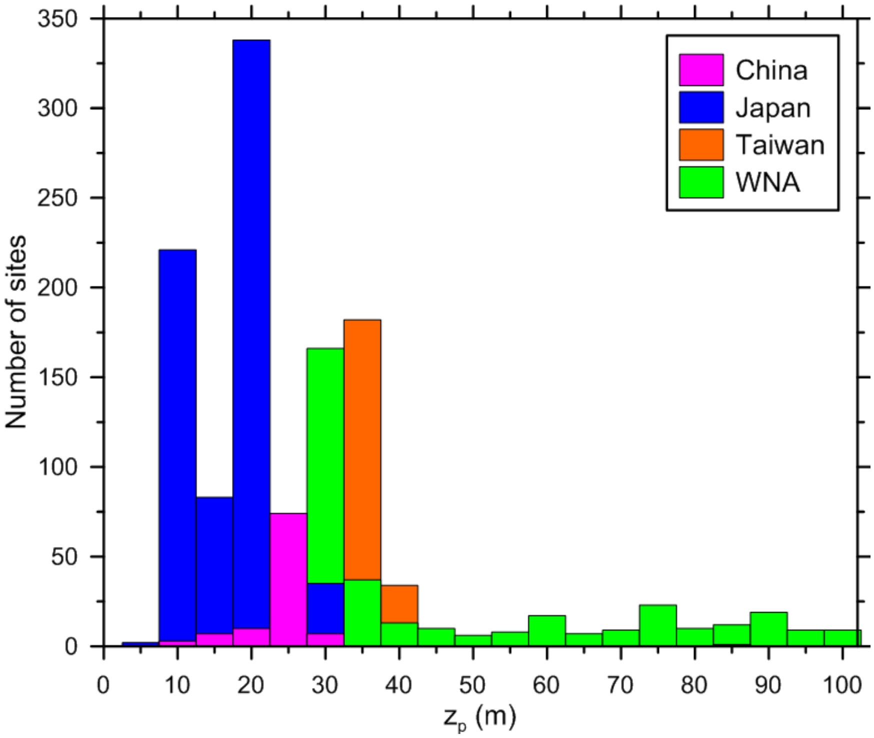

Figure 3.4 Histogram of profile depth bins by region. Profile depths for Japan extend up to 365 m, but are concentrated at 100 m in the figure. Note that there is one station with z_p = 82 m in Japan.

3.3.2 Computation of V_{s30}

When profile depths (z_p) are 30 m or more in depth, V_{s30} is computed as the ratio of 30 m to the shear-wave travel time through the upper 30 m of the site as follows:

$$V_{s30} = \frac{30}{\int_0^{30} \frac{dz}{V_s(z)}} \tag{3.1}$$

where the integral is evaluated in practice through summation across velocities taken as constant within depth intervals.

It is not unusual for shear-wave velocity measurements to extend to depths shallower than 30 m. In such cases, V_{s30} cannot be calculated directly, but the available geophysical data to profile depth z_p can be used to estimate V_{s30}. The average velocity to depth z_p, termed V_{sz}, is calculated similarly to V_{s30}:

$$V_{sz} = \frac{z_p}{\Delta t_z} \tag{3.2}$$

where z_p = profile depth and Δt_z = travel time for shear-waves from depth z_p to the ground surface, calculated as:

$$\Delta t_z = \int_0^{z_p} \frac{dz}{V_s(z)} \tag{3.3}$$

Using these variables, the procedures discussed in this section estimate V_{s30} from V_{sz} conditional on z_p.

The simplest method to estimate V_{s30} from V_{sz} for $z_p < 30$ m is to extend the lowermost velocity in the profile to 30 m (Boore 2004). This method was used in Version 23 of the site database (Chiou et al. 2008). More generally, correlation relationships are used based on borehole measurements. Boore (2004) used profile data from 135 boreholes in California to develop V_{s30}-V_{sz} correlations. Kanno et al. (2006), Cauzzi and Faccioli (2008), Cadet and Duval (2009), and Boore et al. (2011) similarly utilized velocity profiles based on borehole measurements at 691 vertical array sites in Japan that are within the KiK-net network (Kinoshita 1998; Okada et al. 2004). The unpublished Yu and Silva report (R. Darragh, personal communication, 2011) derived a V_{s30}-V_{sz} correlation using 73 KiK-net stations with both measured V_{s30} and assigned Geomatrix 3rd letter. As described by Boore et al. (2011), the KiK-net sites are preferentially located on relatively hard rock geologic conditions, so V_{s30}-V_{sz} correlation relationships will reflect that type of geology.

An expression for relating V_{sz} to V_{s30} is:

$$\log\left(V_{s30}\right) = c_0 + c_1 \log\left(V_{sz}\right) + c_2\left[\log\left(V_{sz}\right)\right]^2 \tag{3.4}$$

where c_0, c_1, and c_2 are regression coefficients that depend on profile depth z_p. Boore (2004) used a linear model (i.e., $c_2 = 0$) and provided coefficients for z_p from 10 to 29 m. Boore et al. (2011) find that the Boore (2004) model is appropriate for alluvial and soft rock sites outside of California, including the K-net sites in Japan (typically located on sediments in urban areas), Turkey, and sites in Europe. This is illustrated in Figure 3.5(b), which shows V_{s20} values for K-net sites that are similar to those for California sites. However, Boore et al. (2011) find the 2004 model biased for regions with stiffer rock site classifications and develop an alternative relationship using the second order polynomial form in Equation (3.4) for depths ranging from 5 to 29 m using the KiK-net data. Figure 3.5(a) illustrates this bias, by the shift towards faster V_{S20} values for KiK-net sites relative to K-net sites.

These differences in velocities are consistent with a statement by Okada et al. (2004) that K-net and KiK-net stations are predominantly located on soil and rock sites, respectively. The KiK-net stations in Japan are located on a nominally uniform grid, which means that a number of stations are in valleys in hilly terrain with shallow sediments over rock. California stations are predominately in urban areas, such as Los Angeles and San Francisco, which are located within broad areas of low topographic relief, underlain by sedimentary basins. Figure 3.6 shows histograms of topographic slopes for California strong-motion sites and Japan KiK-net sites. The slopes at the California borehole sites are systematically lower than those at the KiK-net sites in Japan, indicating the tendency for KiK-net stations to be preferentially sited on stiffer soils or rock.

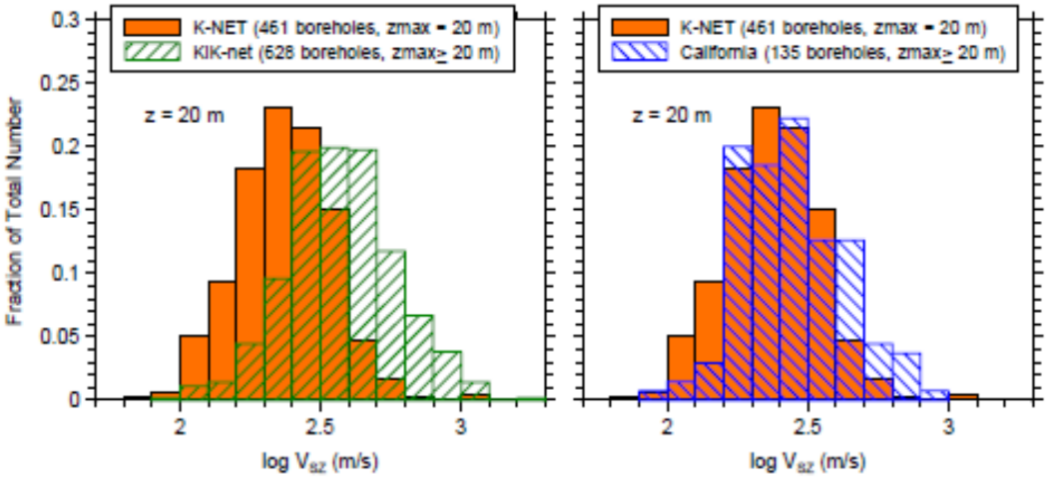

(a) **(b)**

Figure 3.5 Histograms of log V_{s10} and log V_{s20} for shear-wave velocity models from K-net, KiK-net, and California, for z_p = 20 m [from Boore et al. (2011)].

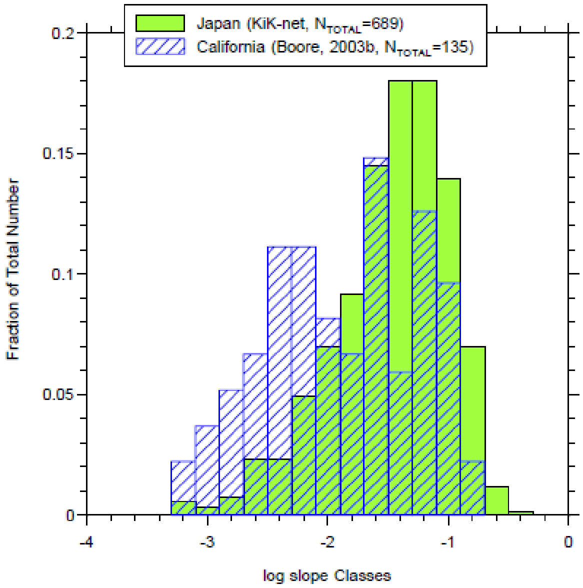

Figure 3.6 **Histogram of ground slopes at sites in California and Japan from which the velocity models were obtained [from Boore et al. (2011)].**

Yu and Silva (R. Darragh, personal communication, 2011) identified bias in the Boore (2004) V_{s30}-V_{sz} correlations during a PEER study of V_s data from 147 sites in southwest China (SWC sites) that recorded the Wenchuan, China, earthquake. The bias (or regional dependence) was identified by calculating V_{s30} at the SWC sites by extending the lowermost velocity in the profile to 30 m (simple extrapolation) and then comparing those results to estimates from Boore (2004), from which an under-prediction bias of 0.139(ln) was found for 32 sites with z_p = 10–20 m. Elevation and terrain proxies for V_{s30} also had significant bias for those sites.

Yu and Silva then developed V_{s30}-V_{sz} correlation, intended for application at SWC sites that are generally stiffer than California, using data from seventy-three selected Kik-net sites having GMX 3rd letter classifications. They developed both linear (c_2=0) and parabolic equations. It was not possible for this relationship to be based on SWC data because very few of those boreholes extend beyond 30 m. A linear relationship was recommended that is not conditioned on additional parameters such as GMX site codes. The aforementioned Boore et al. (2011) study includes many more KiK-net sites and does not use GMX 3rd letter classifications.

Figure 3.7 compares the V_{s30}-V_{sz} correlations from Boore et al. (2011) and Yu and Silva. The differences between the curves increase as z_p decreases, with the Yu and Silva model having a flatter gradient for z_p = 5 and 10 m (leading to higher V_{s30} estimates for lower V_{sz}; lower V_{s30} for high V_{sz}).The differences between the two curves are minor for V_{sz} > 250 m/sec, which is a common condition for SWC sites (the application region for Yu and Silva). Figure 3.8 compares the two correlations to KiK-net data for four values of z_p. As expected, the Boore et al. (2011) parabolic model generally provides a better fit, although the difference is most significant for V_{sz} < 200 m/sec.

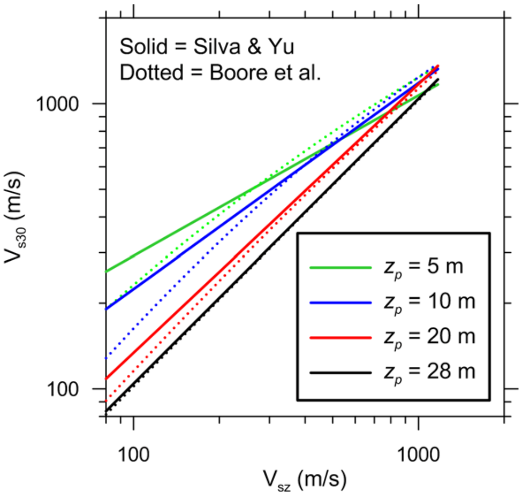

Figure 3.7 **Comparison of V_{s30}-V_{sz} relationships developed by Yu and Silva and Boore et al. (2011) for four profile depths, z_p.**

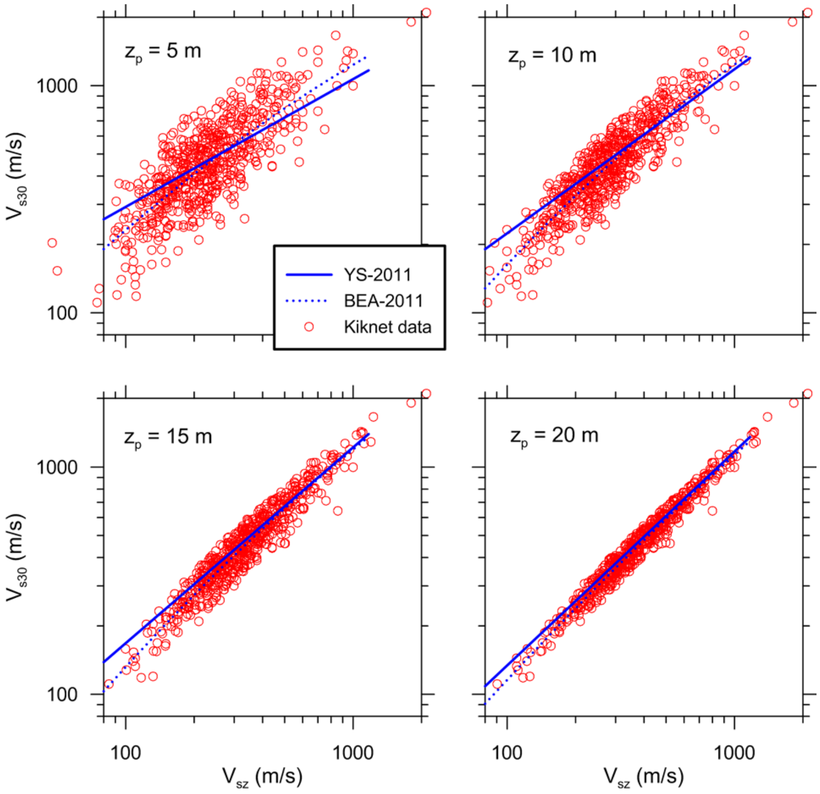

Figure 3.8 **Comparison of V_{s30}-V_{sz} relationships developed by Yu and Silva and Boore et al. (2011) with KiK-net data for four profile depths, z_p.**

3.4 PROXY BASED ESTIMATION OF V_{S30}

3.4.1 Description of the Methods

3.4.1.1 Methods based on Surface Geology or Geotechnical Conditions

Correlations have been developed to relate V_{s30} to surface geologic units and geotechnical site categories (the most widely used of which is the GMX 3rd letter). The California correlations described in this section both used V_{s30} values from the PE&A profile database in their original development. Although the underlying databases were similar, the level of documentation of the correlations varies from well-documented in archival literature (these tend to be based on surface geology) to relatively sparsely documented in principally grey literature (GMX, although a brief summary is provided in Chiou et al. (2008).

Correlations utilizing surface geology are available for California and Italy. For such correlations to be useful, variations of velocities within the broad geological categories typically shown in geological maps (e.g., Quaternary alluvium, Qa) need to be captured. This can be accomplished by either using relatively detailed categories, (e.g., separating thin and deep Qa), region-specific categories (e.g., for alluvium in the Imperial Valley and Los Angeles basin), or geologic information coupled with geomorphologic data (e.g., slope or other terrain descriptors).

For California, V_{s30} statistics (medians and standard deviations) were compiled for nineteen relatively detailed geological categories (including region-specific categories) by Wills and Clahan (2006), which were used in the 2006 site database. Current recommendations are to use the Wills and Clahan (2006) values for rock sites (i.e., Tertiary or older), and to use relations based on ground slope at 3 arc sec resolution for Quaternary sediments (Wills and Gutierrez 2008), as shown in Figure 3.9. The slope based values in Figure 3.9 are modified from those published in Wills and Gutierrez (2008) by converting arithmetic means and standard deviations to the median and standard deviation of a log-normal distribution [using Ang and Tang (1975)]. The alluvial ground slope correlation shows an increase of velocity with slope, which follows expected trends, because flatter slopes tend to be in mid-basin areas having relatively fine-grained alluvium with slower velocities. Figure 3.9 also shows that the standard deviation of velocities decreases as V_{s30} decreases.

The applicability of the Wills and Clahan (2006) correlations to Italy was investigated by Scasserra et al. (2009), who found that the median velocities for Quaternary categories are unbiased relative to Italian data. For rock sites, the California categories were not descriptive of Italian geology, and distinct correlations therefore were developed for appropriate geologic rock categories.

The principal geotechnical site categorization scheme that has been used in previous ground motion studies [e.g., Chiou et al. (2008)] and correlated to V_{s30} was proposed by the consulting firm Geomatrix (GMX) (D. Wells. personal communication, 2005). The GMX scheme has three letters, the last of which represents site condition. The GMX 3rd letter categories and the corresponding site conditions are shown in Table 3.2. The values of V_{s30} in Table 3.2 are based on the PE&A profile database and were used in the 2006 site database as the basis for V_{s30} estimation when surface geological information was not available but Geomatrix 3rd letter classifications were available (Chiou et al 2008).

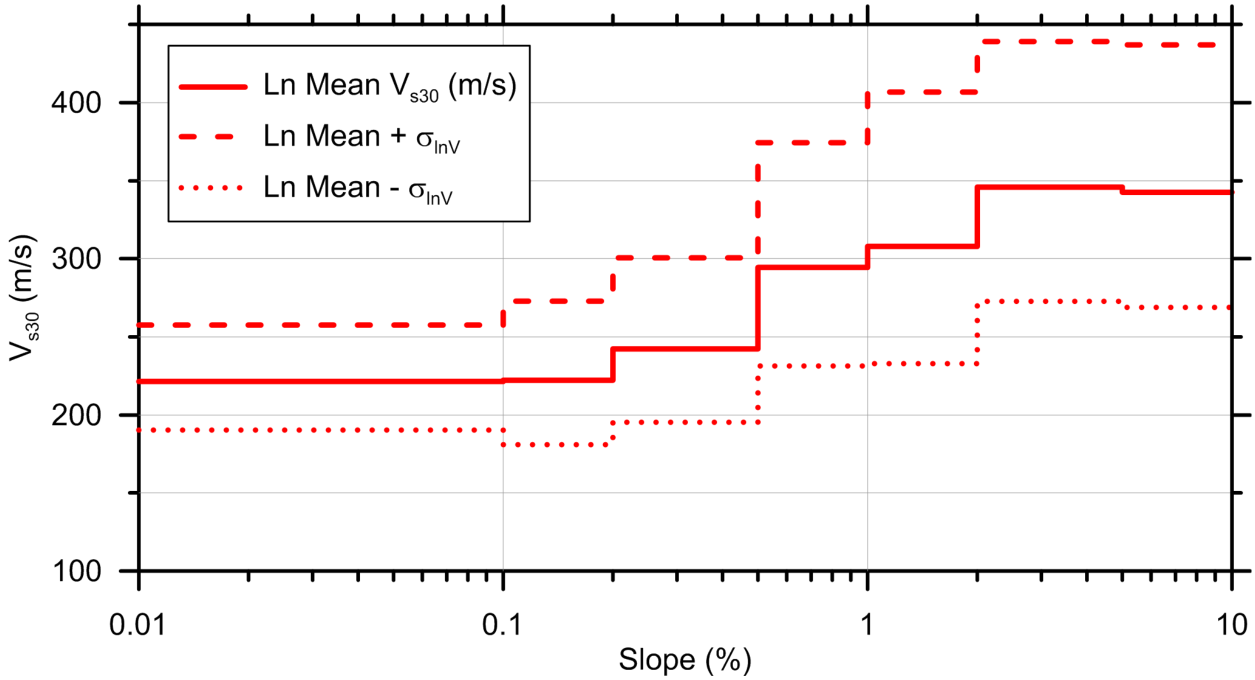

Figure 3.9 Variation of V_{s30} with ground slope within basins [adapted from Wills and Gutierrez (2008)]. Slopes are based on digital ground elevation models at 3 arc sec resolution.

Table 3.2 Geomatrix 3rd letter site categories and recommended V_{s30} and uncertainty [adapted from Chiou et al., (2008)].

Geomatrix Third Letter	*Description*	*Median V_{s30} (m/s)*	*σ_{ln}*	*Mean V_{s30} (m/s)*	*σ*
A	Rock. Instrument on rock (V_s > 600 mps) or <5m of soil over rock.	659.6	0.416	720.2	324.2
B	Shallow (stiff) soil. Instrument on/in soil profile up to 20m thick overlying rock.	424.8	0.431	464.3	211.0
C	Deep narrow soil. Instrument on/in soil profile at least 20m thick overlying rock, in a narrow canyon or valley no more than several km wide.	338.6	0.203	345.4	70.4
D	Deep broad soil. Instrument on/in soil profile at least 20m thick overlying rock, in a broad valley.	274.5	0.335	291.4	110.5
E	Soft deep soil. Instrument on/in deep soil profile with average V_s < 150 mps.	191.3	0.29	199.4	61.4

3.4.1.2 Methods based on Ground Slope, Geomorphology, or Elevation

Correlations have been developed to link surface topographic features to V_{s30}. The most well-known of these correlations relate topographic slope to V_{s30} (Wald and Allen 2007; Allen and Wald 2009) for applications in active tectonic regions with shallow crustal earthquakes and stable continental regions. Techniques in which V_{s30} is estimated based on geomorphology-based categories have been presented by Yong et al. (2013) for California and Matsuoka et al. (2006) for Japan. Another technique that has been used locally for Taiwan stations correlates V_{s30} to elevation within Geomatrix categories (Chiou and Youngs, 2008a; updated in the present work).

Slope Model: The motivation behind development of the V_{s30}-slope correlation is that topographic data are globally available, and slope may be an indicator of near-surface morphology and lithology (http://earthquake.usgs.gov/hazards/apps/V$_{s30}$/custom.php). Steep terrain is expected in mountains, indicating rock, whereas nearly flat slopes occur in basins, indicating soil. Transition zones would be expected to have moderate slopes involving weathered rock and potentially older sediments near basin boundaries. Wald and Allen (2007) developed a correlation between ground slope and measured V_{s30} using available regional data sets, including the PE&A profile database for sites in California. Separate slope-V_{s30} correlations were developed for active and stable continental regions that indicate increasing V_{s30} with increasing topographic slope. Data exists for gradients < 7%, corresponding to a 4° slope. Equations relating V_{s30} to slope were not provided; rather, stepped relationships of slope tied to discrete velocity bands were provided. Elevation did not provide additional predictive power for V_{s30} beyond ground slope.

Terrain Model (California): The Yong et al. (2012) procedure for V_{s30} considers slope along with geomorphologic factors including convexity and texture. This technique utilizes the same globally available SRTM 30-arc-sec surface models employed by Wald and Allen (2007). Hence, for a given location (latitude, longitude), the slope parameters used in the two models should be identical. The convexity element of the classification scheme is intended to distinguish convex-upward topography (characteristic of lowland terraces and alluvial fans) from concave-downward topography (broad valleys and foothills). The texture elements distinguish relatively smooth terrain from terrain having pits and peaks. These textural descriptions should not be confused with soil texture (e.g., fine, course) used in some sediment classification schemes (e.g., Fumal and Tinsley, 1985).

Ground slope, convexity, and texture are jointly analyzed using an automated topography classification scheme by Iwahashi and Pike (2007) to segregate terrain types into sixteen categories, which are depicted in Figure 3.10. As one moves to the right in the matrix, ground slope is decreasing, whereas moving down in the matrix produces less convexity and smoother texture. We note that the classification scheme has relatively fine discretization of rock conditions (rock categories include 1–7, 9, 11, and 13) but limited discretization of soil (e.g., there is no category that would seem to encompass lacustrine or marine clays, which produce the largest site amplification).

Statistics on V_{s30} (median and standard deviation) are provided by Yong et al. (2012) for each of the categories using a California data set derived largely from values in the PE&A profile database.

<u>Terrain Model (Japan):</u> Matsuoka et al. (2006) provide V_{s30} values for categories within the "Japan Engineering Geomorphologic Classification Map (JEGM)," which was released by Wakamatsu et al. (2005). The JEGM actually utilizes geomorphology, surface geology, slope angle, and relative relief to classify locations into geomorphologic units. The empirical correlations are based on shear-wave velocity profiles from 1937 sites. The categories and their median values of V_{s30} are indicated in Figure 3.11 (indicated as "AV_{S30}" in the figure). Categories 1–4 correspond approximately to rock conditions, 5–7 are transitional categories, and categories of 8 and above represent variable soil conditions. Matsuoka et al. (2006) provide intra-category regressions against elevation for categories 8–13, against slope for categories 3, 5, and 8–11, and against distance from hill for categories 8, 10, 13, 15, and 18–19. Maps of JEGM and associated values of V_{s30} have been prepared at 250-m grid-size resolution by Wakamatsu and Matsuoka (2006) and at 1-km grid resolution by Matsuoka et al. (2006). This classification scheme was not included in the 2013 version of the site database, but is noted here for completeness.

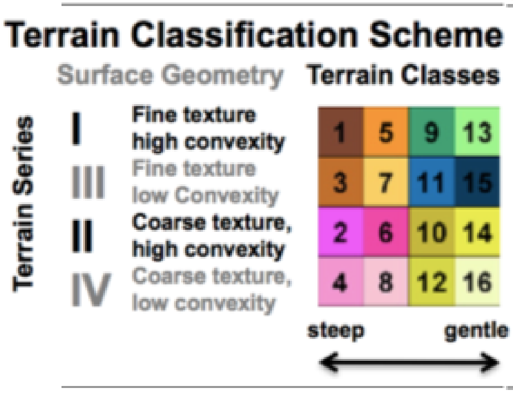

Category	Description
1	Well dissected mountains, summits, etc.
2	Large volcanoe, high block plateaus, etc.
3	Well dissected, low mountains, etc.
4	Volcanic fan, foot slope of high block plateau, etc.
5	Dissected plateaus, etc.
6	Basalt lava plain, glaciated plateau, etc.
7	Moderately eroded mountains, lava flow, etc.
8	Desert alluvial slope, volcanic fan, etc.
9	Well eroded plain of weak rocks, etc.
10	Valley, till plain, etc.
11	Eroded plain of weak rocks, etc.
12	Desert plain, delta plain, etc.
13	Incised terrace, etc.
14	Eroded alluvial fan, till plain, etc.
15	Dune, incised terrace, etc.
16	Fluvial plain, alluvial fan, low lying flat plains, etc.

Figure 3.10 **Variation of slope, texture, and convexity with terrain categories of Yong et al. (2012).**

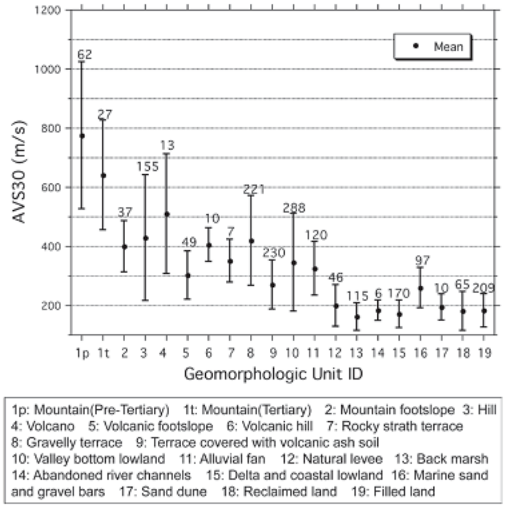

Figure 3.11 **Mean values of V_{s30} (indicated as "AV_{S30}") for geomorphologic categories in JEGM [from Matsuoka et al. (2006)].**

Elevation Model (Taiwan): Chiou and Youngs (2008a) present a model for V_{s30} estimation based on both Geomatrix (GMX) 3rd letter categories (Table 3.2) and elevation that is locally applicable in Taiwan. The model has been updated as part of the NGA-West 2 project by B. Chiou (personal communication, 2012) using the Taiwan sites in the site database. The model is based on the observation that elevation and geology are correlated in Taiwan due to the tectonic setting (Lee et al. 2001), with higher elevations having stiffer materials in GMX soil categories C and D. The analysis used 165 V_{s30} data points to estimate median values of V_{s30} for GMX categories A, B, and E (for which no trends of V_{s30} with elevation were observed) and to establish the following regression relation for GMX categories C and D:

$$\ln(V_{S30}) = \ln(\varphi_1) + \frac{\ln(\varphi_2) - \ln(\varphi_1)}{1 + e^{\left(\ln(\varphi_3) - \ln(Elv)\right)/\varphi_4}} \tag{3.5}$$

The estimated coefficients are given in Table 3.3.

Table 3.3 Coefficients for Taiwan-specific estimation of mean V_{s30} within GMX categories

Category	ϕ_1	ϕ_2	ϕ_3	ϕ_4
A	683.9	-	-	-
B	559.6	-	-	-
C+D	225	513	31.4	0.476
E	204.2	-	-	-

3.4.2 Proxy Evaluation

3.4.2.1 California

It is clear that V_{s30} is most reliably obtained with high-quality geophysical measurements; however, no consensus exists regarding how it should be estimated in the absence of such measurements. In many cases, practical considerations dictate the choice of method to be applied in a given area; for example, in the absence of geological maps, topography or terrain-based methods are the only viable option. However, when the available information does provide options (e.g., when both high-quality geological and topographic information are available), which method should be selected? Ideally this decision would be made on the basis of local or regional studies of the efficacy of these techniques to the region. We investigate the relative reliability of the techniques described above through comparative analysis against a California data set consisting of 475 V_{s30} values based on measurements. An earlier version of these analyses were presented by Stewart et al. (2012). The following section presents a similar analysis using data from Taiwan.

We utilize the California sites in the site database having V_{s30} from measurements and $z_p > 20$ m. For sites with I = 20–29 m, we compute time-averaged velocity to the profile depth (V_{sz}) and then use the Boore (2004) V_{sz} to V_{s30} extrapolation technique as described in Section 3.3.2.

We calculate V_{s30} residuals as follows:

$$R = \ln\left(V_{s30}\right)_{meas} - \ln\left(V_{s30}\right)_{proxy} \tag{3.6}$$

where $(V_{s30})_{meas}$ is a measured value and $(V_{s30})_{proxy}$ is estimated based on a correlation relationship. Note that by taking the natural log of the data, we assume the velocities to be log-normally distributed. Model bias can be estimated from the median of the residuals ($\mu_{\ln V}$). The standard deviation of residuals (σ_{lnV}) can be calculated for the entire set of residuals or sub-sets having certain conditions (e.g., sites within a particular category). The standard deviation term σ_{lnV} represents epistemic uncertainty on velocity, which should be considered in ground motion estimation. Boore et al. (2011) describe procedures by which this uncertainty can be considered in ground motion evaluation from GMPEs.

Figure 3.12 presents histograms of residuals from the geology proxy of Wills and Clahan (2006) and Wills and Gutierrez (2008) (the latter of which uses geology in combination with ground slope for post-Tertiary sediments). We note that the standard deviation increases with age from approximately 0.28 for Quaternary to about 0.43 for Mesozoic bedrock units. When all data are combined together, the median is -0.06 and the standard deviation is 0.33.

Figure 3.13 presents histograms based on the Geomatrix 3rd letter (Chiou et al. 2008). The bias is modest (generally < 0.1) except for category A and E (rock and soft, deep soil in Table 3.2). Standard deviations range from approximately 0.2–0 3 for soils to about 0.4–0.5 for rock. When all data are combined together, the median is -0.08 and the standard deviation is 0.40.

Figure 3.14 presents V_{s30} data plotted versus slope along with the recommended ranges from Wald and Allen (2007). The proxy estimates reasonably well the data median for slopes under about 0.07 m/m and over-predicts approximately from 0.07–0.15 m/m. There are practically no data for steeper slopes. The overall median of residuals is -0.01 and the standard deviation is 0.45.

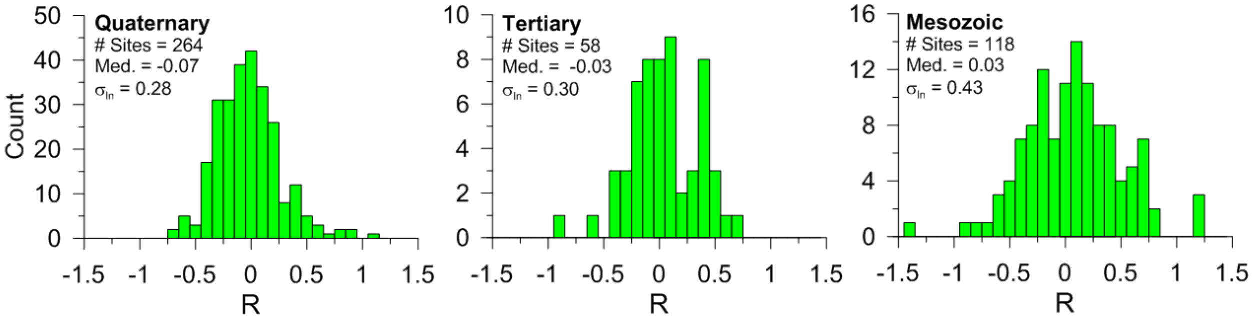

Figure 3.12 **Residuals of V_{s30} from estimates based on the geology proxy using the methods of Wills and Gutierrez (2008) for alluvium and Wills and Clahan (2006) for all other conditions.**

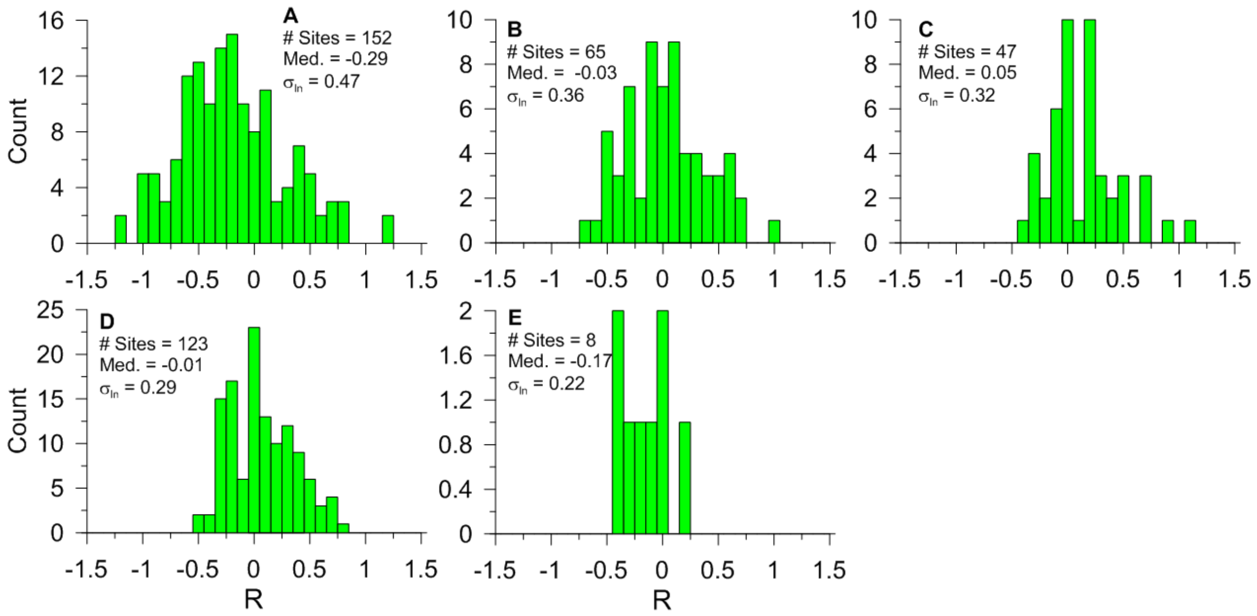

Figure 3.13 Residuals of V_{s30} from estimates based on the geotechnical proxy (Geomatrix 3rd letter) using the methods of Chiou et al. (2008). Based on V_{s30} measurements and V_{sz}-V_{s30} relations.

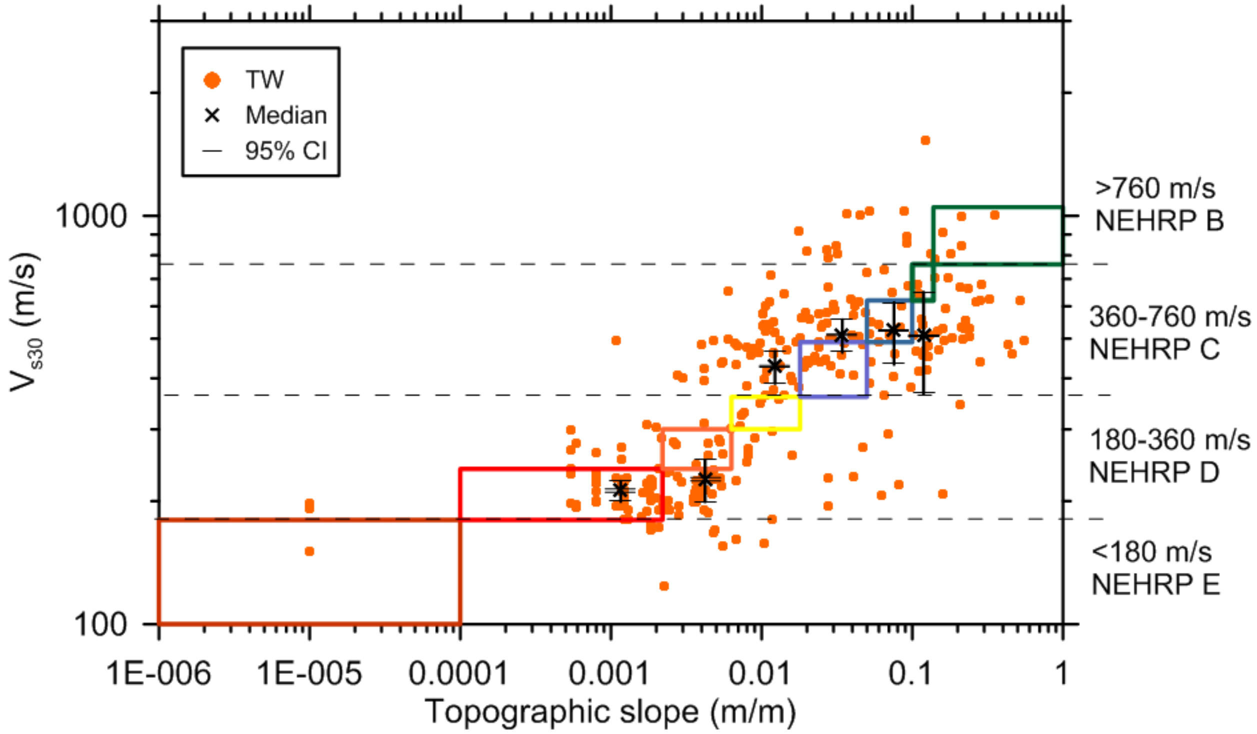

Figure 3.14 V_{s30} versus slope from California data and estimates from Wald and Allen (2007) for active tectonic regions. Color coded polygons correspond to slope ranges within NEHRP classes.

Residuals for the terrain-based method were evaluated by using an updated terrain map relative to that used by Yong et al. (2012), although the data are not adequate to constrain statistically significant medians or standard deviations for most categories. Categories with results considered to be reliable are indicated in Table 3.4. There is relatively little bias except for category 1, and standard deviations range from about 0.2 for softer geology to 0.4–0.6 for rock categories. Looking across all categories, the median of residuals is -0.11 and the standard deviation is 0.42.

Table 3.4 Terrain-based categories by Yong et al. (2012) and corresponding V_{s30} and uncertainty.

Category	*Description*	*# V_{s30} meas.*	μ_{lnV}	σ_{lnV}
1	Well dissected mountains, summits, etc.	39	-0.27	0.36
3	Well dissected, low mountains, etc.	49	-0.11	0.55
4	Volcanic fan, foot slope of high block plateau, etc.	40	0.13	0.47
7	Moderately eroded mountains, lava flow, etc.	44	-0.09	0.36
8	Desert alluvial slope, volcanic fan, etc.	47	-0.07	0.43
12	Desert plain, delta plain, etc.	21	-0.09	0.17
16	Fluvial plain, alluvial fan, low lying flat plains, etc.	33	-0.17	0.19

The relative efficacy of the different proxy-based estimation techniques can be judged on the basis of bias and standard deviation of residuals, as shown in Figure 3.15. Bias is generally small for the proxies investigated with the aforementioned exceptions. The standard deviation results were separated by categories when practical as indicated in Figure 3.15. For comparison, Figure 3.15 also shows an approximate standard deviation for measurements of V_{s30} at single sites with multiple V_s measurements (justification for the plotted value is given in Section 3.5.2.2). This value of σ_{lnV} reflects spatial variations in seismic velocities for modest separation distances between profiles (on the order of 10 m to several hundred meters) but similar geologic conditions. Significantly higher dispersion occurs when the site geology is heterogeneous and V_s measurements reflect significantly variable geologic conditions (e.g., both deep and shallow soil).

As expected, none of the estimation techniques are able to reproduce the low dispersions from measurement. We generally see lower dispersion for softer sites, represented by Quaternary geology, Geomatrix soil categories C-E, and terrain categories 12 and 16. Average dispersion levels (marked as the “overall” sigma in Figure 3.15) from the geology and geotechnical schemes are similar, and are somewhat lower than those from geomorphic schemes.

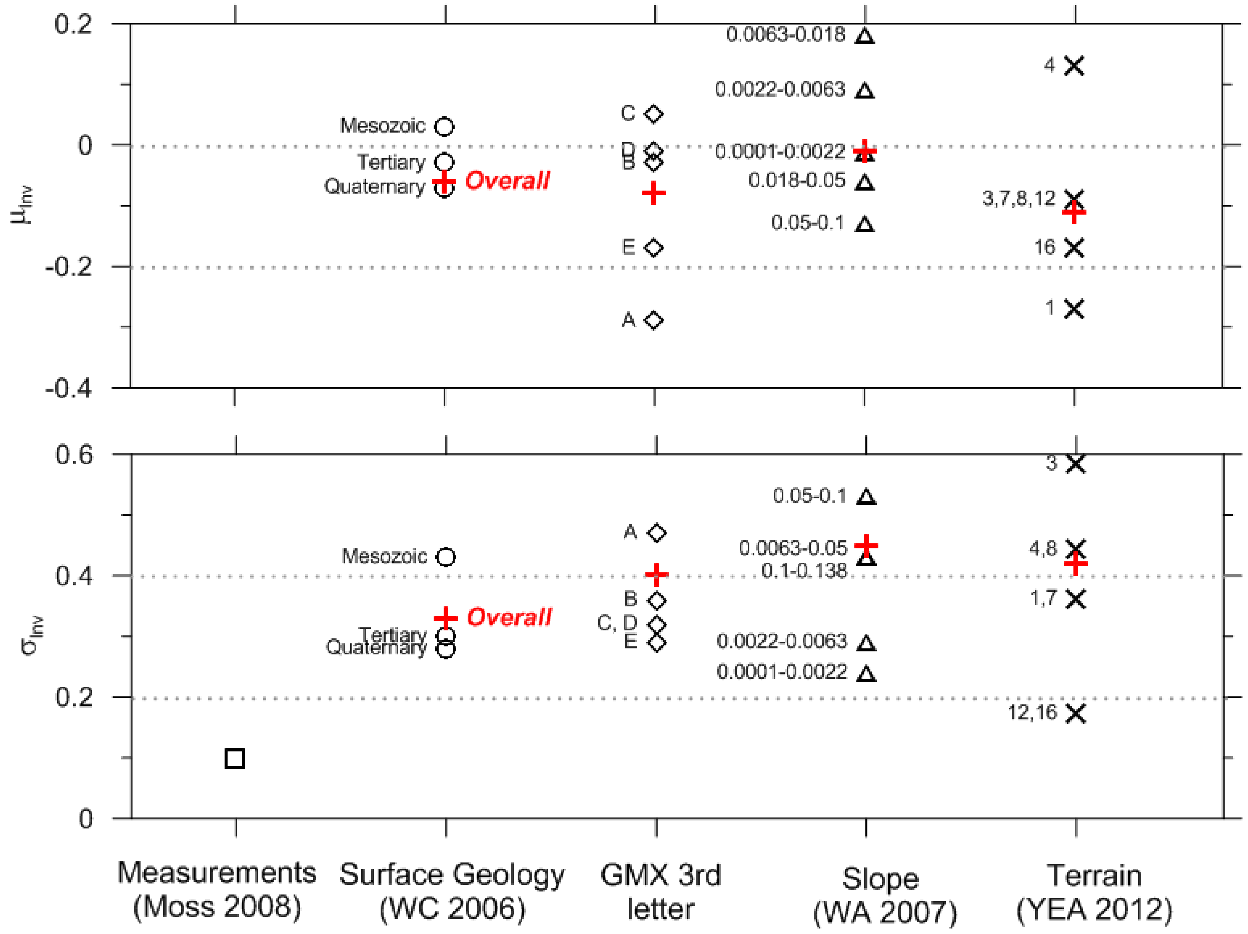

Figure 3.15 **Median and dispersion of V_{s30} prediction residuals for California in natural log units based on the analyses in this study. Results for measurements are derived from data presented by Moss (2008) and Thompson et al. (2012), as discussed in Section 3.5.2.2. Explanation of codes: GMX: A-E, see Table 3.2. Slope: slope categories within various NEHRP classes. Terrain: numbered categories, see Figure 3.10. WC 2006 = Wills and Clahan (2006), WA 2007 = Wald and Allen (2007), YEA 2012 = Yong et al. (2012). Proxy aggregates are marked as “overall.”**

3.4.2.2 Taiwan

This section presents proxy analysis for Taiwan using a database of 301 V_{s30} values based on profiles 20 m or greater in depth from the site database. The same procedures are used as in the previous section for California. Ongoing work performed in collaboration with Dr. Annie Kwok from National Taiwan University is developing geology-based proxy estimation procedures for Taiwan, but these are not available at present. The proxies evaluated in this section are GMX 3rd letter, slope, terrain, and GMX 3rd letter combined with elevation. Note that the first and third of these proxy relationships were derived based on data from California, so some misfit for Taiwan is to be expected. The slope proxy is based on international data, whereas the GMX/elevation model is based on Taiwan data, and hence would be expected *a priori* to have the least bias.

Figure 3.16 presents histograms based on the Geomatrix 3rd letter for Taiwan where the bias is negligible except for category E. Standard deviations range from 0.2 for soft soils to about

0.4 for rock. When all data are combined together, the median is 0.15 and the standard deviation is 0.37.

Figure 3.17 presents V_{s30} data plotted versus slope along with the recommended ranges from Wald and Allen (2007). The proxy estimates reasonably well the data median for slopes under about 0.1 m/m, with over-prediction misfits for steeper slopes. There are practically no data for slopes steeper than approximately 0.3 m/m. The overall median of residuals is 0.07 and the standard deviation is 0.34.

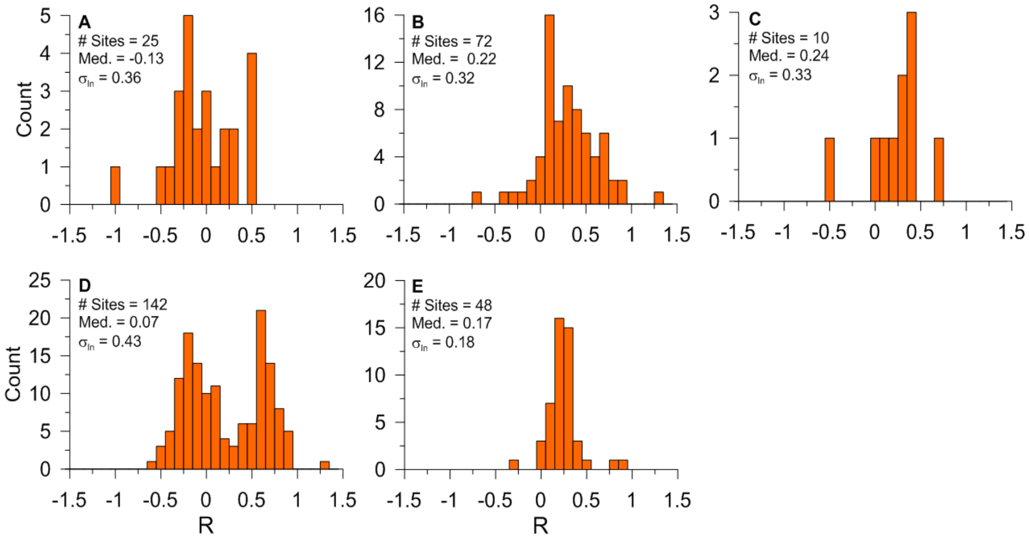

Figure 3.16 **Residuals of V_{s30} from estimates based on the geotechnical proxy (Geomatrix 3rd letter) using the methods of Chiou et al. (2008). Based on V_{s30} measurements and V_{sz}-V_{s30} relations.**

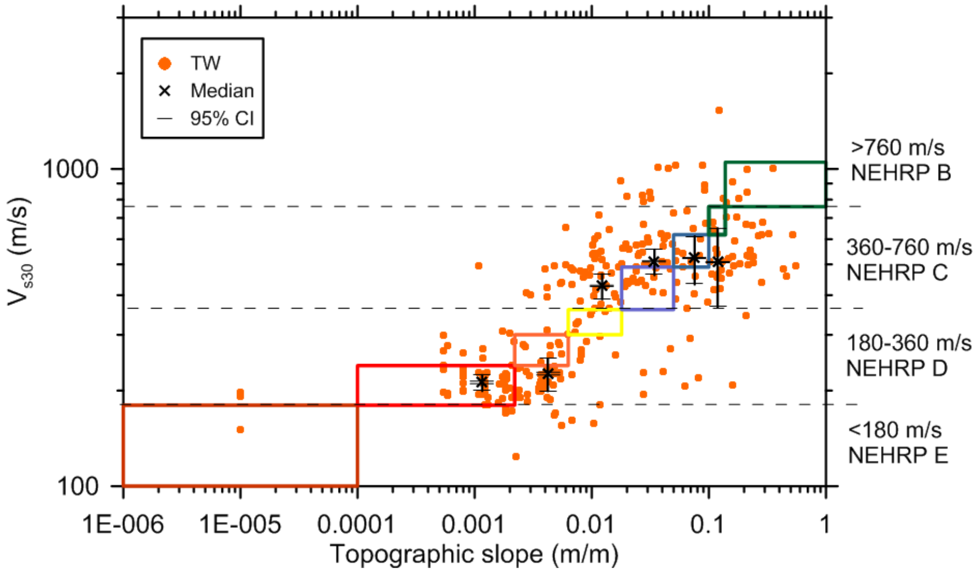

Figure 3.17 **V_{s30} versus slope from California data and estimates from Wald and Allen (2007) for active tectonic regions. Color coded polygons correspond to slope ranges within NEHRP classes. TW = Taiwan.**

Residuals for the terrain-based method were evaluated in categories for which statistically significant medians or standard deviations could be constrained (as was done for the California data). Categories with results considered to be reliable are indicated in Table 3.5. There is relatively little bias except for category 15, and standard deviations range from about 0.2 for softer geology to 0.4–0.5 for harder rock categories. Looking across all categories, the median bias is -0.13 and the standard deviation is 0.42.

Table 3.5 Terrain-based categories by Yong et al. (2012) and corresponding V_{s30}.

Category	*Description*	*# V_{s30} meas.*	μ_{lnV}	σ_{lnV}
1	Well dissected mountains, summits, etc.	19	-0.02	0.28
3	Well dissected, low mountains, etc.	71	-0.01	0.38
7	Moderately eroded mountains, lava flow, etc.	41	0.24	0.49
8	Desert alluvial slope, volcanic fan, etc.	19	0.19	0.32
11	Eroded plain of weak rocks, etc.	29	0.01	0.37
15	Dune, incised terrace, etc.	16	-0.5	0.28
16	Fluvial plain, alluvial fan, low lying flat plains, etc.	49	-0.17	0.18

Figure 3.18a shows relationships between V_{s30} and elevation for GMX 3rd letter categories. Figure 3.18b shows results for categories C and D only along with the recommended relationship (updated from Chiou and Youngs, 2008a). The fitted line in red is computed using Equation (3.5). The fit matches the data well at low elevations ($\leq$ 20 m) but underestimates the increase in V_{s30} as elevation increases, causing bias for high elevations. Corresponding histograms of residuals within GMX categories are shown in Figure 3.19. Looking across all categories, the median bias is 0.02 and the standard deviation is 0.32.

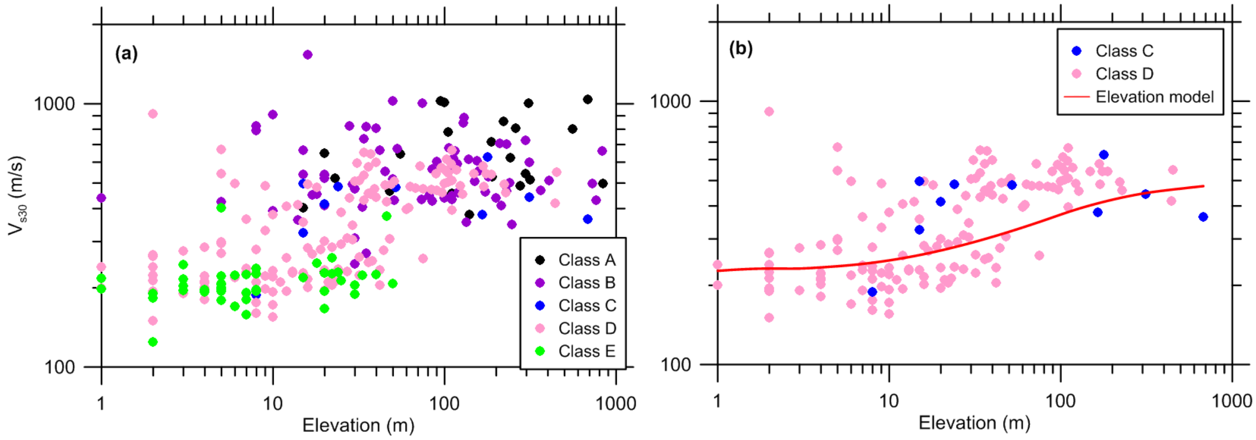

Figure 3.18 **Variation of V_{s30} with elevation within GMX 3rd letter categories: (a) all categories; and (b) categories C and D and elevation-based model from Chiou (personal communication, 2012). The data set used for development of the proxy is not the same as that shown here.**

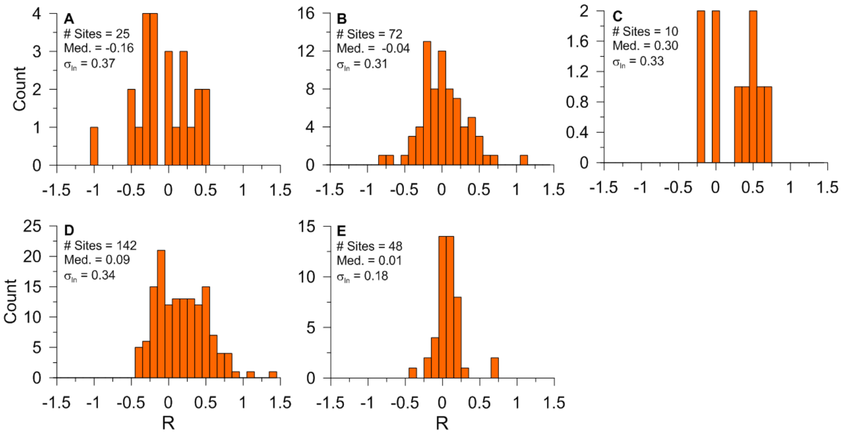

Figure 3.19 **Residuals of V_{s30} from estimates based on elevation-based method within GMX 3rd letter categories using the methods of Chiou and Youngs (2008a). Based on V_{s30} measurements and V_{sz}-V_{s30} relations for Taiwan data.**

The relative efficacy of the different proxy-based estimation techniques can be judged on the basis of bias and standard deviation of residuals, as shown in Figure 3.20. Bias is not negligible, generally ranging from -0.2 to +0.2 without systematic trends for rock or soil sites. The standard deviation results were separated by categories when practical as indicated in Figure 3.20. We generally see lower dispersion for softer sites, such as Geomatrix category E and flat slopes. General dispersion levels provided by the four considered proxies are generally similar.

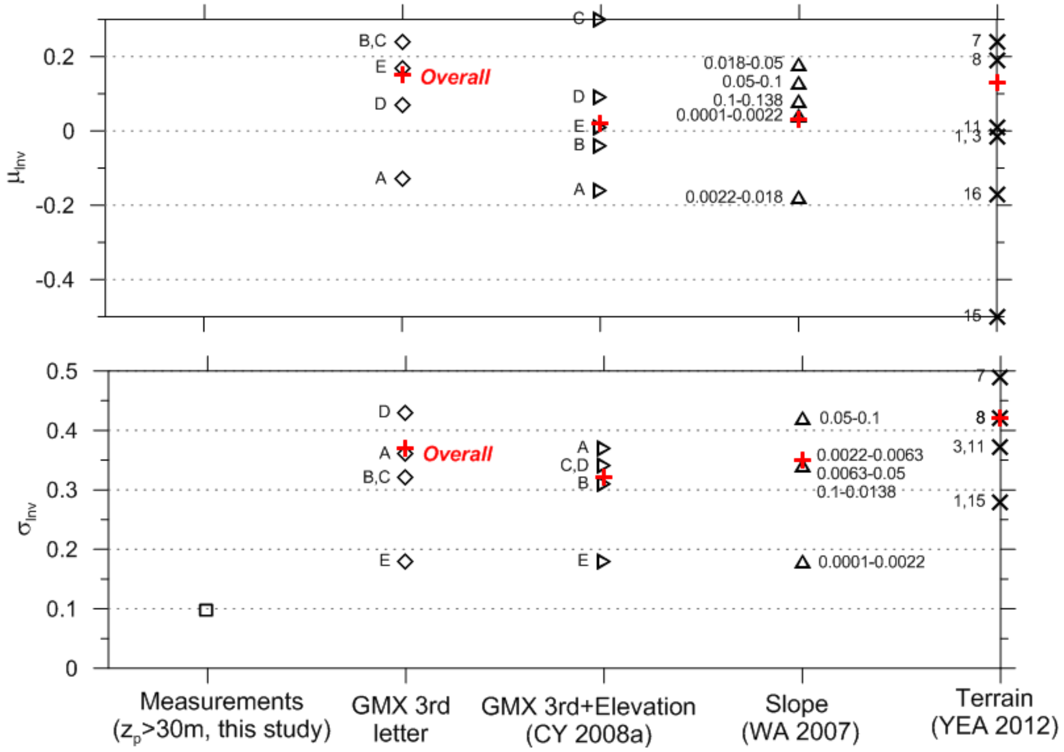

Figure 3.20 **Median and dispersion of V_{s30} prediction residuals for Taiwan in natural log units based on the analyses in this study. All explanations for abbreviations are the same as in Figure 3.15, except for CY 2008a= Chiou and Youngs (2008a). Proxy aggregates are marked as 'overall'.**

3.4.2.3 Japan

In this section we present proxy analysis for Japan using a database of 751 V_{s30} values based on profiles 20 m or greater in depth from the site database. The proxies evaluated in this section are GMX 3rd letter, slope, terrain, and geomorphology-based categories. Note that the first and third of these proxy relationships were derived based on data from California, so some misfit for Japan is to be expected, as occurred for Taiwan. The slope proxy is based on international data, whereas the geomorphology-based analysis is Japan-specific.

Figure 3.21 presents histograms based on the Geomatrix 3rd letter for Japan. The bias is negligible for categories B, C, and D, but significant for A and E. Similar biases were observed for California data. Standard deviations range from 0.20–0.30 for soft soils to about 0.4 for rock. When all data are combined together, the median is -0.14 and the standard deviation is 0.38.

The Japanese data set is different from other regions in that a relatively high percentage of V_{s30} values are derived from rock sites (GMX Category A). This occurs because the NIED ground motion network emphasized locating ground motion stations at rock sites. Figure 3.22 shows the mapped distribution of V_{s30} in Japan. The bias at rock sites that was observed in California and Japan motivated a suggested modification to the GMX A mean V_{s30} value, as described further in Section 3.4.2.4.

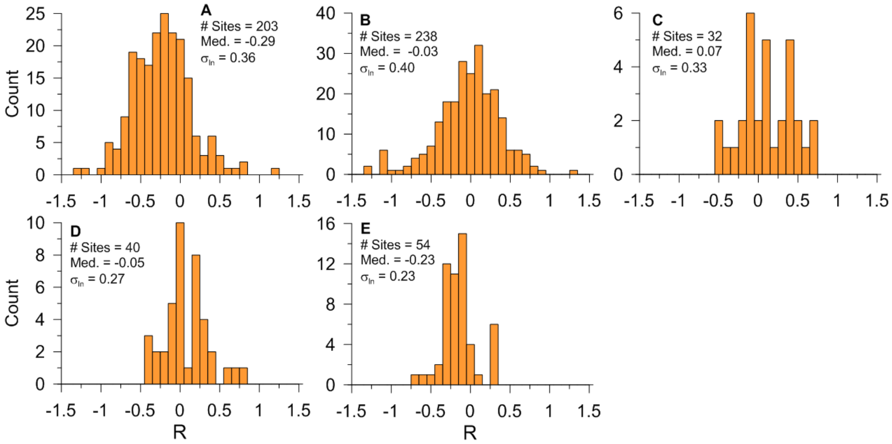

Figure 3.21 **Residuals of V_{s30} from estimates based on the geotechnical proxy (Geomatrix 3rd letter) using the methods of Chiou et al. (2008). Based on V_{s30} measurements and V_{sz}-V_{s30} relations.**

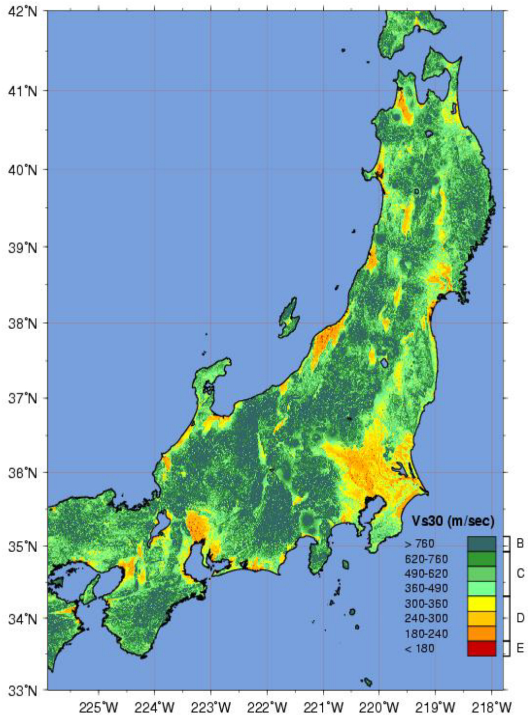

Figure 3.22 Distribution of *Vs30* in Japan (source: http://earthquake.usgs.gov/hazards/apps/vs30/predefined.php).

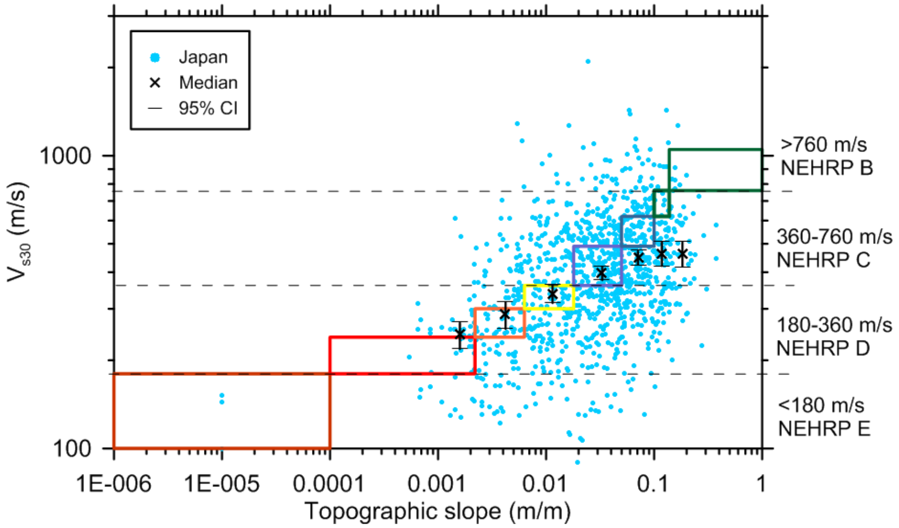

Figure 3.23 V_{s30} versus slope from Japan data and estimates from Wald and Allen (2007) for active tectonic regions. Color coded polygons correspond to slope ranges within NEHRP classes.

Figure 3.23 presents V_{s30} data plotted versus slope along with the recommended ranges from Wald and Allen (2007). The proxy performance is generally good for slopes between 0.004–0.04 m/m, with some under-prediction for slopes flatter that 0.004 m/m and over-prediction for slopes steeper than 0.04 m/m. The overall median of residuals is -0.12 and the standard deviation is 0.42.

Residuals for the terrain- and geomorphology based methods were evaluated in categories for which statistically significant medians or standard deviations could be constrained (as was done for the California data). Categories with results considered to be reliable are indicated in Table 3.6a and 3.6b. The terrain-based proxy has significant negative bias for five of the eight categories. Looking across all categories, the median bias is -0.14 and the standard deviation is 0.43. The most populated Japan-specific geomorphic categories are shown in Table 3.6b. There are modest negative biases in categories 1 and 8, i.e, rock sites, whereas positive biases are found for categories 5, 13, 15 and 17, i.e., soft soils. Considering all categories, the median bias is -0.04 and the standard deviation is 0.42.

The relative efficacy of the different proxy-based estimation techniques can be judged on the basis of bias and standard deviation of residuals, as shown in Figure 3.24. Biases are generally negative for the GMX, slope, and terrain proxies, whereas geomorphology biases are positive. The standard deviation results were separated by categories when practical as indicated in Figure 3.24. As in other regions, we generally see lower dispersion for softer sites, such as Geomatrix category E and flat slopes. General dispersion levels provided by the four considered proxies are generally similar. Average dispersion levels (marked as the 'overall' sigma in Figure 3.24) are generally similar, although the Japan-specific geomorphology-based scheme is lowest.

Table 3.6a Terrain-based categories by Yong et al. (2012) and V_{s30} bias and dispersion.

Category	*Description*	*# V_{s30} meas.*	μ_{lnV}	σ_{lnV}
1	Well dissected mountains, summits, etc.	297	-0.09	0.36
3	Well dissected, low mountains, etc.	188	-0.29	0.41
5	Dissected plateaus, etc.	108	0.00	0.44
7	Moderately eroded mountains, lava flow, etc.	227	-0.05	0.46
9	Well eroded plain of weak rocks, etc.	33	-0.45	0.36
11	Eroded plain of weak rocks, etc.	74	-0.13	0.41
15	Dune, incised terrace, etc.	69	-0.44	0.37
16	Fluvial plain, alluvial fan, low lying flat plains, etc.	20	-0.21	0.37

Table 3.6b **Geomorphology-based categories Matsuoka et al. (2006) and corresponding V_{s30} bias and dispersion.**

Category	*Geomorphologic map unit*	*Description*	*# V_{s30} meas.*	*μ_{lnV}*	*σ_{lnV}*
1	Mountain (Tertiary)	Steeply to very steeply sloping topography with highest elevation and relative relief within a grid cell of approximately more than 200 m. Moderately to severely dissected.	250	-0.39	0.38
3	Hill	Steeply to moderately sloping topography with higher elevation and relative relief within a grid cell of approximately 200 m or less. Moderately dissected.	87	0.03	0.40
5	Volcanic footslope	Gently sloping topography located around skirt of volcano including pyroclastic-, mud- and lava-flow fields, and volcanic fan produced by dissection of volcanic body. Slightly dissected.	21	0.15	0.26
8	Moderately eroded mountains, lava flow, etc.	Fluvial or marine terrace with flat surface and step-like form. Covered with subsurface deposits (gravel or sandy soils) of more than 5 m in thickness.	174	-0.12	0.34
9	Terrace covered with volcanic ash soil	Fluvial or marine terrace with flat surface and step-like form. Covered with cohesive volcanic ash soil of more than 5 m in thickness.	60	0.04	0.25
10	Valley bottom plain	Long and narrow lowland formed by river or stream between steep to extremely steep slopes of mountain, hill, volcano and terrace.	165	0.08	0.37
11	Alluvial fan	Semi-cone-like form comprised of coarse materials, which is formed at boundary between mountains and lowland. Slope gradient is more than 1/1000.	79	0.02	0.31
12	Natural levee	Slightly elevated area formed along the riverbank by fluvial deposition during floods.	16	-0.07	0.36
13	Back marsh	Swampy lowland formed behind natural levees and lowlands surrounded by mountains, hills and terraces.	41	0.21	0.47
15	Delta and coastal lowland	Delta: flat lowland formed at the river mouth by fluvial accumulation. Coastal lowland: flat lowland formed along shoreline by emergence of shallow submarine deposits, including discontinuous lowlands along sea- or lake- shore.	68	0.19	0.44
16	Marine sand and gravel bars	Slightly elevated topography formed along shoreline, comprised of sand and gravel, which was washed ashore by ocean wave and/or current action.	34	0.00	0.36
17	Sand dune	Wavy topography usually formed along shoreline or river, comprised of fine to moderately aeolian sand, generally overlies sandy lowland.	15	0.14	0.35
20	Filled land	Former water body such as sea, lake, lagoon, and river reclaimed as land by filling.	15	-0.04	0.35

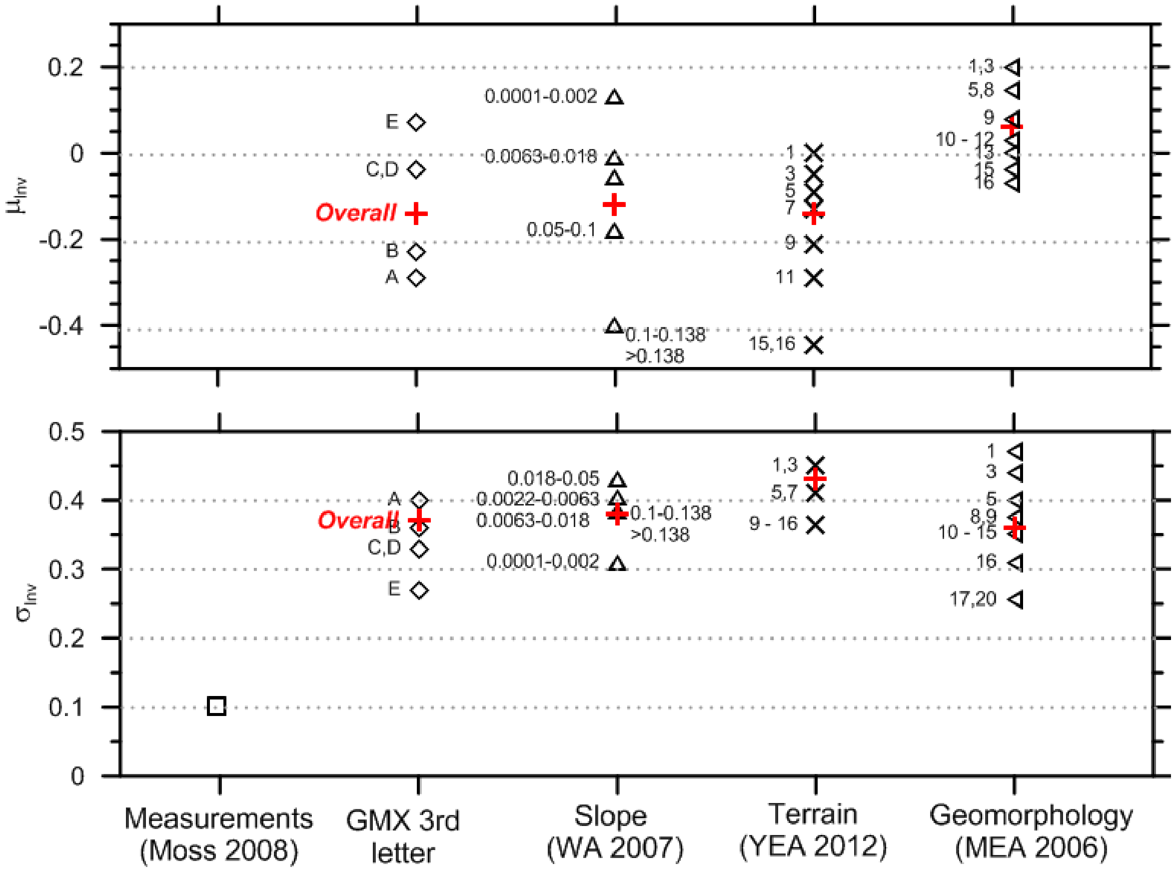

Figure 3.24 **Median and dispersion of V_{s30} prediction residuals for Japan in natural log units based on the analyses in this study. Proxy aggregates are marked as 'overall'.**

3.4.2.4 Adjustments to Recommended V_{s30} values for GMX Classes A and E

As described in Section 3.4.1.1, the GMX 3rd letter proxy was originally derived from California data. The proxy analyses presented above have used a much larger California database as well as substantial additional data for other regions. In this subsection, we address bias in the values for Classes A and E that justify modification of the recommended values. Negative bias for Category A was observed in all three regions investigated (California, Taiwan, and Japan) by amounts ranging from -0.13 to -0.29. In Figure 3.25, we show a joint histogram across all three regions, which indicates a mean and median of 516 and 507 m/sec, respectively. For Class E, the results are more mixed, with California and Japan showing relatively consistent biases of -0.17 and -0.23, whereas Taiwan is positively biased (0.17). We recommend the use of the combined data shown in Figure 3.25 with a mean and median 185 and 182 m/sec, respectively. We recommend updating the general GMX proxy-based estimation with these new values. Table 3.7 presents our recommended values for each GMX category.

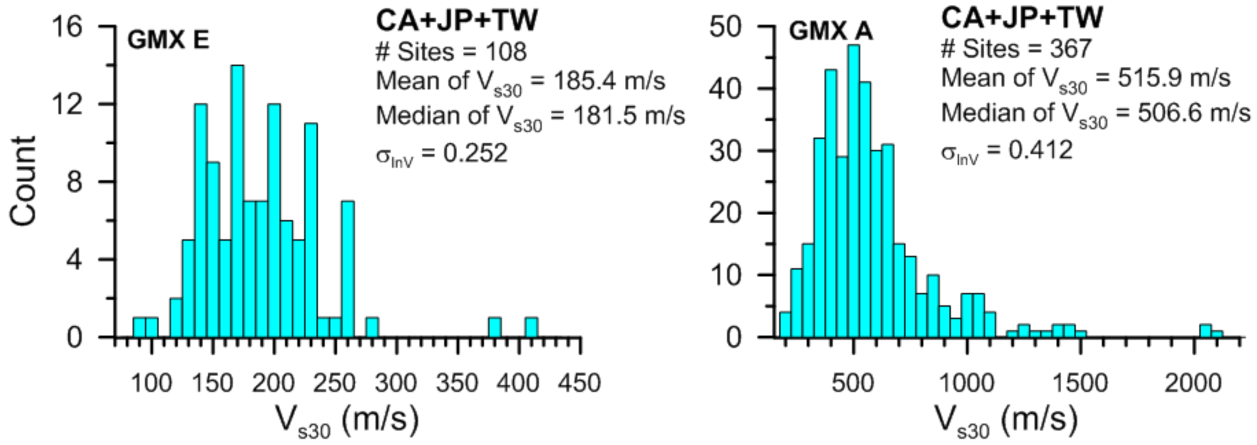

Figure 3.25 Histograms of V_{s30} from sites in California, Japan, and Taiwan for GMX categories A and E. Data utilized is from V_{s30} measurements (for profile depths greater than 20 m) and inferences of V_{s30} from V_{sz}-V_{s30} relations for shallower profiles.

Table 3.7 Recommended V_{s30} for GMX 3rd Letter categories. Values for A and E are modified from those in Chiou et al. (2008).

GMX 3rd letter	*Median V_{s30} (m/s)*	*Mean V_{s30} (m/s)*	σ_{lnV}
A	506.6	515.9	0.412
B	424.8	464.3	0.431
C	338.6	345.4	0.203
D	274.5	291.4	0.335
E	181.5	185.4	0.252

3.5 SELECTION OF PREFERRED V_{S30} AND UNCERTAINTY

3.5.1 Method of Selecting Preferred V_{s30}

For purposes of comparison, the process by which "preferred" V_{s30} values were assigned from available data in the 2006 site database are given below (Chiou et al. 2008).

1. Assigned from measured velocity profile generally from PE&A profile database. Only profiles with depths $z_p \geq 20$ m are considered with constant velocity extrapolation of the deepest V_s measurement to 30 m. A velocity profile is assigned to a strong-motion site if the separation distance is 300 m or less (Borcherdt 2002).
2. Inferred for California sites that recorded the Northridge earthquake from Borcherdt and Fumal (2002) or from other California stations from Wills and Clahan (2006) based on surface geology correlations.

3. Inferred from GMX 3rd letter correlations (Section 3.4.1.1) except for Taiwan sites, where the GMX/elevation procedure of Chiou and Youngs (2008a) was used (similar to that described in 3.4.1.2).
4. Inferred from V_s profiles with depth $z_p < 20$ m using constant velocity extrapolation of the deepest V_s measurement to 30 m.
5. Inferred from site categories by Spudich et al. (1997, 1999) and correlations to V_{s30}. This code is specific to stations in extensional regions.
6. Taken directly or inferred from maps of V_{s30} for Alaska based on VIC (Vibration Instrument Ltd., Tokyo, Japan) high-frequency Rayleigh wave data (Martirosyan et al. 2002). This code is specific to Alaska.

The numbers in the list above (0–5) correspond to codes in the 2006 site database used to identify the source of V_{s30} information. The lowest value of the code have the highest preference for the assignment of V_{s30} (0 is most preferred; 5 is least preferred). The manner by which the codes were sequenced was expert judgment. There are prescribed levels of uncertainty associated with each code, as explained further in the next section.

In the current (2013) site database, the protocols have been updated as a result of the availability of additional proxies and the analysis of proxy performance presented in Section 3.4.2. The following codes are applied to V_{s30} measurements and estimates in the 2013 site database:

1. Assign from measured velocity profile, $z_p \geq 30$ m using the data sources given in Section 3.3.1.
2. Estimated from V_s profiles with depths $10 < z_p < 30$ m using region-dependent correlations with depth in Boore (2004) and Boore et al. (2011).

   (a) Infer from geology-based correlations calibrated for the region where the site is located and using detailed descriptions of geological categories (e.g., distinguishing Quaternary alluvium based on texture and/or age). These maps are typically digital maps or paper maps 1:50,000 scale or smaller.

   (b) Infer from geology-based correlations that do not meet the criteria of 2a (e.g., lack of local calibration, relatively coarse geological mapping).
3. (a) Infer from geotechnical correlations (GMX 3rd letter, etc.) within its calibration region (e.g., California).

   (b) Inferred from generalized geotechnical correlations outside the calibration region.
4. Infer from geomorphologic proxies described in Section 3.4.1.2, including models based on:
5. (a) GMX+Elevation [i.e., Taiwan only, Chiou, personal communication (2012)].

   (b) Ground slope [i.e., Wald and Allen (2007)].

   (c) Terrain-based categories [i.e., Yong et al. (2012)].
6. Infer from local V_s mapping (e.g., microzonation maps).

As before, the low codes corresponding to measurements (0 or 1) receive the highest priority for V_{s30} assignment. The proxy analysis from Section 3.4.2 does not clearly reject any particular proxy-based method for estimating V_{s30}, but does provide a basis for assigning relative weights to proxies based on the regional proxy aggregated mean and standard deviation of residuals ($\mu_{\ln V}$ and $\sigma_{\ln V}$, respectively). The relative weight is taken from the inverse of the residual sum of squares of the aggregated mean and standard deviation:

$$\text{Relative weight for selected proxy and region} = \frac{1}{\mu_{\ln V}^2 + \sigma_{\ln V}^2} \tag{3.7}$$

The actual weight is computed from the relative weights through adjustment to ensure they sum to one. Table 3.8 shows the relative weights and computed proxy weights using this procedure. The computed weights apply only when all proxies are available. If only a subset of proxies is available, the weights are adjusted to sum to one for those proxies. For example, in California, if a site has geology (2a) and ground slope (4b), the weights are 0.67 and 0.33 for the geology- and slope-based estimates of V_{s30}, respectively. The proxies listed in Table 3.8 are those that are available for the respective regions.

Table 3.8 Relative proxy weights by region and applied weights for V_{s30} estimation when each proxy is available for a site.

Region	Proxy	$\mu_{\ln V}$	$\sigma_{\ln V}$	Rel. Wt. (Eq. 3.7)	Weight[1]
CA	Geology	-0.06	0.33	8.89	0.35
	GMX	-0.08	0.40	6.01	0.24
	Slope	-0.01	0.45	4.94	0.20
	Terrain	-0.11	0.42	5.31	0.21
Taiwan	GMX	0.15	0.37	6.27	0.21
	GMX+elev	0.02	0.32	9.73	0.33
	Slope	0.07	0.34	8.30	0.28
	Terrain	0.13	0.42	5.17	0.18
Japan	GMX	-0.14	0.38	6.10	0.28
	Geomorph.	-0.04	0.42	5.62	0.26
	Slope	-0.12	0.42	5.24	0.24
	Terrain	-0.14	0.43	4.89	0.22

[1] Weights in this column apply when all proxies available for a given site

3.5.2 V_{S30} Uncertainties

The preferred V_{S30} value for the site is taken to represent the median estimate of V_{S30} or the mean estimate $\ln(V_{S30})$. The assignment of epistemic uncertainty to V_{S30} is dependent on the estimation method and is expressed as a log standard deviation, $\sigma_{\ln V}$. The manner by which this uncertainty was assigned in the 2006 database (for comparison purposes) and for the present database is described in the following sub-sections.

3.5.2.1 V_{s30} Uncertainty in Vol. 23 Site Database

In the Vol. 23 site database (Chiou et al. 2008), V_{s30} uncertainty was assigned for sites with and without measurements, based principally on the judgment of PE&A and cluster analyses at a limited number of sites with multiple and closely-spaced V_s measurements at the time.

The estimate of V_{S30} uncertainty for sites with measured shear-wave velocities was based in part on the outcome of an analysis of variance of closely spaced V_{S30} measurements in the PE&A profile database. The assigned uncertainty is a function of profile stiffness which was represented by NEHRP classification, as shown in Figure 3.26. As described in Chiou et al. (2008), data from a site in Gilroy, California (NEHRP D site) having sixteen nearby measurements of V_{S30} yielded a standard deviation of $\sigma_{\ln V} = 0.08$, so a value of 0.10 was used for D sites generally. Uncertainty values for other site classes were set based on similar cluster analyses and judgment of PE&A, with the results given in Figure 3.26. The observations of increased uncertainty in V_s for rock sites as compared to soil sites noted by Schneider and Silva (1994) influenced this judgment, resulting in increased $\sigma_{\ln V}$ values of up to 0.3 for Class A sites.

The observed V_{s30} aleatory variability (within category randomness) within surface geological units [Table 2 of Chiou et al. (2008)] formed the basis for the assigned epistemic variability in the V_{S30} values inferred from site geology (Figure 3.26). Similarly, Geomatrix or Spudich within category randomness [Table 3 of Chiou et al. (2008)], along with judgment formed the basis of assigned epistemic variability for other cases shown in Figure 3.26.

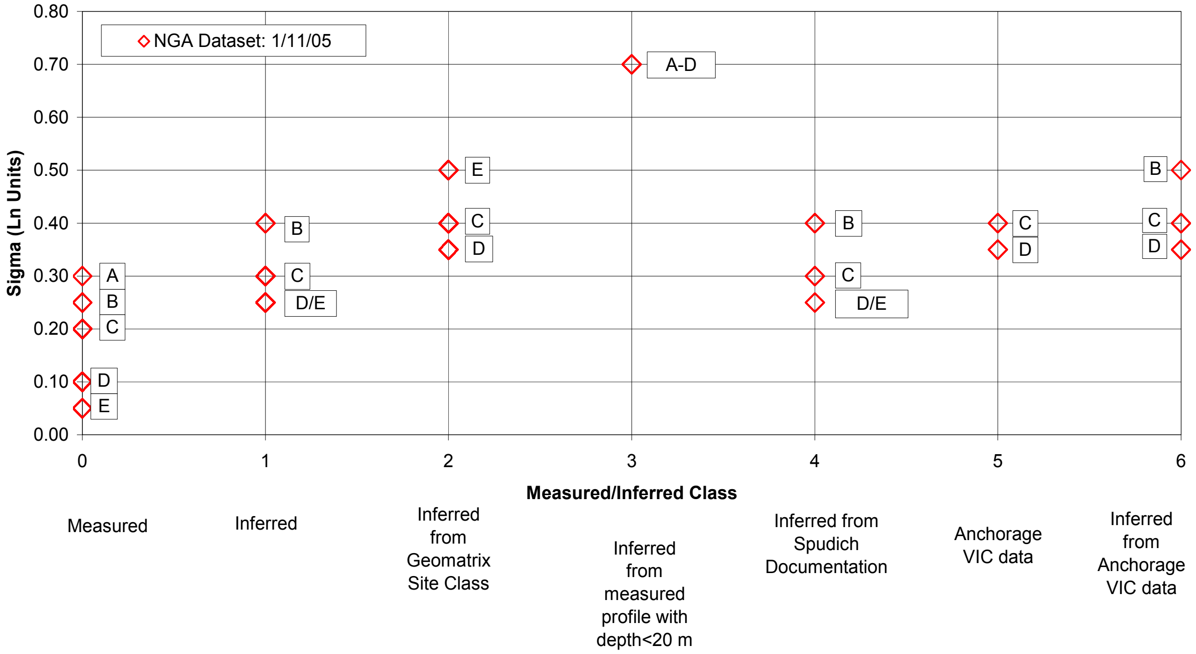

Figure 3.26 Uncertainty of V_{s30} used in Vol. 23 site database [from Chiou et al. (2008)].

3.5.2.2 V_{s30} Uncertainty in Present Site Database

For the current site database, we have re-visited the assignment of $\sigma_{\ln V}$ and attempted to increase the transparency by which the values are assigned, although some judgment is still applied.

(a) V_{s30} uncertainty for Code 0 sites

In the case of code 0 sites, we have re-examined the dispersion of V_{s30} measurements from single sites with multiple profiles. The profile data analyzed include six sites in California from Boore and Asten (2005), two sites in California from Brown et al. (2000), three sites explored with surface wave method by various researchers and reported by Moss (2008), and the DCPP site owned by Pacific Gas & Electric (PG&E, 2011). The profiles from this data set were in some cases derived from combinations of surface wave (SW) and downhole (DH) methods, while in other cases only one measurement type was used. In Figure 3.27, we show $\sigma_{\ln V}$ for the clusters of profiles at these sites against the median V_{s30}. Different colors are used for sites from single and multiple measurement types. Note that we have not included data from Remi-based profiles for this compilation. We also show in the figure values of $\sigma_{\ln V}$ from the proprietary PE&A profile data base for eight sites in California and South Carolina; in those cases, the cluster statics were provided by PE&A (R. Darragh personal communication, 2012) and were in some cases obtained from several different measurement methods at each site (e.g., Treasure Island Geotechnical Array and Gilroy #2).

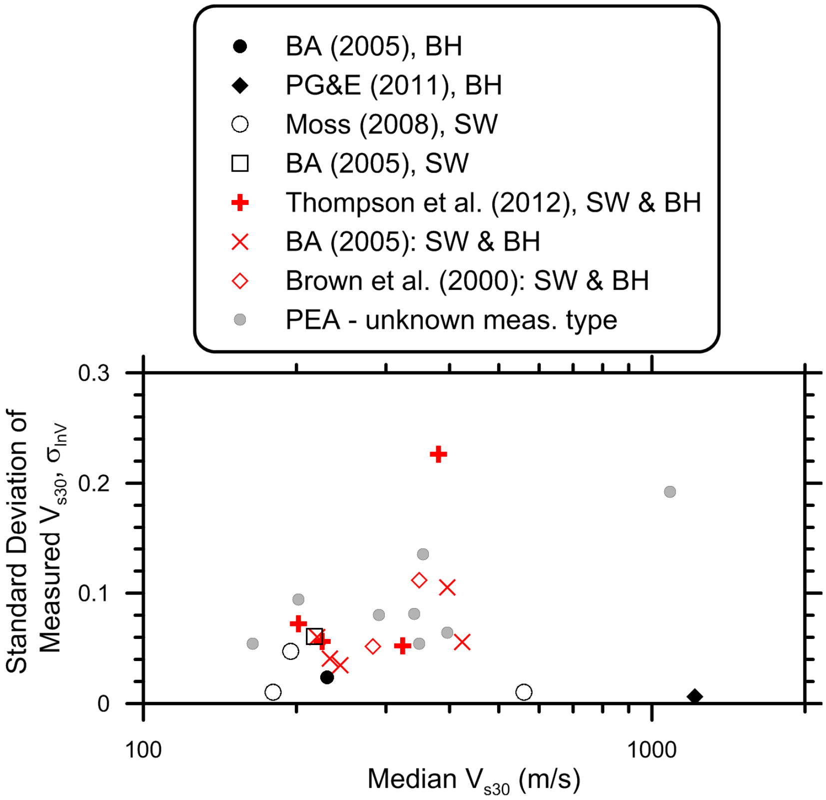

Figure 3.27 **Dispersion of V_{s30} from sites with multiple profiles obtained with surface wave (SW) and/or borehole (BH) methods.**

The velocity dispersions ($\sigma_{\ln V}$) in Figure 3.27 reflect spatial variations in seismic velocities at modest separation distances between profiles (ranging from 10 sec to 100 sec of meters; above references and R. Moss and R. Kayen, personal communication, 2012). For example, V_{s30} uncertainties at the Coyote Creek and William Street Park sites described by Boore and Asten (2005) are derived from profiles at various locations separated by as much as approximately 200 m [see Figure 4 of Boore and Asten (2005)]. In the case of the Thompson et al. (2012), the maximum lateral separation distances of profiles are approximately 450–1400 m. As shown in Figure 3.27, the results have no clear sensitivity to test type (i.e., SW versus BH) nor to whether SW and BH methods were combined at a given site. This suggests that method-to-method variability is modest when the V_s profiles are from sources known to produce reliable results, which is the case for the data utilized here. [We note parenthetically that more method-to-method variability was observed by Moss (2008), which included Remi data from several sites.] Such inter-method variability can arise due to varying levels of quality in the underlying measurements, which can be minimized by only using data from sources known to produce reliable results (which is generally the case for the profiles used in the NGA-West2 project). Inter-method variability can also arise from the different volumes of soils tested in surface wave techniques versus borehole techniques, in which case it largely reflects spatial variability in the velocity structure.

An outlier in Figure 3.27 is Kiknet site TKCH08 ($\sigma_{\ln V} = 0.23$, median $V_{s30} = 380$ m/sec) from Thompson et al. (2012), which is one of four sites investigated with multiple V_s profiles in that study. Values of $\sigma_{\ln V}$ for the other sites range from 0.05–0.07. Google Earth imagery shows the terrain for the sites with modest values of $\sigma_{\ln V}$ to be fairly consistent; whereas site TKCH05 is located in a narrow valley in which some of the profiles are within the valley, and others are near the edge where rock is likely to occur at relatively shallow depths. This example shows that separation distance between profiles is less important than consistency in the terrain, which presumably correlates in most cases to consistent geology. The high value of σ_{lnV} for TKCH08 appears to result from inconsistencies in the underlying geology.

Examining all the available COV and σ_{lnV} values in Figure 3.27, we see the dispersion is not particularly sensitive to site stiffness, as reflected by mean V_{s30}. However, the figure shows a slight trend for increasing dispersion with increasing velocity, clearly additional measurements are required. Based on the available data, our judgment is that when the geology of the profile and strong-motion sites match, and they are separated by distances of several 100 m or less, a reasonable value of the dispersion regardless of mean V_{s30} is approximately $\sigma_{lnV} = 0.06$. As shown by the TKCH05 site, this dispersion is much higher when the site geology is heterogeneous relative to the separation distance between the profile and strong-motion site. Considering all of the above, we consider a value of σ_{lnV}=0.1 to be reasonable for use with code 0, which is similar to the single data point reported for the assignment of σ_{lnV} in the Vol. 23 site database. This constant value replaces the strong increase of σ_{lnV} with site stiffness in the Vol. 23 site database (shown in Figure 3.27). Note that rock dispersion in an absolute sense is still higher than that for soil, since σ_{lnV} is a normalized quantity. We recognize that this value is likely on the high side for a large number of the code 0 sites where the profile and strong-motion station are located at relatively close distances (< ~ 100 m) on similar geology. Conversely, this value is on the low side for sites where the profile and strong-motion stations are on different geologic conditions, although this is expected to be relatively rare.

As shown in Figure 3.27, the database from which σ_{lnV} can be evaluated is limited, especially for firm sites with $V_{s30} > \sim 400$ m/sec and soft sites with $V_{s30} < \sim 200$ m/sec. As additional data are added, the recommendations provided here may change.

(b) V_{s30} uncertainty for Code > 0 sites

For Code 1 sites, uncertainty arises from intra-site variability (as in Code 0) and uncertainty associated with the V_{sz} to V_{s30} extrapolation described in Section 3.3.2. These two sources of uncertainty are assumed to be statistically independent, and thus are combined by summing the associated variances. The V_{sz} to V_{s30} extrapolation uncertainties are dominant, and are based on the standard deviation of residuals as provided in Boore (2004) and Boore et al. (2011). The resulting σ_{lnV} values are shown in Figure 3.28 and decrease with increasing total depth of the profile.

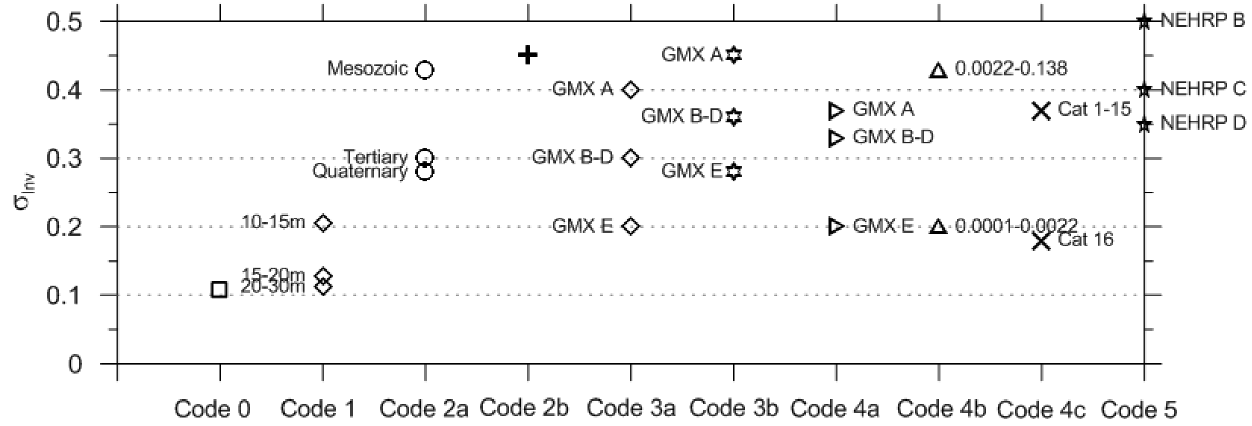

Figure 3.28 Recommend dispersion of V_{s30} in natural log units when derived from various information sources.

For the proxy methods (Code > 1), we assign uncertainties on the basis of the proxy data analysis from Section 3.4.2. We assign weighted standard deviations (σ_{lnV}) for various combinations of proxies using weights computed as described in Section 3.5.1 (Table 3.8). Values of σ_{lnV} for specific codes are discussed in the following and shown in Figure 3.28:

2. (a) Values of σ_{lnV} are provided for three broad geologic categories, based on averaging applicable sub-category σ_{lnV} values provided in Wills and Clahan (2006). The values apply to California and Italian sites.

   (b) We recommend $\sigma_{lnV} = 0.45$ based on judgment.

3. (a) Geometric means of σ_{lnV} values from proxy analysis are assigned for each GMX 3rd letter category. The assigned values are: $\sigma_{lnV} = 0.4$ for Class A, 0.3 for Classes B-D and 0.20 for Class E.

   (b) We sum the variances Code 3a and 0.2 (from cluster measurements reported in Section 3.4.2), giving σ_{lnV} values of 0.45 (A), 0.36 (B-D) and 0.28 (E).

4. (a) Based on the Taiwan proxy analysis, we assign $\sigma_{lnV} = 0.37$ (A), 0.33 (B-D), and 0.20 (E).

(b) Geometric means of σ_{lnV} values from proxy analysis are assigned for various bins of slopes; we use $\sigma_{lnV} = 0.2$ for slopes flatter than 0.0022 and $\sigma_{lnV} = 0.43$ otherwise.

(c) Geometric means of σ_{lnV} values from proxy analysis are assigned for terrain categories. We assign 0.37 for all categories except category 16, for which we assign 0.18.

5. Values unchanged from 2006 database [Figure 5 of Chiou et al. (2008)].

3.6 THREE-DIMENSIONAL VELOCITY MODELS

3.6.1 Introduction

The basin depth parameter Z_x is the depth to a shear-wave isosurface having $V_s = x$ km/sec, which is utilized for site parameterization in three of the NGA GMPEs. Abrahamson and Silva (2008) and Chiou and Youngs (2008b) take $x = 1.0$ km/sec while Campbell and Bozorgnia (2008) take $x = 2.5$ km/sec.

The 2006 site database characterizes basin depth with parameters $Z_{1.0}$, $Z_{1.5}$, and $Z_{2.5}$ which define the depth in meters to shear-wave velocities of 1.0, 1.5, and 2.5 km/sec. Depths to 1.0, 1.5, and 2.5 km/sec shear-wave velocity horizons for stations in southern California were contributed by Robert Graves and Jonathan Stewart based on the SCEC-three-dimensional (3D) model (Version 2.2b, Magistrale et al. 2000), by Boatwright et al. (2004) for stations in the San Francisco Bay area, and by Graves (1994) for stations in the Eel River basin in northern California. Depth data (Z_x) at a station were superseded by values obtained from borehole data, provided a borehole exists and penetrates the velocity horizon. Many of these values were provided from the PE&A database. Additional information about sedimentary basins and depth to basement rock were contributed by Somerville et al. (2002) and Campbell (personal communication, 2003,), respectively. The basin depths derived from those sources have now been replaced by more recent information, mainly Yong et al. (2013).

In the following sections, we describe updates to seismic velocity models from which Z_x can be evaluated for portions of California. We then describe a newly implemented seismic velocity model for Japan from which Z_x values were evaluated. We also briefly list basin depth models for other regions (outside of California and Japan) and describe why they were not suitable for defining Z_x values for use in the NGA-West2 project.

3.6.2 Basin Models in California

3.6.2.1 Southern California

The Southern California Earthquake Center (SCEC) currently has two comprehensive 3D seismic velocity models for the greater southern California region: CVM-S4 and CVM-H11.1.0. While the SCEC community acknowledges differences between the two velocity models, there is no consensus as to what is the preferred model.

The CVM-S4 model is the fourth version of a model developed by Harold Magistrale and others (http://scec.usc.edu/scecpedia/CVM-S). The model is largely based on geological structure models. For the deeper sediments, velocities are estimated using empirical relationships between age of the formation and depth of burial that have been calibrated from regional data (Kohler et al. 2003). For the shallower sediments, velocities are taken from geotechnical borehole measurements. The non-basin velocities in the model are based on a tomographic study by Hauksson (2000). Based on the modeling work of Graves and Pitarka (2010), we have replaced the CVM-S4 shear-wave velocities within Imperial Valley sediments using the mudline relation of Brocher (2005). This change reduced the minimum shear-wave velocity in the Imperial Valley from 818 m/sec to 379 m/sec.

The CVM-H11.1.0 model is the Version 11.1.0 Harvard model that has been developed by John Shaw and others (http://scec.usc.edu/scecpedia/CVM-H). The model consists of basin structures defined using high-quality industry seismic reflection profiles and tens of thousands of direct P-wave velocity measurements from boreholes (Süss and Shaw 2003; Plesch et al. 2009), as well as refinements to the background velocity structure using waveform tomography (Hauksson 2000; Tape et al. 2009). The shear-wave velocities and densities are calculated, in general, from P-wave velocities using empirical rules [e.g., Zhu (2003)].

The basin depth parameters (Z_x) were found by querying the velocity models at 20-m depth increments and tabulating the minimum (shallowest) and maximum (deepest) encounter of $V_s = x$. In most cases, the minimum and maximum depths are the same; however when velocity inversions are present in the depth profile the minimum and maximum depths differ. When the minimum and maximum depths differ, the maximum depth is used. The rationale is that the maximum depth provides a better characterization of large-scale basin structure.

All Southern California sites are within the region covered by CVM-H11.1.0 model, and most are also within the tomography and basin regions covered by CVM-S4. Both models start with the Hauksson (2000) tomography results to specify the velocity structure in the non-basin regions. The tomography results have poor resolution in the shallow crust and therefore the shear-wave velocity at the surface is generally greater than 3 km/sec. Consequently, for sites outside the basin regions, but within the tomography region in CVM-S4, the $Z_{1.0}$ value is zero and the $Z_{2.5}$ value is usually zero for this model. Outside of basin regions, The CVM-H11.1.0 model also includes tomography from the Tape et al. (2009) 3D waveform inversion study, which provides improved resolution (and generally lower shear-wave velocities) in the shallow crust. In addition, CVM-H11.1.0 also applies a transition to a generic Boore and Joyner (1997) rock profile in the near surface (upper 300 m). In application, the Boore and Joyner (1997) rock profile is modified so that a gradual transition to the underlying hard-rock velocities is achieved. Consequently, CVM-H11.1.0 has lower shear-wave velocities than CVMS4 in the near surface of the non-basin regions, and in many cases approaches values of around 1 km/sec at the ground surface. Because the Boore and Joyner (1997) rock profile is modified, there is no clear metric to distinguish which sites use the generic velocity model. If model reports both $Z_{1.0} = 0$ and $Z_{2.5} = 0$, then both values are set to -999 to reflect that the model has no information regarding the site. If the model reports $Z_{1.0} = 0$ and $Z_{2.5} > 0$, then $Z_{1.0}$ is set as -999 and the $Z_{2.5}$ is retained because the tomography model may have some resolution on this part of the velocity structure.

Figures 3.29 and 3.30 present the spatial variation of $Z_{1.0}$ for the CVM-H11.1.0 and CVM-S4 models, respectively.

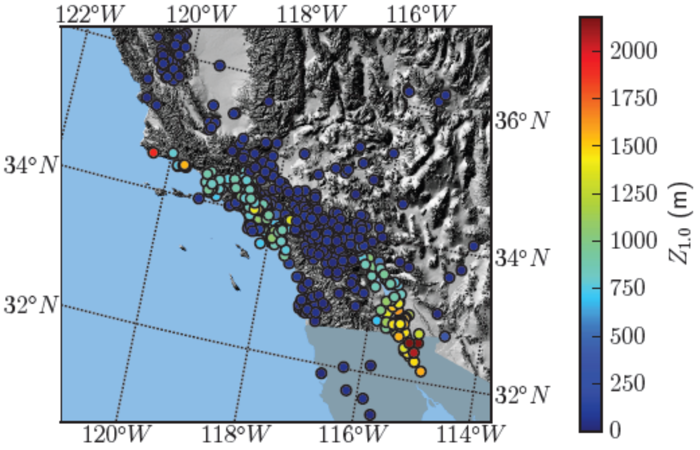

Figure 3.29 **Depth to 1 km/sec ($Z_{1.0}$) reported by the CVM-H11.1.0 model. CVM-H11.1.0 model provides $Z_{1.0}$ values for 746 sites.**

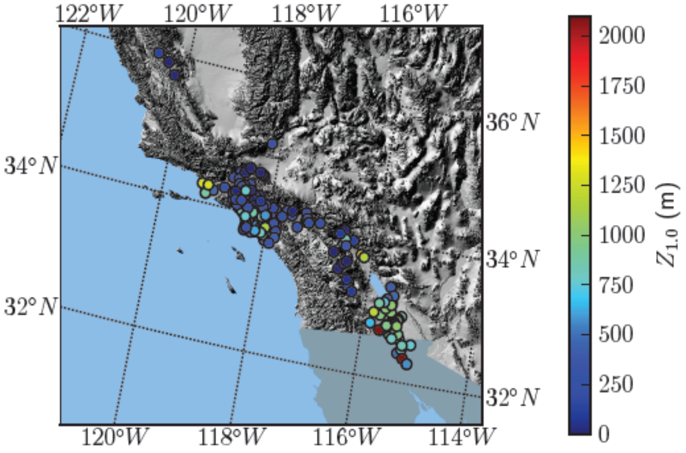

Figure 3.30 **Depth to 1 km/sec ($Z_{1.0}$) reported by the CVM-S4 model. The CVM-S4 model provides $Z_{1.0}$ values for only 242 sites.**

The histogram of $Z_{1.0}$ values from CVM-S4 and CVM-H11.1.0 is shown in Figure 3.31. There are significant differences between the $Z_{1.0}$ values provided by the two models. The CVM-S4 model generally provides shallower $Z_{1.0}$ with a mean of 446 m, whereas the CVM-H11.1.0 models have a mean $Z_{1.0}$ of 705 m.

The histograms of $Z_{2.5}$ values from CVM-S4 and CVM-H11.1.0 are shown in Figure 3.32. The mean $Z_{2.5}$ values computed from CVM-S4 and CVM-H11.1.0 are 2551 m and 2610 m, respectively. The similarities in these values indicate that the $Z_{2.5}$ parameter is relatively stable between the two models.

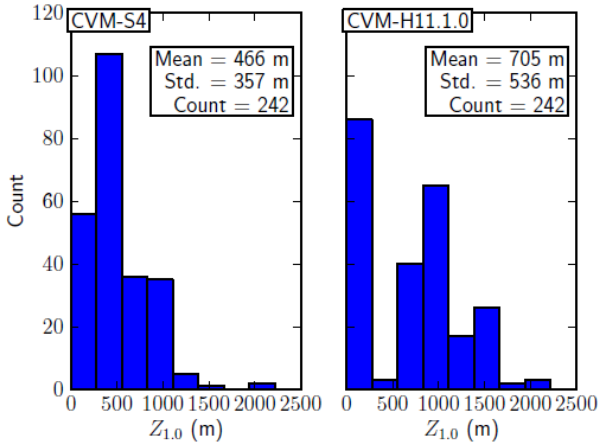

Figure 3.31 **Histogram of the $Z_{1.0}$ values computed from the CVM-S4 and CVMH11.1.0 models.**

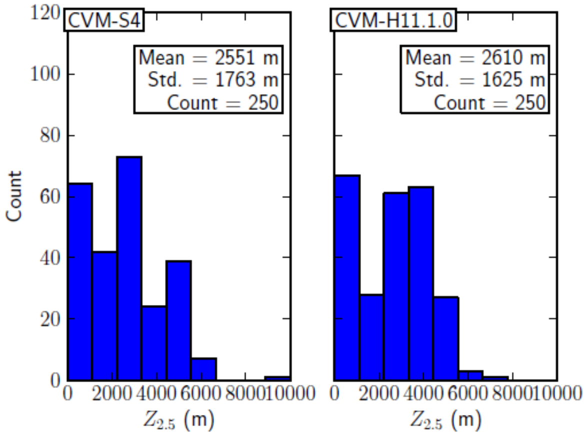

Figure 3.32 **Histogram of the $Z_{2.5}$ values computed from the CVM-S4 and CVMH11.1.0 models.**

A number of the sites for which $Z_{1.0}$ and $Z_{2.5}$ have been tabulated in the southern California region for the NGA-West2 project were also included in the original NGA (2008) site database. The 2008 values were obtained only from a single 3D model: CVM-S2.2b. The primary changes from V2.2b to V4.0 of CVM-S are:

- A new San Bernardino Valley basement is based on recent USGS inversion of gravity data confirmed by comparison to a seismic reflection line. The new model features a deep trough in the central valley, in contrast to the previous flat-bottomed valley model. The new basement joins smoothly to the relatively shallow Chino basin to the west.
- A new model for the Salton Trough is motivated by the needs of TeraShake simulations of southern San Andreas fault events. Depth to basement is defined by a combination of seismic refraction surveys, inversion of gravity observations, surface geology, and boreholes. Sediment velocity-depth gradients depend on the nature of the basement, smoothly merging into deep meta-sedimentary basement,

and having a discontinuity above shallow crystalline basement. The model includes the portion of the Trough south of the international border with Mexico.

- A new V_p-density relation is used that is based on density measurements from oil well samples in the Los Angeles basin and the San Gabriel Valley, geotechnical boreholes throughout southern California, and 12 oil wells along the LARSE lines. The newly determined V_p-density ratio is constant, in contrast to the old relation. This is true even for low V_p, as defined by the geotechnical data. The new densities are higher, for a given V_p, than from the old model. Because density is correlated to Poisson’s ratio [using the relation of Ludwig et al. (1970)], the density increase will tend to lower the Poisson’s ratio. The reduction of Poisson’s ratio, in turn, will lower V_p / V_s. In summary, changing the V_p -density relation produces a new V_s model.
- As part of SCEC's work in producing a comprehensive platform for maintaining and distributing the Community Velocity Models (CVM-H and CVM-S), the CVM-S4 software was analyzed, and a "bug-fix" version was developed by Geoff Ely at the University of Southern California. The patches to the code primarily involved the explicit initialization of variables to zero values (initialization was implicit in older versions, the behavior of which is compiler and platform dependent). The effect of the initialization change does not have any systematic effect on the velocity values produced by the code. The non-initialized values tend to scatter about the initialized values within a range of a few percent in most cases. The overall impact of the changes was determined to be of minor significance on the resulting values produced by the code.

3.6.2.2 Northern California

The 2006 site database (Chiou et al 2008) includes basin depth parameters derived from Model 05.0.0 of a 3D Bay Area velocity model described in Boatwright et al. (2004), Brocher (2005) and Hardebeck et al. (2007). Similar to the SCEC model, this 3D velocity model is based on a structural and geological model of the region, which is converted to V_p and then to V_p. This model has been updated and Version 08.3.0 was used to select basin parameters for the present work (available from http://earthquake.usgs.gov/research/structure/3dgeologic/download.php). The model updates are described in Aagaard et al. (2008, 2010). The new models provide improved predictions of surface wave arrivals from small San Francisco Bay Area seismic events.

3.6.3 Basin Models in Other Regions

Basin depth models for particular regions have been developed from various geophysical data sources including gravity surveys, reflection/refraction surveys, and deep boreholes. Basin models outside of southern California and the San Francisco Bay Area that have been used in ground motion simulations, but not necessarily to extract depth parameters for empirical ground motion studies, include:

- Statewide California models based on tomography (Lin et al. 2010)
- Eel River basin in northern California (Graves 1994)

- Puget Sound and Seattle areas [e.g., Symons and Crosson (1997); Brocher et al. (2001)]
- Tokyo Bay region, Japan (Sato et al 1999)
- Osaka and Kobe regions, Japan (Kagawa et al. 2004)
- Adapazari basin, Turkey (Goto et al. 2005)

It is important to distinguish between basin and velocity models. These basin models describe only the basin depths. To evaluate depth parameters defined from a shear-wave isosurface such as $Z_{1.0}$, $Z_{1.5}$, and $Z_{2.5}$, a 3D model of seismic velocities is required. Such models are only available for California and Japan. Hence, the references given above were not used in the NGA-West 2 project.

For Japan, we utilize the NIED (National Research Institute for Earth Science and Disaster Prevention) seismic velocity model. The basin model was developed through a combination of deep boreholes, reflection and refraction surveys, micro-tremor surveys, and gravity surveys (Fujiwara et al. 2006; Earthquake Research Committee 2008). Additionally, tomography was used to verify and refine the basin structure. The velocity profiles found within the model are monotonically increasing, thus eliminating the need for both the minimum and maximum depth. The data for the basin depths was downloaded from http://www.j-shis.bosai.go.jp/map/?lang=en (last accessed on 11/2/2011). The report (in Japanese) that describes this work can be downloaded from: http://www.j-shis.bosai.go.jp/map/JSHIS2/data/DOC/Report/337/DOC-Report-2009.zip (last accessed on 11/2/2011).

A map of basin depth values for $Z_{1.0}$ and $Z_{2.5}$ are shown in Figure 3.33. The Tokyo basin is evident in the maps from large $Z_{1.0}$ and $Z_{2.5}$ values. The Niigata basin is evident only in the $Z_{2.5}$ map.

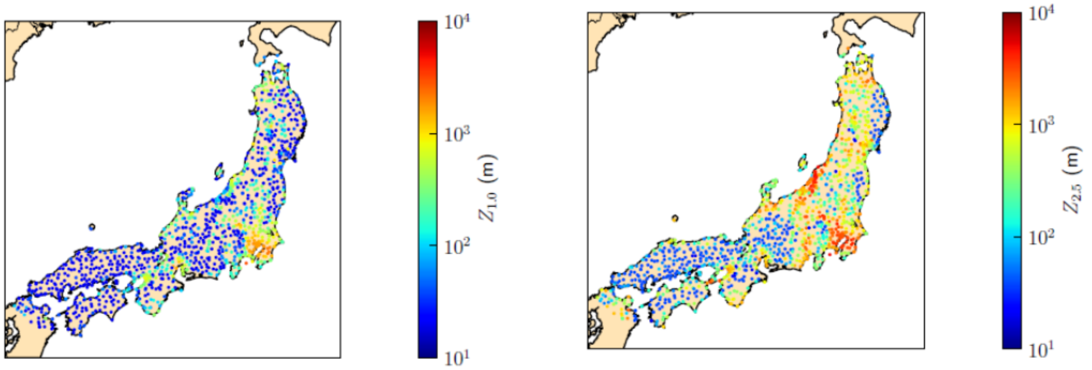

Figure 3.33 The spatial distribution of the $Z_{1.0}$ and $Z_{2.5}$ basin depth parameter.

4 Propagation Path Table

4.1 ORGANIZATION AND OBJECTIVES OF PROPAGATION PATH TABLE

Unlike the source table and site database, the propagation path metadata parameters are not collected but calculated based on the geometry of the finite fault rupture plane and the location of the station. The main objective of the propagation path table is to develop stable estimates of parameters that describe the path effects. The key metadata parameters include various distance measures, a hanging wall indicator, radiation pattern coefficients, and directivity parameters. Section 4.2 details the path parameters. Section the 4.3 is a brief note on the consideration for alternative distance estimates for multiple fault/rupture events. Section 4.4 details the methods used to estimate the new distance measure proposed during the NGA-West2 project.

Major participants in the propagation path table development for NGA-West 2 included members of the Task 1 working group (Brian Chiou, Paul Spudich, Badie Rowshandel, Jenny Watson-Lamprey, Jack Baker, and Shrey Shahi) and the following additional project researchers: Timothy D. Ancheta (PEER), Tadahiro Kishida (PEER), Jennifer Donahue (Geosyntec), Katie Wooddell (PG&E), and Robert Youngs (AMEC). Nancy Collins and her colleagues at the URS Corporation reviewed and checked the path metadata of an early version of the NGA-West1 database. Paul Spudich of USGS checked the distance measures R_{RUP} and R_{JB} for the NGA-West2 database.

4.2 PATH PARAMETERS

Data in the propagation path table include six source-to-site distance measures (epicentral distance, R_{EPI}, hypocentral distance, R_{HYP}, shortest distance to rupture plane, R_{RUP}, Joyner-Boore distance, R_{JB}, distance measured perpendicular to the fault strike from the surface projection of the up-dip edge of the fault plane, $R_{X,}$ distance measured parallel to the fault strike from the midpoint of the surface projection of the fault plane, R_Y), a hanging wall indicator, radiation pattern coefficients, source-to-site azimuth, and directivity parameters. Schematics showing the definitions of the hanging wall indicator, source-to-site azimuth, and the five source-to-site distance measures are provided in Figures 4.1 through 4.5. New parameters developed during the NGA-West2 project include the local strike parallel direction, various local distance metrics and corresponding event segment parameters, and the distance measured parallel from the midpoint of the fault, R_Y. Many of the new parameters were developed to test the effect of multiple segment ruptures on the source-to-site distance measures. Furthermore, directivity parameters have been expanded to include multiple models of directivity that are being developed within the

NGA-West2 project. The set of directivity models considered is intended to aid the direct inclusion of directivity effects into the updated GMPEs for the NGA-West2 project.

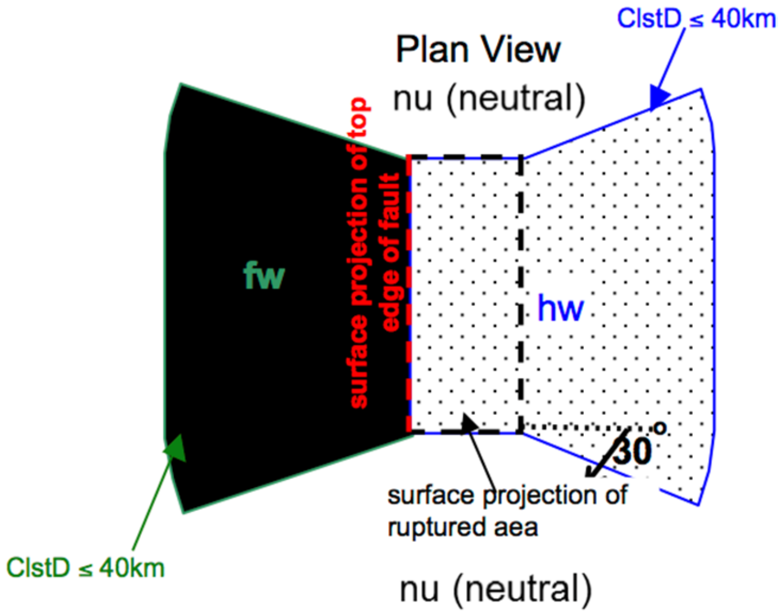

Figure 4.1 A plan view representation of areas which delineate the hanging wall indicators. hw = for sites on the hanging wall, fw = for sites on the footwall, nu = for neutral sites.

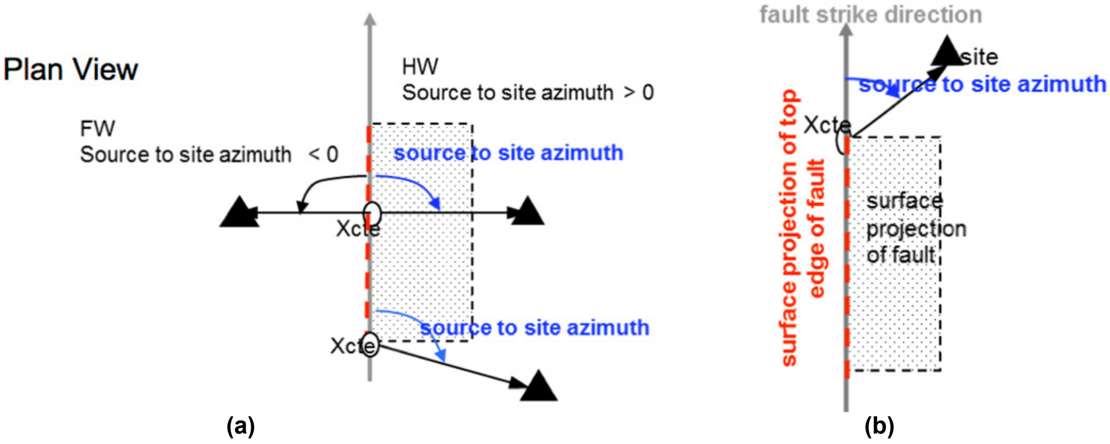

Figure 4.2 (a) A plan view definition of the source to site azimuth for dipping dip-slip faults; and (b) a plan view definition of the source to site azimuth for dipping strike-slip faults. Xcte is site's closest point on the surface projection of top edge of fault (red dotted line). Various sites are illustrated in black triangles.

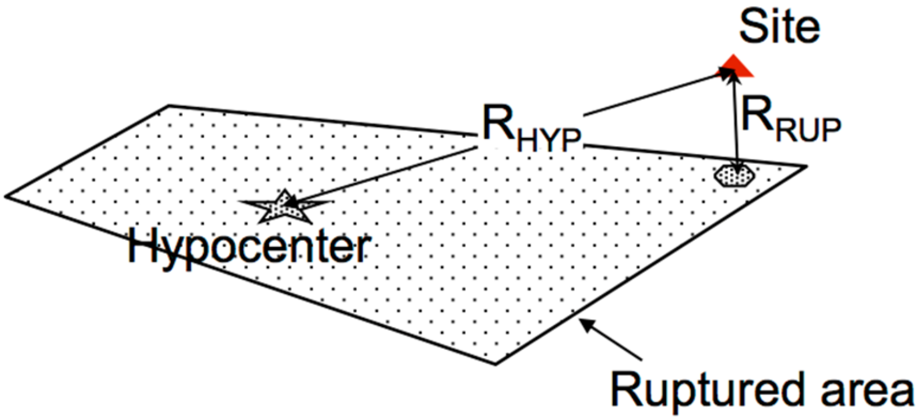

Figure 4.3 A schematic of the closest distance to the rupture plane (R_{RUP}) and the hypocenter distance (R_{HYP}) measure for example fault plane.

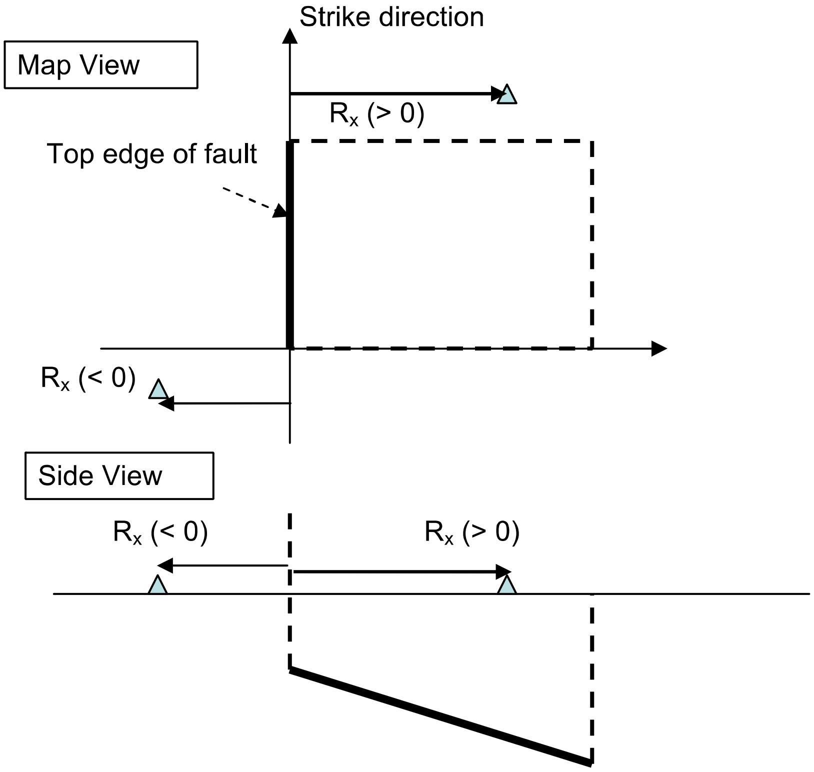

Figure 4.4 A map (top) and side (bottom) view schematic of the source-to-site distance measure R_X for an example fault (thick black line) plane and stations located on the hanging wall ($R_X > 0$) and footwall ($R_X < 0$) side. Taken from Chiou and Youngs (2008).

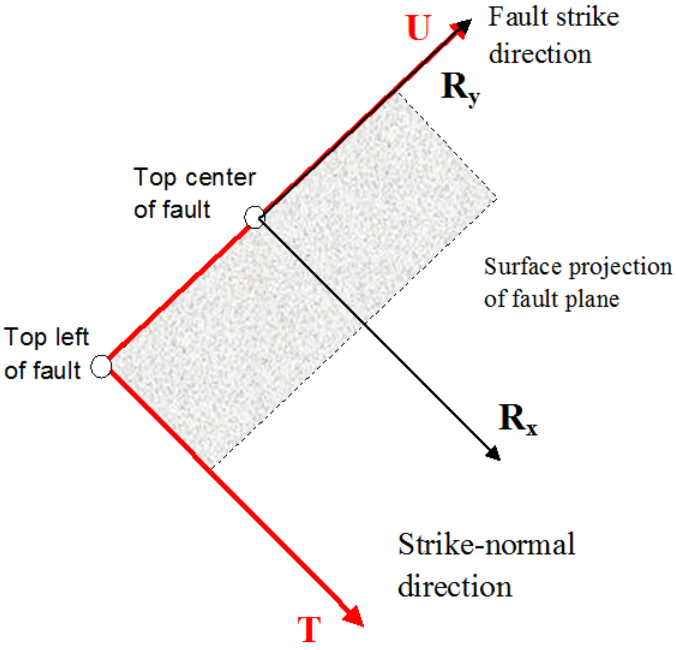

Figure 4.5 A map view schematic of the source-to-site distance measure R_Y and R_X and the U and T parameters from the generalized coordinate system in Spudich and Chiou (2008). Positive directions are shown.

Computation of the above metadata requires a 3D representation of finite fault rupture plane (the finite fault model) and station coordinates as inputs. For the case of single-segment finite-fault model, the ruptured area is simply represented by a rectangle. For the case of multiple-segment non-vertical finite fault, representing the 3D ruptured area is not as straightforward as the above because gap or intersection exists between two successive rectangles. To remedy this problem, a simplified version of the method developed by Robert Youngs (personal communication) was used to construct the down-dip portion of a multi-segment fault. First, create dipping rectangles by projecting (perpendicular to the strike of each rectangle) the top of fault down-dip to a common depth; bottom edges of the resulting rectangles are disconnected. Then, the bottom edges are connected by moving the pertinent vertices to the intersecting point of the two bordering edges. This method transforms disconnected rectangles to connected trapezoids. It is important to note that R_X and R_Y were calculated differently than all other distance metrics in the case of a multiple-segment/rupture finite fault. As stated above, R_X and R_Y were estimated using the GC2 methodology, which provides a smooth transition in the distances around bends in the fault segments (i.e., changes in strike). All other distances were based on the closest segment or minimum distance when estimated for each segment.

The definition of each directivity parameter and the method to calculate directivity parameter for multiple-segment fault is described in the report by each of the members of Directivity Working Group and have been summarized in the working group report (Spudich et al. 2012).

The strike-parallel direction at a recording site is ambiguous when the finite fault model has multiple segments. The consensus definition reached by the NGA developers is that the local strike-parallel direction is the fault strike direction averaged over a 20 km (or less) stretch of fault segment beginning at the closest point on the fault and extending towards the epicenter.

4.3 CALCULATION OF DISTANCE METRICS CONSIDERING MULTIPLE-SEGMENT RUPTURE PLANES

In addition to the consideration of the down dip projection of planes from multiple-segment ruptures, distance metrics calculated relative to the closest or to the dominant (in relative ruptured area) fault segments may produce less scatter in residuals. To investigate this effect, alternative distance parameters are estimated for both conditions however; the distances reported in the flatfile correspond to the closest fault segment.

4.4 CALCULATION OF NEW DISTANCE PARAMETER, R_Y

The R_X distance parameter alone will not give the true distance from the fault. For this reason, an R_Y term is required to compliment the R_X term when calculating the distance to the fault. The R_Y distance term is measured parallel to the strike of the fault measured from the midpoint of the fault. R_Y is zero at the midpoint of the fault and positive and increasing in the direction of the strike. R_Y is negative and decreasing in the opposite direction of the strike (see Figure 4.5). The R_Y parameter (similarly for R_X) is estimated differently for events with and without a finite fault model, described below as Method 1 and Method 2.

For events with a finite fault model, the generalized coordinate system "GC2" developed by Spudich and Chiou (personal communication, 2013) uses T and U in a similar fashion to R_X and R_Y. In the GC2 coordinate system, which has been adopted by the NGA-West2 database, the distance parameter T is analogous with R_X and is measured in the strike normal direction. The distance parameter U is measured along strike, but begins at the end of the fault (see Figure 4.5). The first method for the calculation of R_Y may use the following equation:

$$R_Y = U - L/2 \tag{4.1}$$

where U is from GC2 and L is the rupture length. In the NGA-West2 flat file, if a finite rupture model (single and multiple-segment) is available for an event, Method 1 was used to calculate R_Y. If a finite rupture model was not available, R_Y was calculated using Method 2. Method 2 uses the simulated fault geometries described in Section 2.5, most of which are single segment, single rupture models. For Method 2, three possible source-to-site scenarios exist:

1. The source-to site-azimuth is either 90º or -90º.
5. The source-to-site azimuth neither 90º nor -90º, the distance (J, in km) and the bearing from the fault to the site are calculated using the latitude and longitude of the northern edge of the fault and the site.
6. The source-to-site azimuth is neither 90º nor -90º, and the true bearing1 from the northern end of the fault to the site is greater than 90º or less than 270º.

The three scenarios are represented in Figure 4.6. For Scenario #1 the distance J and the bearing from the south end of the fault to the site are calculated using the latitude and longitude of the site and latitude and longitude of the southern end of the fault. Using the distances J and R_X, the distance D can then be calculated. Next compare the strike of the fault to the bearing from the southern end of the fault to the northern end (SNbearing) of the fault. If the strike and the

SNbearing are the same, so for instance if in Scenario #1, the strike and the SNbearing are both 0º, the distance R_Y is then calculated as follows:

$$R_Y = D - L/2 \tag{4.2}$$

If the strike and the SNbearing are not the same, i.e., in Scenario #1, the SNbearing is 0º and the strike is 180º, the distance R_Y is then calculated as follows:

$$R_Y = -1 * (D - L/2) \tag{4.3}$$

For Scenario #2, the distance *J* and the bearing from the fault to the site are calculated using the latitude and longitude of the northern edge of the fault and the site. In this case, *J* and the distance R_X can be used to calculate the distance off the end of the fault, *D*. Similar to Scenario #1, if the strike of the fault and the SNbearing are the same, the distance R_Y is then calculated as follows:

$$R_Y = L/2 + D \tag{4.4}$$

If the strike and the SNbearing are not the same, the distance R_Y is then calculated as follows:

$$R_Y = -1 * (D + L/2) \tag{4.5}$$

For Scenario #3, the distance, *J*, is calculated from the southern end of the fault. Using the distance Rx with J, the distance off the end of the fault, D is calculated. Comparing the strike and the SNbearing, if the strike of the fault and the SNbearing are the same, the distance R_Y is then calculated as follows:

$$R_X = -1 * (D + L/2) \tag{4.6}$$

If the strike and the SNbearing are not the same, the distance R_Y is then calculated as follows:

$$R_Y = L/2 + D \tag{4.7}$$

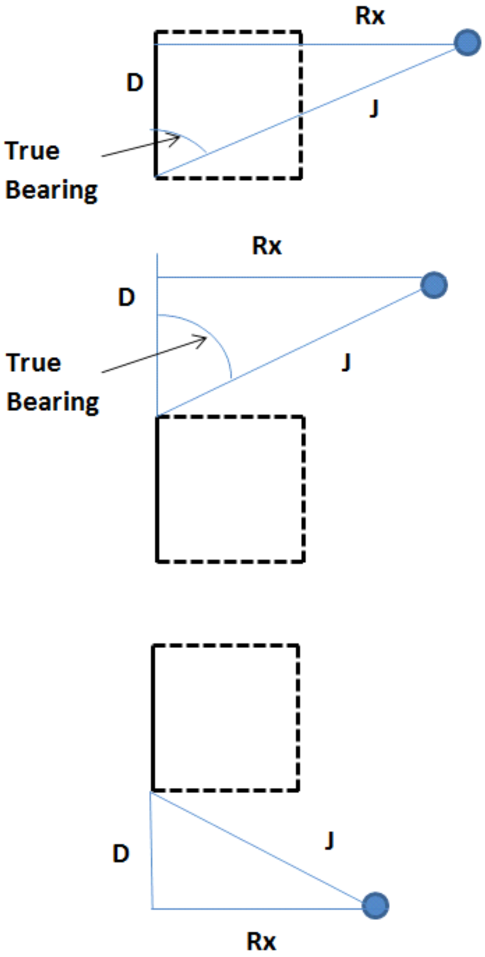

Figure 4.6 Plan view of scenarios #1 (top), #2 (middle) and #3 (bottom) in the Method 2 calculation of R_Y. Example fault plane shown as square with the top of rupture as the solid black line. Example stations for the three scenarios are shown as a filled circle.

5 Record Catalog and Ground Motion Intensity Measures

5.1 ORGANIZATION AND OBJECTIVES OF THE RECORD CATALOG

We began with the record catalog developed in the original NGA-West1 project described by Chiou et al. (2008). The record catalog consists of a summary table containing a list of the records and processing information and the time series, spectra, and duration text files. The summary table is the master file that contains a list of all the selected and processed strong-motion records, and the directory and file names for the times series, spectra, and duration files. When a recording was added to the catalog it was assigned a unique record sequence number (RSN). The acceleration, velocity, and displacement time series are provided for each available component of each recording. Additionally, for each component there are eleven spectra files corresponding to the eleven damping levels and one duration file containing the as-recorded response spectra and durations measured using Arias Intensity. The as-recorded acceleration time series served as input in the calculation of the rotated spectra used in NGA-West1 project and new rotated spectra that is used in the NGA-West2 project.

Major participants in the development of the source tables included Brian Chiou (CDOT), Robert Darragh (PE&A), and Walt Silva (PE&A), Timothy Ancheta (PEER), Albert Kottke (PEER), Tadahiro Kishida (PEER), Rob Graves (USGS), Jack Boatwright (USGS), and David Boore (USGS). Additionally, the information contained in the table and files was improved through numerous discussions with the GMPE developers not mentioned above.

The objectives of this work were to provide the time series, spectra, and duration files for the use of the GMPE developers. Additionally, the record catalog will serve to update the PEER online ground motion database. Section 5.2 details the information contained in the record catalog table. Section 5.3 details the intensity measures calculated for each component and Section 5.4 details the text file generation and formatting.

The key contents of the record table to be fed into the flatfile include the list of records, text file path and filter corners selected/used. Key parameters estimated from the record catalog include peak time series metrics (PGA, PGV, PGD) and RotDnn spectra.

5.2 OVERVIEW OF RECORD TABLE

The record table started from a catalog file developed by PE&A during the NGA-West1 project. The current record table is a list of the available records in the database along with two unique identifiers (RNS and EQID) and a path to provide a link from the record sequence number to the directory and files of the time series, spectra and duration text files. Additionally, the processing flag (e.g., pass-through or processed with PEER methodology) and the high-pass and low-pass filter corners (see Section 6.1) selected for each component of each record is listed. The record table is used as input into the rotated spectra calculation routine, which uses the as-recorded time series as described below. Original record names collected from world-wide strong-motion networks use inconsistent naming conventions. Original names of the record are preserved in the site database. A uniform text file naming convention each component was assigned a unique character string with a maximum of eight characters. The first five−six characters was reserved for either the station ID provided by the network or an abbreviation of the station name. The final two−three characters was reserved for the station azimuth (e.g., up, 090, 180). The extension of the text file describes the information contained within. For example the acceleration, velocity, and displacement text files have the extensions AT2, VT2, and DT2. An electronic version of the record table is not provided herein as the all information contained within can be found in the flatfile.

5.3 OVERVIEW OF INTENSITY MEASURES

The NGA-West1 project used a ground motion intensity measure introduced by Boore et al. (2006) called GMRotI50. The measure is obtained by computing the geometric means of response spectra for all non-redundant rotations of a given pair of orthogonal, horizontal component recorded motions, and then by finding the geometric mean corresponding to the 50th percentile of the resulting set of geometric means. Motivation for its use included a reduction of the aleatory uncertainty in the ground motion prediction equations and the independence of period and senor orientation.

The NGA-West2 project has selected a new rotated measure called RotDnn described by Boore (2010). RotD50, or 50th percentile or median amplitude of response spectra over all non-redundant rotations, will be used in the development of the updated ground motion prediction equations. The minimum and maximum rotated response spectra, RotD00 and RotD100, will be used to relate RotD50 to the maximum rotated component and investigation of directivity in the ground motion recordings. The motivation for its use comes from the simplicity in the definition, calculation, and a move to a maximum rotated component in the building code. A brief definition is provided in Section 5.4 along with a discussion on the effect of different filter corners on the rotated spectra. Also included in Section 5.4 is a summary of the method for translating RotD50 into the maximum component by the NGA-West2 Directionality Working Group.

Other ground motion intensity measures provided include the as-recorded three-component spectra, durations relative to the normalized Arias intensity, and GMRotI50. The period set in the NGA-West2 database is compared to the NGA-West1 database in Figure 5.1. The spectra for 11 different damping ratios are also provided (0.5, 1, 2, 3, 5, 7, 10, 15, 20, 25, 30%).

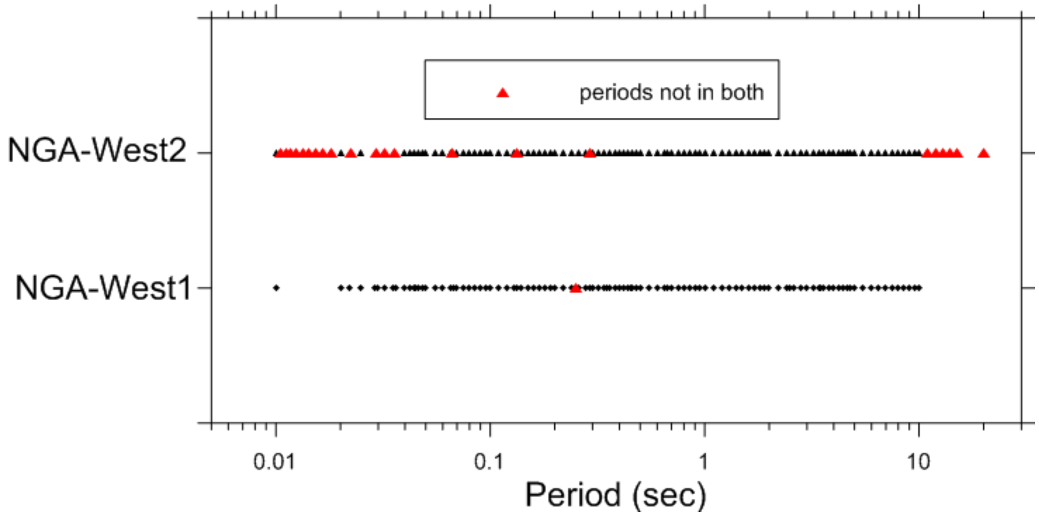

Figure 5.1 **Comparison of the period set used in the NGA-West1project and the NGA-West2 project. Red triangles along the NGA-West2 line represent new periods added. The red triangle along the NGA-West1 line represent a period removed.**

5.4 RotDnn

As described in Boore (2010), the RotDnn spectra are a set of spectra over all non-redundant rotation angles where 'nn' represents the fractile of the spectra sorted by amplitude. The 'D' indicates that rotation angle will be specific to the period of the oscillator. The RotDnn can be computed from the rotation of the two as-recorded orthogonal horizontal ground motions. For any rotation angle, θ, the rotated time series, a_{ROT}, can be computed from the orthogonal horizontal-component time series, $a_1(t)$ and $a_2(t)$, using Equation 5.1:

$$a_{ROT}(t;\theta) = a_1(t)\cos(\theta) + a_2(t)\sin(\theta) \tag{5.1}$$

The response spectra for the rotated time series are calculated for the non-redundant rotation angles 0–180°. Three fractiles, the minimum (nn = 00), mean (nn = 50), and the maximum (nn = 100) spectral amplitude are considered in the NGA-West2 project. Further discussion and examples can be found in Boore (2010).

For the NGA-West 2 database, the computation of the RotDnn spectra was performed by a program written by Dave Boore. The RotDnn spectra may be estimated without the knowledge of the recorded azimuth. However, the corresponding rotation angles will be unknown. A summary of the recordings in the NGA-West2 database that correspond to these cases are listed in Table 5.1. When the starting time between the two horizontal components is not aligned or one of the two horizontal components (H1 and H2) is missing, any rotational spectra cannot be computed. Therefore, Table 5.1 also lists the records that will not have a rotational spectra.

Since the three-component time series were processed independently, the time series used in Equation 5.1 may have different lengths (but same start time) and different selected filter corners. Time series with different lengths had the longer of the two truncated to an equal length by removing time samples at the end. The effect of different selected high pass filter corners is discussed in Section 5.4.1 below.

Table 5.1 Summary of records not used for the calculation of RotDnn spectra.

Reason to not rotate	Record Sequence Number (RSN)
H1,H2 start time not aligned	189, 586, 588, 829, 831, 6880, 6883, 6897, 6918
H1 and or H2 azimuth unknown (i.e., uncertain components are orthogonal)	134,137,144,313,816-820,848,1054,1122-1128,1130,1132,1133,1134,1630,1633,1965,2013,4039,4519,4572,5954,6066-6076,6088-6094,6103-6109, 6121,6122,6127
H1 and or H2 not available	29,168,177,260,267,361,365,378,473,474,475,500,660, 805,1171,1298,1635,1753,2136,3569

5.4.1 Effect of Non-Equal Filter Corners on RotD50

The effect of non-equal filter corners on the RotD50 spectra is important as the PEER processing methodology recommends each component to be processed independently. To investigate the effect on the NGA-West2 database, a subset of records were selected to compare the RotD50 spectra from the as filtered (non-equal) and re-filtered with equal high-pass filter corner. The selection of the subset records was based on two factors: (1) largest percent difference in the high-pass filter corners; and (2) if the components contain a long-period pulse. It was assumed that time series that are polarized (i.e., a large pulse only in one of the horizontal components) might lead to the most difference in RotD50 during this comparison. The subset of records is shown in Table 5.2. Table 5.2 also lists the selected high-pass filter corner and the pulse ID given by Baker and Shahi (2011). Since the newly added records in the NGA-West2 database have not been given a pulse ID, only records originally included in the NGA-West1 database were selected.

Table 5.2 **Set of records from the NGA-West2 database used in the comparison of non-equal/equal filter corner derived RotD50. HP-H1 and HP-H2 are the high-pass filter corners selected for the two horizontal components.**

Record Sequence Number	EQID	Earthquake Name	Station Name	HP-H1 (Hz)	HP-H2 (Hz)	Fault Normal Is Pulse	Fault Parallel Is Pulse
1119	0129	Kobe, Japan	Takarazuka	0.000	0.130	1	0
1045	0127	Northridge-01	Newhall - W Pico Canyon Rd.	0.000	0.100	1	1
171	0050	Imperial Valley-06	El Centro - Meloland Geot. Array	0.000	0.080	1	0
407	0080	Coalinga-05	Oil City	0.130	0.800	1	0
645	0113	Whittier Narrows-01	LB - Orange Ave	0.040	0.130	1	0
183	0050	Imperial Valley-06	El Centro Array #8	0.000	0.030	1	0
1085	0127	Northridge-01	Sylmar - Converter Sta East	0.080	0.230	1	0
182	0050	Imperial Valley-06	El Centro Array #7	0.024	0.060	1	1
1548	0137	Chi-Chi, Taiwan	TCU128	0.020	0.050	1	1
1484	0137	Chi-Chi, Taiwan	TCU042	0.020	0.050	1	0
1519	0137	Chi-Chi, Taiwan	TCU087	0.020	0.050	1	0
1530	0137	Chi-Chi, Taiwan	TCU103	0.020	0.050	1	0
184	0050	Imperial Valley-06	El Centro Differential Array	0.000	0.023	1	1
1481	0137	Chi-Chi, Taiwan	TCU038	0.025	0.050	1	1
170	0050	Imperial Valley-06	EC County Center FF	0.060	0.000	1	0
982	0127	Northridge-01	Jensen Filter Plant	0.050	0.100	1	0
1479	0137	Chi-Chi, Taiwan	TCU034	0.020	0.040	1	0
1485	0137	Chi-Chi, Taiwan	TCU045	0.020	0.040	0	1
1486	0137	Chi-Chi, Taiwan	TCU046	0.030	0.060	1	0

1503	0137	Chi-Chi, Taiwan	TCU065	0.030	0.060	1	0
1515	0137	Chi-Chi, Taiwan	TCU082	0.020	0.040	1	0
1524	0137	Chi-Chi, Taiwan	TCU095	0.020	0.040	0	1
1525	0137	Chi-Chi, Taiwan	TCU096	0.020	0.040	0	1
2495	0172	Chi-Chi, Taiwan-03	CHY080	0.480	0.048	1	0
181	0050	Imperial Valley-06	El Centro Array #6	0.050	0.013	1	1
1402	0137	Chi-Chi, Taiwan	NST	0.030	0.050	0	1
1063	0127	Northridge-01	Rinaldi Receiving Station	0.050	0.080	1	1
174	0050	Imperial Valley-06	El Centro Array #11	0.050	0.080	1	0
418	0082	Coalinga-07	Coalinga-14th & Elm (Old CHP)	0.200	0.080	1	0
529	0101	N. Palm Springs	North Palm Springs Post Office	0.130	0.200	1	0
158	0050	Imperial Valley-06	Aeropuerto Mexicali	0.150	0.230	1	0
316	0073	Westmorland	Parachute Test Site	0.060	0.090	1	1
1483	0137	Chi-Chi, Taiwan	TCU040	0.020	0.030	1	1
1526	0137	Chi-Chi, Taiwan	TCU098	0.020	0.030	1	1
180	0050	Imperial Valley-06	El Centro Array #5	0.040	0.020	1	0
723	0116	Superstition Hills-02	Parachute Test Site	0.080	0.120	1	0
802	0118	Loma Prieta	Saratoga - Aloha Ave	0.100	0.050	1	0
803	0118	Loma Prieta	Saratoga - W Valley College	0.100	0.050	0	1
1471	0137	Chi-Chi, Taiwan	TCU015	0.020	0.030	0	1
1487	0137	Chi-Chi, Taiwan	TCU047	0.020	0.030	0	1
1493	0137	Chi-Chi, Taiwan	TCU053	0.020	0.030	1	0

1502	0137	Chi-Chi, Taiwan	TCU064	0.020	0.030	0	1
1511	0137	Chi-Chi, Taiwan	TCU076	0.100	0.050	1	0
2457	0172	Chi-Chi, Taiwan-03	CHY024	0.024	0.012	1	0
173	0050	Imperial Valley-06	El Centro Array #10	0.060	0.033	1	1
764	0118	Loma Prieta	Gilroy - Historic Bldg.	0.180	0.100	0	1
150	0048	Coyote Lake	Gilroy Array #6	0.070	0.100	1	0
319	0073	Westmorland	Westmorland Fire Station	0.070	0.100	0	1
722	0116	Superstition Hills-02	Kornbloom Road (temp)	0.140	0.200	0	1
1148	0136	Kocaeli, Turkey	Arcelik	0.070	0.040	0	1
2627	0172	Chi-Chi, Taiwan-03	TCU076	0.040	0.056	1	0
161	0050	Imperial Valley-06	Brawley Airport	0.032	0.043	1	0
1505	0137	Chi-Chi, Taiwan	TCU068	0.030	0.020	1	1
1161	0136	Kocaeli, Turkey	Gebze	0.060	0.080	1	0
1244	0137	Chi-Chi, Taiwan	CHY101	0.030	0.040	1	0
1463	0137	Chi-Chi, Taiwan	TCU003	0.030	0.020	0	1
1468	0137	Chi-Chi, Taiwan	TCU010	0.030	0.020	0	1
1476	0137	Chi-Chi, Taiwan	TCU029	0.030	0.040	1	0
1510	0137	Chi-Chi, Taiwan	TCU075	0.030	0.040	1	0
1605	0138	Duzce, Turkey	Duzce	0.060	0.080	0	1
415	0080	Coalinga-05	Transmitter Hill	0.100	0.070	1	0
767	0118	Loma Prieta	Gilroy Array #3	0.100	0.070	0	1
1529	0137	Chi-Chi, Taiwan	TCU102	0.040	0.050	1	1

983	0127	Northridge-01	Jensen Filter Plant Generator	0.080	0.100	1	0
1410	0137	Chi-Chi, Taiwan	TAP003	0.040	0.030	1	0
1411	0137	Chi-Chi, Taiwan	TAP005	0.040	0.030	0	1
250	0061	Mammoth Lakes-06	Long Valley Dam (Upper Left Abut.)	0.300	0.230	1	0
178	0050	Imperial Valley-06	El Centro Array #3	0.050	0.040	1	1
185	0050	Imperial Valley-06	Holtville Post Office	0.050	0.060	1	1
1013	0127	Northridge-01	LA Dam	0.100	0.120	1	1
179	0050	Imperial Valley-06	El Centro Array #4	0.050	0.040	1	0
496	0097	Nahanni, Canada	Site 2	0.100	0.080	0	1
1496	0137	Chi-Chi, Taiwan	TCU056	0.040	0.033	1	0
1084	0127	Northridge-01	Sylmar - Converter Station	0.200	0.230	1	0
1595	0137	Chi-Chi, Taiwan	WGK	0.070	0.060	0	1
3317	0175	Chi-Chi, Taiwan-06	CHY101	0.032	0.028	1	0
821	0121	Erzican, Turkey	Erzincan	0.090	0.100	1	1
292	0068	Irpinia, Italy-01	Sturno (STN)	0.100	0.090	1	1
159	0050	Imperial Valley-06	Agrarias	0.120	0.130	1	0
3475	0175	Chi-Chi, Taiwan-06	TCU080	0.072	0.068	0	1

The effect of the non-equal filter corners is represented in the ratio between RotD50 computed from time series using non-equal and equal high-pass filter corners. In order to calculate the ratio, the subset of time series in Table 5.2 were re-filtered to the case of equal high-pass filter corners. The re-filtering was performed only for the horizontal component with the lowest high-pass filter corner. For example, the first record listed (RSN 1119) had the H1 component re-filtered using a high pass filter corner of 0.13 Hz. A summary of the ratio between RotD50 using non-equal and equal filter corners for the subset records is shown in Figure 5.2. In Figure 5.2 the period is normalized by the lowest useable period and therefore, unity corresponds to the lowest useable period. The ratio at frequencies less than the lowest usable frequency appears unbiased (close to unity) while become biased at frequencies greater. Based on Figure 5.2, the effect of non-equal filter corners is insignificant within the recommended usable bandwidth. A discussion on the recommend usable bandwidth is found in Section 6.2.

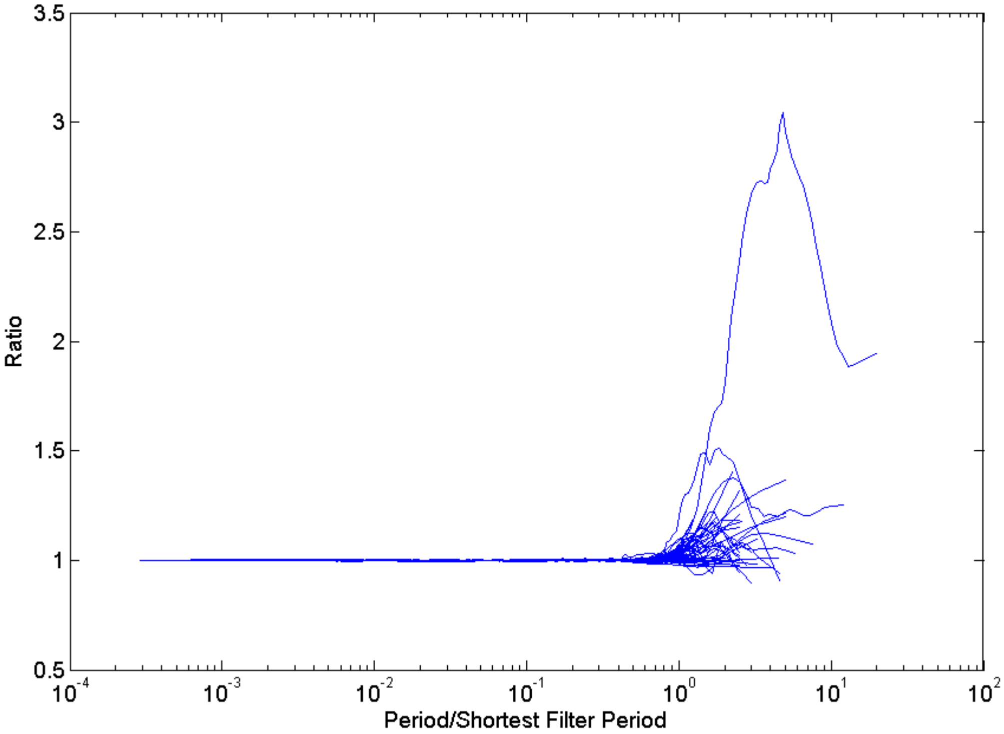

Figure 5.2 **A summary of the ratio between RotD50 using non-equal and equal filter corners for the subset records.**

5.4.2 Converting RotD50 to RotD100

Shahi and Baker (2012) as part of PEER NGA-West2 examined different methods of representing the intensity of ground motion in the horizontal plane using a response spectrum which is a one-dimensional representation of ground-motion intensity. The study focused on two orientation-independent representations of the response spectrum: RotD50 and RotD100. The new ground-motion models will predict the RotD50 spectrum at a site due to a future earthquake, while the NEHRP (2009) provisions recommend using RotD100 for seismic design.

Shahi and Baker (2012) proposed a model to predict the ratio of RotD100 to RotD50, which can be used as a multiplicative factor with the RotD50 predictions from the new NGA-West2 ground-motion models to predict the RotD100 ground-motion intensity. The proposed model was compared and found to be consistent with similar models built in the past [e.g., Watson-Lamprey and Boore (2007)]. The proposed model advances that earlier work by using a larger data set, utilizing the recently adopted RotD50 definition instead of GMRotI50 and using mixed effects regression to account for inter-event terms. The differences between the proposed model and corresponding NEHRP (2009) ratios were also explained.

Along with modeling the ratio of RotD100 to RotD50, they also modeled the probability distribution of orientations in which the RotD100 intensity is observed relative to the strike of the fault. The orientations of RotD100 were observed to be uniformly distributed when the closest distance between the fault and the site was greater than 5 km or if the period under consideration was less than 1 sec. Only for the cases when the site was within 5 km of the fault and at periods greater than 1 sec, the orientation of RotD100 was more likely to be closer to the strike-normal than strike-parallel direction. Relationship between the orientations of RotD100 at different periods was also studied, and the difference between the orientations was modeled using truncated exponential distribution. Together these models can help solve a practical problem of converting between two important intensity measures while helping deepen the understanding of the directionality of ground-motion by studying the distribution of orientations in which RotD100 occurs and dependence of RotD100 to RotD50 ratio on different seismological parameters. Conditional mean spectra conditioned on an orientation and on RotD100 observation at a particular period were also discussed [see Shahi and Baker (2012)].

It is anticipated that these results will help bridge the gap between the work of seismic hazard analysts, who typically use a geometric mean or RotD50 values, and some engineers, who prefer to work with RotD100 response spectra.

5.5 ALTERNATE GROUND MOTION MEASURES

Other measures included in the NGA-West2 database are various durations estimated from Arias intensity, the three-component as-recorded spectra, and GMRotI50 for all records included in the database. The spectra used the same period and damping ratio set as the RotDnn spectra. As mentioned before, RotD50 is used as the intensity measure that is used to develop the new NGA-West2 GMPEs.

5.5.1 Duration

Duration of ground shaking can be defined as the time difference between two levels of a normalized plot of cumulative squared acceleration. For the NGW-West2 project, nineteen durations were selected based on the difference in time between a lower bound (always 5%) and upper bound normalized Arias intensity. The nineteen different upper bound values ranged from 10 to 100% stepping by 5% increments. A text file reporting the nineteen selected durations and their corresponding normalized Arias intensity was created for all available components for the records included in the database.

5.5.2 As Recorded and GMRotI50 Spectra

The as-recorded spectra and GMRotI50 were computed even though RotDnn is the new primary ground motion measure in the NGA-West2 project. The as-recorded spectra were computed using a FORTRAN code called SPCTLR.FOR created by PE&A. The GMRotI50 spectra were computed using a FORTRAN code developed by Dave Boore. The methods for calculating the as-recorded and GMRotI50 remained unchanged from the NGA-West1 program and is detailed in Section 6.1 and Boore et al. (2006).

6 Strong-Motion Record Processing

In coordination with PEER, PE&A in general, collected digitized but otherwise unprocessed accelerograms from various agencies around the world and uniformly processed the raw accelerograms. The processing methodology remains generally unchanged except in the filter type preferred. The processing in the NGA-West2 project used an acausal Butterworth filter, whereas for the NGA-West1 project a causal Butterworth filtered records were preferred, when available. The change from causal to acausal filters was to reduce phase distortions as discussed in Boore and Akkar (2003), Boore and Bommer (2005), and Boore (2005). Strong-motion record processing has two major objectives to make the data useful for engineering analysis: (1) correction for the response of the strong-motion instrument itself; and (2) reduction of random noise in the recorded time series. A large portion of the NGA recordings were processed using the PEER processing procedure discussed in Section 6.1 (Figure 6.1); the remaining recordings were entered into the database without additional processing (pass-through records). Considerations in adding pass-through records are discussed in Section 6.3. The PEER processing methodology was applied to most raw accelerograms. One exception was for records from stations that experienced permanent displacement where the methodology described in Section 6.6 was also used.

Time series were also carefully re-evaluated to extend their usable frequency, late P- and S-wave triggers were identified and flagged, checked for alignment in absolute time between components, and remove duplicate recordings from co-located instruments.

6.1 PEER RECORD PROCESSING METHODOLOGY

The PEER processing concentrated on extending both the high- and low-frequency ranges of the useable signal in the recordings (spectral accelerations) on an individual component basis. This processing scheme (Figure 6.1) consists generally of low- and high-pass acausal Butterworth filters applied in the frequency domain. Corner frequencies were selected by visual examination of the Fourier amplitude spectra and integrated displacements. If necessary, a simple baseline correction was applied for cases where filtering did not remove non-physical trends in the displacement time series. The baseline correction consisted of fitting a polynomial to the displacement time series and subtraction of the corresponding acceleration from the filtered acceleration time series. This step also ensures compatibility between the processed acceleration and the velocity/displacement time series as discussed in Boore et al. (2012). PEER and other organizations (e.g., ITACA, ITalian ACcelerometric Archive) post-process the pad-striped accelerations; PEER uses a baseline correction procedure (Figure 6.1). An alternate solution would be to provide the velocity and displacement values at the first time point of the pad-stripped data for both the ground motions and the oscillator responses at all periods and dampings [e.g., Boore (2010b)].

Examples of PEER processing results at both high- and low-frequencies can be found in Silva and Darragh (1985) and Darragh et al. (2004) and is discussed in Abrahamson and Silva (1997) and Chiou et al. (2008). PEER and other processing methodologies are compared in Douglas and Boore (2011) and Boore et al. (2012).

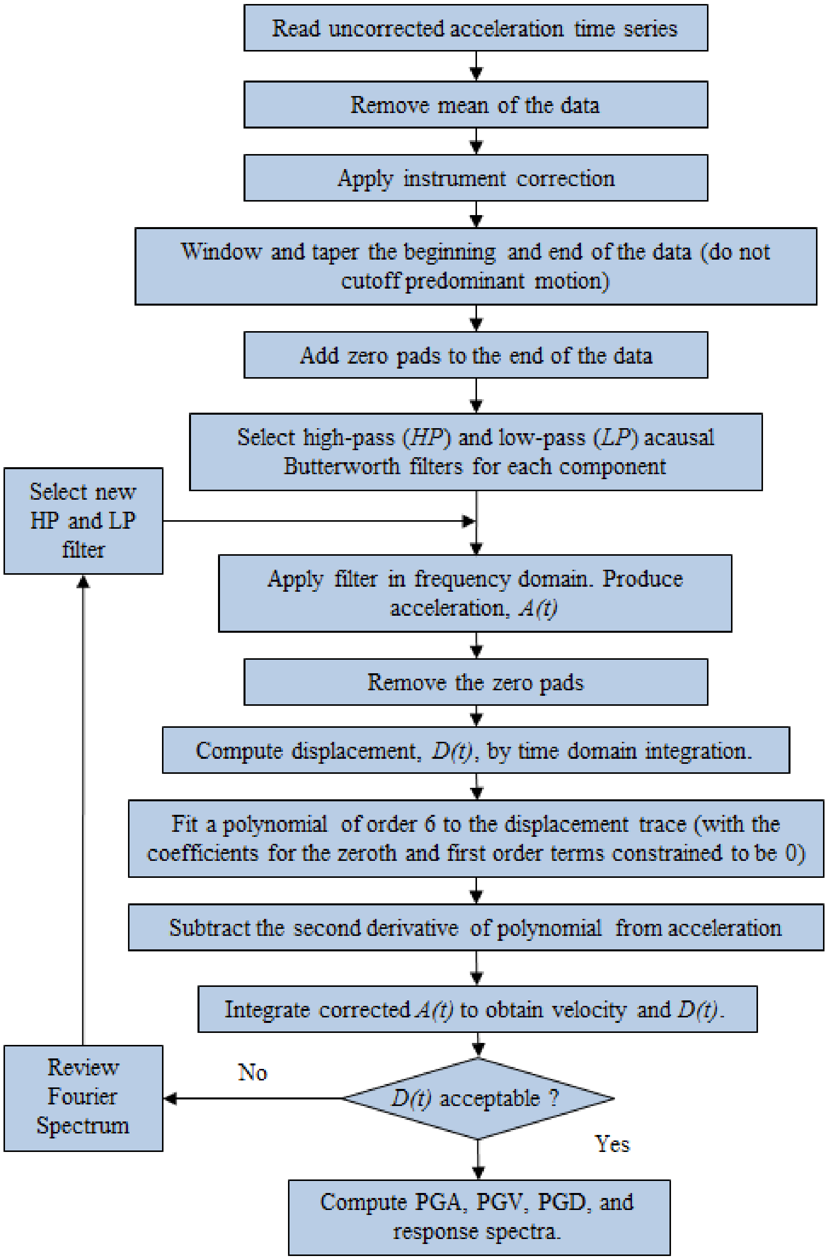

Figure 6.1 PEER record processing procedure [from Boore et al. (2012)].

6.2 ASSESSMENT OF USABLE FREQUENCY RANGE

Response spectral values were provided to a highest frequency of 100 Hz in the NGA database even if the low-pass filter applied had a much lower corner frequency. As noted by Douglas and Boore (2011): "There is no inconsistency here, for the PSAs (response spectral values) at oscillator frequencies near 100 Hz are being determined by lower frequencies in the input record…" For NGA-West2, PGA is taken equivalent to the 100 Hz spectral value (5% damped PSA) even at hard rock locations.

In contrast, at low frequencies, the minimum useable frequency is a critical issue. For example, the causal 5-pole Butterworth filters commonly used in PEER processing in NGA-West1 has a significant reduction (0.707, or -3 db) in response at the filter corner frequency. Hence it was recommended that the usable bandwidth of these records for the purpose of engineering analysis extend from 100 Hz to the high-pass corner frequency multiplied by a factor of 1.25 (Abrahamson and Silva 1997). With the 1.25 factor, the lowest usable spectral frequency is the Fourier frequency at which the filter response is about -1/2 db down from the maximum response. Using the same -1/2 db criterion, the recommended low-frequency limit for each pass-through record was selected according to the Butterworth filter order and the number of filter passes (e.g., 1.5 for time domain filtering with two passes) used in the record processing, as recommended by Boore (2004, written communication). For pass-through records filtered with an Ormbsy filter, the useable bandwidth extends from 100 Hz to the filter corner (e.g., 0.20 Hz, for a record filtered with an Ormsby between 0.20 and 0.10 Hz).

Uniformity in the processing of the record catalog has been significantly improved over the NGA-West1 database. Although it was concluded in various studies discussed in Section 6.5 that the causality had an insignificant effect on the statistics of the record parameters (e.g., PGA and Sa) an acausal filter was preferred in the NGA-West2 record processing. Since a filter type was now preferred, all previously included records in the NGA-West1 database were reviewed to expand their useable bandwidth and re-processed with the preferred filter type. The result of the re-processing has more than doubled the records with a useable bandwidth up to a period of 10 second (maximum period provided in the NGA-West1 project) as shown in Figure 6.2.

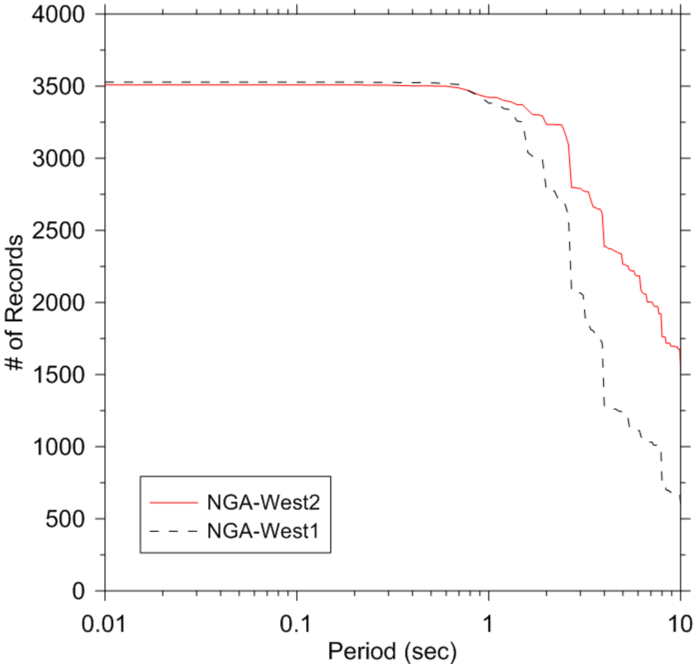

Figure 6.2 **Comparison of number of records with a highest useable period versus period using records included in both NGA-West1 (dashed black) and West-2 (solid red). The small offset at low periods is due to the removal of stations detailed in Section 7.**

6.3 PASS-THROUGH RECORDS

There are two main reasons why many records were entered into the NGA-West1 database without additional processing (Darragh et al. 2004). First, more recent digitally–recorded data generally do not benefit from additional processing and were entered into the database after review of the Fourier amplitude spectra and time series (for example, for glitches). Second, some acceleration data (for example, CSMIP data starting with the 1992 Cape Mendocino earthquake) were available only in Volume II format (filtered and base-line corrected). These data were simply entered into the database in standard format after a similar review. A pass-through record was identified as '#' in the column 'PE&A Processing Flag' of NGA-West2 flatfile. Filter type and filter corner frequency used in the processing of a pass-through record were also entered into the database, if they were available. During the NGA-West2 project, more than 1600 recordings that were originally passed-through in NGA-West1 had their raw (e.g., Volume 1) accelerograms collected and were processed using the standard PEER record processing methodology.

6.4 LATE P-WAVE AND S-WAVE TRIGGERS

The unprocessed three-component acceleration histories were evaluated for late triggers either on the vertical or horizontal components. The evaluation concentrated on time series made on triggered analog recorders (e.g., SMA) since these time series do not, in general, record the first onset of motion. In addition, time series from early digital recorders with limited pre-event memory (e.g., 5 sec or less) were evaluated. Recordings that potentially did not record the large\peak amplitude portion of the P-wave (vertical components) or S-wave (horizontal components) due to a late trigger (or insufficient pre-event memory) were flagged in the NGA flatfile. Explanations of the flags are included in Table 6.1.

Table 6.1 Summary of late P-wave and S-wave trigger flags.

Flag	Description
d	Digital with pre-event memory, did not record the first P-wave onset. In the digital case we are confident that we recorded the largest amplitude (provided, later peaks are > the nominal trigger level of 0.005 g, which depends on instrument, array, etc.)
?	Analog recording that probably recorded largest amplitudes on the vertical component but the P-wave onset not recorded, OR probably recorded largest amplitudes on the horizontal component(s) for the S-wave.
Y	Late trigger, probably did not record the largest vertical amplitude, The characteristic diagnostic is that the largest amplitude is at start of recording on the vertical component.
DNP	Did not process the vertical component (e.g., late trigger)
DNR	Did not record the vertical component.

6.5 REVIEWS OF TIME SERIES AND RESPONSE SPECTRA

The processing was in general different than the processing done by the agency that collected the data. This was necessarily the case as record processing largely relies on judgment as to where (in frequency) noise has significantly contaminated a recording at both high- and low-frequency ranges. More importantly, record processing (filtering) must, by definition, distort a record (side effects) and different processing procedures result in different side effects or distortions. Record processors are faced with the dilemma as to which set of side effects are the most or least desirable. The use of causal versus acausal filters discussed later is an example of such a dilemma.

During the NGA-West1 program, strong-motion time series and (5%-damped) pseudo spectral accelerations were extensively reviewed at the NGA-COSMOS Joint Working Group Meeting on Data Processing on March 17th, 2004, and several summaries were presented at the International Workshop on Strong-Motion Record Processing sponsored by Consortium of Organizations for Strong-Motion Observation Systems (COSMOS; www.COSMOS-eq.org/events/wkshop_records_processing/index.html). At the NGA-COSMOS joint meeting the results of a large number of time domain and spectral domain (5%-damped pseudo spectral acceleration) comparisons were presented and discussed. Two hundred and seventy-one time domain and spectral domain comparisons were made between the NGA and the California Geological Survey (CGS) Strong Motion Instrumentation Program (CSMIP) Volume II and III data sets. The comparison included all records common to both data sets. The processed records are from thirty-four California earthquakes ranging from the 1979 Imperial Valley earthquake to the 1989 Loma Prieta earthquake. Similar comparisons were made on strong-motion data from a smaller set of sixteen earthquakes processed by the USGS. These data started with the 1974 Hollister earthquake and ended with the 1989 Loma Prieta earthquake. Forty-eight time domain and 108 spectral domain comparisons were presented.

The differences in response spectra between NGA-West1 records and those processed by either CGS or USGS were mainly associated with: (1) selection of the high-pass and low-pass filter corner frequencies that define the effective passband; and (2) the type of filter used (causal or acausal). The presented comparisons showed that the different processing procedures produced zero difference, on average, in elastic response spectra across the useable (common) frequency band. Outside of the common useable bandwidth, large spectra differences may be observed due to differences in the filter corner frequencies. Incidentally, on a number of records the PEER processing resulted in an expanded bandwidth due to the selection of filters independently on each component rather than an entire record (three components) or on a policy basis [see Douglas and Boore (2011), page 399 for more discussion].

Acausal filtering results in fewer phase distortions as discussed in Boore and Akkar (2003), Boore and Bommer (2005), and Boore (2005). The greater distortion present with causal filtering may affect spectral values, especially inelastic spectra, at frequencies much higher than the high-pass filter corner frequency. This occurs because the response spectrum measures a peak value in the time domain, and this measurement is affected by the phasing of the ground motion over a wide frequency range. The Boore and Akkar (2003) work presented the analysis from two recordings from the Hector Mine earthquake and a limited number of other recordings. They state "the question on whether to use causal or acausal filters depends on the intended use of the data, desirability for compatible processed acceleration, velocity and displacement time series and considerations of computer storage space." An advantage of causally filtered time series is compatibility; that is, velocity, displacement and acceleration response spectra computed from the acceleration time series will match the data provided. In contrast, acausal filters require that the padded portions of the processed time series also be distributed to maintain compatibility between time series and spectra [see Boore and Bommer (2005) for more discussion] or provide the velocity and displacement values at the first point of the pad-stripped data, for both the time histories and the oscillator response at all periods and dampings (Boore et al. 2012). The phase distortion, however, can distort the displacement time series, particularly at periods near the filter corner period. On the other hand, acausal filters generally result in an artificial and significant ramp in displacement, preceding the arrival of long period energy from the source. For analyses of spatial arrays, where relative timing is important, causal filtering is preferred, as is done in seismological observatories for earthquake locations.

The sensitivity to filtering method presented by PE&A at the NGA-COSMOS joint working group meeting showed that for most of the nearly 1000 components studied, the elastic response spectra differences associated with the different filtering methods are small, and they do not appear to result in systematic high or low bias of spectra within the common pass band. Bazzurro et al. (2004), in another large spectral domain study, support the above observation. They found that elastic and inelastic spectra from causal and acausal filtered records are statistically indistinguishable from each other provided the same filter order and corner frequencies have been used. The causally filtered records, however, result in a slightly larger variability in both elastic and inelastic response. It was concluded that the effects of filter causality on NGA regression results are considered to be insignificant. Boore et al. (2012) came to a similar conclusion that data from "PEER NGA can be used with confidence that the post processing has not affected the bulk of the results."

6.6 PROCESSING METHODOLOGY FOR STATIC DISPLACEMENTS

An exception to the above conclusion is for a small group of near-source records having large static displacements (i.e., tectonic displacements or "fling step"). Standard PEER processing of the time series does not allow for the displacements to have a static offset or residual displacement (i.e., frequency = 0 Hz). To preserve the static displacement, a static baseline correction method such as those described in Iwan et al. (1985), Graizer (1979), and Darragh et al. (2004) could be used in lieu of a high-pass filtering. The peak ground displacement and, to a lesser extent, peak ground velocity values for PEER processed records are typically lower than for static baseline corrected cases. Interestingly, a comparison of the peak-to-peak displacement shows that the value from the standard PEER processed time history is approximately the same as the value from the static baseline corrected time history (Darragh et al 2004). This suggests that the standard processing, which does not preserve static fields, may result in similar dynamic loads to structures. As noted by Boore (2001), the difference in the acceleration response spectra between time series which have been processed using a standard approach and those using a static baseline correction approach are relatively small for periods less than about 20 sec, which is greater than the maximum 10-sec period used in the PEER-NGA data set.

6.7 CALIFORNIA SMALL-TO-MODERATE MAGNITUDE DATA SELECTION

The main data selection goal was to expand the Chiou et al. (2010) data set to include uniformly processed waveforms and spectra at the standard PEER spectral periods and damping ratios. Also, aftershock sequence data were included, as well as data from earthquakes that occurred after September 2008, the date of the most recent event in Chiou et al. (2010) data set. Following Chiou et al. (2010), we retain only data obtained from the high-sampling-rate (80 to 100 points per sec) broadband instruments and strong-motion accelerographs. Broadband instruments with lower sampling rate (20 points per sec) are deemed less reliable for high-frequency ground motion parameters and are therefore not included in the database. We prefer data from the accelerograph (the HL_ or HN_ channels), when available, to data from the broadband instrument. Also, the selected stations were carefully reviewed for Geomatrix 1st letter, several of the BDSN stations are in deeply embedded adits and are not considered free-field for GMPE development.

6.8 VETTING OF THE CALIFORNIA SMALL-TO-MODERATE MAGNITUDE EARTHQUAKE DATA

During the development of the California small-to-moderate magnitude database a vetting process was performed on the recording, event, and site information. As mentioned in Section 1.3, time series were delivered by request from the various data providers on an event basis (usually requested by event start time). An effort was made to check the following:

- Association of the data to the event requested.
- Station gain, instrument natural frequency, and instrument damping.
- Site information as discussed in Section 3.2
- Review of selected record processing filter corners

A check on the event and station information (especially gain) used a comparison of the distance attenuation predicted from the GMPE in Chiou et al. (2010). The selected event information included in the flatfile and an average V_{s30} based on the event set of stations was used. As shown in Figure 7.1, plots of the prediction are compared to the individual station as-recorded three-component PGA, PGV, and pseudo spectra acceleration at periods 0.3 and 1 sec. Due to slight mismatch in the prediction and the event mean, a station component was flagged if it occurred outside the +/-4 σ limit. In Figure 6.3, a single station at a distance of 200 km would be flagged for review.

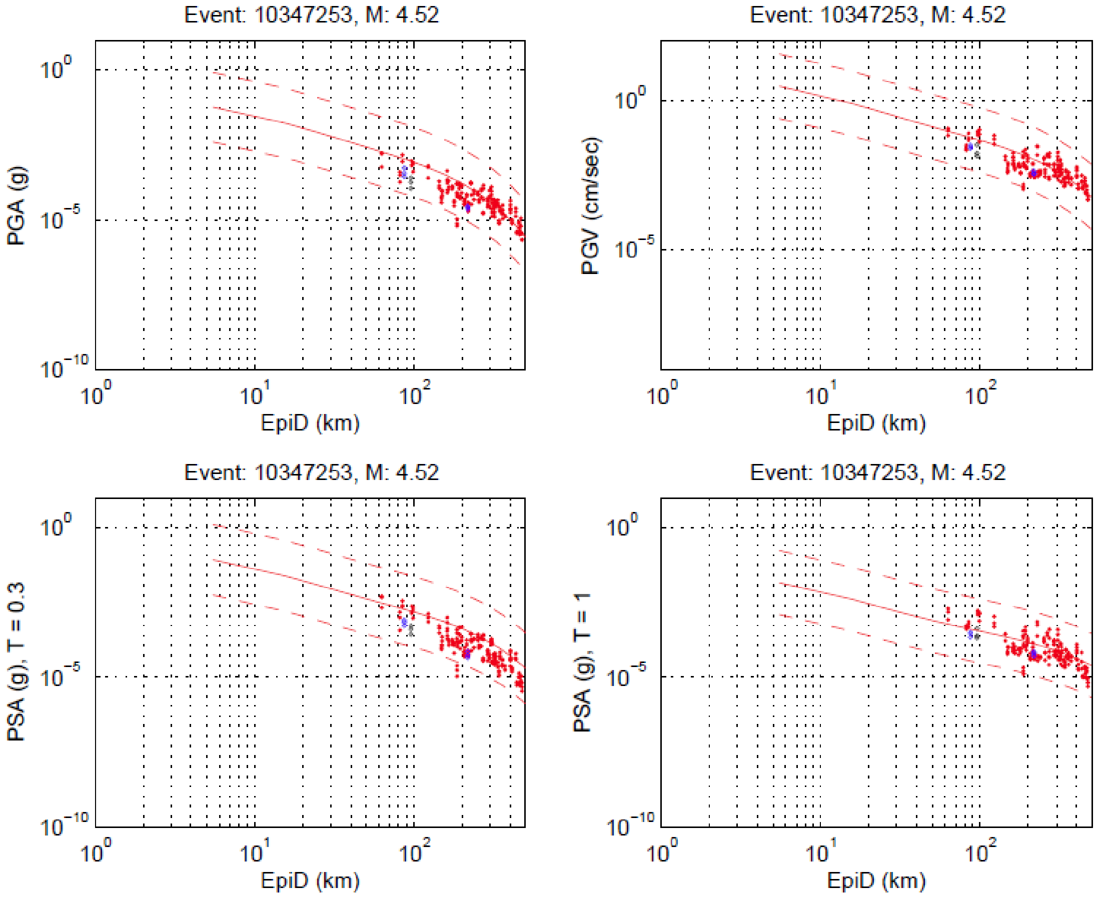

Figure 6.3 Plot of event 10347254 median (solid line) and +/- 4s (dashed lines) based on the Chiou et al. (2010) CA specific model and the as-recorded three-component (data points) PGA, PGV, and Psa$_{T=0.3s}$ and Psa$_{T=1s}$. The red data points are stations provided by Caltech (CIT), blue are provided by BDSN, black are provided by CGS, and blue open circles are provided by USGS.

Initially, these comparisons led to an update of the station gain, natural frequency and damping for selected sites. In a second phase, the comparisons were used to correct event IDs assigned to the data (e.g., event ID was incorrectly associated to a set of records or a record was incorrectly associated with an event). When the initial vetting process was complete the comparison was used to flag individual stations that may have incorrect gains or poorly selected filter corners. For example, recordings with spectral values a factor of 9.8 (10), or a power of 10 were flagged to check unit conversion to *g* or gain.

An additional check on the computed response spectral shape was used to flag individual components that may have poorly selected filter corners or incorrect time steps (*dt*). An example, of spectral shape checking is given in the Figure 6.4. Records were flagged by comparing the spectral shape of an individual record to the Chiou and Youngs (2008) prediction. If the spectra fell outside a +/-2σ band, the record was flagged for review. Additionally, it was noted if the flag was based on a short or long period as records from flagged at short periods may be located on rock sites (i.e., low kappa sites). An effort was made to delineate such sites during the review. For example in Figure 6.4, the record RSN 105982 may be flagged based on the short-period deviation, while record RSN 106005 may be flagged based on the long-period deviation.

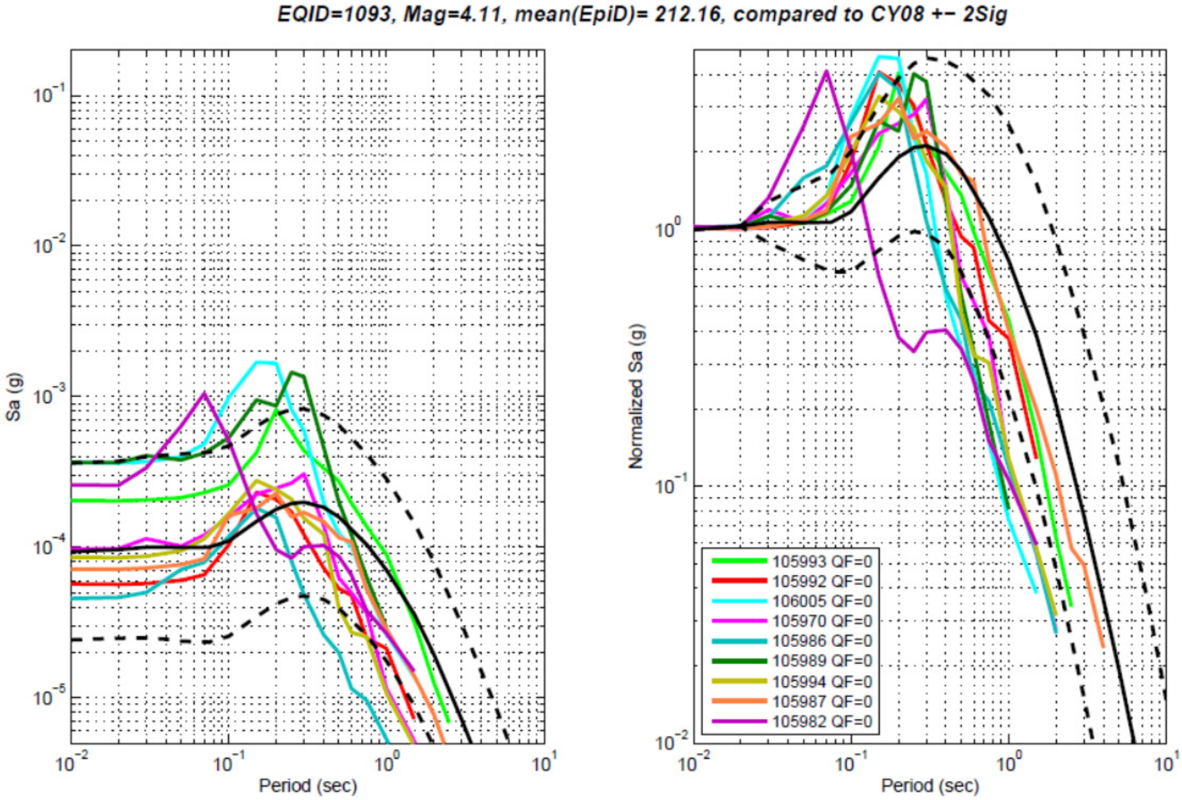

Figure 6.4 Plot of the spectral shapes for EQID 1093. These plots were used for additional checking of the processed data (figure from R. Kamai). Solid black line is Chiou and Youngs (2008) prediction with +/-2σ in dashed black lines.

7 Flatfile Documentation

7.1 OVERVIEW OF THE NGA-WEST2 FLATFILE

Eleven flatfiles were created by merging ground-motion parameters and key metadata on the four tables: record catalog, earthquake source, site database, and path table. The flatfiles were used as input data in the NGA-West2 GMPE regression analyses and to disseminate the core NGA-West2 data to the research and engineering communities. The NGA-West2 flatfiles include PGA, PGV, PGD and 11 dampings (0.5, 1, 2, 3, 5, 7, 10, 15, 20, 25, 30%) pseudo spectral acceleration at 111 periods, for the RotD50 fractile. The flatfile also includes 270 columns of metadata. The flatfiles used to develop NGA-West2 GMPEs will be available at:

http://peer.berkeley.edu/ngawest2/databases/

once the project is finalized. The flatfile has been and will continue to be the basic documentation of the PEER-NGA data sets. A discussion on metadata documentation, updates, and quality are included below in Section 7.2.

Participants included in the creation of the NGA-West2 flatfiles were Timothy Ancheta (PEER), Sanaz Rezaeian (PEER), Tadahiro Kishida (PEER), Brian Chiou (CDOT), and Robert Darragh (PE&A). Additionally, the information contained in the flatfiles was improved through numerous discussions with the GMPE developers not mentioned above.

7.2 METADATA DOCUMENTATION

Documentation of the NGA-West1 flatfile metadata was initially prepared in April of 2005 by Brian Chiou to provide basic definitions and some explanations of each column in the flatfile. The explanations were given in the form of an excel spreadsheet for the NGA-West1 project (http://peer.berkeley.edu/assets/NGA_Documentation.xls) was also included as Appendix A of Chiou et al. (2008). Appendix D included herein is an updated table to reflect extensive additions to the flatfile metadata and any changes made to the previously included information. A summary of the updated, added, and removed metadata is included in Section 7.2.1. A significant effort was made toward uniformity in the metadata reported and metadata quality. The numerous metadata quality flags are briefly reviewed in Section 7.2.2. Appendix E provides definitions for several of the site classifications collected during the project. These are the Geomatrix 3-letter site classification (D. Wells, personal communication, 2005,), NEHRP site classification (BSSC, 1994), Spudich et al. (1999) site classification for extensional regimes, extended NEHRP (Wills et al. 2000), and Campbell and Bozorgnia GEOCODE (2003).

7.2.1 Metadata Changes

As discussed in the above section, additional metadata has been added and existing metadata updated during the course of the project (e.g., additional stations and earthquakes). Significant changes were made to metadata that served as input parameters to the NGA-West 2 GMPEs. All event parameters (e.g., $\mathbf{M}$, Z_{TOR}), station information (e.g., location, and V_{s30}), and path metrics (e.g., site-source distances) were systematically reviewed and updated if necessary. When updated, quality was improved. Updates included, additional V_{s30} measurements, updated station coordinates, new filter corners selected. The reported response spectra has now been updated from GMRotI50 to RotDnn and reported for ten damping levels other than 5%. Added metadata include new directivity parameters, earthquake classification, additional distance metrics (U, R_X, R_Y), and time series and spectra quality flags (e.g., late S- and P-wave trigger flags), among others. A complete list and description of the metadata is included in Appendix D.

Due to limited resources and time constraints a subset of metadata included in the NGA-West1 project was updated. Additionally, metadata that was collected in the NGA-West1 project was not further populated/updated in the NGA-West2 flatfile and some cases removed. Metadata columns remove however were outdated or redundant metrics. When a column is removed it is noted with a header as not used. A complete list of removed columns is included in Appendix D. Records that were initially included but during the metadata review have been removed are shown Table 7.1.

Table 7.1 Summary of the set of records removed from the NGA-West2 database.

Reason to remove stations	Record Sequence Number (RSN)
dt warning	994, 1009, 1010, 1068, 3549, 3550, 3551
late S-wave trigger	1625, 1778, 1796, 1798, 1815, 1839, 2010
co-located stations	1081, 1178, 1179, 1251, 1252, 1253, 1254, 1255, 1306, 1400, 1401, 1403, 1405, 1407, 1408, 1461, 1462, 1556, 1595, 1596, 2262, 2556, 2802, 3041, 3364
gain	4405,9471, 11293, 11322, 11711, 11743,12025, 12029, 12823, 13058, 13087, 13097, 14007, 14164, 1558, 14748, 15005, 15513, 15972, 16684,17008, 17036, 17469, 17605, 17628, 17790

7.2.2 Metadata Quality

Although the NGA-West2 flatfile working group aimed at uniformity in the metadata, incomplete information was common for the entire set of recordings. To aid the user in understanding the varying quality of metadata a summary of the available metadata quality flags is provided. The metadata described in this section include, the basin depths ($Z1.0$, $Z1.5$, and $Z2.5$), station locations, rupture geometry, distance metrics, and time series and spectra flags. A discussion on the V_{s30} uncertainty in included in Section 3.5.2.

Basin depths as described in Section 3.6 consist of a depth to a shear-wave velocity horizon. Columns CU though CZ contains a summary of basin depths compiled from multiple sources also described in Section 3.6. The value reported is based on a similar hierarchy to the V_{s30} column where depths from measured velocity profiles are preferred over depths extracted from 3-D basin models. However, unlike V_{s30}, we have not provided a basin depth code to indicate the preferred source on the flatfile. The basin code is however provided in the site database.

Station locations were extracted from local network station lists and reported as latitude and longitude. The accuracy and geographic reference system used by the network providers is not uniform. Due to time constrains the geographic reference system used by each network was not collected nor have all the station locations been visited. However, effort was made to use NAD83 for station in the United States and WGS84 where possible.

Event rupture geometry (strike, dip, length, width, and Z_{TOR}) was either based on a finite fault inversion or simulated rupture geometry as detailed in Section 2.5. To indicate the source of the rupture geometry the 'Finite Rupture Model' flag in column AE may be used. If the flag is '1,' the event information was extracted from the published finite fault model. If the flag is '0,' some or all of the rupture geometry was based on the simulated fault plane. The accuracy of the distance metrics will vary predominantly based on the accuracy of the rupture geometry.

The time series included in the flatfile may also have varying quality according to recording date. Due to the evolution in instrumentation and triggering procedures, records may be an analog/digital recording or may have little to no pre-event samples. A consistent evaluation of the all the time series components were performed and quality was listed in late P- and S-wave trigger flags.

The response spectra quality is determined by two metrics: the processing flag and the useable bandwidth. It is important to review this information when using the flatfile as the entire period set is provided even outside the useable bandwidth. Although extensive effort was made toward uniformity in the processing methodology records, there were many records that were pass-through or had static displacements. The pass-through records can be found using the processing flag. Additional spectral quality flags discussed in Section 6.8 should also be considered.

8 Summary

This report serves as a documentation of the data included in the NGA-West2 ground motion database. The ground motion database includes the revised NGA-West1 database and additional three-component ground motion recordings from numerous selected large magnitude events (**M** > 6) that occurred throughout the world since 2003, the date when the NGA-West1 database was frozen. Additionally, the NGA-West2 database includes a set of three-component ground motion recordings from small-to-moderate events (3 < **M** < 5.5) that occurred in California between 1998 and 2011. The total number of three-component recordings in the NGA-West2 database is 21336 records from 600 shallow crustal events. This is an extremely rich database of recorded ground motions that can be used for a wide range of applications in earthquake engineering and science.

The included time series were uniformly processed using the PEER methodology. Records in the NGA-West1 database were re-filtered, when possible, to expand the usable period range and the raw time series was processed using an acuasal filter. In addition to providing selected filter corners used in the processing, the time series were assessed for effects of data clipping (i.e., missing p-wave) due to recordings that were from triggered rather than continuously recorded instrumentation.

Spectral accelerations at eleven different damping levels (0.5, 1, 2, 3, 5, 7.5, 10, 15, 20, 25, and 30 %) were computed. The preferred intensity measure to be used in the NGA-West2 GMPE development is RotD50 at periods ranging from 0.01 to 20 sec.

Metadata that were collected were used to define important event and station information used in the development of GMPEs and also by the engineering community. Throughout the process of adding data, a systematic check and review was performed by experts and the NGA-West2 GMPE developers. New types of metadata include a new event classification, additional directivity parameters, late-trigger flags, and a new distance parameter, R_Y. Additionally, updates to the various site metadata have included information that were not available during the NGA-West1 project (e.g., V_{s30} estimated from new boring data and new V_{s30} proxy methods), and revisions based on new findings in the literature.

As in the NGA-West1 project, summary flatfiles and time series data files have been created to facilitate an efficient dissemination of the core NGA data to the research and engineering communities.

REFERENCES

Aagaard B.T., Brocher T.M., Dolenc D., Dreger D., Graves R.W., Harmsen S., Hartzell S., Larsen S., McCandless K., Nilsson S., Petersson N.A., Rodgers A., Sjögreen B., Zoback M.L. (2008). Ground motion modeling of the 1906 San Francisco earthquake II: Ground motion estimates for the 1906 earthquake and scenario events, *Bull. Seismol. Soc. Am.,* 98(2): 1012–1046, doi 10.1785/0120060410.

Aagaard B.T., Graves R.W., Rodgers A., Brocher T.M., Simpson R.W., Dreger D., Petersson N.A., Larsen S.C., Ma S., Jachens R.C. (2010). Ground-motion modeling of Hayward fault scenario earthquakes, Part II: Simulation of long-period and broadband ground motions, *Bull. Seismol. Soc. Am.,* 100(6): 2945–2977.

Abrahamson N.A. Silva W.J. (1997). Empirical response spectral attenuation relations for shallow crustal earthquakes, *Seismol. Res. Lett.,* 68(1): 94 –127.

Abrahamson N.A., Silva W.J. (2008). Summary of the Abrahamson and Silva NGA ground-motion relations, *Earthq. Spectra,* 24: 67–97.

Aki, K., Richards P.G. (1980). *Quantitative Seismology*, W.H. Freemann and Company, San Francisco, CA.

Al Atik L., Abrahamson N., Bommer J., Scherbaum F., Cotton F., Kuehn N. (2010). Variability of ground-motion prediction models and its components, *Seismol. Res. Lett.,* 81(5): 794-801.

Allen C.R., Amand P., Richter C.F., Nordquist J.M. (1965). Relationship between seismicity and geologic structure in the southern California region, *Bull. Seismol. Soc. Am.,* 55(4): 753–797.

Ancheta T.D., Bozorgnia Y., Darragh R., Silva W.J., Chiou B., Stewart J.P., Boore D.M., Graves R., Abrahamson N.A., Campbell K.W., Idriss I.M., Youngs R.R., Atkinson G.M. (2012). PEER NGA-West2 Database: A database for ground motions recorded in shallow crustal earthquakes in active tectonic regions, *Proceedings, 15th World Conference on Earthquake Engineering*, Lisbon, Portugal.

Ang A.H.-S., Tang W.H. (1975). *Probability Concepts in Engineering Planning and Design. Volume 1: Basic Principles*, John Wiley & Sons, NY.

Asano K., Iwata T. (2009). Surface rupture process of the 2004 Chuetsu, Mid-Nagata Prefecture, Japan, earthquake inferred from waveform inversion with dense strong-motion data, *Bull. Seismol. Soc. Am.,* 99: 123–140.

Atkinson G.M., Morrison M. (2009). Regional variability in ground motion amplitudes along the west coast of North America, *Bull. Seismol. Soc. Am.,* 99: 2393 –2409.

Baltay A.S., Hanks T.C., Beroza G.C. (2012). Understanding the NGA-West ground motion prediction equations for PGA and PGV, *Seismol. Res. Lett.,* 83(2): 354.

Bazzurro P., Sjoberg B., Luco N., Silva W.J., Darragh R. (2004). Effects of strong motion processing procedures on time histories, elastic and inelastic spectra, *Proceedings, COSMOS Workshop on Strong-Motion Record Processing, Richmond, California*, pp. 1–39.

Beavan J., Samsonov S., Motagh M., Wallace L., Ellis S. Palmer N. (2010). The Darfield (Canterbury) earthquake: Geodetic observation and preliminary source model, *Bull. New Zealand Soc. Earthq. Eng.,* 43(4): 228–235.

Beavan J., Fielding E., Motagh M., Samsonov S., Donnelly N. (2011). Fault location and slip distribution of the 22 February 2011 Mw 6.2 Christchurch, New Zealand, earthquake from geodetic data, *Seismol. Res. Lett.,* 82(6): 789–799.

Benetatos C., Kiratzi A. (2006). Finite-fault slip models for the 15 April 1979 (Mw 7.1) Montenego earthquake and its strongest aftershock of 24 May 1979 (Mw 6.2), *Tectonophysics,* 421: 129–143,

Boatwright J., Blair L., Catchings R., Goldman M., Perosi F., Steedman C. (2004). Using twelve years of USGS refraction lines to calibrate the Brocher and others (1997) 3D velocity model of the Bay Area, U.S. Geological Survey, *USGS Open File Report 2004-1282*.

Bommer J.J., Stafford P.J., Alarcon J.E., Akkar S. (2007). The influence of magnitude range on empirical ground-motion prediction, *Bull. Seismol. Soc. Am.,* 97: 2152–2170.

Bommer J.J., Stafford P.J., Akkar S. (2010). Current empirical ground-motion prediction equations for Europe and their application to Eurocode 8, *Bull. Earthq. Eng.*, 8: 5–26.

Boore D.M. (2001). Effect of baseline corrections on displacements and response spectra from several recordings of the 1999 Chi-Chi, Taiwan, earthquake, *Bull. Seismol. Soc. Am.,* 91(5): 1199–1211.

Boore D.M. (2004). Estimating (30) S V (or NEHRP Site Classes) from shallow velocity models (depths < 30 m), *Bull. Seismol. Soc. Am.,* 94: 591–597.

Boore D.M. (2005). On pads and filters: Processing strong-motion data, *Bull. Seismol. Soc. Am.,* 95(2): 745–750.

Boore D.M. (2010). Orientation-independent, nongeometric-mean measures of seismic intensity from two horizontal components of motion. *Bull. Seismol. Soc. Am.,* 100: 1830–1835

Boore D.M. (2010b). TSPP – A collection of FORTRAN programs for processing and manipulating time series, U.S. Geological Survey, *USGS Open File Report 2008-1111* (Revision 2.11), 57 pgs.

Boore D.M., Atkinson G.M (1989). Spectral scaling of the 1985-1988 Nahanni, Northwest Territories, earthquakes, *Bull. Seismol. Soc. Am.,* 79: 1736–1761.

Boore, D.M. Atkinson, G.M. (1992). Source spectra for the 1988 Saguenay, Quebec earthquakes. *Bull. Seismol. Soc. Am.,* 82: 683–719.

Boore D.M., Akkar S. (2003). Effects of causal and acausal filters on elastic and inelastic response spectra, *Earthq. Eng. Struct. Dyn.*, 32:1729–1748.

Boore D.M., Asten M.W. (2005). Comparisons of shear-wave slowness in the Santa Clara Valley, California, using blind interpretations of data from invasive and noninvasive methods, *Bull. Seismol. Soc. Am.,* 98: 1983–2003.

Boore D.M., Bommer J.J. (2005). Processing of strong-motion accelerograms: Needs, options and consequences, *Soil Dyn. Earthq. Eng.*, 25: 93–115.

Boore D.M., Atkinson G.M. (2008). Ground-motion prediction equations for the average horizontal component of PGA, PGV, and 5%-damped PSA at spectral periods between 0.01 s and 10.0 s, *Earthq. Spectra,* 24: 99–138.

Boore D.M., Watson-Lamprey J., Abrahamson N.A. (2006). GMRotD and GMRotI: Orientation-independent measures of ground motion, *Bull. Seismol. Soc. Am.,* 94(6A): 1502–1511.

Boore D.M., Thompson E.M., Cadet H. (2011). Regional correlations of VS30 and velocities averaged over depths less than and greater than 30 m, *Bull. Seismol. Soc. Am.,* 101(6): 3046–3059.

Boore D.M., Azari Sisi A., Akkar S. (2012*).* Using pad-stripped acausally filtered strong-motion data, *Bull. Seismol. Soc. Am.,* 102: 751–760.

Boore D.M., Joyner W.B. (1997). Site amplifications for generic rock sites, *Bull. Seismol. Soc. Am.,* 87: 327–341.

Borcherdt R.D. (2002). Empirical evidence for acceleration-dependent amplification factors, *Bull. Seismol. Soc. Am.,* 92(2): 761–782.

Borcherdt R.D., Fumal T.E. (2002). Shear-wave velocity compilation for Northridge strong-motion recording sites, U.S. Geological Survey, *USGS Open File Report 2002-107*.

Bozorgnia Y., Abrahamson N.A., Campbell K.W., Rowshandel B., Shantz T. (2012). NGA-West2: A comprehensive research program to update ground motion prediction equations for shallow crustal earthquakes in active tectonic regions, *Proceedings, 15th World Conference on Earthquake Engineering*, Lisbon, Portugal.

Brocher T.M. (2005). A regional view of urban sedimentary basins in northern California based on oil industry compressional-wave velocity and density logs, *Bull. Seismol. Soc. Am.,* 95(6)2093–2114, doi 10.1785/0120050025.

Brocher T.M., Parsons T., Blakely R.J., et al. (2001). Upper crustal structure in Puget Lowland, Washington: Results from the 1998 Seismic Hazards Investigation in Puget Sound, *J. Geophys. Res. Solid Earth*, 106 (B7): 13541–13564.

Brown L.T., Diehl J.G., Nigbor R.L. (2000). A simplified procedure to measure average shear wave velocity to a depth of 30 meters (VS30), *Proceedings,.12th World Conference on Earthquake Engineering*, Paper 677, Auckland, New Zealand.

BSSC (1994). *NEHRP Recommended Provisions for Seismic Regulations for New Buildings, Part 1 – Provisions,* Building Seismic Safety Council, *FEMA 222a*, Federal Emergency Management Agency, Washington, D.C.

Cadet H., Duval A.-M. (2009). A shear wave velocity study based on the KiK-net borehole data: A short note, *Seismol. Res. Lett.,* 80: 440–445.

Campbell K.W., Bozorgnia Y. (2008). NGA ground motion model for the geometric mean horizontal component of PGA, PGV, PGD and 5% damped linear elastic response spectra for periods ranging from 0.01 to 10 s, *Earthq. Spectra,* 24: 139–171.

Cauzzi C., Faccioli E. (2008). Broadband (0.05 to 20 s) prediction of displacement response spectra based on worldwide digital records, *J. Seismology*, 12: 453–475.

Chiou B.S.-J., Wen K.L. (2006). Appendix C: estimation of VS30 at CWB/s free-field sites in NGA model for the average horizontal component of peak ground motion and response spectra, *PEER Report No. 2008/10*, Pacific Earthquake Engineering Research Center, University of California, Berkeley, CA.

Chiou B.S.-J., Youngs R.R. (2006). Chiou and Youngs PEER-NGA empirical ground motion model for the average horizontal component of peak acceleration, peak velocity, and pseudo-spectral acceleration for spectral periods of 0.01–10 sec, *Interim Report submitted to PEER*, Pacific Earthquake Engineering Research Center, University of California, Berkeley, CA.

Chiou B.S.-J., Youngs R.R. (2008a). An NGA model for the average horizontal component of peak ground motion and response spectra, *Earthq. Spectra,* 24: 173–216.

Chiou B.S-J., Youngs R.R. (2008b). An NGA model for the average horizontal component of peak ground motion and response spectra, *Earthq. Spectra,* 24(1): 173–215.

Chiou B.S.-J., Makdisi F.I., Youngs R.R. (2000). Style-of-faulting and footwall/hanging wall effects on strong ground motion, FY 1995 *NEHRP Award Number 1434-95-G-2614*, Final Report, 21 pgs.

Chiou B.S.-J., Darragh R.B., Gregor N., Silva W.J. (2008). NGA project strong-motion database, *Earthq. Spectra,* 24(1): 23–44.

Chiou B.S.-J., Youngs R.R., Abrahamson N.A., Addo K. (2010). Ground-motion attenuation model for small-to-moderate shallow crustal earthquakes in California and its implications on regionalization of ground-motion prediction models, *Earthq. Spectra,* 26(4): 907–926.

Cirella A., Piatanesi A., Tinti E., Cocco M. (2009). Rupture process of the 2007 Niigata-ken Chuetsu-oki earthquake by non-linear joint inversion of strong motion and GPS data, Submitted to *Geophys*ic*al Research Letters***.**

Cox B.R., Beekman A.N. (2011). Intra-method variability in ReMi dispersion methods and V_S estimates at shallow bedrock sites, *J. Geotech. Enviro. Eng.,* 137(4): 1–10.

Cua G., Heaton T.H. (2012). Characterizing average properties of southern California ground motion amplitudes and envelopes, submitted to *Bulletin Seismological Society of America.*

Custódio S., Liu P.P., Archuleta R.J. (2005). The 2004 M_w 6.0 Parkfield, California, earthquake: Inversion of near-source ground motions using multiple datasets, *Geophys. Res. Lett.,* 32:L23312.

Darragh R.B., Silva W.J., Gregor N. (2004). Strong motion record processing procedures for the PEER center, *Proceedings of COSMOS Workshop on Strong-Motion Record Processing*, Richmond, California, pp. 1–12.

Douglas J. (2004). An investigation of analysis of variance as a tool for exploring regional variability of ground motions, *J. Seismology*, 8: 485–496.

Douglas J. (2007). On the regional dependence of earthquake response spectra, ISET, *J. Earthq. Tech.*, 44: 71–99.

Douglas J., Boore D.M. (2011). High-frequency filtering of strong-motion records, *Bull. Earthq. Eng.,* 9: 395–409.

Dreger D. Gee S.L., Lombard P., Murray M.H., Romanowicz B. (2004). Rapid finite-source analysis and near-fault strong-ground motions: Application to the 2003 M_w 6.5 San Simeon and 2004 M_w 6.0 Parkfield earthquakes, *Seismol. Review Lett.,* 76(1): 40–48.

Fumal T.E., Tinsley J.C. (1985). Mapping shear-wave velocities of near-surface geologic materials. In: J.I. Ziony (ed.), *Evaluating Earthquake Hazards in the Los Angeles Region-An Earth-Science Perspective. U.S. Geological Survey Professional Paper 1360*, pp. 101–126.

Gardner J.K., aKnopoff L. (1974). Is the sequence of earthquakes in southern California, with aftershocks removed, Poissonian? *Bull. Seismol. Soc. Am.,* 64: 1363–1367.

Goto, H., Sawada S., Morikawa H., Kiku H., Ozalaybey S. (2005). Modeling of 3D subsurface structure and numerical simulation of strong ground motion in the Adapazari Basin during the 1999 Kocaeli Earthquake, Turkey, *Bull. Seismol. Soc. Am.,* 95(6): 2197–2215.

Graves R.W. (1994). Simulating the 3D basin response in the Portland and Puget Sound regions from large subduction zone earthquakes, *USGS Award: 1434-93-G-2327*, Annual Technical Report.

Graves R.W., Pitarka A. (2010). Broadband ground-motion simulation using a hybrid approach, *Bull. Seismol. Soc. Am.,* (5A): 2095–2123.

Grazier V.M. (1979). Determination of the true ground displacement by using strong motion records, Izvestiya Academy of Sciences, USSR, *Physics of the Solid Earth*, 15(12): 875–885.

Hardebeck J.L., Boatwright J., Dreger D., Goel R., Graizer V., Hudnut K., Ji C., Jones L., Langbein J., Lin J., Roeloffs E., Simpson R., Stark K., Stein R., Tinsley J. C. (2004). Preliminary report on the 22 December 2003 M_w 6.5 San Simeon, California earthquake, *Seismol. Review Lett.,* 75(2):155–172.

Hauksson E., Yang, W. Shearer P.M. (2012). Waveform relocated earthquake catalog for southern California (1981 to 2011), submitted to *Bulletin of the Seismological Society of America.*

Hauksson E. (2000). Crustal structure and seismicity distribution adjacent to the pacific and North America plate boundary in southern California, *J. Geophys. Res.,* 105(B6): 13875–13903.

Hikima K., Kodetsu K. (2005). Rupture process of the 2004 Chuetsu (mid-Niigata prefecture) earthquake, Japan: A series of events in a complex system, *Geophys. Res. Lett.,* 32.

Holden C. (2011). Kinematic source model of the 22 February 2011 M_w 6.2 Christchurch earthquake using strong motion data, *Seismol. Res. Lett.,* 82(6): 783–788.

Hough S.E., Dreger D.S. (1995). Source parameters of the 23 April 1992 M 6.1 Joshua Tree, California, earthquake and its aftershocks: Empirical Green's function analysis of GEOS and TERRAscope data, *Bull. Seismol. Soc. Am.,*, 85(6): 1576–1590.

Hu Z., Yu C., Tao K., Cui X., Ning J., Wang Y. (2008). Focal mechanism solutions of Wenchuan earthquake and its strong aftershocks obtained from initial P-wave polarity analysis *Chinese J. Geophys.,* 51(6):1711–1718 (in Chinese).

Hubbard J., Shaw J.H., Klinger Y. (2010). Structural setting of the M_w 7.9 Wenchuan, China earthquake, *Bull. Seismol. Soc. Am.,* 100(5B): 2713–2735.

Iwahashi J., Pike R.J. (2007). Automated classifications of topography from DEMs by an unsupervised nested-means algorithm and a three-part geometric signature, *Geomorphology*, 86(3–4): 409–440.

Iwan W.D., Moser M.A., Peng C.-Y. (1985), Some observations on strong-motion earthquake measurement using a digital accelerograph, *Bull. Seismol. Soc. Am.,* 75(5): 1225–1246.

Jackson J., Bouchon M., Fielding E., Funning G., Ghorashi M., Hatzfeld D., Nazari H., Parsons B., Priestley K., Talebian M., Tatar M., Walker R., Wright T. (2006). Seismotectonic, rupture process, and earthquake-hazard aspects of the 2003 December 26 Bam, Iran, earthquake, *Geophysical Journal International.*

Ji C, Larson K.M., Tan Y., Hudnut K.W., Choi K. (2004). Slip history of the 2003 San Simeon earthquake constrained by combining 1-Hz GPS, strong motion and teleseismic data, *Geophys. Res. Lett.,* 31 L17608.

Kagawa T, Zhao B., Miyakoshi K., Irikura K. (2004). Modeling of 3D basin structures for seismic wave simulations based on available information on the target area: case study of the Osaka Basin, Japan, *Bull. Seismol. Soc. Am.,* 94(4): 1353–1368.

Kanno T., Narita A., Morikawa N., Fujiwara H., Fukushima Y. (2006). A new attenuation relation for strong ground motion in Japan based on recorded data, *Bull. Seismol. Soc. Am.,* 96: 879–889.

Kinoshita S. (1998). Kyoshin-net (K-NET), *Seismol. Res. Lett.,* 69: 309–332.

Kishida,T., Darragh R.B. (2012). Wenchuan aftershock relocation using S-P times, *Draft Report to PEER*.

Kohler M, Magistrale H., Clayton R. (2003). Mantle heterogeneities and the SCEC reference three-dimensional seismic velocity model version 3, *Bull. Seismol. Soc. Am.,* 93(2)757.

Koketsu, K., Yokota Y., Ghasemi H., Hikima K., Miyake H., Wang Z. (2008). Source process and ground motions of the 2008 Wenchuan earthquake. *Investigation report of the 2008 Wenchuan earthquake,* China, Grant-in-Aid for Special Purposes of 2008, MEXT No. 2090002.

Lee C.T., Cheng C.-T., Liao C.-W., Tsai Y.-B. (2001). Site classification of Taiwan freefield strong-motion stations, *Bull. Seismol. Soc. Am.,* 91(5): 1283–1297.

Lin G., Thurber C.H., Zhang H., Hauksson E., Shearer P.M., Waldhauser F., Brocher T.M.,Hardebeck J., (2010). A California statewide three-dimensional seismic velocity model from both absolute and differential times, *Bull. Seismol. Soc. Am.,* 100(1): 225–240.

Ludwig W.J., Nafe J.E., Drake C.L. (1970). Seismic refraction, in *The Sea*, A.E. Maxwell (ed.), Vol. 4, Wiley-Interscience, New York, pp. 53-84.

Magistrale, H., Day S., Clayton R.W., Graves R.W. (2000). The SCEC Southern California reference three-dimensional seismic velocity model Version 2, *Bull. Seismol. Soc. Am.,* 90: S65–S76.

Martirosyan A., Dutta U., Biswas U., Papageorgiou N., Combellick R. (2002). Determination of site response in Anchorage, Alaska, on the basis of spectral ratio methods, *Earthq. Spectra,* 18(1): 85–104.

Matsuoka M., Wakamatsu K., Fujimoto F., Midorikawa S. (2006). Average shear-wave velocity mapping using Japan engineering geomorphologic classification map, *J. Struct. Mecha. Earthq. Eng.*, 23(1): 57s–68s.

Miyake, H., Koketsu K., Hikima K., Shinohara M., Kanazawa T. (2010). Source fault of the 2007 Chuetsu-oki, Japan, earthquake, times, *Bull. Seismol. Soc. Am.,* 100(1): 384–391.

Moss R.E.S. (2008). Quantifying measurement uncertainty of thirty-meter shear-wave velocity, *Bull. Seismol. Soc. Am.,* 98(3)1399–1411.

Moss R.E.S. (2009). Reduced uncertainty of ground-motion prediction equations through Bayesian variance analysis, *PEER Report No. 2009/105*, Pacific Earthquake Engineering Research Center, University of California, Berkeley, CA.

Moss R.E.S. (2011). Reduced sigma of ground-motion prediction equations through uncertainty propagation, *Bull. Seismol. Soc. Am.,* 101(1): 250–257.

Okada Y., Kasahara K., Hori S., Obara K., Sekiguchi S., Fujiwara H., Yamamoto A. (2004). Recent progress of seismic observation networks in Japan-Hi-net, F-net, K-NET and KiK-net, *Earth Planets Space*, 56: xv–xxviii.

Pacific Gas and Electric Company (2011). Evaluation of shear wave velocity at the DCPP ISFSI, GeoSciences Department, Calculation Document, *Document No. GEO.DCPP.10.02*.

Piatanesi A., Cirella A., Spudich P., Cocco M. (2007). A global search inversion for earthquake kinematic rupture history: Application to the 2000 western Tottori, Japan earthquake, *J. Geophys. Res.*, 112: B07314.

Plesch A., Tape C., Shaw J. (2009). CVM-H 6.0: Inversion integration, the San Joaquin valley and other advances in the community velocity model. In: 2009 Southern California Earthquake Center Annual Meeting, *Proceedings and Abstracts*, 19: 260–261.

Power M., Chiou B., Abrahamson N.A., Bozorgnia Y., Shantz T., Roblee C. (2008). An overview of the NGA project, *Earthq. Spectra*, 24: 3–21.

Rowshandel B. (2006, 2010, 2013). Directivity models produced for the Next Generation Attenuation West 2 (NGA-West 2) project.

Sandikkaya M.A., M.T. Yilmaz, B.S. Bakir, and O. Yilmaz (2010). Site classification of Turkish national strong-motion stations, *J. Seismology,* 14:543–563. DOI 10.1007/s10950-009-9182-y.

Sato T., Graves R.W., Somerville P.G. (1999). Three-dimensional finite-difference simulations of long-period strong-motions in the Tokyo metropolitan area during the 1990 Odawara Earthquake (MJ 5.1) and the Great 1923 Kanto Earthquake (MS 8.2) in Japan, *Bull. Seismol. Soc. Am.,* 89: 579–607.

Scasserra G., J.P. Stewart, R.E. Kayen, and G. Lanzo (2009). Database for earthquake strong motion studies in Italy, *Journal of Earthquake Engineering,* 13(6):852–881.

Scognamiglio L., Tinti E., Michelini A., Dreger D.S., Cirella A., Cocco M., Mazza S., Piatanesi A. (2010). Fast determination of moment tensors and rupture history: What has been learned from the 6 April 2009 L' Aquila earthquake sequence, *Seismol. Res. Lett.,* 81(6): 892–906.

Shahi S.K., Baker J.W. (in preparation). An efficient algorithm to identify strong velocity pulses in multi-component ground-motions.

Silva W.J., Darragh R.B. (1985). Engineering characterization of earthquake strong ground motion recorded at rock sites. *Electric Power Research Institute TR-1002261,* Palo Alto, CA.

Silva W.J., Gregor N., Darragh R.B. (1999). Near fault ground motions, *A PEARL report to PG&E/CEC/Caltrans, Award No. SA2193-59652*.

Silva W.J., Yu T. (2011). Shear wave velocity at sites that recorded the M 7.9 Wenchuan earthquake in south-west China, *Draft Report to PEER*.

Somerville P.G., et al. (1997). Magnitude scaling of the near fault rupture directivity pulse, *Physics of the Earth and Planetary Interior,* 137(2003): 201–212.

Somerville P.G., Collins N., Graves R., Pitarka A. (2002). Development of an engineering model of basin generated surface waves, *Proceedings*, *SMIP03 Seminar on Utilization of Strong-Motion Data*, pp. 1–21.

Spudich P., Fletcher J.B., Hellweg M., Boatwright J., Sullivan C., Joyner W.B., Hanks T.C., Boore D.M., McGarr A., Baker L.M., Lindh A.G. (1996). Earthquake ground motions in extensional tectonic regimes, U.S. Geological Survey, *USGS Open File Report 96-292.*

Spudich P., Chiou B. (2008). Directivity in NGA earthquake ground motions: analysis using isochrone theory, *Earthq. Spectra,* 24: 279–298.

Stewart J.P., Lanzo G., Pagliaroli A., Scasserra G., DiCapua G., Peppolini S., Darragh R., Gregor N. (2012). Ground motion recordings from the Mw 6.3 2009 L'Aquila earthquake in Italy and their engineering implications, *Earthq. Spectra,* 28(1): 317–345.

Stewart J.P., Seyhan E., Boore D.M., Campbell K.W., Erdik M., Silva W.J. (2012). Site effects in parametric ground motion models for the GEM-PEER global GMPEs project, *Proceedings, 15th World Conference on Earthquake Engineering*, Lisbon, Portugal.

Süss M., Shaw J. (2003). P-wave seismic velocity structure derived from sonic logs and industry reflection data in the Los Angeles basin, California, *J. Geophys. Res.*, 108(B3): 2170.

Suzuki W., Aoki S., Sekiguchi H. (2010) Rupture process of the 2008 Iwate-Miyagi Nairku, Japan, earthquake derived from near-source strong-motion records, *Bull. Seismol. Soc. Am.,* 100(1): 256–266.

Symons N.P., Crosson R.S. (1997). Seismic velocity structure of the Puget Sound region from 3-D non-linear tomography, *Geophys. Res. Lett.,* 24(21): 2593–2596.

Tape C., Liu Q., Maggi A., Tromp J. (2009). A joint tomography of the southern California crust, *Science*, 325(5943): 988.

Thompson E.M., Baise L.G., Tanaka Y., Kayen R.E. (2012). "A taxonomy of site response complexity," *Soil Dyn. and Earthq. Eng.*, 41: 32–43.

Wakamatsu K., Kubo S., Matsuoka M., Hasegawa K., Sugiura M. (2005). *Japan Engineering Geomorphologic Classification Map with CD-ROM Database*, University of Tokyo Press, Tokyo. (in Japanese with English abstract and manual).

Wakamatsu K., Matsuoka M. (2006). Development of the 7.5-arc-second engineering geomorphologic classification database and its application to seismic microzoning, *Bull. Earthq. Res. Institute*, The University of Tokyo, 81: 317–324.

Wald D.J., Allen T.I. (2007). Topographic slope as a proxy for seismic site conditions and amplification, *Bull. Seismol. Soc. Am.,* 97: 1379–1395.

Waldhauser F., Schaff D. (2008). Large-scale relocation of two decades of northern California seismicity using cross-correlation and double-difference methods, *J. Geophys. Res.*, 113: B08311.

Wang W., Zhao L., Li J., Yao Z.-X. (2008). Rupture process of the M_S 8.0Wenchuan earthquake of Sichuan, China, *Chinese J. Geophys.,* 51(5): 1403–1410 (in Chinese with English abstract).

Watson-Lamprey, J. Boore D.M. (2007). Beyond SaGMRotI: conversion to SaArb, SaSN, and SaMaxRot, *Bull. Seismol. Soc. Am.,* 97(5): 1511-1524.

Wei S., Fielding E., Leprince S., Sladen A., Avouac J-P., Helmberger D., Hauksson E., Chu R., Simons M., Hudnut K., Herrring T., Briggs R. (2011). Superficial simplicity of the 2010 M_w 7.2 El Mayor-Cucapah earthquake of Baja, California, *Nature.*

Wills C.J., Clahan K.B. (2006). Developing a map of geologically defined site- condition categories for California, *Bull. Seismol. Soc. Am.,* 96: 1483–1501.

Wills C.J., Gutierrez C. (2008). Investigation of geographic rules for improving site-conditions mapping, *Calif. Geo. Sur. Final Tech. Rept.*, 20 pgs. (Award No. 07HQGR0061).

Wills C.J., Silva W.J. (1998). Shear wave velocity characteristic of geologic units in California, *Earthq. Spectra,* 14(3): 533–556.

Wooddell K.E., Abrahamson N.A. (2012). New earthquake classification scheme for mainshocks and aftershocks in the NGA-West2 ground motion prediction equations, *Proceedings*, *15th World Conf. Earthquake Engineering*, Lisbon, Portugal.

Yang W., Hauksson E., Shearer P. (2012). Computing a large refined catalog of focal mechanisms for southern California (1981–2010), manuscript in preparation.

Yong A., Hough S.E., Iwahashi J., Braverman A. (2012). Terrain-based site conditions map of California with implications for the contiguous United States, *Bull. Seismol. Soc. Am.,* 102: 114–128.

Yong A., Martin A., Stokoe K., Diehl J. (2013), ARRA-funded V_{S30} measurements using multi-technique approach at California and central-eastern United States strong motion stations, U.S. Geological Survey, *USGS Open-File Report 2013-1102*, U.S. Pasadena, CA.

Yong A., Martin A., Stokoe K., Diehl J. (2013). ARRA-funded Vs30 measurements at California and Central-eastern U.S. strong motion stations, U.S. Geological Survey, *USGA Open-File Report* (in review).

Zhao B., Shi Y., Gao Y. (2011). Relocation of aftershocks of the Wenchuan MS 8.0 earthquake and its implications to seismotectonics, *Earthq. Science,* 24: 107–113.

Zhen Y., Ma H., Lu J., Ni S., Li Y., Wei S. (2009). Mechanism solution for Wenchuan aftershock earthquakes and its relationship to the earthquake structure, Science in China D, *Science in China Press*, 39: 413–426 (in Chinese).

Zhu L. (2003). Refining the Southern California 3D model in the Los Angeles Area, *U.S. Geological Survey Award 03HQGR0100.*

Appendix A: Rectangular Fault Source Table Explanation Multiple-Segment Event Location and Mechanism Table

The link to the Source Table is here: http://peer.berkeley.edu/ngawest2/databases/.

Table A.1 Source table column explanation.

Column	Column Name (units)	Description
A	EQID	An arbitrary unique ID assigned to each earthquake for identification.
B	Earthquake Name	The common name of earthquake. The earthquake name may include the general area or country where earthquake occurred. In the case of multiple earthquakes in the same general area/country (for example there are eight earthquakes in the source table that are located in Imperial Valley, CA), a number was used to distinguish between these events.
C	Earthquake Magnitude	Moment magnitude. When the moment magnitude was not available the surface wave, local or duration magnitude was used.
D	Magnitude Type	If the listed earthquake magnitude is NOT a moment magnitude, this column identifies the type of magnitude ML = local magnitude MS = surface-wave magnitude Mb = body wave magnitude U = unknown magnitude type (-999) = unknown
E	Finite Fault Flag	If 1, a geometric representation of the ruptured area was developed using observed surface rupture, published slip model(s), aftershock distribution (and time after mainshock), etc.
F	Hypocenter Latitude (deg)	Hypocenter latitude adopted by NGA-West2 project
G	Hypocenter Longitude (deg)	Hypocenter longitude adopted by NGA-West2 project
H	Hypocenter Depth (km)	Hypocenter depth (km) adopted by NGA-West2 project
I	Total Fault Length (km)	The total length of the rectangular fault (including all fault segments for multiple-segment (complex) ruptures
J	Total Fault Width	The maximum width of the rectangular fault (including all fault segments for

	(km)	multiple-segment (complex) ruptures
K	Total Rectangular Fault Area (km*km)	The total area of the rectangular fault (including all fault segments for multiple-segment (complex) ruptures
L	Number of fault segments	Number of segments. Nearly all faults have a single rectangular fault. The maximum is 12.
M	Fault Segment Number	Segment number. Nearly all faults only have a single segment number (1).
N	Strike of fault segment (deg)	Strike angle of the fault plane used to approximate the causative fault surface. 0^o <= Strike <= 360^o. Convention of fault strike, dip, and rake follows that described in Aki and Richards (1980, p106) (see Figure 2.1)
O	Dip of fault segment (deg)	Dip angle of the fault plane. 0^o <= Dip <= 90^o. (see note above)
P	Segment Fault Length (km)	Length of the rectangular fault segment. (see Figure 2.1)
Q	Segment Fault Width (km)	Down-dip width of the rectangular fault segment. (see Figure 2.1)
R	Rake Angle (deg)	Rake is the angle measured on the fault plane counterclockwise from the reference strike direction to the average slip direction (see Figure 2.1). -180^o <= Rake <= 180^o
S	Latitude Fault Segment Upper Left Corner (deg)	Convention of fault upper left corner (ULC) follows that described in Aki and Richards (1980, p106)
T	Longitude Fault Segment Upper Left Corner (deg)	Convention of fault upper left corner (ULC) follows that described in Aki and Richards (1980, p106)
U	Depth of Fault Segment Upper Left Corner (km)	Convention of fault upper left corner (ULC) follows that described in Aki and Richards (1980, p106)
V to AD	Fault Segment 2	Information for this fault segment following the order of information given for fault segment 1
AE to AM	Fault Segment 3	Information for this fault segment following the order of information given for fault segment 1
AN to AV	Fault Segment 4	Information for this fault segment following the order of information given for fault segment 1
AW to BE	Fault Segment 5	Information for this fault segment following the order of information given for fault segment 1
BF to BN	Fault Segment 6	Information for this fault segment following the order of information given for fault segment 1
BO to BW	Fault Segment 7	Information for this fault segment following the order of information given for fault segment 1
BX to CF	Fault Segment 8	Information for this fault segment following the order of information given for fault segment 1
CG to CO	Fault Segment 9	Information for this fault segment following the order of information given for fault segment 1
CP to CX	Fault Segment 10	Information for this fault segment following the order of information given for fault segment 1
CY to DG	Fault Segment 11	Information for this fault segment following the order of information given for fault segment 1
DH to DP	Fault Segment 12	Information for this fault segment following the order of information given for fault segment 1

Table A.2 Fault parameters for multiple-segment rupture events.

Segment	Length (km)	Width (km)	Rake (deg.)	Dip (deg.)	Strike (deg.)	Ztor (km)	Bottom D (km)	HypLat (dec.)	HypLon (dec.)	HypD (km)
0012a	29.7	21.7	61	75	51	6	27	34.99	-119.02	15.6
0012b	35	12.9	61	75	51	0	12.5	35.11	-118.82	12.5
0025a-1	15.9	12	180	90	137.1	0	12	35.96	-120.50	10
0025a-2	9.1	12	180	90	145.8	0	12	-	-	-
0030a	16	16.1	83	54	290	3	16.03	34.44	-118.41	13
0030b	16	11.3	83	45	285	0	8	34.39	-118.41	8
0125a-1	15.7	15	180	90	356.1	0	15	34.20	-116.44	7
0125a-2	3.4	15	180	90	8.6	0	15	-	-	-
0125a-3	17.7	15	180	90	338.5	0	15	-	-	-
0125a-4	3.3	15	180	90	358.8	0	15	-	-	-
0125a-5	11.1	15	180	90	325	0	15	-	-	-
0125a-6	4.7	15	180	90	295.7	0	15	-	-	-
0125a-7	15.9	15	180	90	319.8	0	15	-	-	-
0129a	40	20	180	85	230	0.2	20.12	34.60	135.01	17.9
0129b	20	20	180	80	45	0.2	19.9	34.59	135.02	17.9
0136a-1	4	20.3	180	80	270	0	20	-	-	-
0136a-2	1.3	20.3	180	80	272.3	0	20	-	-	-
0136a-3	28	20.3	180	80	245.2	0	20	-	-	-
0136a-4	4.2	20.3	180	80	329.9	0	20	-	-	-
0136a-5	28	20.3	180	80	275.4	0	20	-	-	-
0136a-6	1	20.3	180	80	319.9	0	20	-	-	-
0136a-7	28	20.3	180	80	269.8	0	20	40.75	29.99	16
0136a-8	0.5	20.3	180	80	327.4	0	20	-	-	-
0136a-9	9	20.3	180	80	270.8	0	20	-	-	-
0136a-10	20	20.3	180	80	262.5	0	20	-	-	-
0136a-11	5.5	20.3	180	80	303.2	0	20	-	-	-
0136a-12	8	20.3	180	80	262.5	0	20	-	-	-
0137a-1	11.7	20	55	30	34.6	0	20	-	-	-
0137a-2	23.9	35.8	55	34	0.7	0	20	23.85	120.82	8
0137a-3	4	28.3	55	45	330.2	0	20	-	-	-
0137a-4	11.6	37.7	55	32	7.1	0	20	-	-	-
0137a-5	3.8	40	55	30	50.5	0	20	-	-	-
0137a-6	16.8	40	55	30	0.7	0	20	-	-	-
0137a-7	5.8	42.6	55	28	30.2	0	20	-	-	-
0137a-8	6.7	28.3	55	45	81.9	0	20	-	-	-
0137a-9	3.7	40	55	30	19.4	0	20	-	-	-
0138a-1	16.5	20	182	65	278.6	0	18.126	-	-	-
0138a-2	8.9	20	182	65	271.1	0	18.126	-	-	-
0138a-3	9.5	20	182	65	254.2	0	18.126	40.83	31.13	14

0138a-4	11.9	20	182	65	269.7	0	18.126	-	-	-
0144a-1	9	16	-9	88	298.4	0	16	-	-	-
0144a-2	6.8	16	-9	88	279.2	0	16	-	-	-
0144a-3	10.2	16	-9	88	304.5	0	16	-	-	-
0144a-4	10.1	16	-9	88	277.5	0	16	-	-	-
0144a-5	4.7	16	-9	88	310.1	0	16	-	-	-
0144a-6	16.6	16	-9	88	276.6	0	16	36.84	49.39	16
0144a-7	14.3	16	-9	88	292	0	16	-	-	-
0158a	30	16.2	179	85	346	0	16.14	34.60	-116.26	14.8
0158b	21	16.2	179	75	322	0	15.65	34.61	-116.25	14.8
0158c	18	16.2	179	85	322	0	16.14	34.47	-116.23	14.8
0169a-1	5.2	24	90	32	214.8	0	12.72	-	-	-
0169a-2	15.2	24	90	32	238.3	0	12.72	-	-	-
0169a-3	24.7	24	90	32	268	0	12.72	63.54	-147.44	8.9027
0169b-1	10.4	15	171	80	302.3	0	14.78	-	-	-
0169b-2	24.6	15	171	80	297.1	0	14.78	-	-	-
0169b-3	56.4	15	171	80	295.8	0	14.78	-	-	-
0169b-4	34.2	15	171	80	289.2	0	14.78	-	-	-
0169b-5	22.7	15	171	80	298.1	0	14.78	-	-	-
0169b-6	16	15	171	80	286	0	14.78	-	-	-
0169b-7	39.5	15	171	80	279.9	0	14.78	63.54	-146.96	9.7
0169b-8	9.9	15	171	80	271.5	0	14.78	-	-	-
0169c-1	11.6	15	171	90	318.9	0	15.01	-	-	-
0169c-2	4.1	15	171	90	2	0	15.01	-	-	-
0169c-3	23.7	15	171	90	315.7	0	15.01	-	-	-
0169c-4	14.7	15	171	90	310.1	0	15.01	-	-	-
0169c-5	13.7	15	171	90	329.9	0	15.01	62.79	-143.30	9.7
0277a	150	45	110	35	228	0	25.81	30.99	103.36	10
0277b	150	40	165	65	232	0	36.25	31.84	104.35	10
0280a	18	12	-90	45	355	0.5	8.99	32.30	-115.27	5.45
0280b	51	12	-180	75	312	0.57	12.16	32.28	-115.32	2.02
0280c	66	18	-170	60	311	0.51	16.1	32.27	-115.33	1.81
0280d	9	6	-180	50	335.2	0.61	5.21	32.58	-115.71	1.76

Appendix B: Wenchuan Aftershock Location and Mechanism Tables

Table B.1 **Wenchuan aftershock hypocenter locations from the ISC and the corrected locations adopted in the source table.**

Earthquake Name	Hypocenter Locations by ISC			Hypocenter Locations after Corrections			Correction Method
	Lat (deg)	Lon (deg)	Depth (km)	Lat (deg)	Lon (deg)	Depth (km)	
Wenchuan, China-01	32.549	105.48	14	32.609	105.372	20.1	Zhao et al.
Wenchuan, China-02	31.26	103.669	14	31.296	103.448	10.0	Zhao et al.
Wenchuan, China-03	31.27	103.819	14	31.311	103.689	17.9	Zhao et al.
Wenchuan, China-04	31.43	104.059	21	31.443	103.843	13.3	Zhao et al.
Wenchuan, China-05	30.95	103.419	14	31.019	103.176	17.5	Zhao et al.
Wenchuan, China-06	31.53	104.279	11	31.611	104.027	13.1	Zhao et al.
Wenchuan, China-07	31.45	104.489	13	31.487	104.316	11.8	Table 2.3
Wenchuan, China-08	31.729	104.55	20	31.781	104.26	8.2	Zhao et al.
Wenchuan, China-09	31.309	103.449	14	31.353	103.192	13.6	Zhao et al.
Wenchuan, China-10	32.2	105.08	13	32.244	104.89	17.1	Zhao et al.
Wenchuan, China-11	31.27	103.58	10	31.286	103.595	5.4	Zhao et al.
Wenchuan, China-12	31.34	103.629	16	31.345	103.379	12.4	Zhao et al.
Wenchuan, China-13	32.779	105.699	15	32.816	105.526	13.8	Table 2.3
Wenchuan, China-14	32.759	105.61	10	32.824	105.474	11.4	Zhao et al.
Wenchuan, China-15	32.02	104.849	14	32.095	104.628	14.8	Zhao et al.
Wenchuan, China-16	32.72	105.61	13	32.797	105.455	11.8	Zhao et al.
Wenchuan, China-17	31.28	103.629	10	31.314	103.389	12.1	Zhao et al.
Wenchuan, China-18	32.72	105.629	10	32.757	105.456	8.8	Table 2.3
Wenchuan, China-19	31.02	103.65	9	31.065	103.407	14.9	Zhao et al.
Wenchuan, China-20	31.479	104.129	14	31.554	103.96	15.5	Zhao et al.
Wenchuan, China-21	32.72	105.639	10	32.767	105.514	8.7	Zhao et al.
Wenchuan, China-22	31.34	103.58	13	31.307	103.373	13.8	Zhao et al.
Wenchuan, China-23	31.26	103.589	13	31.269	103.484	8.9	Zhao et al.
Wenchuan, China-24	31.29	103.769	13	31.272	103.552	10.0	Zhao et al.
Wenchuan, China-25	31.409	104.12	10	31.426	103.908	7.7	Zhao et al.
Wenchuan, China-26	31.389	103.73	10	31.148	103.631	5.0	Zhao et al.

Wenchuan, China-27	31.1	103.589	10	31.061	103.378	13.0	Zhao et al.
Wenchuan, China-28	30.899	103.54	11	30.933	103.406	13.0	Zhao et al.
Wenchuan, China-29	31.139	103.599	10	31.165	103.475	12.4	Zhao et al.
Wenchuan, China-30	31.159	103.69	10	31.252	103.599	2.1	Zhao et al.
Wenchuan, China-31	30.969	103.48	9	30.97	103.305	15.6	Zhao et al.
Wenchuan, China-32	31.209	103.68	24	31.298	103.424	12.3	Zhao et al.
Wenchuan, China-33	32.099	104.65	10	32.136	104.477	8.8	Table 2.3
Wenchuan, China-34	31.36	104.05	17	31.393	103.882	17.1	Zhao et al.
Wenchuan, China-35	31.1	103.65	20	31.184	103.442	13.2	Zhao et al.
Wenchuan, China-36	31.26	103.62	17	31.288	103.457	16.0	Zhao et al.
Wenchuan, China-37	31.069	103.339	14	30.97	103.232	11.7	Zhao et al.
Wenchuan, China-38	31.159	103.559	10	31.296	103.465	19.1	Zhao et al.
Wenchuan, China-39	31.05	103.42	14	31.325	103.488	16.9	Zhao et al.
Wenchuan, China-40	31.2	103.79	17	31.248	103.681	21.2	Zhao et al.
Wenchuan, China-41	31.25	103.879	20	31.281	103.669	13.6	Zhao et al.
Wenchuan, China-42	31.149	103.449	17	31.091	103.257	6.1	Zhao et al.
Wenchuan, China-43	32.349	105.239	18	32.361	105.046	18.9	Zhao et al.
Wenchuan, China-44	32.24	105.099	23	32.33	104.913	14.9	Zhao et al.
Wenchuan, China-45	31.399	104.12	12	31.481	103.894	17.3	Zhao et al.
Wenchuan, China-46	31.049	104.58	15	31.242	104.468	19.0	Zhao et al.
Wenchuan, China-47	31.95	104.239	15	31.987	104.066	13.8	Table 2.3
Wenchuan, China-48	31.87	104.569	9	31.842	104.315	1.8	Zhao et al.
Wenchuan, China-49	31.579	104.11	15	31.598	103.994	16.7	Zhao et al.
Wenchuan, China-50	31.43	103.98	16	31.467	103.807	14.8	Table 2.3
Wenchuan, China-51	31.389	103.629	20	31.367	103.495	6.9	Zhao et al.
Wenchuan, China-52	31.389	104.16	11	31.451	103.955	8.3	Zhao et al.
Wenchuan, China-53	32.33	105.169	22	32.545	105.271	9.2	Zhao et al.
Wenchuan, China-54	31.1	103.48	18	31.194	103.528	11.0	Zhao et al.
Wenchuan, China-55	31.27	103.809	14	31.271	103.597	13.9	Zhao et al.
Wenchuan, China-56	32.22	105.089	9	32.379	104.987	19.7	Zhao et al.
Wenchuan, China-57	31.639	104.339	10	31.719	104.14	14.6	Zhao et al.
Wenchuan, China-58	31.319	104.239	15	31.386	103.772	17.3	Zhao et al.
Wenchuan, China-59	32.15	105.059	15	32.187	104.886	13.8	Table 2.3
Wenchuan, China-60	32.759	105.65	15	32.796	105.477	13.8	Table 2.3
Wenchuan, China-61	31.829	104.379	9	31.276	103.938	9.7	Zhao et al.
Wenchuan, China-62	31.03	103.4	25	30.887	103.289	15.5	Zhao et al.
Wenchuan, China-63	32.24	105.19	21	32.381	105.131	8.4	Zhao et al.
Wenchuan, China-64	31.19	103.8	13	31.212	103.539	22.0	Zhao et al.

Table B.2 **Preferred planes from the selected focal mechanism for Wenchuan aftershocks. When available the conjugate (preferred and auxiliary) fault planes are listed.**

Earthquake Name	Preferred Fault Plane			Auxiliary Fault Plane			Data Source
	Strike (deg)	Dip (deg)	Rake Angle (deg)	Strike (deg)	Dip (deg)	Rake Angle (deg)	
Wenchuan, China-01	59	81	-180	329	90	-9	Zhen et al.
Wenchuan, China-02	220	73	-166	126	77	-17	Zhen et al.
Wenchuan, China-03	228	35	110				Working Group
Wenchuan, China-04	210	24	116	2	69	79	Zhen et al.
Wenchuan, China-05	231	54	121	6	46	55	Zhen et al.
Wenchuan, China-06	244	75	176	335	86	15	Hu et al.
Wenchuan, China-07	228	35	110				Working Group
Wenchuan, China-08	220	55	90	40	35	90	Hu et al.
Wenchuan, China-09	241	61	-173	148	84	-29	Zhen et al.
Wenchuan, China-10	239	48	8	62	42	92	Zhen et al.
Wenchuan, China-11	228	35	110				Working Group
Wenchuan, China-12	290	60	-39	42	57	-143	Zhen et al.
Wenchuan, China-13	86	62	-170	351	81	-28	Zhen et al.
Wenchuan, China-14	196	87	-157	105	67	-3	Zhen et al.
Wenchuan, China-15	220	71	111	350	28	44	Hu et al.
Wenchuan, China-16	123	66	39	15	55	150	ISC
Wenchuan, China-17	279	83	-11	10	80	-173	Hu et al.
Wenchuan, China-18	170	65	110	309	32	54	Zhen et al.
Wenchuan, China-19	263	12	120	52	80	84	Hu et al.
Wenchuan, China-20	221	61	128	342	46	42	Hu et al.
Wenchuan, China-21	65	84	-148	331	58	-7	Hu et al.
Wenchuan, China-22	209	85	-162	117	72	-5	Hu et al.
Wenchuan, China-23	228	35	110				Working Group
Wenchuan, China-24	228	35	110				Working Group
Wenchuan, China-25	187	55	89	8	35	91	Hu et al.
Wenchuan, China-26	228	35	110				Working Group
Wenchuan, China-27	7	24	148	127	78	69	Hu et al.
Wenchuan, China-28	228	35	110				Working Group
Wenchuan, China-29	228	35	110				Working Group
Wenchuan, China-30	228	35	110				Working Group
Wenchuan, China-31	202	42	97	14	48	84	Hu et al.
Wenchuan, China-32	261	76	26	164	65	164	Hu et al.
Wenchuan, China-33	232	65	165				Working Group
Wenchuan, China-34	243	88	-155	153	65	-2	Hu et al.
Wenchuan, China-35	193	48	63	50	48	117	Hu et al.
Wenchuan, China-36	44	79	-176	313	86	-11	Hu et al.
Wenchuan, China-37	228	35	110				Working Group
Wenchuan, China-38	228	35	110				Working Group

Wenchuan, China-39	228	35	110				Working Group
Wenchuan, China-40	281	51	152	30	69	42	Hu et al.
Wenchuan, China-41	228	35	110				Working Group
Wenchuan, China-42	228	35	110				Working Group
Wenchuan, China-43	232	65	165				Working Group
Wenchuan, China-44	232	65	165				Working Group
Wenchuan, China-45	228	35	110				Working Group
Wenchuan, China-46	228	35	110				Working Group
Wenchuan, China-47	193	86	-124	98	34	-7	Hu et al.
Wenchuan, China-48	232	65	165				Working Group
Wenchuan, China-49	200	38	160	306	78	54	Hu et al.
Wenchuan, China-50	228	35	110				Working Group
Wenchuan, China-51	228	35	110				Working Group
Wenchuan, China-52	213	23	76	48	68	96	Hu et al.
Wenchuan, China-53	232	65	165				Working Group
Wenchuan, China-54	232	65	165				Working Group
Wenchuan, China-55	228	35	110				Working Group
Wenchuan, China-56	232	65	165				Working Group
Wenchuan, China-57	209	44	111	1	50	71	Hu et al.
Wenchuan, China-58	228	35	110				Working Group
Wenchuan, China-59	232	65	165				Working Group
Wenchuan, China-60	250	87	172	341	82	3	Hu et al.
Wenchuan, China-61	228	35	110				Working Group
Wenchuan, China-62	228	35	110				Working Group
Wenchuan, China-63	232	65	165				Working Group
Wenchuan, China-64	228	35	110				Working Group

Appendix C: Site Database Explanation

The link to the Site Database is here: http://peer.berkeley.edu/ngawest2/databases/.

Abbreviations used in this document (in alphabetical order)

Active crustal regions: ACRs; Ancheta et al., (2013): AEA13; Boatwright et al. (2004): BEA04; Boore (2004): B04; Boore et al., (2011): CA; California; BEA11; Chiou and Youngs (2008a): CY08a; Chiou et at., (2008): CEA08; Digital Elevation Maps: DEMs; Geomatrix; GMX; Iwahashi and Pike (2007): IP07; Magistrale et al., (2000): MEA00; National Research Institute for Earth Science and Disaster Prevention: NIED; Pacific Engineering and Analysis: PEA; San Francisco Bay Area: SFBA; Shuttle Radar Topography Mission: SRTM; Site Database: SDB; Southern California; SoCal; Wald and Allen (2007): WA07; Wills and Clahan (2006): WC06; Wills and Gutierrez (2008): WG08; Yong et al., (2012): YEA12.

PART I: Basic station information

Column identifier	Column name	Description
A	Source of Data	Defines the source of the information used to populate the site database. When the source is given as a file name, the file was provided by PEA. Otherwise, the source is listed as a conventional reference.
B	Region	Defines the country/region of each strong-motion station based on the latitude/longitude information of the station.
C	SSN	A unique sequence number assigned to each strong-motion station for identification purpose. SSN = "Station Sequence Number"
D	Station Name	Strong motion station name (when multiple names exist from prior databases, the most descriptive name is adopted)
E	Station ID	Station ID assigned by data provider (USGS, CGS/CSMIP, etc). When it is not available, Station ID is given a "-999". It is listed in Flatfile as Column "Station ID No.".
F	Alternate Station ID	When data providers have used more than one station ID, the alternate is given here.
G	Latitude	Uses NAD83. Data from data provider. Listed in Flatfile as “Station Latitude."
H	Longitude	Uses NAD83. Data from data provider. Listed in Flatfile as “Station Longitude."

I	Station housing	Code for station housing, adapted from Geomatrix 1st letter. See Table 3.1 in AEA13 for description.

PART II: Recommended V_{s30} values

J	V_{s30} for Analysis (m/s)	Preferred V_{s30} value in m/s, from measurements or proxy analysis. See Section 3.5.1 in AEA13 for details.
K	$\sigma_{\ln V}$	Log standard deviation (ln units). For V_{s30} code 0, based on data (see AEA13 Section 3.5.2.2a). For Vs30 code > 0, $\sigma_{\ln V}$ taken as the weighted uncertainties of V_{s30} assigned to each station by proxy methods (see AEA13 Section 3.5.2.2b).
L	Preferred NEHRP Based on V_{s30}	The preferred NEHRP site class was determined based on the V_{s30} for analysis values. The following V_{s30} table was used: $A \geq 1500$ m/s $760 \leq B < 1500$ m/s $360 < C < 760$ m/s $180 < D \leq 360$ m/s $E \leq 180$ m/s
M	V_{s30} Code	The following hierarchy was used to assign a V_{s30} to each recording station. See Section 3.5.1 in AEA13 0 Measured velocity profile, $z_p \geq 30$m, where z_p is the profile depth (defined in column O) 1 Inferred from V_s profile, $10 < z_p < 30$m 2 a) Inferred from geology-based correlations calibrated for the region where the station is located and using geological map with relatively detailed descriptions of geological categories (e.g., distinguishing Quaternary alluvium based on texture and/or age). These maps are typically 1:500,000 scale or smaller. 2 b) Inferred from geology-based correlations that do not meet the criteria of 2a (e.g., lack of local calibration, relatively coarse geological mapping). 3 a) Inferred from geotechnical correlations (GMX, etc.) within its calibration region (i.e. CA). 3 b) Inferred from generalized geotechnical correlations (GMX, etc.) outside the calibration region. 4 Inferred from geomorphological proxies, including models based on: a) GMX+Elevation (Taiwan only, CEA08) b) Ground slope (i.e. WA07) c) Terrain-based categories (i.e. YEA12) 5 Inferred from local V_s mapping (e.g., microzonation maps).

PART III: Measured V_s (m/s)

N	V_{sz} (m/s)	Time-averaged shear wave velocity to profile depth z_p, for $z_p \leq 30$ m
O	Profile depth, z_p (m)	Maximum depth of V_s profile in m.
P	Measured V_{s30} (m/s) when $z_p > 30$ m; inferred from V_{sz} otherwise	Measured V_{s30} values if $z_p \geq 30$m and extrapolated values if $z_p < 30$m. See Section 3.3.2 in AEA13 for description of extrapolation procedures.
Q	PEA Profile No (Update Jan2012)	V_s profile numbers from PEA profile database.
R	Source of V_s profile	Defines the source of the V_s profile.

S	V_{s30} by Boore 2004 (m/s)	Estimations of V_{s30} when $z_p < 30$ from shallow velocity models using extrapolation procedure of B04. See Section 3.3.2 in AEA13 for applicability.
T	V_{s30} by Boore et al. 2011 (m/s)	Estimations of V_{s30} when $z_p < 30$ from shallow velocity models using extrapolation procedure of BEA11. See Section 3.3.2 in AEA13 for applicability.
U	Extrapolated V_{s30} (m/s)	Extrapolations from V_{sz} to V_{s30} values based on profile depths Boore's methods.
V	V_{s30} by Yu&Silva 2011 (m/s)	Estimations of V_{s30} when $z_p < 30$ from shallow velocity models using extrapolation procedure developed for SW China in unpublished report by Yu and Silva (2011).

PART IV: Geotechnical proxy

W	Geomatrix Site Code	Geomatrix three letter site classifications. Combination of GMX 1st, 2nd and 3rd letters. When any letter is not available, it is replaced by a "-".
X	Geomatrix Site Code: 3rd Letter	Geotechnical Subsurface Characteristics: A = Rock. Instrument on rock (V_s > 600 mps) or < 5m of soil over rock. B = Shallow (stiff) soil. Instrument on/in soil profile up to 20m thick overlying rock. C = Deep narrow soil. Instrument on/in soil profile at least 20m thick overlying rock, in a narrow canyon or valley no more than several km wide. D = Deep broad soil. Instrument on/in soil profile at least 20m thick overlying rock, in a broad valley. E = Soft deep soil. Instrument on/in deep soil profile with average Vs<150 mps CD = Deep soil site, valley dimensions not known. -999 = When it is not available.
Y	Inferred V_{s30} from Geomatrix Site Code	Inferred V_{s30} from GMX 3rd letter based on proxy analyses (CEA08). A regional fix is done for Class A for Japan only and an overall fix is done for Class E. For originally used inferred V_{s30} from GMX 3rd letter from PEA profile database: GMX 3rd letter A -- 659.6 m/s B -- 424.8 m/s C -- 338.6 m/s D -- 274.5 m/s E -- 191.3 m/s
Z	Sigma 3a	Uncertainties from proxy analysis for V_{s30} code 3a. See 'V_{s30} Code' for definition of 3a. See AEA13 Section 3.5.2.2b for further information on how the sigma was assigned.
AA	Sigma 3b	Uncertainties from proxy analysis for V_{s30} code 3b.
AB	C_3	Category assigned by Brian Chiou in lieu of GMX 3rd letter. Same as GMX 3rd letter, except a single category is used for C and D. See Appendix C in CY08a and for update see Section 3.4.1.2 in AEA13.
AC	Elevation (m)	Elevation of strong motion station (Taiwan only). From http://w3r2.ncree.narl.org.tw/ and Brian Chiou personal communication, 2012).
AD	V_{s30} Inferred (m/s)	Inferred V_{s30} from Geotechnical proxy supplemented with elevation, Taiwan only.

AE	V_{s30} Model for elevation, Taiwan (m/s)	Model for V_{s30} estimation based on both Geomatrix (GMX) 3rd letter categories and elevation. Applicable in Taiwan only.
AF	Sigma 4a	Uncertainties from proxy analysis for V_{s30} code 4a. See 'V_{s30} Code' for definition of 4a. See AEA13 Section 3.5.2.2b for further information on how the sigma was assigned.

PART V: Ground slopes and related proxies

AG	30 arc sec slope	Ground slope from Shuttle Radar Topography Mission (i.e. SRTM) 30 arcsec Digital Elevation Maps (i.e. DEMs). Provided by Wald and Quitoriano, personal communication 2012
AH	3 arc sec slope	Ground slope from SRTM 3 arcsec Digital Elevation Maps (i.e. DEMs). Provided by Wills and Guttierez, personal communication 2012, for CA sites
AI	Wald's estimate of V_{s30} (m/s)	Inferred V_{s30} from slope proxy for ACRs by WA07, using 30 arc sec slope.
AJ	Inferred V_{s30} from slope proxy (m/s)	Inferred V_{s30} from slope proxy for ACRs. PEER (Stewart and Seyhan) estimate using 30 arcsec slope and recommendations in WA07. Difference from Column AI is that the estimate is made by PEER instead of Wald group.
AK	Sigma 4b	Uncertainties from proxy analysis for V_{s30} code 4b. See 'V_{s30} Code' for definition of 4b. See AEA13 Section 3.5.2.2b for further information on how the sigma was assigned.

PART VI: Surface geology proxy

AL	Preferred Geology proxy V_{s30} (m/s)	Assigned V_{s30} values from Column "Slope Category Mean V_{s30}", if available, if not available then assigned from Column "Geology unit mean V_{s30}".
AM	Sigma 2a	Uncertainties from proxy analysis for V_{s30} code 2a. See 'V_{s30} Code' for definition of 2a. See AEA13 Section 3.5.2.2b for further information on how the sigma was assigned.
AN	Sigma 2b	Uncertainties from proxy analysis for V_{s30} code 2b.
AO	Geologic Description	Description of the geologic unit based on geologic maps that can be distinguished by their shear-wave velocity. For alluvium, a geographical description is used, e.g., alluvium is thin in narrow valleys and small basins. See Table 1 in WC06.
AP	Alternate geologic description	Brief description of profile characteristics from various sources, including Boore (2003: USGS OFR 03-191) for CA sites, Abrahamson et al. (1987: Earthquake Spectra, Vol 3, Issue 2) for SMART I sites, and Papaioannou (ITSAK, personal communication, 2003) for Greek sites. Not updated in NGA-West2 project.
AQ	Geology unit mean V_{s30} (m/s)	Mean V_{s30} from profiles within each geologic unit. From WC06
AR	Geology median V_{s30} (m/s)	Median V_{s30} from profiles within each geologic unit. From WC06
AS	Slope Category Mean V_{s30} (m/s)	Mean V_{s30} based on the slope category with 3 arc sec resolution DEMs. From WG08. See also AEA13 Section 3.4.1.1

PART VII: Terrain proxy

AT	Terrain category per IP07, from ArcGIS	Geomorphology-based terrain categories from SRTM 30 arc sec DEMs based on a terrain-based site conditions map using ArcGIS.
AU	Model V_{s30} for terrain categories (m/s)	Estimated V_{s30} in terrain categories. From YEA12. See also AEA13 Section 3.4.1.2.

AV	Sigma 4c	Uncertainties from proxy analysis for V_{s30} code 4c. See 'Vs30 Code' for definition of 4c. See AEA13 Section 3.5.2.2b for further information on how the sigma was assigned.

PART VIII: California/Japan 3D velocity and basin models

AW	Northern CA/Southern CA - H11 $Z_{1.0}$ (m)	Defines depth to V_s = 1.0 km/sec from 3-D velocity models or site profile. Sources used are -- ***SoCal***: Harvard Model (3D SCEC Community Velocity Model, http://scec.usc.edu/scecpedia/CVM-H; ***SFBA***: Aagard et al. (2010) ; ***Eel River basin***: Graves (1994); ***Any location***: depth from the PE&A Profile Data Base when a velocity of 1.0 km/sec (or similar) is encountered.
AX	Northern CA/Southern CA - H11 $Z_{1.5}$ (m)	Depth to V_s = 1.5 km/sec [See note for Northern CA/Southern CA - H11 Z_1 (m)].
AY	Northern CA/Southern CA - H11 $Z_{2.5}$ (m)	Depth to V_s = 2.5 km/sec [See note for Northern CA/Southern CA - H11 Z_1 (m)].
AZ	Northern CA/Southern CA - S4 $Z_{1.0}$ (m)	Defines depth to V_s = 1.0 km/sec from 3-D velocity models or site profile. Sources used are -- ***SoCal***: 3D SCEC Community Velocity Model, MEA00, Version 2.2b, http://scec.usc.edu/scecpedia/CVM-S); ***SFBA***: Aagard et al. (2010); ***Eel River basin***: Graves (1994); ***Any location***: depth from the PE&A Profile Data Base when a velocity of 1.0 km/s (or similar) is encountered.
BA	Northern CA/Southern CA - S4 $Z_{1.5}$ (m)	Depth to V_s = 1.5 km/sec [See note for Northern CA/Southern CA - S4 Z_1 (m)].
BB	Northern CA/Southern CA - S4 $Z_{2.5}$ (m)	Depth to V_s = 2.5 km/sec [See note for Northern CA/Southern CA - S4 Z_1 (m)].
BC	NIED-VS Minimum depth (m) to V_s=1000m/s	NIED seismic velocity models for minimum $Z_{1.0}$. Data from http://www.j-shis.bosai.go.jp/map/?lang=en (last accessed on 11/2/2011 by Rob Graves and Albert Kottke).
BD	NIED-VS Maximum depth (m) to V_s=1000m/s	For maximum $Z_{1.0}$ (See NIED-VS Minimum depth (m) to V_s = 1000m/s).
BE	NIED-VS Minimum depth (m) to V_s=1500m/s	NIED seismic velocity models for minimum $Z_{1.5}$.
BF	NIED-VS Maximum depth (m) to V_s=1500m/s	For maximum $Z_{1.0}$ (See NIED-VS Minimum depth (m) to V_s = 1500m/s).
BH	NIED-VS Minimum depth (m) to V_s=2500m/s	NIED seismic velocity models for minimum $Z_{2.5}$.
BI	NIED-VS Maximum depth (m) to V_s=2500m/s	For maximum $Z_{1.0}$ (See NIED-VS Minimum depth (m) to V_s = 2500m/s).

PART IX: Basin depth codes for SFBA, SoCal and Japan

BJ	Basin depth code for $Z_{1.0}$ *(0: Profile, 1: Aagard, 2: NIED, 3: SCEC CVM-S, 4: SCEC CVM-H)*	Identifier to indicate source of the preferred basin depth $Z_{1.0}$. We use profile-based depth where available (code 0), otherwise a local 3-D velocity model is used.
BK	Basin depth code for $Z_{1.5}$ *(0: Profile, 1: Aagard, 2: NIED, 3: SCEC CVM-S, 4: SCEC CVM-H)*	Identifier to indicate source of basin depth $Z_{1.5}$.
BL	Basin depth code for $Z_{2.5}$ *(0: Profile, 1: Aagard, 2: NIED, 3: SCEC CVM-S, 4: SCEC CVM-H)*	Identifier to indicate source of basin depth $Z_{2.5}$.

Appendix D: Flatfile Column Explanation

Column	Column Name (units)	Description
A	Record Sequence Number	An arbitrary unique number assigned to each strong-motion record in the flatfile for identification.
B	EQID	An arbitrary unique ID assigned to each earthquake for identification.
C	Earthquake Name	The common name of earthquake. The naming usually includes the name of the general area or country where earthquake occurred. In case of multiple earthquakes in the same general area/country (for example there are 8 earthquakes in the flatfile that are from Imperial Valley, CA), we used a number to distinguish between these events. Events with a numerical ID are from the NCSN or SCSN earthquake ID.
D	YEAR	Year of earthquake.
E	MODY	Month and Day (UTC) of earthquake.
F	HRMN	Origin time (UTC) of earthquake (Hour and Minute)
G	Station Name	The unique name of strong-motion station, which may differ slightly from data provider station name. When it is part of an array, a short phrase is sometimes added to indicate the location of the instrument (for example, "Rio Del Overpass E Ground" and "Rio Del Overpass W Ground").
H	Station Sequence Number	An arbitrary unique sequence number assigned to each strong-motion station for identification.
I	Station ID No.	Station ID assigned by data provider (USGS, CGS/CSMIP, etc.). When it is not available, Station ID is assigned a value of "-999".
J	Earthquake Magnitude	Moment magnitude of earthquake. When there are multiple reliable estimates of earthquake magnitude, the average value of the reliable estimates is used.
K	Magnitude Type	If the listed earthquake magnitude is NOT a moment magnitude, this column identifies the type of magnitude ML = local magnitude MS = surface-wave magnitude Mb = body wave magnitude U = unknown magnitude type (-999) = unknown
L	Magnitude Uncertainty: Kagan Model	Magnitude uncertainty assigned using Kagan's model (Kagan, 2002).
M	Magnitude Uncertainty: Statistical	Magnitude uncertainty is taken as the standard deviation of the reliable magnitude estimates.

N	Magnitude Sample Size	Number of magnitude estimates used to compute the standard deviation.
O	Magnitude Uncertainty: Study Class	Magnitude uncertainty is assigned by PE&A based on the quality of special studies that yielded the magnitude estimates and is defined as: 0.3 --> Older events not well studied 0.2 --> Older events well studied or recent events not well studied 0.1 --> Recent events well studied
P	Mo (dyne.cm)	Seismic moment calculated from earthquake magnitude, treating it as a moment magnitude (Mw) regardless of magnitude type; Log10(Mo) = 3/2 * Mw + 16.05
Q	Strike (deg)	Strike angle of the fault plane used to approximate the causative fault surface. 0^{o} <= Strike <= 360^{o}. Convention of fault strike, dip, and rake follows that described in Aki and Richards (1980, p106). (see Figure 2.1)
R	Dip (deg)	Dip angle of the fault plane. 0^{o} <= Dip <= 90^{o}. (see note above)
S	Rake Angle (deg)	Rake is the angle measured on the fault plane counterclockwise from the reference strike direction to the average slip direction (see figure 2.1). -180^{o} <= Rake <= 180^{o}
T	Mechanism Based on Rake Angle	Mechanism Class Rake Angles --- Strike - Slip 00 -180 < Rake < -150 -30 < Rake < 30 150 < Rake < 180 --- Normal 01 -120 < Rake < -60 --- Reverse 02 60 < Rake < 120 --- Reverse - Oblique 03 30 < Rake < 60 120 < Rake < 150 --- Normal - Oblique 04 -150 < Rake < -120 -60 < Rake < -30
U	P-plunge (deg)	This and the next 3 columns list the plunge and trend of the P- and T-axes. P- and T-axes are the maximum (P) and minimum (T) compressive principal stresses given by the fault plane solution. It is suggested that the plunge of the axes may be used to classify fault type, the advantage being that the classification may be more physically based than a simple classification based on rake angle (as the previous column), and furthermore the classification is not dependent on the choice of fault plane.
V	P-trend (deg)	(see note above)
W	T-plunge (deg)	(see note above)
X	T-trend (deg)	(see note above)
Y	Hypocenter Latitude (deg)	See NGA data report for hypocenter references.
Z	Hypocenter Longitude (deg)	See NGA data report for hypocenter references.
AA	Hypocenter Depth (km)	See NGA data report for hypocenter references.
AB	Coseismic Surface Rupture: 1=Yes; 0=No; 99=Unknown	Presence or absence of primary surface rupture.
AC	Coseismic Surface Rupture (Including	This column is mainly an effort to fill the 'Unknown' in the previous column with a value inferred from indirect evidence of surface rupture.

	Inferred)	
AD	Basis for Inference of Surface Rupture	sfdoc = the reference documents the presence or absence of surface faulting sfdis = surface faulting discussed in references locdis = location of earthquake discussed in references M<6 = Magnitude < 6.0, likelihood of existence of surface rupture is small M>7 = Magnitude > 7.0, likelihood of existence of surface rupture is large
AE	Finite Rupture Model: 1=Yes; 0=No	If 1, a geometric representation of the ruptured area was developed using observed surface rupture, published slip model(s), aftershock distribution (and time after mainshock), etc.
AF	Depth to Top Of Fault Rupture Model	Depth to the top of the finite rupture model (km). Datum is may be ground surface or sea level depending on source.
AG	Fault Rupture Length (km)	Total length ("L") of the finite rupture model
AH	Fault Rupture Width (km)	Width ("W") of the finite rupture model (= A / L)
AI	Fault Rupture Area (km^2)	Total area ("A") of the finite rupture model
AJ	Avg Fault Disp (cm)	The average amount of slip over the ruptured area. It's computed as Mo/(Mu*A*1.0E+10) where Mu=3.58e11.
AK	Rise Time (s)	The time required for the completion of slip at a point on the fault plane. When there are multiple estimates of rise time, the average value is used.
AL	Avg Slip Velocity (cm/sec)	Avg Slip Velocity = (Avg Fault Displacement) / (Rise time)
AM	Static Stress Drop (bars)	Static stress drop is calculated as 7/16*Mo/(A*1.0E+10/pi)^1.5/1.0E+06.
AN	Preferred Rupture Velocity (km/sec)	Rupture velocity (Vr) is the speed at which a rupture front moves along the fault during an earthquake. When there are multiple estimates of rupture velocity, the average value is used.
AO	Average Vr/Vs	Ratio of rupture velocity (Vr) to shear-wave velocity (Vs) in the source region. When there are multiple estimates, the average value is used.
AP	Percent of Moment Release in the Top 5 Km of Crust	This column is calculated from an appropriate slip model. See NGA data report for the slip model used for each earthquake.
AQ	Existence of Shallow Asperity: 0=No; 1=Yes	(see note below)
AR	Depth to Top of Shallowest Asperity (km)	An asperity is defined by Somerville et al. (1999) as a rectangular region in which the slip exceeds, in a specified way, the slip averaged over the entire fault rupture. If the depth of the top of the shallowest asperity was less than 5 km, the earthquake is classified as a shallow asperity event, and the "Existence of Shallow Asperity" column has a value of 1. If the depth of the top of the shallowest asperity was greater than 5 km, the earthquake is classified as a deep asperity event, and the "Existence of Shallow Asperity" column has a value of 0.
AS	Earthquake in Extensional Regime: 1=Yes; 0=No	Extensional regions are regions in which the lithosphere is expanding. Aside from obvious evidence of areal expansion, such as contemporary geodetic measurements and in situ stress measurement, extensional regimes usually present some or all of the following features: a mixture of normal faulting and strike slip earthquakes, recent volcanism, aligned volcanic features, lithospheric thinning, and high heat flow. (Text is excerpted from Spudich et al. (1997).)
AT	Fault Name	Name of the causative fault. It is taken from the fault database of the

		National Seismic Hazard Maps (Frankel et al., 2002)
AU	Slip Rate (mm/Yr)	Slip rate on the causative fault. It is taken from the fault database of the National Seismic Hazard Maps (Frankel et al., 2002).
AV	EpiD (km)	Distance from the recording site to the epicenter.
AW	HypD (km)	Distance from the recording site to the hypocenter.
AX	Joyner-Boore Dist. (km)	Shortest horizontal distance from the recording site to the vertical projection of the rupture on the surface
AY	Campbell R Dist. (km)	Shortest distance from the recording site to the seismogenic portion of the ruptured area (Campbell, 1997). This distance measure assumes that rupture within the near-surface sediment or the shallow portion of fault gouge is non-seismogenic. The depth below which rupture is seismogenic was estimated using updated guidelines from Campbell (personal communication).
AZ	RmsD (km)	Root-mean-squared distance
BA	ClstD (km)	Closest distance from the recording site to the ruptured fault area
BB	Rx (km)	Horizontal distance (km) from top edge of rupture. Measured perpendicular to the fault strike.
BC	FW/HW Indicators	This column mimics the FW/HW indicator defined in Abrahamson and Somerville (1996). hw: site is within hanging wall region fw: site is within the footwall region nu: site is in the neutral region na: not applicable as fault dip is greater than 70°
BD	Source to Site Azimuth (deg)	The (finite) source to site direction: It is the angle measured clockwise from the fault strike direction to the direction connecting the site and the site's closest point on the surface projection of top edge of fault. This column can be used an alternative to the FW/HW indicator given previously.
BE	X	Somerville et al. (1997) X parameter (nondimensional units). For multiple-segment faults calculated following a method of Boatwright (2007).
BF	Theta.D (deg)	Somerville et al. (1997) θ parameter (degrees). For multiple- segment faults calculated following a method of Boatwright (2007).
BG	SSGA (Strike Slip only)	Somerville et al. (1997) $X cos(\theta)$ parameter. For multiple-segment faults calculated following a method of Boatwright (2007) Calculated for sites within 50km (ClstD) of a strike-slip fault (mechanism = 0).
BH	Y	Somerville et al. (1997) Y parameter (nondimensional units). For multiple-segment faults calculated following a method of Boatwright (2007).
BI	Phi.D (deg)	Somerville et al. (1997) ϕ parameter (degrees). For multiple- segment faults calculated following a method of Boatwright (2007).
BJ	SSGA (Dip Slip)	Somerville et al. (1997) $Y cos(\phi)$ parameter (degrees). For multiple-segment faults calculated following a method of Boatwright (2007). Calculated for sites within 50km (ClstD) on the footwall (FW) or hanging wall (HW) of a dip-slip fault (mechanism not equat to 0).
BK	s (km)	s parameter in Spudich and Chiou (2008). s is the length of fault that ruptures toward site.
BL	d (km)	d parameter in Spudich and Chiou (2008). d is the width of fault that ruptures toward site.
BM	c.tilde.prime	$\tilde{c}'$ parameter in Spudich et al. (2004). The approximate isochrone velocity ratio, has an angular behavior similar to cos(Theta.D) and cos(Phi.D). To calculate c.tilde.prime, Vr/beta (Vs) is assumed to be 0.8 for all earthquakes.

		$\tilde{c}' = \left(\frac{\beta}{V_r} + D^{-1}(ClstD - HypD)\right)^{-1}, D > 0$ $\tilde{c}' = \frac{\beta}{V_r}, D = 0$
BN	m5	Obsolete, no longer used
BO	D (km)	D parameter in Spudich and Chiou (2008). Distance between hypocenter and Xc, the point on the fault plane closest to the site
BP	Rfn.Hyp	Amplitude at the site of a fault normal component of a point earthquake source at the event hypocenter.
BQ	Rfp.Hyp	Amplitude at the site of a fault parallel component of a point earthquake source at the event hypocenter.
BR	Rfn.Clst	Amplitude at the site of a fault normal component of a point earthquake source at the closest point on the fault, computed using the Spudich and Chiou (2008) Appendix A formalism.
BS	Rfp.Clst	Amplitude at the site of a fault parallel component of a point earthquake source at the closest point on the fault, computed using the Spudich and Chiou (2008) Appendix A formalism.
BT	Rfn.Imd	Obsolete, no longer used
BU	Rfp.Imd	Obsolete, no longer used
BV	GMX's C1	First Letter of Geomatrix's Site Classification: Instrument Housing -- Structure Type and Instrument Location. Descriptions included in Appendix D.
BW	GMX's C2	Second Letter of Geomatrix's Site Classification: Mapped Local Geology. Descriptions included in Appendix D.
BX	GMX's C3	Third Letter of Geomatrix's Site Classification: Geotechnical Subsurface Characteristics. Descriptions included in Appendix D.
BY	Campbell's GEOCODE	Site Classification defined by Campbell and Bozorgnia (2003), with suggested Vs30 from Wills and Silva (1998) and extended NEHRP site classes as defined by Wills et al., (2000). Descriptions included in Appendix D.
BZ	Bray and Rodriguez-Marek SGS	Site Classification defined by Bray and Rodriguez-Marek (1997; personal communication, 2003). Descriptions included in Appendix D.
CA	Depth	An assessment of 'soil depth' used in Bray and Rodriguez-Marek SGS. S = alluvium is shallower than 60 m D = alluvium is greater than 60 m
CB	Preferred NEHRP Based on Vs30	The preferred NEHRP site class was determined based on the preferred Vs 30 values. Descriptions included in Appendix D.
CC	Preferred Vs30 (m/sec)	Vs30 assignment hierarchy discussed in Section 3.5.1.
CD	not used	
CE	Measured/Inferred Class	This column identifies the source of the preferred Vs30. The numeric value is related to assignment hierarchy discussed in Section 3.5.1. If assignment is based on a numeric and character (e.g., 2a), it is translated into a numeric value 2.1.
CF	Sigma of Vs30 (in natural log units)	Uncertainty of Vs30. Sigma (standard deviation) values are estimated based on the source of the preferred Vs30 value and site category.
CG	NEHRP Classification from CGS's Site Condition Map	Extended NEHRP – UBC Site Classification for CA (Wills et al., 2000; Wills, personal communication (2003)). Descriptions included in Appendix D.
CH	Geological Unit	Currently this column is populated only for CA sites with information from California Geological Survey (CGS). For non-CA sites, this column is blank.
CI	Geology	A short description of geology from various sources.
CJ	Owner	Owner of strong-motion instrument/record. It is not necessarily the most recent owner.

CK	Station Latitude	From data provider, when available.
CL	Station Longitude	From data provider, when available.
CM	STORIES	Number of stories above ground.
CN	INSTLOC	Location of instrument in structure.
CO	Depth to Basement Rock	Campbell-Bozorgnia definition of sediment depth (text is excerpted from an e-mail written by Ken Campbell to Maury Power, dated 5/19/03). The general criteria used to estimate sediment depth can be described by the following: 1. Set D = 0 for a site categorized as Firm Rock (Hard Rock of Campbell, 1997). Firm Rock has a V_{s30} of around 817 + 365 m/sec for those sites for which a measured value of V_{s30} is available. These sites are located primarily in California. This V_{s30} corresponds approximately to NEHRP site class BC and stiffer according to the classification proposed by CGS (Wills et al., 2000). Geologically, Firm Rock can be defined as pre-Tertiary sedimentary rock and "hard" volcanic deposits, high-grade metamorphic rock, crystalline rock, and the "harder" units of the Franciscan Complex generally described as sandstone, greywacke, shale, chert, and greenstone. 2. Where the depth to Firm Rock is known, set D to that depth (e.g., in the LA Basin where a map showing the depth to basement complex (crystalline rock) is available or in the San Francisco Bay Area where depth to Franciscan or crystalline rock is available). 3. Where the depth to Firm Rock is not known but where basin depth can be inferred from gravity and/or density data, set D to that depth. 4. Where no other information is available, but a local or regional velocity model is available, set D to the depth corresponding to seismic basement (defined as V_p approximately equal to 5.0 km/sec or greater and/or V_s approximately equal to 2.9 km/sec or greater). 5. Where multiple types of information are available, judgment must be applied to determine the best estimate of D, roughly using the order of items 1-4 above as the priority assigned to each type of data.
CP	Site Visited	Site visited by geologist or engineer. This is a sparsely populated column; currently only sites in Southern California are populated.
CQ	NGA Type	Categories for V_{s30} estimation as defined in Borcherdt (personal communication, 2003; 1994, 2002) and Borcherdt and Fumal (2002) 1. Measured value at the station <300 m (a) USGS OFR, ROSRINE, Agbabian; (b) NUREG; (c) SASW; (d) Data gaps in V_{s30} record 2. Estimate based on velocities measured at nearby sites (< 1500 m distance) in same geologic unit; site visited by geologist 3. Estimate based on velocities measured at site in same geologic unit and judged to have similar materials; site visited by geologist 4. Estimate based on average velocity for the geologic unit; site visited by geologist 5. Estimate based on average velocity for the geologic unit where geologic unit is defined based on large-scale geologic/physical properties map (1:24,000 to 1:100,000 scale) 6. Estimate based on average velocity for the geologic unit where geologic

		unit is defined based on small-scale geologic map (1:250,000 to 1:750,000 scale) This is a sparsely populated column; currently only sites in Southern California are populated.
CR	Age	Geological age of surface material.
CS	Grain Size	Grain size of surface material: Aggregate, Coarse, or Fine.
CT	Depositional History	
CU	Z1 (m)	Depth to Vs=1.0 km/sec. This column is populated with stations within the 3-D velocity models of Southern California named CVM--S4 is the version 4 model developed by Harold Magistrale and others (http://scec.usc.edu/scecpedia/CVM--S), N. Cal (Aagaard), and the Eel River basin (Graves, 1994), with the addition of information from the PE&A Profile Data Base of depths to 1 km/sec, 1.5 km/sec and 2.5 km/sec when these velocities were measured at the site.
CV	Z1.5 (m)	Depth to Vs = 1.5 km/sec (see note for CU)
CW	Z2.5 (m)	Depth to Vs = 2.5 km/sec (see note for CU)
CX	Z1 (m)	Depth to Vs=1.0 km/sec. This column is populated with stations within the 3-D velocity models of S. Cal using CVM--H11.1.0 is the version 11.1.0 Harvard model developed by John Shaw and others (http://scec.usc.edu/scecpedia/CVM--H), N. Cal (Aagaard), and the Eel River basin (Graves, 1994), with the addition of information from the PE&A Profile Data Base of depths to 1 km/sec, 1.5 km/sec and 2.5 km/sec when these velocities were measured at the site.
CY	Z1.5 (m)	Depth to Vs = 1.5 km/sec (see note for CX)
CZ	Z2.5 (m)	Depth to Vs = 2.5 km/sec (see note for CX)
DA	Depth to Franciscan Rock (km)	This column is populated only for stations in the Bay Area.
DB	Basin	Name of the sedimentary basin. This column and the next 6 columns contain basin parameters defined and used in Joyner (2000) and Somerville et al. (2002). These columns are sparsely populated.
DC	h (m)	Depth to basement.
DD	hnorm (m)	= h / Rsbe.
DE	Rsbe (m)	Closest distance from the station to the basin edge.
DF	Rcebe (m)	Perpendicular distance from the station to the basin edge.
DG	Rebe (m)	Distance from the epicenter to the basin edge along a line between the epicenter and the station.
DH	Rsbe1 (m)	Distance from the station to the basin edge along a line between the epicenter and the station.
DI	File Name (Horizontal 1)	Directory name and file name of time history data files. Note that file name is made up of station abbreviation and instrument orientation. If the orientation is XXX then that component did not record the event.
DJ	File Name (Horizontal 2)	(Same as above)
DK	File Name (Vertical)	(Same as above)
DL	H1 component azimuth (degrees)	Azimuth (deg)
DM	H2 component azimuth (degrees)	Azimuth (deg)
DN	Type of Recording	A - Analog D - Digital A large portion of this column is not populated.

DO	Instrument Model	A large portion of this column is not populated.
DP	PEA Processing Flag	PEA: Acceleration time history record was processed using PE&A's standard processing procedure starting with the Volume 1 (uncorrected) time history ; #: Acceleration time history record is directly from the Volume 2 (corrected) accelerogram as received from the data provider (pass-through records), except for the ChiChi aftershocks records. In the case of ChiChi aftershocks, equivalents to the Volume 2 records were created by the NGA-West1 project.
DQ	Type of Filter	This column lists the type of filter used by PE&A or data providers (mainly USGS and CSMIP) to remove noise at long and short periods. O - Ormsby A - Acausal Butterworth C - Causal Butterworth
DR	npass	Number of passes of filter.
DS	nroll	This column lists the 'nroll' parameter of the Butterworth filter. -999 when not applicable (Ormsby filter).
DT	HP-H1 (Hz)	Corner frequency of the high-pass filter of component H1. 1. When this component is unavailable, corner frequency is -999. 2. If filter was not applied, corner frequency is 0 3. The definition of corner frequency varies with the filter type. In the case of a Butterworth filter, the corner frequency is the frequency at which the filter response is at -3db of the maximum response. In the case of an Ormsby filter, the corner frequency is the beginning point of the transition frequency band.
DU	HP-H2 (Hz)	Corner frequency of the high-pass filter of component H2. (see note for HP-H1)
DV	LP-H1 (Hz)	Corner frequency of the low-pass filter of component H1. (see note for HP-H1)
DW	LP-H2 (Hz)	Corner frequency of the low-pass filter of component H2. (see note for HP-H1)
DX	Factor	This column ("Factor") gives the ratio of the lowest usable frequency ("LUF") to the corner frequency ("HP") of the high-pass filter. The recommended lowest usable frequency is the frequency above which spectra from high-pass filtered data are relatively unaffected by the filter. For convenience, "LUF" is evaluated in terms of "Factor". "Factor" is determined according to the filter type and order of the filter. 1. When a Butterworth filter is used, "LUF" is taken as the frequency at which filter response is -0.5db down from the maximum response (or 94% of the maximum). "Factor" is then determined from the number of passes ("npass") and "nroll" of the Butterworth filter. 2. For Ormsby filter, "Factor" is 1. 3. When filter is not applied (blank "HP"), empirical relationship is used to determine "LUF" and the value for "Factor" becomes irrelevant.
DY	Lowest Usable Freq - H1 (Hz)	This column ("LUF") is the product of "HP-H1" and "Factor", except when "HP-H1" is -999 or 0. When "HP-H1" is -999, "LUF" is again -999. When "HP-H1" is 0, "LUF" is determined from an empirical relationship between "LUF" and earthquake magnitude and type of recording.
DZ	Lowest Usable Freq - H2 (Hz)	(see note above)
EA	Lowest Usable Freq - Ave. Component (Hz)	This column is the recommended lowest usable frequency for the average horizontal component. It is taken as the larger of the two previous columns. If any of the two previous columns is -999 (i.e., one or both of the two

		horizontal components did not record the event), this column is left blank.
EB	PGA (g)	This and the next 114 columns list the peak acceleration (PGA), peak velocity (PGV), peak displacement (PGD), and pseudo spectral accelerations (5%-damped) at 111 periods. 1. Listed ground-motion value may be the as recorded motions, RotDnn from Boore (2010), or GMRotI50 from Boore (2005). 2. Pseudo spectral acceleration and absolute acceleration are in units of g. 3. Ground-motion data for the CEOR records of the Kobe earthquake were left out of the flatfile. Interested users may acquire the ground-motion data directly from CEOR.
EC	PGV (cm/sec)	
ED	PGD (cm)	
EE	T0.010S	
……..	……..	
IK	T20.000S	
IL	Ave Strike (deg)	
IM	TYPE(CRjb = 0)	Fault classification using a CRjb distance = 0. C1 are class 1 events and C2 are class 2 events. See Section 2.6 for more details.
IN	CRjb	CRjb for the class 2 events in column IM (km)
IO	TYPE (Rjb = 2)	Fault classification using a CRjb distance = 2 km. C1 are class 1 events and C2 are class 2 events.
IP	CRjb	CRjb for the class 2 events in column IO (km)
IQ	TYPE (Rjb = 5)	Fault classification using a CRjb distance = 5 km. C1 are class 1 events and C2 are class 2 events.
IR	CRjb	CRjb for the class 2 events in column IQ (km)
IS	TYPE (Rjb = 10)	Fault classification using a CRjb distance = 10 km. C1 are class 1 events and C2 are class 2 events.
IT	CRjb	CRjb for the class 2 events in column IS (km)
IU	TYPE (Rjb = 20)	Fault classification using a CRjb distance = 20 km. C1 are class 1 events and C2 are class 2 events.
IV	CRjb	CRjb for the class 2 events in column IU (km)
IW	TYPE (Rjb = 40)	Fault classification using a CRjb distance = 40 km. C1 are class 1 events and C2 are class 2 events.
IX	CRjb	CRjb for the class 2 events in column IW (km)
IY	U	Generalized U Coordinate at the site, produced using the algorithm in Appendix A of Spudich and Chiou (2008)
IZ	IDP	Isochrone Directivity Parameter, produced using the algorithm in Appendix A of Spudich and Chiou (2008).
JA	XCI (ξ⍰)	Directivity Parameter, B. Rowshandel (using the methodology presented in the NGA-W2 Task-1 Report on Directivity)
JB	XCI1 (ξ1)	Directivity Parameter, B. Rowshandel (using the methodology presented in the NGA-W2 Task-1 Report on Directivity)
JC	Damping (%)	Damping values used are 0.5, 1, 2, 3, 5, 7, 10, 15, 20, 25, 30
JD	RotD fractile	Fractiles used are 00, 50, 100.
JE	Instrument Natural Frequency (Hz)	This and the following two columns (JG-JI) are instrument information for stations used in the California small-to-moderate magnitude data processing.
JF	Instrument Damping	As decimal.
JG	Instrument Type	‘A’ for acceleration time history. ‘V’ for a velocity time history.
JH	Quality Flag	Judgment on the quality of the time history recording
JI	Spectral Quality Flag	Judgment on the quality of the spectra
JJ	Late S-trigger	See Table 6.1 for flag explanation.
JK	Late P-trigger	See Table 6.1 for flag explanation.

JL	Idirectivity	Pulse-like (1) or non-pulse-like (0) indicator determined using the method presented in Shahi and Baker (in preparation)
JM	Tp	The pseudo-period of the extracted pulse using the method presented in Shahi and Baker (in preparation.)
JN	Ry	Horizontal distance (km) from the top edge of the rupture, measure along fault strike.

Appendix E: Site Classification Definitions

GMX First Letter	Instrument Structure Type
I	Free-field instrument or instrument shelter. Instrument is located at or within several feet of the ground surface, and not adjacent to any structure.
A	One-story structure of lightweight construction. Instrument is located at the lowest level and within several feet of the ground surface.
B	Two- to four-story structure of lightweight construction, or very large tall) one-story warehouse-type building. Instrument is located at the lowest level and within several feet of the ground surface. Also, Haviland Hall and Mt. Hamilton Lick Observatory are two-story buildings founded on rock. The instrumentation is in a vault with the instrument founded on rock at these two BDSN stations.
A,B	Used for small generally lightweight structures for which we cannot determine the number of stories from the available information. These sites generally have COSMOS site code 4 which defines a reference station described as either a 1- or 2-story, small, light building. This classification is mainly used in the small-moderate magnitude data set.
C	One- to four-story structure of lightweight construction. Instrument is located at the lowest level in a basement and below the ground surface.
D	Five or more story structure of heavy construction. Instrument is located at the lowest level and within several feet of the ground surface.
E	Five or more story structure of heavy construction. Instrument is located at the lowest level in a basement and below the ground surface.
F	Structure housing instrument is buried below the ground surface about 1-2 m, at a shallow depth. e.g., tunnel or seismic vault (e.g., U. S. Array design) but shallow embedment (use 'T' for deeper embedments or 'V' for deeply embedded vaults, both not considered "free-field")
I,F	These sites generally have COSMOS site code 3 for which the sensors have been buried/set in ground at shallow or near surface depths (e.g., the U. S. Array station design). This classification is mainly used in the small-moderate magnitude western and EUS data sets.
G	Structure of light or heavyweight construction, instrument not at lowest level.
H	Dam either earth or concrete (station at toe of embankment or on abutment).
J	Concrete Dam structural instrumentation (none in data base).

K	Near a one-story structure of lightweight construction. Instrument is located outside on the ground surface, within approximately 3 m from the structure.
L	Near a two- to four-story structure. Instrument is located outside on the ground surface, within approximately 6 m of the structure.
M	Near a two- to four-story structure with basement. Instrument is located outside on the ground surface, within approximately 6 m of the structure.
N	Near a five- to eight-story structure. Instrument is located outside on the ground surface, within approximately 10 m of the structure.
O	Near a five- to eight-story structure with basement. Instrument is located outside on the ground surface, within approximately 10 m of the structure.
P	Castle of masonry construction, massive 1-3 stories
Q	Associated with a structure, size of structure is not known
S	Associated with a structure and in the basement, size of structure is not known.
T	Associated with a deep tunnel, e.g., a) L'Aquila - Parking: Pleistocene terrace above a pedestrian tunnel on the edge's slope of the terrace, nearby structure to the station is a car park. b) Various BDSN stations (e.g., WDC, WENL, YBH).
U	Il Moro is on an embankment between two roads and retaining walls.
V	Deeply embedded seismic vault
W	Structural response e.g., roof, penstock, etc. (e.g., CSMIP 23732, San Bernardino - Devil's Canyon Penstock)
Z	At depth in borehole or missile silo

GMX Second Letter	Mapped local geology sedimentary or metasedimentary
H	Holocene (Recent) Quaternary (< 11,000 ybp).
Q	Pleistocene Quaternary (< 1.8my bp).
P	Pliocene Tertiary (< 5my bp).
M	Miocene Tertiary (< 24my bp).
O	Oligocene Tertiary (< 34my bp).
E	Eocene Tertiary (< 55my bp).
L	Paleocene Tertiary (< 65my bp).
K	Cretaceous (< 144my bp).
F	Franciscan Formation (Cretaceous/Late Jurassic).
J	Jurassic (< 206my bp).
T	Triassic (<248my bp).
Z	Permian or older (> 248my bp). Igneous or meta-igneous:
V	Volcanic (extrusive).
N	Intrusive.
G	Granitic.

GMX Third Letter	Geotechnical subsurface characteristics
A	Rock. Instrument on rock (Vs > 600 mps) or < 5m of soil over rock.
B	Shallow (stiff) soil. Instrument on/in soil profile up to 20m thick overlying rock.
C	Deep narrow soil. Instrument on/in soil profile at least 20m thick overlying rock, in a narrow canyon or valley no more than several km wide.
D	Deep broad soil. Instrument on/in soil profile at least 20m thick overlying rock, in a broad valley.
E	Soft deep soil. Instrument on/in deep soil profile with average Vs < 150 mps.
CD	Deep soil site, valley dimensions not known.

For many Italian events, the third letter is followed by a "*". This denotes classifications inferred from local geology information provided with the unprocessed data

GMX Third Letter (number)	Central Weather Bureau (CWB) of Taiwan Site Categories
1	Hard site.
2	Medium site.
3	Soft soil site.

Campbell's GEOCODE	Description
A	Firm Soil: Holocene; recent alluvium, alluvial fans, undifferentiated Quaternary deposits., Vs30 298±92 m/sec; NEHRP D
B	Very Firm Soil: Pleistocene; older alluvium or terrace deposits. Vs30 368±80 m/sec; NEHRP CD
C	Soft Rock: Sedimentary rock, soft volcanic deposits of Tertiary age, “softer” Franciscan, low grade metamorphic rocks such as mélange, serpentine, schist. Vs30 421±109 m/sec; NEHRP CD
D	Firm Rock: Older sedimentary rock and hard volcanic deposits, high grade metamorphic rock, crystalline rock, “harder” Franciscan Vs30 830±339 m/sec; NEHRP BC
E	Shallow Soils (10 m deep)
F	Extremely soft or loose Holocene age soils such as beach sand or recent floodplain, lake, swamp estuarine, and delta deposits.

Bray and Rodriguez-Marek SGS	Description	Comments
A	HARD ROCK	Hard, strong, intact rock; Vs30 1500 m/sec
B	ROCK	Most “unweathered” California rock cases (Vs30 760 m/sec or < 6 m of weathered rock or soil).
C	WEATHERED SOFT ROCK/ SHALLOW STIFF SOIL	Weathered rock zone > 6 m and < 60 m (Vs30 > 360 m/s increasing to > 700 m/sec); Soil depth < 60 m
D	DEEP STIFF SOIL	Soil depth > 60 m and < 3 m of soft soils
E	SOFT CLAY	Thickness of soft clay > 3 m
F	SPECIAL	Potentially Liquefiable Sand or peat: Holocene loose sand with high water table (zw £ 6 m) or organic peat.
U	Unknown Conditions	Unknown Conditions

NEHRP site classification	Average shear-wave velocity to a depth of 30 m
A	> 1500 m/sec
B	760 m/sec- 1500 m/sec
C	360 m/sec– 760 m/sec
D	180 m/sec – 360 m/sec
E	< 180 m/sec

PEER REPORTS

PEER reports are available as a free PDF download from http://peer.berkeley.edu/publications/peer_reports_complete.html. Printed hard copies of PEER reports can be ordered directly from our printer by following the instructions at http://peer.berkeley.edu/publications/peer_reports.html. For other related questions about the PEER Report Series, contact the Pacific Earthquake Engineering Research Center, 325 Davis Hall mail code 1792, Berkeley, CA 94720. Tel.: (510) 642-3437; Fax: (510) 665-1655; Email: peer_editor@berkeley.edu

PEER 2013/03 *PEER NGA-West2 Database.* Timothy D. Ancheta, Robert B. Darragh, Jonathan P. Stewart, Emel Seyhan, Walter J. Silva, Brian S.J. Chiou, Katie E. Wooddell, Robert W. Graves, Albert R. Kottke, David M. Boore, Tadahiro Kishida, and Jennifer L. Donahue. May 2013.

PEER 2013/02 *Hybrid Simulation of the Seismic Response of Squat Reinforced Concrete Shear Walls.* Catherine A. Whyte and Bozidar Stojadinovic. May 2013.

PEER 2013/01 *Housing Recovery in Chile: A Qualitative Mid-program Review.* Mary C. Comerio. February 2013.

PEER 2012/08 *Guidelines for Estimation of Shear Wave Velocity.* Bernard R. Wair, Jason T. DeJong, and Thomas Shantz. December 2012.

PEER 2012/07 *Earthquake Engineering for Resilient Communities: 2012 PEER Internship Program Research Report Collection.* Heidi Tremayne (Editor), Stephen A. Mahin (Editor), Collin Anderson, Dustin Cook, Michael Erceg, Carlos Esparza, Jose Jimenez, Dorian Krausz, Andrew Lo, Stephanie Lopez, Nicole McCurdy, Paul Shipman, Alexander Strum, Eduardo Vega. December 2012.

PEER 2012/06 *Fragilities for Precarious Rocks at Yucca Mountain.* Matthew D. Purvance, Rasool Anooshehpoor, and James N. Brune. December 2012.

PEER 2012/05 *Development of Simplified Analysis Procedure for Piles in Laterally Spreading Layered Soils.* Christopher R. McGann, Pedro Arduino, and Peter Mackenzie–Helnwein. December 2012.

PEER 2012/04 *Unbonded Pre-Tensioned Columns for Bridges in Seismic Regions.* Phillip M. Davis, Todd M. Janes, Marc O. Eberhard, and John F. Stanton. December 2012.

PEER 2012/03 *Experimental and Analytical Studies on Reinforced Concrete Buildings with Seismically Vulnerable Beam-Column Joints.* Sangjoon Park and Khalid M. Mosalam. October 2012.

PEER 2012/02 *Seismic Performance of Reinforced Concrete Bridges Allowed to Uplift during Multi-Directional Excitation.* Andres Oscar Espinoza and Stephen A. Mahin. July 2012.

PEER 2012/01 *Spectral Damping Scaling Factors for Shallow Crustal Earthquakes in Active Tectonic Regions.* Sanaz Rezaeian, Yousef Bozorgnia, I. M. Idriss, Kenneth Campbell, Norman Abrahamson, and Walter Silva. July 2012.

PEER 2011/10 *Earthquake Engineering for Resilient Communities: 2011 PEER Internship Program Research Report Collection.* Eds. Heidi Faison and Stephen A. Mahin. December 2011.

PEER 2011/09 *Calibration of Semi-Stochastic Procedure for Simulating High-Frequency Ground Motions.* Jonathan P. Stewart, Emel Seyhan, and Robert W. Graves. December 2011.

PEER 2011/08 *Water Supply in regard to Fire Following Earthquake.* Charles Scawthorn. November 2011.

PEER 2011/07 *Seismic Risk Management in Urban Areas. Proceedings of a U.S.-Iran-Turkey Seismic Workshop.* September 2011.

PEER 2011/06 *The Use of Base Isolation Systems to Achieve Complex Seismic Performance Objectives.* Troy A. Morgan and Stephen A. Mahin. July 2011.

PEER 2011/05 *Case Studies of the Seismic Performance of Tall Buildings Designed by Alternative Means.* Task 12 Report for the Tall Buildings Initiative. Jack Moehle, Yousef Bozorgnia, Nirmal Jayaram, Pierson Jones, Mohsen Rahnama, Nilesh Shome, Zeynep Tuna, John Wallace, Tony Yang, and Farzin Zareian. July 2011.

PEER 2011/04 *Recommended Design Practice for Pile Foundations in Laterally Spreading Ground.* Scott A. Ashford, Ross W. Boulanger, and Scott J. Brandenberg. June 2011.

PEER 2011/03 *New Ground Motion Selection Procedures and Selected Motions for the PEER Transportation Research Program.* Jack W. Baker, Ting Lin, Shrey K. Shahi, and Nirmal Jayaram. March 2011.

PEER 2011/02 *A Bayesian Network Methodology for Infrastructure Seismic Risk Assessment and Decision Support.* Michelle T. Bensi, Armen Der Kiureghian, and Daniel Straub. March 2011.

PEER 2011/01 *Demand Fragility Surfaces for Bridges in Liquefied and Laterally Spreading Ground.* Scott J. Brandenberg, Jian Zhang, Pirooz Kashighandi, Yili Huo, and Minxing Zhao. March 2011.

PEER 2010/05 *Guidelines for Performance-Based Seismic Design of Tall Buildings.* Developed by the Tall Buildings Initiative. November 2010.

PEER 2010/04 *Application Guide for the Design of Flexible and Rigid Bus Connections between Substation Equipment Subjected to Earthquakes.* Jean-Bernard Dastous and Armen Der Kiureghian. September 2010.

PEER 2010/03 *Shear Wave Velocity as a Statistical Function of Standard Penetration Test Resistance and Vertical Effective Stress at Caltrans Bridge Sites.* Scott J. Brandenberg, Naresh Bellana, and Thomas Shantz. June 2010.

PEER 2010/02 *Stochastic Modeling and Simulation of Ground Motions for Performance-Based Earthquake Engineering.* Sanaz Rezaeian and Armen Der Kiureghian. June 2010.

PEER 2010/01 *Structural Response and Cost Characterization of Bridge Construction Using Seismic Performance Enhancement Strategies.* Ady Aviram, Božidar Stojadinović, Gustavo J. Parra-Montesinos, and Kevin R. Mackie. March 2010.

PEER 2009/03 *The Integration of Experimental and Simulation Data in the Study of Reinforced Concrete Bridge Systems Including Soil-Foundation-Structure Interaction.* Matthew Dryden and Gregory L. Fenves. November 2009.

PEER 2009/02 *Improving Earthquake Mitigation through Innovations and Applications in Seismic Science, Engineering, Communication, and Response. Proceedings of a U.S.-Iran Seismic Workshop.* October 2009.

PEER 2009/01 *Evaluation of Ground Motion Selection and Modification Methods: Predicting Median Interstory Drift Response of Buildings.* Curt B. Haselton, Ed. June 2009.

PEER 2008/10 *Technical Manual for Strata.* Albert R. Kottke and Ellen M. Rathje. February 2009.

PEER 2008/09 *NGA Model for Average Horizontal Component of Peak Ground Motion and Response Spectra.* Brian S.-J. Chiou and Robert R. Youngs. November 2008.

PEER 2008/08 *Toward Earthquake-Resistant Design of Concentrically Braced Steel Structures.* Patxi Uriz and Stephen A. Mahin. November 2008.

PEER 2008/07 *Using OpenSees for Performance-Based Evaluation of Bridges on Liquefiable Soils.* Stephen L. Kramer, Pedro Arduino, and HyungSuk Shin. November 2008.

PEER 2008/06 *Shaking Table Tests and Numerical Investigation of Self-Centering Reinforced Concrete Bridge Columns.* Hyung IL Jeong, Junichi Sakai, and Stephen A. Mahin. September 2008.

PEER 2008/05 *Performance-Based Earthquake Engineering Design Evaluation Procedure for Bridge Foundations Undergoing Liquefaction-Induced Lateral Ground Displacement.* Christian A. Ledezma and Jonathan D. Bray. August 2008.

PEER 2008/04 *Benchmarking of Nonlinear Geotechnical Ground Response Analysis Procedures.* Jonathan P. Stewart, Annie On-Lei Kwok, Yousseff M. A. Hashash, Neven Matasovic, Robert Pyke, Zhiliang Wang, and Zhaohui Yang. August 2008.

PEER 2008/03 *Guidelines for Nonlinear Analysis of Bridge Structures in California.* Ady Aviram, Kevin R. Mackie, and Božidar Stojadinović. August 2008.

PEER 2008/02 *Treatment of Uncertainties in Seismic-Risk Analysis of Transportation Systems.* Evangelos Stergiou and Anne S. Kiremidjian. July 2008.

PEER 2008/01 *Seismic Performance Objectives for Tall Buildings.* William T. Holmes, Charles Kircher, William Petak, and Nabih Youssef. August 2008.

PEER 2007/12 *An Assessment to Benchmark the Seismic Performance of a Code-Conforming Reinforced Concrete Moment-Frame Building.* Curt Haselton, Christine A. Goulet, Judith Mitrani-Reiser, James L. Beck, Gregory G. Deierlein, Keith A. Porter, Jonathan P. Stewart, and Ertugrul Taciroglu. August 2008.

PEER 2007/11 *Bar Buckling in Reinforced Concrete Bridge Columns.* Wayne A. Brown, Dawn E. Lehman, and John F. Stanton. February 2008.

PEER 2007/10 *Computational Modeling of Progressive Collapse in Reinforced Concrete Frame Structures.* Mohamed M. Talaat and Khalid M. Mosalam. May 2008.

PEER 2007/09 *Integrated Probabilistic Performance-Based Evaluation of Benchmark Reinforced Concrete Bridges.* Kevin R. Mackie, John-Michael Wong, and Božidar Stojadinović. January 2008.

PEER 2007/08 *Assessing Seismic Collapse Safety of Modern Reinforced Concrete Moment-Frame Buildings.* Curt B. Haselton and Gregory G. Deierlein. February 2008.

PEER 2007/07 *Performance Modeling Strategies for Modern Reinforced Concrete Bridge Columns.* Michael P. Berry and Marc O. Eberhard. April 2008.

PEER 2007/06 *Development of Improved Procedures for Seismic Design of Buried and Partially Buried Structures.* Linda Al Atik and Nicholas Sitar. June 2007.

PEER 2007/05 *Uncertainty and Correlation in Seismic Risk Assessment of Transportation Systems.* Renee G. Lee and Anne S. Kiremidjian. July 2007.

PEER 2007/04 *Numerical Models for Analysis and Performance-Based Design of Shallow Foundations Subjected to Seismic Loading.* Sivapalan Gajan, Tara C. Hutchinson, Bruce L. Kutter, Prishati Raychowdhury, José A. Ugalde, and Jonathan P. Stewart. May 2008.

PEER 2007/03 *Beam-Column Element Model Calibrated for Predicting Flexural Response Leading to Global Collapse of RC Frame Buildings.* Curt B. Haselton, Abbie B. Liel, Sarah Taylor Lange, and Gregory G. Deierlein. May 2008.

PEER 2007/02 *Campbell-Bozorgnia NGA Ground Motion Relations for the Geometric Mean Horizontal Component of Peak and Spectral Ground Motion Parameters.* Kenneth W. Campbell and Yousef Bozorgnia. May 2007.

PEER 2007/01 *Boore-Atkinson NGA Ground Motion Relations for the Geometric Mean Horizontal Component of Peak and Spectral Ground Motion Parameters.* David M. Boore and Gail M. Atkinson. May. May 2007.

PEER 2006/12 *Societal Implications of Performance-Based Earthquake Engineering.* Peter J. May. May 2007.

PEER 2006/11 *Probabilistic Seismic Demand Analysis Using Advanced Ground Motion Intensity Measures, Attenuation Relationships, and Near-Fault Effects.* Polsak Tothong and C. Allin Cornell. March 2007.

PEER 2006/10 *Application of the PEER PBEE Methodology to the I-880 Viaduct.* Sashi Kunnath. February 2007.

PEER 2006/09 *Quantifying Economic Losses from Travel Forgone Following a Large Metropolitan Earthquake.* James Moore, Sungbin Cho, Yue Yue Fan, and Stuart Werner. November 2006.

PEER 2006/08 *Vector-Valued Ground Motion Intensity Measures for Probabilistic Seismic Demand Analysis*. Jack W. Baker and C. Allin Cornell. October 2006.

PEER 2006/07 *Analytical Modeling of Reinforced Concrete Walls for Predicting Flexural and Coupled–Shear-Flexural Responses.* Kutay Orakcal, Leonardo M. Massone, and John W. Wallace. October 2006.

PEER 2006/06 *Nonlinear Analysis of a Soil-Drilled Pier System under Static and Dynamic Axial Loading.* Gang Wang and Nicholas Sitar. November 2006.

PEER 2006/05 *Advanced Seismic Assessment Guidelines.* Paolo Bazzurro, C. Allin Cornell, Charles Menun, Maziar Motahari, and Nicolas Luco. September 2006.

PEER 2006/04 *Probabilistic Seismic Evaluation of Reinforced Concrete Structural Components and Systems.* Tae Hyung Lee and Khalid M. Mosalam. August 2006.

PEER 2006/03 *Performance of Lifelines Subjected to Lateral Spreading.* Scott A. Ashford and Teerawut Juirnarongrit. July 2006.

PEER 2006/02 *Pacific Earthquake Engineering Research Center Highway Demonstration Project.* Anne Kiremidjian, James Moore, Yue Yue Fan, Nesrin Basoz, Ozgur Yazali, and Meredith Williams. April 2006.

PEER 2006/01 *Bracing Berkeley. A Guide to Seismic Safety on the UC Berkeley Campus.* Mary C. Comerio, Stephen Tobriner, and Ariane Fehrenkamp. January 2006.

PEER 2005/16 *Seismic Response and Reliability of Electrical Substation Equipment and Systems*. Junho Song, Armen Der Kiureghian, and Jerome L. Sackman. April 2006.

PEER 2005/15 *CPT-Based Probabilistic Assessment of Seismic Soil Liquefaction Initiation.* R. E. S. Moss, R. B. Seed, R. E. Kayen, J. P. Stewart, and A. Der Kiureghian. April 2006.

PEER 2005/14 *Workshop on Modeling of Nonlinear Cyclic Load-Deformation Behavior of Shallow Foundations.* Bruce L. Kutter, Geoffrey Martin, Tara Hutchinson, Chad Harden, Sivapalan Gajan, and Justin Phalen. March 2006.

PEER 2005/13 *Stochastic Characterization and Decision Bases under Time-Dependent Aftershock Risk in Performance-Based Earthquake Engineering.* Gee Liek Yeo and C. Allin Cornell. July 2005.

PEER 2005/12 *PEER Testbed Study on a Laboratory Building: Exercising Seismic Performance Assessment.* Mary C. Comerio, editor. November 2005.

PEER 2005/11 *Van Nuys Hotel Building Testbed Report: Exercising Seismic Performance Assessment.* Helmut Krawinkler, editor. October 2005.

PEER 2005/10 *First NEES/E-Defense Workshop on Collapse Simulation of Reinforced Concrete Building Structures.* September 2005.

PEER 2005/09 *Test Applications of Advanced Seismic Assessment Guidelines.* Joe Maffei, Karl Telleen, Danya Mohr, William Holmes, and Yuki Nakayama. August 2006.

PEER 2005/08 *Damage Accumulation in Lightly Confined Reinforced Concrete Bridge Columns.* R. Tyler Ranf, Jared M. Nelson, Zach Price, Marc O. Eberhard, and John F. Stanton. April 2006.

PEER 2005/07 *Experimental and Analytical Studies on the Seismic Response of Freestanding and Anchored Laboratory Equipment.* Dimitrios Konstantinidis and Nicos Makris. January 2005.

PEER 2005/06 *Global Collapse of Frame Structures under Seismic Excitations.* Luis F. Ibarra and Helmut Krawinkler. September 2005.

PEER 2005//05 *Performance Characterization of Bench- and Shelf-Mounted Equipment.* Samit Ray Chaudhuri and Tara C. Hutchinson. May 2006.

PEER 2005/04 *Numerical Modeling of the Nonlinear Cyclic Response of Shallow Foundations.* Chad Harden, Tara Hutchinson, Geoffrey R. Martin, and Bruce L. Kutter. August 2005.

PEER 2005/03 *A Taxonomy of Building Components for Performance-Based Earthquake Engineering.* Keith A. Porter. September 2005.

PEER 2005/02 *Fragility Basis for California Highway Overpass Bridge Seismic Decision Making.* Kevin R. Mackie and Božidar Stojadinović. June 2005.

PEER 2005/01 *Empirical Characterization of Site Conditions on Strong Ground Motion.* Jonathan P. Stewart, Yoojoong Choi, and Robert W. Graves. June 2005.

PEER 2004/09 *Electrical Substation Equipment Interaction: Experimental Rigid Conductor Studies.* Christopher Stearns and André Filiatrault. February 2005.

PEER 2004/08 *Seismic Qualification and Fragility Testing of Line Break 550-kV Disconnect Switches.* Shakhzod M. Takhirov, Gregory L. Fenves, and Eric Fujisaki. January 2005.

PEER 2004/07 *Ground Motions for Earthquake Simulator Qualification of Electrical Substation Equipment.* Shakhzod M. Takhirov, Gregory L. Fenves, Eric Fujisaki, and Don Clyde. January 2005.

PEER 2004/06 *Performance-Based Regulation and Regulatory Regimes.* Peter J. May and Chris Koski. September 2004.

PEER 2004/05 *Performance-Based Seismic Design Concepts and Implementation: Proceedings of an International Workshop.* Peter Fajfar and Helmut Krawinkler, editors. September 2004.

PEER 2004/04 *Seismic Performance of an Instrumented Tilt-up Wall Building.* James C. Anderson and Vitelmo V. Bertero. July 2004.

PEER 2004/03 *Evaluation and Application of Concrete Tilt-up Assessment Methodologies.* Timothy Graf and James O. Malley. October 2004.

PEER 2004/02 *Analytical Investigations of New Methods for Reducing Residual Displacements of Reinforced Concrete Bridge Columns.* Junichi Sakai and Stephen A. Mahin. August 2004.

PEER 2004/01 *Seismic Performance of Masonry Buildings and Design Implications.* Kerri Anne Taeko Tokoro, James C. Anderson, and Vitelmo V. Bertero. February 2004.

PEER 2003/18 *Performance Models for Flexural Damage in Reinforced Concrete Columns.* Michael Berry and Marc Eberhard. August 2003.

PEER 2003/17 *Predicting Earthquake Damage in Older Reinforced Concrete Beam-Column Joints.* Catherine Pagni and Laura Lowes. October 2004.

PEER 2003/16 *Seismic Demands for Performance-Based Design of Bridges.* Kevin Mackie and Božidar Stojadinović. August 2003.

PEER 2003/15 *Seismic Demands for Nondeteriorating Frame Structures and Their Dependence on Ground Motions.* Ricardo Antonio Medina and Helmut Krawinkler. May 2004.

PEER 2003/14 *Finite Element Reliability and Sensitivity Methods for Performance-Based Earthquake Engineering.* Terje Haukaas and Armen Der Kiureghian. April 2004.

PEER 2003/13 *Effects of Connection Hysteretic Degradation on the Seismic Behavior of Steel Moment-Resisting Frames.* Janise E. Rodgers and Stephen A. Mahin. March 2004.

PEER 2003/12 *Implementation Manual for the Seismic Protection of Laboratory Contents: Format and Case Studies.* William T. Holmes and Mary C. Comerio. October 2003.

PEER 2003/11 *Fifth U.S.-Japan Workshop on Performance-Based Earthquake Engineering Methodology for Reinforced Concrete Building Structures.* February 2004.

PEER 2003/10 *A Beam-Column Joint Model for Simulating the Earthquake Response of Reinforced Concrete Frames.* Laura N. Lowes, Nilanjan Mitra, and Arash Altoontash. February 2004.

PEER 2003/09	*Sequencing Repairs after an Earthquake: An Economic Approach.* Marco Casari and Simon J. Wilkie. April 2004.
PEER 2003/08	*A Technical Framework for Probability-Based Demand and Capacity Factor Design (DCFD) Seismic Formats.* Fatemeh Jalayer and C. Allin Cornell. November 2003.
PEER 2003/07	*Uncertainty Specification and Propagation for Loss Estimation Using FOSM Methods.* Jack W. Baker and C. Allin Cornell. September 2003.
PEER 2003/06	*Performance of Circular Reinforced Concrete Bridge Columns under Bidirectional Earthquake Loading.* Mahmoud M. Hachem, Stephen A. Mahin, and Jack P. Moehle. February 2003.
PEER 2003/05	*Response Assessment for Building-Specific Loss Estimation.* Eduardo Miranda and Shahram Taghavi. September 2003.
PEER 2003/04	*Experimental Assessment of Columns with Short Lap Splices Subjected to Cyclic Loads.* Murat Melek, John W. Wallace, and Joel Conte. April 2003.
PEER 2003/03	*Probabilistic Response Assessment for Building-Specific Loss Estimation.* Eduardo Miranda and Hesameddin Aslani. September 2003.
PEER 2003/02	*Software Framework for Collaborative Development of Nonlinear Dynamic Analysis Program.* Jun Peng and Kincho H. Law. September 2003.
PEER 2003/01	*Shake Table Tests and Analytical Studies on the Gravity Load Collapse of Reinforced Concrete Frames.* Kenneth John Elwood and Jack P. Moehle. November 2003.
PEER 2002/24	*Performance of Beam to Column Bridge Joints Subjected to a Large Velocity Pulse.* Natalie Gibson, André Filiatrault, and Scott A. Ashford. April 2002.
PEER 2002/23	*Effects of Large Velocity Pulses on Reinforced Concrete Bridge Columns.* Greg L. Orozco and Scott A. Ashford. April 2002.
PEER 2002/22	*Characterization of Large Velocity Pulses for Laboratory Testing.* Kenneth E. Cox and Scott A. Ashford. April 2002.
PEER 2002/21	*Fourth U.S.-Japan Workshop on Performance-Based Earthquake Engineering Methodology for Reinforced Concrete Building Structures.* December 2002.
PEER 2002/20	*Barriers to Adoption and Implementation of PBEE Innovations.* Peter J. May. August 2002.
PEER 2002/19	*Economic-Engineered Integrated Models for Earthquakes: Socioeconomic Impacts.* Peter Gordon, James E. Moore II, and Harry W. Richardson. July 2002.
PEER 2002/18	*Assessment of Reinforced Concrete Building Exterior Joints with Substandard Details.* Chris P. Pantelides, Jon Hansen, Justin Nadauld, and Lawrence D. Reaveley. May 2002.
PEER 2002/17	*Structural Characterization and Seismic Response Analysis of a Highway Overcrossing Equipped with Elastomeric Bearings and Fluid Dampers: A Case Study.* Nicos Makris and Jian Zhang. November 2002.
PEER 2002/16	*Estimation of Uncertainty in Geotechnical Properties for Performance-Based Earthquake Engineering.* Allen L. Jones, Steven L. Kramer, and Pedro Arduino. December 2002.
PEER 2002/15	*Seismic Behavior of Bridge Columns Subjected to Various Loading Patterns.* Asadollah Esmaeily-Gh. and Yan Xiao. December 2002.
PEER 2002/14	*Inelastic Seismic Response of Extended Pile Shaft Supported Bridge Structures.* T.C. Hutchinson, R.W. Boulanger, Y.H. Chai, and I.M. Idriss. December 2002.
PEER 2002/13	*Probabilistic Models and Fragility Estimates for Bridge Components and Systems.* Paolo Gardoni, Armen Der Kiureghian, and Khalid M. Mosalam. June 2002.
PEER 2002/12	*Effects of Fault Dip and Slip Rake on Near-Source Ground Motions: Why Chi-Chi Was a Relatively Mild M7.6 Earthquake.* Brad T. Aagaard, John F. Hall, and Thomas H. Heaton. December 2002.
PEER 2002/11	*Analytical and Experimental Study of Fiber-Reinforced Strip Isolators*. James M. Kelly and Shakhzod M. Takhirov. September 2002.
PEER 2002/10	*Centrifuge Modeling of Settlement and Lateral Spreading with Comparisons to Numerical Analyses***.** Sivapalan Gajan and Bruce L. Kutter. January 2003.
PEER 2002/09	*Documentation and Analysis of Field Case Histories of Seismic Compression during the 1994 Northridge, California, Earthquake.* Jonathan P. Stewart, Patrick M. Smith, Daniel H. Whang, and Jonathan D. Bray. October 2002.
PEER 2002/08	*Component Testing, Stability Analysis and Characterization of Buckling-Restrained Unbonded Braces*^{TM}*.* Cameron Black, Nicos Makris, and Ian Aiken. September 2002.

PEER 2002/07 *Seismic Performance of Pile-Wharf Connections.* Charles W. Roeder, Robert Graff, Jennifer Soderstrom, and Jun Han Yoo. December 2001.

PEER 2002/06 *The Use of Benefit-Cost Analysis for Evaluation of Performance-Based Earthquake Engineering Decisions*. Richard O. Zerbe and Anthony Falit-Baiamonte. September 2001.

PEER 2002/05 *Guidelines, Specifications, and Seismic Performance Characterization of Nonstructural Building Components and Equipment*. André Filiatrault, Constantin Christopoulos, and Christopher Stearns. September 2001.

PEER 2002/04 *Consortium of Organizations for Strong-Motion Observation Systems and the Pacific Earthquake Engineering Research Center Lifelines Program: Invited Workshop on Archiving and Web Dissemination of Geotechnical Data, 4–5 October 2001*. September 2002.

PEER 2002/03 *Investigation of Sensitivity of Building Loss Estimates to Major Uncertain Variables for the Van Nuys Testbed.* Keith A. Porter, James L. Beck, and Rustem V. Shaikhutdinov. August 2002.

PEER 2002/02 *The Third U.S.-Japan Workshop on Performance-Based Earthquake Engineering Methodology for Reinforced Concrete Building Structures*. July 2002.

PEER 2002/01 *Nonstructural Loss Estimation: The UC Berkeley Case Study.* Mary C. Comerio and John C. Stallmeyer. December 2001.

PEER 2001/16 *Statistics of SDF-System Estimate of Roof Displacement for Pushover Analysis of Buildings.* Anil K. Chopra, Rakesh K. Goel, and Chatpan Chintanapakdee. December 2001.

PEER 2001/15 *Damage to Bridges during the 2001 Nisqually Earthquake.* R. Tyler Ranf, Marc O. Eberhard, and Michael P. Berry. November 2001.

PEER 2001/14 *Rocking Response of Equipment Anchored to a Base Foundation.* Nicos Makris and Cameron J. Black. September 2001.

PEER 2001/13 *Modeling Soil Liquefaction Hazards for Performance-Based Earthquake Engineering.* Steven L. Kramer and Ahmed-W. Elgamal. February 2001.

PEER 2001/12 *Development of Geotechnical Capabilities in OpenSees.* Boris Jeremić. September 2001.

PEER 2001/11 *Analytical and Experimental Study of Fiber-Reinforced Elastomeric Isolators*. James M. Kelly and Shakhzod M. Takhirov. September 2001.

PEER 2001/10 *Amplification Factors for Spectral Acceleration in Active Regions.* Jonathan P. Stewart, Andrew H. Liu, Yoojoong Choi, and Mehmet B. Baturay. December 2001.

PEER 2001/09 *Ground Motion Evaluation Procedures for Performance-Based Design.* Jonathan P. Stewart, Shyh-Jeng Chiou, Jonathan D. Bray, Robert W. Graves, Paul G. Somerville, and Norman A. Abrahamson. September 2001.

PEER 2001/08 *Experimental and Computational Evaluation of Reinforced Concrete Bridge Beam-Column Connections for Seismic Performance*. Clay J. Naito, Jack P. Moehle, and Khalid M. Mosalam. November 2001.

PEER 2001/07 *The Rocking Spectrum and the Shortcomings of Design Guidelines.* Nicos Makris and Dimitrios Konstantinidis. August 2001.

PEER 2001/06 *Development of an Electrical Substation Equipment Performance Database for Evaluation of Equipment Fragilities.* Thalia Agnanos. April 1999.

PEER 2001/05 *Stiffness Analysis of Fiber-Reinforced Elastomeric Isolators.* Hsiang-Chuan Tsai and James M. Kelly. May 2001.

PEER 2001/04 *Organizational and Societal Considerations for Performance-Based Earthquake Engineering.* Peter J. May. April 2001.

PEER 2001/03 *A Modal Pushover Analysis Procedure to Estimate Seismic Demands for Buildings: Theory and Preliminary Evaluation.* Anil K. Chopra and Rakesh K. Goel. January 2001.

PEER 2001/02 *Seismic Response Analysis of Highway Overcrossings Including Soil-Structure Interaction.* Jian Zhang and Nicos Makris. March 2001.

PEER 2001/01 *Experimental Study of Large Seismic Steel Beam-to-Column Connections.* Egor P. Popov and Shakhzod M. Takhirov. November 2000.

PEER 2000/10 *The Second U.S.-Japan Workshop on Performance-Based Earthquake Engineering Methodology for Reinforced Concrete Building Structures.* March 2000.

PEER 2000/09 *Structural Engineering Reconnaissance of the August 17, 1999 Earthquake: Kocaeli (Izmit), Turkey.* Halil Sezen, Kenneth J. Elwood, Andrew S. Whittaker, Khalid Mosalam, John J. Wallace, and John F. Stanton. December 2000.

PEER 2000/08 *Behavior of Reinforced Concrete Bridge Columns Having Varying Aspect Ratios and Varying Lengths of Confinement.* Anthony J. Calderone, Dawn E. Lehman, and Jack P. Moehle. January 2001.

PEER 2000/07 *Cover-Plate and Flange-Plate Reinforced Steel Moment-Resisting Connections.* Taejin Kim, Andrew S. Whittaker, Amir S. Gilani, Vitelmo V. Bertero, and Shakhzod M. Takhirov. September 2000.

PEER 2000/06 *Seismic Evaluation and Analysis of 230-kV Disconnect Switches.* Amir S. J. Gilani, Andrew S. Whittaker, Gregory L. Fenves, Chun-Hao Chen, Henry Ho, and Eric Fujisaki. July 2000.

PEER 2000/05 *Performance-Based Evaluation of Exterior Reinforced Concrete Building Joints for Seismic Excitation.* Chandra Clyde, Chris P. Pantelides, and Lawrence D. Reaveley. July 2000.

PEER 2000/04 *An Evaluation of Seismic Energy Demand: An Attenuation Approach.* Chung-Che Chou and Chia-Ming Uang. July 1999.

PEER 2000/03 *Framing Earthquake Retrofitting Decisions: The Case of Hillside Homes in Los Angeles.* Detlof von Winterfeldt, Nels Roselund, and Alicia Kitsuse. March 2000.

PEER 2000/02 *U.S.-Japan Workshop on the Effects of Near-Field Earthquake Shaking.* Andrew Whittaker, ed. July 2000.

PEER 2000/01 *Further Studies on Seismic Interaction in Interconnected Electrical Substation Equipment.* Armen Der Kiureghian, Kee-Jeung Hong, and Jerome L. Sackman. November 1999.

PEER 1999/14 *Seismic Evaluation and Retrofit of 230-kV Porcelain Transformer Bushings.* Amir S. Gilani, Andrew S. Whittaker, Gregory L. Fenves, and Eric Fujisaki. December 1999.

PEER 1999/13 *Building Vulnerability Studies: Modeling and Evaluation of Tilt-up and Steel Reinforced Concrete Buildings.* John W. Wallace, Jonathan P. Stewart, and Andrew S. Whittaker, editors. December 1999.

PEER 1999/12 *Rehabilitation of Nonductile RC Frame Building Using Encasement Plates and Energy-Dissipating Devices.* Mehrdad Sasani, Vitelmo V. Bertero, James C. Anderson. December 1999.

PEER 1999/11 *Performance Evaluation Database for Concrete Bridge Components and Systems under Simulated Seismic Loads.* Yael D. Hose and Frieder Seible. November 1999.

PEER 1999/10 *U.S.-Japan Workshop on Performance-Based Earthquake Engineering Methodology for Reinforced Concrete Building Structures.* December 1999.

PEER 1999/09 *Performance Improvement of Long Period Building Structures Subjected to Severe Pulse-Type Ground Motions*. James C. Anderson, Vitelmo V. Bertero, and Raul Bertero. October 1999.

PEER 1999/08 *Envelopes for Seismic Response Vectors.* Charles Menun and Armen Der Kiureghian. July 1999.

PEER 1999/07 *Documentation of Strengths and Weaknesses of Current Computer Analysis Methods for Seismic Performance of Reinforced Concrete Members.* William F. Cofer. November 1999.

PEER 1999/06 *Rocking Response and Overturning of Anchored Equipment under Seismic Excitations.* Nicos Makris and Jian Zhang. November 1999.

PEER 1999/05 *Seismic Evaluation of 550 kV Porcelain Transformer Bushings.* Amir S. Gilani, Andrew S. Whittaker, Gregory L. Fenves, and Eric Fujisaki. October 1999.

PEER 1999/04 *Adoption and Enforcement of Earthquake Risk-Reduction Measures.* Peter J. May, Raymond J. Burby, T. Jens Feeley, and Robert Wood.

PEER 1999/03 *Task 3 Characterization of Site Response General Site Categories*. Adrian Rodriguez-Marek, Jonathan D. Bray, and Norman Abrahamson. February 1999.

PEER 1999/02 *Capacity-Demand-Diagram Methods for Estimating Seismic Deformation of Inelastic Structures: SDF Systems*. Anil K. Chopra and Rakesh Goel. April 1999.

PEER 1999/01 *Interaction in Interconnected Electrical Substation Equipment Subjected to Earthquake Ground Motions.* Armen Der Kiureghian, Jerome L. Sackman, and Kee-Jeung Hong. February 1999.

PEER 1998/08 *Behavior and Failure Analysis of a Multiple-Frame Highway Bridge in the 1994 Northridge Earthquake.* Gregory L. Fenves and Michael Ellery. December 1998.

PEER 1998/07 *Empirical Evaluation of Inertial Soil-Structure Interaction Effects.* Jonathan P. Stewart, Raymond B. Seed, and Gregory L. Fenves. November 1998.

PEER 1998/06 *Effect of Damping Mechanisms on the Response of Seismic Isolated Structures.* Nicos Makris and Shih-Po Chang. November 1998.

PEER 1998/05 *Rocking Response and Overturning of Equipment under Horizontal Pulse-Type Motions.* Nicos Makris and Yiannis Roussos. October 1998.

PEER 1998/04 *Pacific Earthquake Engineering Research Invitational Workshop Proceedings, May 14–15, 1998: Defining the Links between Planning, Policy Analysis, Economics and Earthquake Engineering.* Mary Comerio and Peter Gordon. September 1998.

PEER 1998/03 *Repair/Upgrade Procedures for Welded Beam to Column Connections.* James C. Anderson and Xiaojing Duan. May 1998.

PEER 1998/02 *Seismic Evaluation of 196 kV Porcelain Transformer Bushings.* Amir S. Gilani, Juan W. Chavez, Gregory L. Fenves, and Andrew S. Whittaker. May 1998.

PEER 1998/01 *Seismic Performance of Well-Confined Concrete Bridge Columns.* Dawn E. Lehman and Jack P. Moehle. December 2000.

ONLINE PEER REPORTS

The following PEER reports are available by Internet only at http://peer.berkeley.edu/publications/peer_reports_complete.html.

PEER 2012/103 *Performance-Based Seismic Demand Assessment of Concentrically Braced Steel Frame Buildings.* Chui-Hsin Chen and Stephen A. Mahin. December 2012.

PEER 2012/102 *Procedure to Restart an Interrupted Hybrid Simulation: Addendum to PEER Report 2010/103.* Vesna Terzic and Bozidar Stojadinovic. October 2012.

PEER 2012/101 *Mechanics of Fiber Reinforced Bearings.* James M. Kelly and Andrea Calabrese. February 2012.

PEER 2011/107 *Nonlinear Site Response and Seismic Compression at Vertical Array Strongly Shaken by 2007 Niigata-ken Chuetsu-oki Earthquake.* Eric Yee, Jonathan P. Stewart, and Kohji Tokimatsu. December 2011.

PEER 2011/106 *Self Compacting Hybrid Fiber Reinforced Concrete Composites for Bridge Columns.* Pardeep Kumar, Gabriel Jen, William Trono, Marios Panagiotou, and Claudia Ostertag. September 2011.

PEER 2011/105 *Stochastic Dynamic Analysis of Bridges Subjected to Spacially Varying Ground Motions.* Katerina Konakli and Armen Der Kiureghian. August 2011.

PEER 2011/104 *Design and Instrumentation of the 2010 E-Defense Four-Story Reinforced Concrete and Post-Tensioned Concrete Buildings.* Takuya Nagae, Kenichi Tahara, Taizo Matsumori, Hitoshi Shiohara, Toshimi Kabeyasawa, Susumu Kono, Minehiro Nishiyama (Japanese Research Team) and John Wallace, Wassim Ghannoum, Jack Moehle, Richard Sause, Wesley Keller, Zeynep Tuna (U.S. Research Team). June 2011.

PEER 2011/103 *In-Situ Monitoring of the Force Output of Fluid Dampers: Experimental Investigation.* Dimitrios Konstantinidis, James M. Kelly, and Nicos Makris. April 2011.

PEER 2011/102 *Ground-motion prediction equations 1964 - 2010.* John Douglas. April 2011.

PEER 2011/101 *Report of the Eighth Planning Meeting of NEES/E-Defense Collaborative Research on Earthquake Engineering.* Convened by the Hyogo Earthquake Engineering Research Center (NIED), NEES Consortium, Inc. February 2011.

PEER 2010/111 *Modeling and Acceptance Criteria for Seismic Design and Analysis of Tall Buildings.* Task 7 Report for the Tall Buildings Initiative - Published jointly by the Applied Technology Council. October 2010.

PEER 2010/110 *Seismic Performance Assessment and Probabilistic Repair Cost Analysis of Precast Concrete Cladding Systems for Multistory Buildlings.* Jeffrey P. Hunt and Božidar Stojadinovic. November 2010.

PEER 2010/109 *Report of the Seventh Joint Planning Meeting of NEES/E-Defense Collaboration on Earthquake Engineering. Held at the E-Defense, Miki, and Shin-Kobe, Japan, September 18–19, 2009*. August 2010.

PEER 2010/108 *Probabilistic Tsunami Hazard in California.* Hong Kie Thio, Paul Somerville, and Jascha Polet, preparers. October 2010.

PEER 2010/107 *Performance and Reliability of Exposed Column Base Plate Connections for Steel Moment-Resisting Frames.* Ady Aviram, Božidar Stojadinovic, and Armen Der Kiureghian. August 2010.

PEER 2010/106 *Verification of Probabilistic Seismic Hazard Analysis Computer Programs.* Patricia Thomas, Ivan Wong, and Norman Abrahamson. May 2010.

PEER 2010/105 *Structural Engineering Reconnaissance of the April 6, 2009, Abruzzo, Italy, Earthquake, and Lessons Learned.* M. Selim Günay and Khalid M. Mosalam. April 2010.

PEER 2010/104 *Simulating the Inelastic Seismic Behavior of Steel Braced Frames, Including the Effects of Low-Cycle Fatigue.* Yuli Huang and Stephen A. Mahin. April 2010.

PEER 2010/103 *Post-Earthquake Traffic Capacity of Modern Bridges in California.* Vesna Terzic and Božidar Stojadinović. March 2010.

PEER 2010/102 *Analysis of Cumulative Absolute Velocity (CAV) and JMA Instrumental Seismic Intensity (I_{JMA}) Using the PEER–NGA Strong Motion Database.* Kenneth W. Campbell and Yousef Bozorgnia. February 2010.

PEER 2010/101 *Rocking Response of Bridges on Shallow Foundations.* Jose A. Ugalde, Bruce L. Kutter, and Boris Jeremic. April 2010.

PEER 2009/109 *Simulation and Performance-Based Earthquake Engineering Assessment of Self-Centering Post-Tensioned Concrete Bridge Systems.* Won K. Lee and Sarah L. Billington. December 2009.

PEER 2009/108 *PEER Lifelines Geotechnical Virtual Data Center.* J. Carl Stepp, Daniel J. Ponti, Loren L. Turner, Jennifer N. Swift, Sean Devlin, Yang Zhu, Jean Benoit, and John Bobbitt. September 2009.

PEER 2009/107 *Experimental and Computational Evaluation of Current and Innovative In-Span Hinge Details in Reinforced Concrete Box-Girder Bridges: Part 2: Post-Test Analysis and Design Recommendations.* Matias A. Hube and Khalid M. Mosalam. December 2009.

PEER 2009/106 *Shear Strength Models of Exterior Beam-Column Joints without Transverse Reinforcement.* Sangjoon Park and Khalid M. Mosalam. November 2009.

PEER 2009/105 *Reduced Uncertainty of Ground Motion Prediction Equations through Bayesian Variance Analysis.* Robb Eric S. Moss. November 2009.

PEER 2009/104 *Advanced Implementation of Hybrid Simulation.* Andreas H. Schellenberg, Stephen A. Mahin, Gregory L. Fenves. November 2009.

PEER 2009/103 *Performance Evaluation of Innovative Steel Braced Frames.* T. Y. Yang, Jack P. Moehle, and Božidar Stojadinovic. August 2009.

PEER 2009/102 *Reinvestigation of Liquefaction and Nonliquefaction Case Histories from the 1976 Tangshan Earthquake.* Robb Eric Moss, Robert E. Kayen, Liyuan Tong, Songyu Liu, Guojun Cai, and Jiaer Wu. August 2009.

PEER 2009/101 *Report of the First Joint Planning Meeting for the Second Phase of NEES/E-Defense Collaborative Research on Earthquake Engineering.* Stephen A. Mahin et al. July 2009.

PEER 2008/104 *Experimental and Analytical Study of the Seismic Performance of Retaining Structures.* Linda Al Atik and Nicholas Sitar. January 2009.

PEER 2008/103 *Experimental and Computational Evaluation of Current and Innovative In-Span Hinge Details in Reinforced Concrete Box-Girder Bridges. Part 1: Experimental Findings and Pre-Test Analysis.* Matias A. Hube and Khalid M. Mosalam. January 2009.

PEER 2008/102 *Modeling of Unreinforced Masonry Infill Walls Considering In-Plane and Out-of-Plane Interaction.* Stephen Kadysiewski and Khalid M. Mosalam. January 2009.

PEER 2008/101 *Seismic Performance Objectives for Tall Buildings.* William T. Holmes, Charles Kircher, William Petak, and Nabih Youssef. August 2008.

PEER 2007/101 *Generalized Hybrid Simulation Framework for Structural Systems Subjected to Seismic Loading.* Tarek Elkhoraibi and Khalid M. Mosalam. July 2007.

PEER 2007/100 *Seismic Evaluation of Reinforced Concrete Buildings Including Effects of Masonry Infill Walls.* Alidad Hashemi and Khalid M. Mosalam. July 2007.

The Pacific Earthquake Engineering Research Center (PEER) is a multi-institutional research and education center with headquarters at the University of California, Berkeley. Investigators from over 20 universities, several consulting companies, and researchers at various state and federal government agencies contribute to research programs focused on performance-based earthquake engineering.

These research programs aim to identify and reduce the risks from major earthquakes to life safety and to the economy by including research in a wide variety of disciplines including structural and geotechnical engineering, geology/seismology, lifelines, transportation, architecture, economics, risk management, and public policy.

PEER is supported by federal, state, local, and regional agencies, together with industry partners.

PEER Core Institutions:
University of California, Berkeley (Lead Institution)
California Institute of Technology
Oregon State University
Stanford University
University of California, Davis
University of California, Irvine
University of California, Los Angeles
University of California, San Diego
University of Southern California
University of Washington

PEER reports can be ordered at http://peer.berkeley.edu/publications/peer_reports.html or by contacting

Pacific Earthquake Engineering Research Center
University of California, Berkeley
325 Davis Hall, mail code 1792
Berkeley, CA 94720-1792
Tel: 510-642-3437
Fax: 510-642-1655
Email: peer_editor@berkeley.edu

ISSN 1547-0587X